UNIVERSITÀ
DEGLI STUDI
DI BRESCIA

DOTTORATO DI RICERCA IN INGEGNERIA MECCANICA E INDUSTRIALE (DRIMI)

TeSE – Energy, Fluid & Thermal, and Manufacturing Systems and Technologies

Settore Scientifico Disciplinare (SSD): ING-IND/16

CICLO XXXV

Biomanufacturing Technologies for Tissue Engineering

Dottorando
Leonardo Riva

Relatore
Dott.ssa Paola Serena Ginestra

Advisor
Prof.ssa Elisabetta Ceretti

A.A. 2021-2022

Thesis purpose

Additive manufacturing (AM) has been experiencing strong growth in recent years, especially in sectors such as automotive, aerospace, and biomedical. The main features that have increased its interest are undoubtedly the ability to obtain complex geometries and the possibility to easily modify the final product at low cost. These properties allow for high product customization, which is particularly important in the biomedical field where each person has different needs. Additive manufacturing in the biomedical field is mainly used for the fabrication of models, implants and prosthetics, instrumentation, and for tissue engineering. However, 3D printing also presents some issues. The first is the choice of technology and its associated process. The AM includes a wide range of different technologies, each with its own characteristics and possibilities. Along with the technology, the most suitable material must then be identified. The mechanical properties must be compatible with the final purpose of the object, and usually the number of materials available is smaller compared to traditional technologies. The diversity of the processes, with their associated materials, also makes it difficult to set guidelines that are valid for every printing method, therefore each application requires its own optimization. Moreover, unlike other additive manufacturing products, biomedical products often have to meet biocompatibility and toxicity constraints, and a general lack of standards and regulations on additive manufacturing of biomedical devices makes it more complicated. This thesis focuses on the production of biomedical devices through some of the most popular additive technologies. For each application, the processes and materials deemed most suitable for the purpose were chosen. Subsequently, several printing optimizations were performed to achieve the desired mechanical and biological properties. Specifically, the work focused mainly on the fabrication of two models. The first to study the development of black floaters within the vitreous body of the eye, and the second to emulate the behavior of mandibular bone during drilling for the installation of dental implants.

The eye model consists of two main elements, a scaffold and a hydrogel. The scaffold contains and provides support to the hydrogel. It must be transparent, biocompatible easily handled in the laboratory. It is printed by stereolithography. The hydrogel, on the other hand, is intended to provide a 3D environment for cell growth and development. Therefore, it must be biocompatible and have adequate mechanical properties together with good printability. The 3D scaffold structure was made by material extrusion.

The mandibular bone model was made by fused filament fabrication. The model consists of two parts, a solid outer part to emulate cortical bone, and a porous inner part to emulate trabecular bone. Drilling tests were performed with a dental drill attached to collaborative robots.

Finally, the research covered two additional areas, the study of the properties of lattice structures made by laser-based- powder bed fusion and the evaluation of different surface finish treatments.

In conclusion, this thesis focused on the production of biomedical devices through additive manufacturing. Each technology presented its own specific problems and issues to be addressed. Finally, the study and optimization of the printing parameters allowed the achievement of good results and a deeper understanding of the processes.

Sommario

La manifattura additiva (AM) sta avendo una forte crescita negli ultimi anni, soprattutto in settori come l'automotive, l'aerospace e il biomedicale. Le principali caratteristiche che ne hanno aumentato l'interesse sono senza dubbio la capacità di ottenere geometrie complesse e la possibilità di modificare facilmente il prodotto a bassi costi. Queste proprietà permettono un'elevata personalizzazione del prodotto, particolarmente importante nel settore biomedicale dove ogni persona ha bisogni e necessità diversi. La manifattura additiva nel campo biomedicale è utilizzata soprattutto per la realizzazione di modelli, impianti e protesi, strumentazioni e per il settore dell'ingegneria tissutale. L'utilizzo della stampa 3D presenta tuttavia anche alcune problematiche. La prima è la scelta della tecnologia e del relativo processo. L'AM comprende una vasta gamma di tecnologie differenti, ognuna con proprie caratteristiche e possibilità. Insieme alla tecnologia, va poi individuato il materiale più adatto. La proprietà meccaniche devono essere compatibili con lo scopo finale dell'oggetto e, di solito, il numero di materiali disponibili è ridotto rispetto alle tecnologie tradizionali. La diversità dei processi, coi relativi materiali, inoltre, rende difficile la stesura di linee guida valide per ogni metodo di stampa, rendendo di fatto necessaria un'ottimizzazione per ogni applicazione. A differenza, poi, di altri prodotti della manifattura additiva, i prodotti biomedicali spesso devono anche rispettare vincoli di biocompatibilità e tossicità. A complicare quest'ultimo punto si aggiunge anche una generale mancanza di standard e regolamenti sulla realizzazione additiva di dispositivi biomedicali. Questo lavoro di tesi è focalizzato sull'utilizzo di alcune tra le più diffuse tecnologie additive per la produzione di dispositivi biomedicali. Per ogni applicazione sono stati scelti i processi e i materiali ritenuti più adatti allo scopo. Successivamente, sono state svolte diverse ottimizzazioni di stampa per ottenere le proprietà meccaniche e biologiche desiderate. In particolare, il lavoro si è concentrato principalmente sulla realizzazione di due modelli, il primo per lo studio dello sviluppo dei *black floaters* all'interno del corpo vitreo dell'occhio, il secondo per l'emulazione del comportamento dell'osso mandibolare durante la foratura per l'installazione di impianti dentali.

Il modello dell'occhio è composto da due elementi principali, un supporto e un *hydrogel*. Il supporto serve a contenere e supportare l'*hydrogel*. Deve essere trasparente, biocompatibile facilmente manovrabile in laboratorio. La sua realizzazione è avvenuta tramite stereolitografia. L'*hydrogel*, invece, ha lo scopo di fornire un'ambiente 3D per la crescita e sviluppo delle cellule. Deve perciò anche lui essere biocompatibile e con adeguate caratteristiche meccaniche e di stampabilità. La struttura 3D è stata realizzata tramite *material extrusion*.

Il modello di osso mandibolare è stato realizzato tramite *fused filament fabrication*. Il modello si compone di due parti, una parte esterna piena per emulare l'osso corticale, e una parte interna porosa per emulare l'osso trabecolare. Le prove di foratura sono state realizzate con un trapano dentistico agganciato a robot collaborativi.

La ricerca ha infine toccato ulteriori due ambiti, lo studio delle proprietà di strutture lattice realizzate tramite *laser based- powder bed fusion* e la valutazione di diversi trattamenti di finitura superficiale.

Per concludere, in questo lavoro di tesi si è affrontata tematica della realizzazione di dispositivi biomedicali tramite manifattura additiva. Le varie tecnologie utilizzate hanno permesso di affrontare le diverse problematiche peculiari a ogni processo. Lo studio e l'ottimizzazione dei parametri di stampa ha, infine, permesso l'ottenimento di buoni risultati e un approfondimento della conoscenza sui processi.

Index

Chapter 1

Introduction

In this first chapter a brief introduction on Additive Manufacturing (AM) and biomanufacturing is presented. Firstly, the main additive technologies for the realization of biomedical devices are shown. Secondly, some of the most widely used materials are listed, divided in metals and polymers. Finally, some examples of applications are presented.

1.1 Additive Manufacturing and Bioprinting

Additive Manufacturing (AM) is defined by ASTM F2792 as the process of joining materials to make objects from 3D model data, usually layer upon layer, as opposed to subtractive manufacturing methodologies [1]. It was originally used for rapid prototyping purposes but in these last few years the quality of the produced samples made it spread globally. The growth scenario is based on the change in the demanded necessities that can be summed up in: decrease in volumes, increase in complexity and increase in personalization. These points made the market go from the mass production systems to mass customization systems characterized by a fragmentation of the market, a decrease in the good's life cycle and by increased performances [2]. AM is one of the main tools that can be used to face these changes. Today AM has application in almost every field, from aerospace to constructions, from oil and gas to medical applications.

One of the biggest advantages of AM is the freedom in designing the object. With a layer-by-layer production method there are almost no constraints in the obtainable geometry and it is possible to build parts not achievable, or hardly achievable, by other manufacturing processes. Furthermore, AM allows to create net shape objects with a saving in terms of material waste, in fact the "buy to fly" ratio, the ratio between the input material weight and the final part weight, can be reduced almost to 1 while with traditional machining can rise up to 10 or 20. Moreover, Parts manufactured with conventional methods pass through a lot of different processes: casting, rolling, machining etc. AM allows to build the object in one single step saving a lot of time in terms of logistics and assembly, in fact, parts that before were assembled together now can be produced as a single part. Finally, another high advantage of AM is the possibility to customize the final object. With AM, there are almost no differences in cost for the building of a series of personalized samples or identical parts. The difference between several designs is straightforward with negligible added cost and no need of special preparation [3], the only thing to do is to upload a different CAD model.

There are however some issues that still require research and further development. AM is not ready yet for mass production basically for two reasons: it is a time consuming technology compared to traditional machining and both the materials and the printers have a high costs. These two reasons make AM still not ready for mass production, while for customized products with complex geometry can result more cost effective. Another problem of AM is caused by its layer by layer construction method. The microstructure of the material inside each layer is different compared to the one on the boundaries. This causes an anisotropic behavior with different mechanical properties along the vertical and horizontal directions. Along the building direction the object has usually higher tensile strength and strain.

3D printing for biological purposes is having a significant growth in recent years. Bioprinting combines engineering, life science and 3D printing technologies. Bioprinting can be defined as a biofabrication method in which cells, bioactive molecules, biomaterials, or cell-aggregates are printed to fabricate a construct [4], that can be either a biological model, system, therapeutic product or organ-like structure [5]. Depending on the final application, materials must possess certain characteristics. Some of the most important ones are: biocompatibility, biodegradability, provide a suitable environment for cells, and be easily processable.

In the next sections a brief explanation of the main AM and Bioprinting technologies and materials used for this thesis is proposed, followed by some examples of application.

1.2 Additive technologies

Additive manufacturing comprehends a wide range of technologies based on very different manufacturing processes. Nevertheless, they all have common steps (Fig. 1). Specifically, the object is designed through a CAD software. Then the file is saved as a STL geometry. The STL is fed into a slicing software, which

divides it into layers and for each layer generates the manufacturing path. Finally, this new file is fed into the printer that produces the part. In this section some of the most used technologies to produce biomedical devices are presented.

Fig. 1 Additive manufacturing steps [6].

1.2.1 Laser based powder bed fusion

Laser based powder bed fusion (LB-PBF), also known as selective laser melting (SLM) or direct metal laser sintering (DMLM) [7], is one of the most common metal additive technologies. It consists in a high intensity laser that selectively melts a thin layer of metal powder. The systems consist in a roller, two platforms and a laser (Fig. 2). The roller spreads a thin powder layer from the reservoir platform to the building platform. Then, the laser melts the powder accordingly to the designed path. When the scanning is completed the building platform is lowered, the reservoir platform is raised, and a new layer of powder is spread by the roller. The process continues cyclically in this way until the part is fully built [8]. To prevent the oxidation of the parts during the printing, the build chamber is filled with inert gases such as Argon or Nitrogen. Once the print is finished the excess powder is removed and the part is mechanically detached from the building platform.

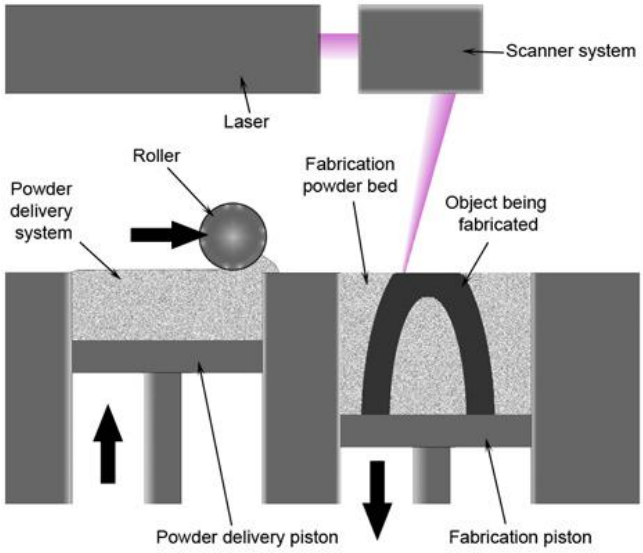

Fig. 2 LB-PBF process [9].

In this process many different parameters can be identify that can influence the final result. The main ones are: laser power, layer thickness, scanning velocity, hatch spacing (distance between laser passes) and scanning strategies [10]. The parameters can be modified according to the outcome to optimize, such as performance or productivity.

LB-PBF allows to produce fully dense parts, however, the properties may differ significantly from a counterpart produced with traditional technologies. The steep thermal gradient due to the rapid melting and solidification of the powder leaves residual stresses and a different microstructure within the part. While the rapid cooling results in a finer microstructure with higher mechanical properties, residual stresses often require some post-processing in order to meet the final requirements.

Many different materials can be processed by LB-PBF technology. Probably the most widely used are Titanium alloys and Steel alloys, but other materials such as Cobalt-Chromium alloys, Aluminum alloys, and Magnesium alloys are also being studied more and more.

Today, due to their properties, parts produced with this technology find applications in areas such as aerospace, automotive and biomedical [11].

1.2.2 Stereolithography

Stereolithography (SLA) was the first AM technology to be developed and was first commercialized in 1987 by 3D System [12]. SLA consists in the solidification and photopolymerization of a liquid resin caused by UV irradiation. Based on the movement of the building platform, SLA can be classified as bottom-up and top-down (Fig. 3). In the bottom-up configuration the building platform is placed just under the bath surface at distance equal to the layer thickness. Once the resin is solidified the platform moves down and new resin cover the surface. In the top-down configuration the platform is dipped at the bottom of the resin tank where a transparent surface let go through the UV light coming from below. Again, once the resin is solidified the platform is risen, new resin fills the space, and the process continues [13]. The top-down configuration offers some advantages with respect to the bottom-up one. Firstly, the prints are smoother because the resin is in contact with the smooth bottom surface of the tank. Secondly, it requires a lower amount of resin inside the tank. Thirdly, the photopolymerized layer is not in contact with the atmosphere limiting the oxygen inhibition. Finally, it is safer due to light being confined inside the printer [14].

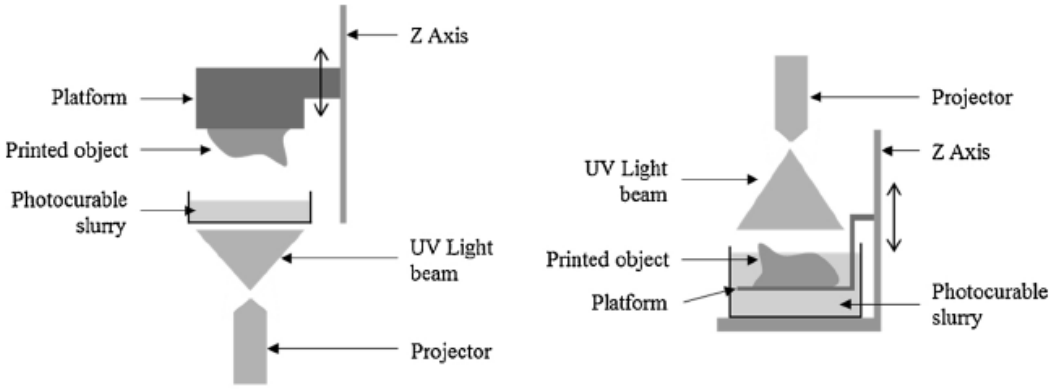

Fig. 3 SLA configurations: top-down (left), bottom-up (right) [15].

In addition, in recent years new systems, such as continuous and volumetric stereolithography, have been developed that increase printing speed.

The as build objects, however, require a post- process to be fully completed. Firstly, the excess resin is rinsed and washed off with a solvent, then the piece is post-cured again with UV light. This step completes the photopolymerization of the resin and improve the mechanical properties of the part.

SLA resins consist of several components mixed together to achieve the desired printability. The main ones are: the monomer/oligomer, the diluent, the chain transfer agent and the photoinitiator. The monomer/oligomer is the reactive prepolymer that gets photopolymerized by the UV light. The diluent is used to reach the desired viscosity of the resin. It also should react with the prepolymer and solidified

with it. The chain transfer agent governs the degree of crosslinking, thus the final properties of the part. The photoinitiator is responsible for initiating the reaction. Upon UV light exposure it generates reactive species that react with the prepolymer and start the polymerization.

Stereolithography shares all the advantages of the AM technologies such as complex shapes fabrication. Among them, however, it is the most accurate one. While the other technologies usually have an accuracy of 50-200 µm, SLA can reach 20 µm. Furthermore, the costs are competitive, and more and more materials are being developed [16].

Like any other technology, also SLA have some drawbacks. The main ones, at least for the most common printers, are a relatively slow printing process due to a lot of downtimes and the possibility to process only one material at a time. However, these issues are being studied and solutions are under development.

Nowadays, stereolithography is certainly one of the most popular additive technologies and finds applications in many fields such as robotic actuators, microfluidics devices and medical devices.

1.2.3 Material extrusion

1.2.3.1 Fused Filament Fabrication

Fused Filament fabrication (FFF) is one of the most widespread AM technologies. It was first developed and commercialized by Stratasys in the 1990s. An FFF printer is basically a computer numerically controlled (CNC) machine equipped with an extruder nozzle. The machine consists of a nozzle, a printing plate, and a reel of material, usually polymeric (Fig. 4). The material is pushed into the nozzle where it is heated and brought to a semi-liquid state [17]. At this point, it is extruded and deposited on the printing plate. Once the layer is completed, the printing plate, or the nozzle, moves of the height of the layer and the new layer is printed. The printer can be equipped with one or more printing nozzle. In the case of a single nozzle, the loaded material will be the modeling material. In the case, instead, of two or more nozzles, an additional modeling material or a support material can be loaded into the additional nozzles. The support material allows the fabrication of overhangs and complex shapes that otherwise would collapse during the printing. The support material can be either easily breakable or soluble [18]. The building plate and the building chamber can also be heated to reduce the thermal gradient and improve the adhesion between layers.

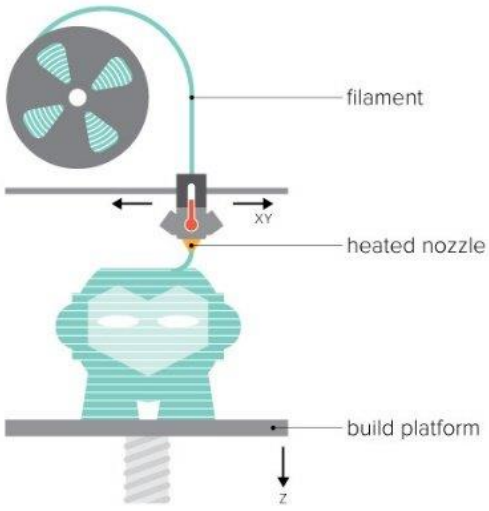

Fig. 4 FFF printing process [19].

Many different process parameters can influence the quality and the final properties of the print [20]. The main ones are: layer thickness, part orientation, nozzle diameter, line width, printing speed, nozzle temperature and plate temperature. All these parameters have an effect on the final result, and they also influence each other. The optimization of the printing parameters depends on the material used and the purpose of the part produced. However, there are general rules that link the parameters to the properties trend.

The most used materials are thermoplastics polymers. Polylactic Acid (PLA), Acrylonitrile butadiene styrene (ABS) and Polycarbonate (PC) are some of the most widespread. To improve the mechanical properties composite filaments have been developed. Composite filaments are composed of two phases, a matrix and reinforcement. The matrix is the base material, the reinforcements are other components added to the matrix. They can be in the form of fibers (short or continuous), particles and nanoparticles [21].

Nowadays, FFF finds application in many fields. In the biomedical area some examples are bone tissue scaffolds, intrauterine system prototype and dental implants.

1.2.3.2 Extrusion bioprinting

Extrusion bioprinting is the most common and accessible method for bioprinting [22]. The printing mechanism is the same as the FFF, but in this case the material is loaded into a cartridge. The material is extruded through the nozzle via a mechanical force that can be either compressed air, a piston or a screw (Fig. 5).

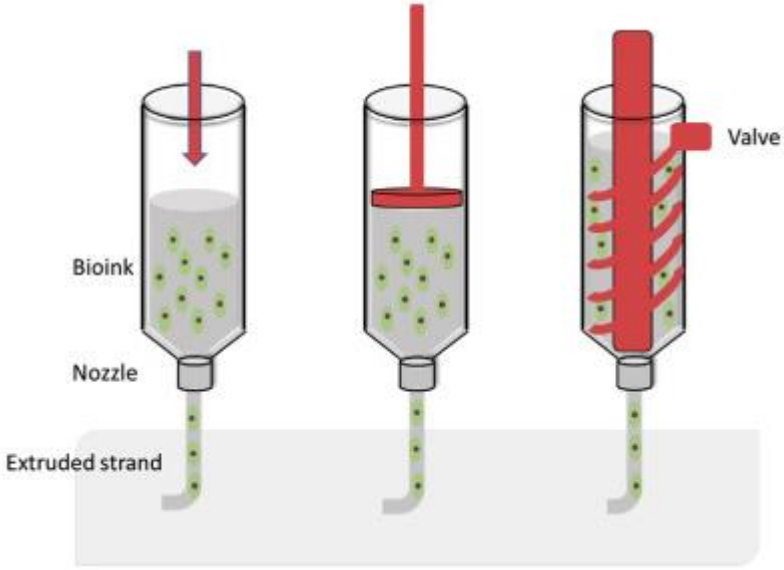

Fig. 5 Extrusion bioprintig methods: pneumatic (left), Piston driven (middle) and screw driven (right) [23].

Extrusion bioprinting material are usually hydrogels, or bioinks, containing single-cell suspensions or cells aggregates. Hydrogels consists in natural polymers with a high water content. This characteristic makes the material very weak structurally, so a crosslinking process is needed after printing to stabilize the structure. The crosslinking of hydrogels can occur in several forms: physically, chemically, or thermally. In some cases, when the material is particularly weak, a supporting bath may be used. The supporting bath consist in a bath of a gel-like material in which the hydrogel is extruded. The bath supports the hydrogel and maintain the stability of the structure until the crosslinking process is finished.

Printability of the hydrogel is a crucial point in extrusion bioprinting. Printability can be defined as the ability to maintain the designed 3D structure. Printability is characterized by three elements: extrudability, filament fidelity and structural integrity [24]. Extrudability refers to the ability to extrude a

continuous and stable filament. Filament fidelity is the similarity between the extruded filament and the designed one. Filament fidelity is not easy to obtain due to the swelling, flow or spreading of the hydrogel during crosslinking and after printing. Structural integrity refers to the maintenance of the printed structure over time. Unfortunately, printability, while critical for the stability of the final structure, can be a problem from a biological point of view. In fact, the more rigid the hydrogel, the more the cells will have difficulty moving, aggregating and performing their biological functions, resulting in a decreased viability. For this reason, it is necessary to find a compromise between the two needs.

The bioprinting process can be divided into three steps: plan, print and process [25]. Planning is divided into structure design and hydrogel selection. Print design should be as simplified as possible consider the feasibility of some variables like needle size, building plate, and printing speed. Hydrogel selection, as stated above, should be based on printability and cell viability. Possible impacting factors are printing pressure and extrusion temperature. Once the planning phase is over, the actual printing phase starts. All parameters are set into the printer and the 3D structure is build. The last step is process. In this step the 3D structure is cultured and analyzed based on the specific need of the application. It is important to consider factors like the length of the study and the media formulation.

Finally, some of the main bioprinting applications are tissue development, disease modeling and biochemical signaling.

1.3 Materials

Additive manufacturing technologies are able to process almost every type of materials, from and polymers to concrete and hydrogels. In this section the material used for this thesis are presented.

1.3.1 Metals

1.3.1.1 17-4 PH Steel

17-4 PH, or AISI 630, is a precipitation hardening (PH) stainless steel. It is a martensitic steel hardened by the precipitation of spherical particles rich in copper in the martensitic matrix [26]. It is one of the most common PH steels and finds application in many fields such as aerospace, chemical and medical [27]. 17-4 PH presents good corrosion resistance up to 315 °C, high strength and toughness [28]. Its final properties are often achieved after an aging treatment with temperatures ranging between 480 and 620 °C. The aging temperature also governs the treatment time, which can vary from a few minutes to a few hours.

Thanks to their high weldability that allows to be processed by powder bed technologies, PH steels have been extensively used in AM [29]. The obtainable mechanical properties of AM 17-4 PH SS not always match the ones obtained by traditional wrought processes. The final result, in fact, is highly influenced by the printing parameters. Laser power, scanning speed and energy density affects surface morphology, volumetric density and mechanical strength [30]. This is because different printing parameters induce a different microstructure in the parts. Other factor influencing the final properties are the building orientation and the cooling rate. LB-PBF processed 17-4 PH parts may not be fully martensitic and retain some austenitic structure [31]. One possibility for improving the final properties of printed parts, as well as optimizing the printing parameters according to the final application, could be to develop powders specifically for AM. In fact, as for many other alloys, the 17-4 PH powder currently used in 3D printing has been developed traditional technologies like castings and forging [32]. Nevertheless, due to its properties, there is a big interest in developing 17-4 PH steel for additive technologies.

For this thesis the LaserForm 14-4PH (B) powder (3DSystems©, Rock Hill, SC) was used (Table 1) [33].

Table 1: powder composition of a LB-PBF 17-4 PH steel.

Element	Fe	Cr	Ni	Cu	Si	Mn	Nb
% of weight	Balance	15-17.5	3-5	3-5	< 1	< 1	0.15-0.45

1.3.1.2 Cobalt-Chromium

Cobalt-Chromium (Co-Cr) alloys are some of the most used biomaterials for density and orthopedics [34]. Their high elastic modulus, biocompatibility, and corrosion resistance make them the material of choice in applications that undergo friction and wear [35]. These properties, together with the design freedom derived from the LB-PBF technology, meant that they were intensively studied in the last few years [36].

Chromium forms a solid solution with cobalt and its responsible for the corrosion resistance. Cr content within alloys usually ranges from 25 to 30 %, higher percentages could result if formation of brittle phases. Other common elements are molybdenum (Mo), niobium (Nb) and carbon (C). molybdenum and niobium are a solution strengthening elements, while carbon highly affect mechanical properties and plasticity [37].

The final properties of the product depend on many factors such as powder, build orientation, process parameters and post processing. The microstructure of a LB-PBF Co-Cr alloy differs greatly from a cast or forged one due to the faster solidification occurring during the AM process. The grains present a columnar structure with a growth along the building direction, opposite to the heat flow direction. The main factors that determine the final grain morphology are the temperature gradient and growth velocity of the solidification front [38]. These factors, ultimately, are dependent on the chosen printing parameters. In fact, laser power, scanning speed, hatch spacing, and layer thickness determine the energy density absorbed by material.

Post processing is often carried out on Co-Cr samples to improve the mechanical and functional properties. Hot isostatic pressing (HIP) is one of the most used for its ability to reduce porosity, residual stresses and microstructural inhomogeneity. Additionally, surface finishing processes like laser polishing can improve the aesthetic of the part and help reach the designed tolerance.

1.3.1.3 Lattice structures

Lattice structures are not a material but 3D structures difficult to realize with traditional technologies but possible with AM. They have been added to the list because they offer great possibilities in the fabrication of biomedical devices like implants and prosthesis.

Cellular structures are usually divided in two major groups: stochastic porous structures and cellular lattice structures [39]. Stochastic porous structures are characterized by pores located randomly throughout the entire volume of the object, thus the mechanical properties present a wide values range and are difficult to control. Cellular lattice structures consist in a unit cell repeated in all direction making the properties controllable and repeatable. Consequently, lattice structures with the same volume fractures present better mechanical properties than stochastic porous structures. Lattice structures can be either strut-based or triply periodic minimal surface (TPMS) (Fig. 6). In the strut-bases structure, the unit cell is made of struts and nodes, where the nodes are the meeting points of the strut's ends. In the TPMS structures the unit cell is composed by an algorithm generated surface with zero mean curvature [40,41].

Fig. 6 Example of strut-based (left) and triply periodic minimal surface (right) structures [42].

The properties of the object can be optimized for a specific loading condition by working on the topology of the unit cell and the dimensions of its components [43].

The interest in lattice material is increasing widely mainly due to the possibility to obtain light-weight, well performing and multifunctional products for different fields of application like aerospace, automotive and biomedical.

The properties of the lattice structures depend by various factors: cell geometry, material, strut dimension, loading direction and boundary condition [44].

Regarding the general behavior of lattice structures, the deformation process usually is composed of three regions: elastic, yielding, and post-yielding where the stress reaches a maximum before dropping to a plateau related to the densification of the material [45].

1.3.2 Polymers

1.3.2.1 Synthetic polymers

Acrylonitrile Butadiene Styrene

Acrylonitrile Butadiene Styrene (ABS) is an amorphous thermoplastic polymer with a glass transition temperature of around 105 °C. It is composed by 3 main monomers: acrylonitrile, styrene and polybutadiene (Fig. 7). It can be considered as a biphasic system in which the first two elements constitute the hard and rigid matrix, while the latter represents the rubbery part dispersed inside. Acrylonitrile provides tensile strength and thermal and chemical resistance, styrene improves stiffness and processability and butadiene increases toughness and low temperature properties [46].

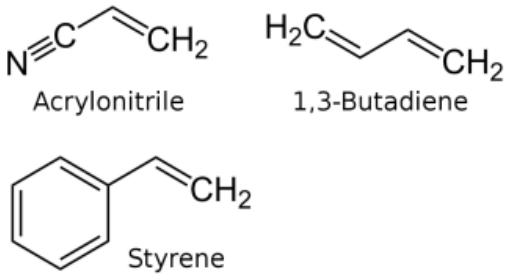

Fig. 7 ABS monomers [47]

Being made by 3 elements ABS is extremely versatile in its final properties. In fact, changing the ratio between the components also changes the properties. Acrylonitrile ranges between 15 to 35 %, styrene from 40 to 60 % and butadiene from 5 to 30 % [48].

ABS is best known for its high impact resistance and toughness [49]. It also characterized by a good surface finishing, chemical resistance and a wide range of operating temperature from -20 to 80 °C. However, it is highly sensitive to UV radiation which limits its use outdoor. A summary of its physical and mechanical properties is visible in Table 2.

Table 2: ABS properties.

Density	1.02e3-1.08e3 kg/m^3
Glass temperature	88-120 °C
Young's modulus	2-2.9 GPa
Tensile strength	30-50 MPa
Toughness (G)	1.35-2.04 KJ/m^2
Temperature range of usefulness	(-20) – (+80) °C

The great quality of abs is not having a specific characteristic but having an excellent set of properties. For this reason, it was one of the first polymers to be implemented in AM and still one of the most widely used.

For this thesis ABSPlus P430 filament (Stratasys©, Eden Praire, MN) was used.

Polylactic Acid

Polylactic Acid (PLA) is a thermoplastic polyester [48] (Fig. 8). It was first synthetized in 1932 by Wallace Carother at DuPont laboratories. Nowadays is one of the most used bioplastics. In Fact. the monomer lactic acid (LA) is derived from natural sources [50]. It is mostly produced from the fermentation of corn starch, sugarcane, potatoes, wheat, rice and other biomasses. PLA can be produced by direct polymerization of lactic acid or by the ring opening polymerization of lactide, lactic acid cyclic dimer. The latter process is usually preferred because it can produce high molecular weight PLA [51].

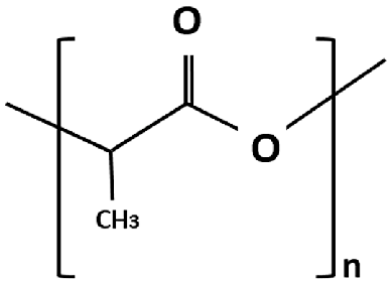

Fig. 8 PLA monomer [52]

Usually, PLA has good mechanical properties. It has better tensile young modulus, tensile strength and flexural strength than other common polymers such as polypropylene (PP), polystyrene (PS) and polyethylene (PE). However, it possesses low toughness, thermal stability and elongation at break so its application is limited where plastic deformation at high stresses is required [53]. PLA presents two mesoforms, D and L. The ratio between the two mesoforms determine the final properties of the material. For example, a PLA with a D mesaform percentage lager than 20% is usually amorphous, while a high crystalline PLA is obtained with an L mesaform percentage higher than 90%. PLA has very good processability and can also be blended with other polymers to improve the desired property. Furthermore, it is recyclable and eco-friendly. A summary of the main physical and mechanical properties of PLA is visible in Table 3.

Table 3: PLA properties.

Density	1.24e3-1.27e3 kg/m^3
Glass temperature	52-60 °C
Melting point	145-175 °C
Young's modulus	3.3-3.6 GPa

Tensile strength	55-72 MPa
Toughness (G)	3.32-6.49 KJ/m^2
Elongation at yield	2-3.5 %Strain

However, the main and desirable properties of PLA are its biocompatibility and biodegradability. Being a biopolymer, the biodegradation occurs by hydrolysis of the polymer or by the attack of micro-organism found in the environment. The rate of degradation is influenced by properties like crystallinity, molecular weight and water diffusion and other factors like temperature and humidity. PLA does not have any toxic or carcinogenic effects and it has been approved for application in contact with body fluids such as implants, surgical sutures and drug delivery.

Nowadays PLA is probably the most used material in FFF with an annual growth rate of around 20%.

For this thesis Pearl White PLA filament (Ultimaker©, Utrecht, Netherlands) was used.

Polycarbonate

Polycarbonates (PCs) are a class of polymers with a carbonate group in their backbone [54]. PCs where first synthetized in the 1880s and nowadays they are widespread in different fields. Based on the R group in their structure (Fig. 9), they can be divided into aliphatic or aromatic polycarbonates. Compared to the aromatic, aliphatic PCs do not possess any particular properties, so they received less attention over time [55]. Between the aromatic PCs, the most common is the one derived from bisphenol A. The main process to synthetized PC is through polycondensation in phosgene. This process is advantageous due to the moderate reaction conditions required, the easy synthesis and the high quality of the final product. However, the use of chlorinated solvents and the toxicity of phosgene are points that require special attention from the environmental point of view. Other synthesis mechanisms are melt transesterification and ROP of cyclic oligomers [56].

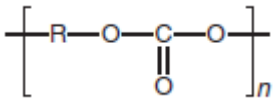

Fig. 9 Polycarbonate structure

PC is used as an engineering polymer due to its strength, toughness, excellent impact resistance and transparency. It has thermal and dimensional stability, it is light, biocompatible and easily processable. The major drawbacks are high melt viscosity, notch sensitivity and limited chemical and UV resistance. Some of the PC physical and mechanical properties are visible in Table 4.

Table 4: PC properties.

Density	1.19e3-1.21e3 kg/m^3
Glass temperature	142-158 °C
Young's modulus	2.32-2.44 GPa
Tensile strength	62.7-72.4 MPa
Fracture toughness	2.1-2.3 MPa.m^0.5
Elongation	110-150 %Strain

PC finds application in many fields. Example of articles produce with PC are safety goggles and telephone parts, bumpers, headlights lenses and helmets [57]. For outdoor application it requires a coating to reduce UV degradation.

PC is also used in blends. Approximately 15 percent of the PC is destined for the production of blend, especially with ABS or SAN [46].

For this thesis black PC filament (Ultimaker©, Utrecht, Netherlands) was used.

Resins

Photosensitive resins are liquid prepolymers that crosslink and harden due to irradiation. In order to be functional, they must possess adequate chemical, optical and rheological properties [58]. These properties directly influence the curing kinetics, cure depth and resin spreading, fundamental elements for a successful printing. What gives the resin its properties are the components within it. The main elements are: photoinitiators, monomers/oligomers and additives such as photoabsorbers, sensitizers and diluents.

Photoinitiators react with the energy from the irradiation and generate a reactive species. The reactive species then react with the monomer/oligomer and start the polymer chain growth. Photoinitiators can be either free radicals or cationic. Free radical photoinitiators are divide in Norrish type-I and type-II. Type-I constitute most of the commercially available free radical photoinitiators. They undergo α-cleavage reaction governed by light wavelength and intensity [59]. The most common type of type-I free radical initiator are acyl phosphine oxides due to their fast photolysis and efficient extent of cure and polymerization rate. On the other hand, cationic photoinitiators are usually iodonium and sulfonium salts. They are characterized by thermal stability, solubility in monomers and efficiency.

Monomers/oligomers are the main elements of the resins. They have a great impact on the final geometric accuracy and mechanical properties. The most common monomers/oligomers are methacrylates, epoxides and vinyl ethers. Acrylates undergo free radical photopolymerization. Their main advantages are low viscosity controllable mechanical properties and rapid curing. However, the present poor dimensional stability due to high shrinkage. Epoxides and vinyl ethers, instead, undergo cationic photopolymerization. Epoxides present good mechanical properties, dimensional stability and polymerization goes on for a long time after the end of the irradiation. Nevertheless, they exhibit low toughness [60]. Vinyl ethers increase the reactiveness and curing rate when mixed with epoxides.

Compared to monomers, oligomers are bigger molecules with higher functionality and more voluminous groups.

Additives increase the performance of the resins. Photoabsorbers reduces light penetration inside the resin and allows for the fabrication of thinner layers. Sensitizers increases the formation of the reactive species. Finally, diluents regulate the viscosity.

In biomedical application resins must be biocompatible, with no cytotoxic or mutagenic effects. Photoinitiators are the main cause of cytotoxicity that generally increases with their concentrations. A known biocompatible photoinitiator is N,N-dimethylaminobenzoic acid ethyl ester and camphorquinone.

For this thesis namely biocompatible resins Clear and Tough resin (3DResyns©, Barcelona, Spain) and Dental LT and Elastic 50A resins (both from Formlabs©, Somerville, MA) were used.

1.3.2.2 Natural polymers

Gelatin

Gelatin is a natural biopolymer made by amino acids linked by peptides [56]. It is derived by the controlled hydrolysis of collagen found in cattle bones, hides, pig skin mammals and fish. In brief, collagen is cut into small pieces, washed and transferred in hot water to decrease the fat content. After being dried, it is then treated with a solution that can be either acid or alkaline. After that gelatin is extracted at high temperature, purified and shaped to its final form depending in its final application [61]. Acid and Alkaline solutions give two different types of gelatins. The acid solution result in gelatin type A, while the alkaline solution result in gelatin type B. The two types of gelatins differ in their physicochemical properties. For example, at physiological pH, type A is positively charged, and type B is

negatively charged due to a different isoelectric point. It has also been reported that type A is slightly more viscous while type B has better biocompatibility.

Despite some differences due to the source of collagen and the production process, gelatins present desirable properties such as good biocompatibility, water solubility, plasticity, promotion of cell adhesion and formation of transparent gels [62]. Gelation is driven by hydrogen bonding and van der Waals interaction. However, it occurs by cooling at temperature around 30 °C, thus an additional crosslinking is necessary to maintain gelation at body temperature.

Partly due to its relatively low cost, gelatins find application as emulsifiers, gelling agents in food, pharmaceutical and cosmetics manufacturing [63]. In the medical field is used as matrix for implants, device coater and long-term delivery system.

Alginate

Alginates are natural polymers derived from alginic acids. They are usually extracted from brown algae by treating them in aqueous alkali solutions. The extract is then filtered, sodium or calcium chloride is added and alginate precipitates. After filtration and conversion alginate powder is produced [64]. Another, less common, way to produce alginate is through bacterial biosynthesis. Though bacterial modification is possible to produce alginates with custom features. One of the most common alginates is sodium alginate.

Alginates consist of two copolymers, D-mannuronic acid (M) and L-guluronic acid (G), arranged in blocks (Fig. 10). Blocks can be either made of consecutive M, consecutive G or alternating MG. Alginates derived from different sources differs in the quantity of G and M and in the blocks length [65].

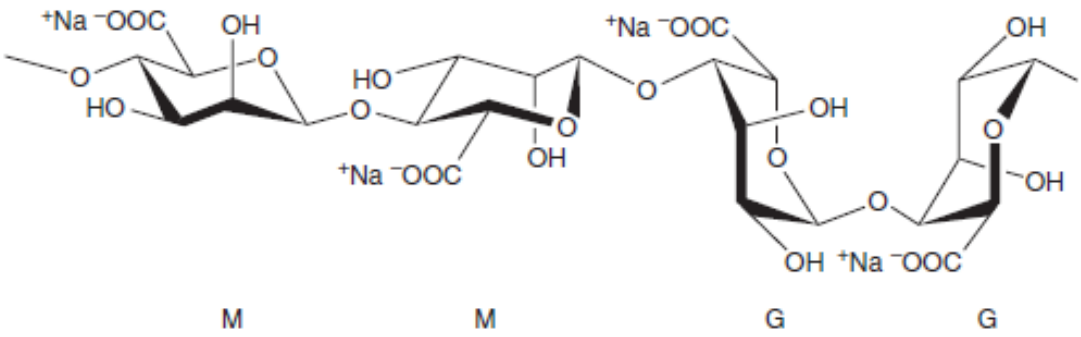

Fig. 10 Example of Sodium alginate structure

Alginates can be turned into a hydrogel via chemical or physical crosslinking. The most common way to crosslink alginate is through contact with divalent cations such as Ca^{2+}. Calcium Chloride ($CaCl_2$) is probably the most used agent to provide cations. The cations react with the G residues that fold and form rigid structure. Only the G residues reacts with the cations, thus the composition of the alginate plays a main role in determine the physical properties of the hydrogel. $CaCl_2$ crosslinking, however, is fast and difficult to control, often resulting in a nonuniform structure. Other possible alginates crosslinking methods are covalent crosslinking, thermal gelation and cell crosslinking.

Alginate hydrogels have a high water content, holding more than 98% of water inside the structure. They also are mucoadhesive, biocompatible and non-immunogenic, making it very suitable for biomedical applications [61]. Some examples are tissue engineering for the regeneration of various tissues, cells encapsulation for controlled drug release and wound healing [66].

Decellularized Extracellular Matrix

The extracellular matrix is the noncellular component of tissues. It is composed of proteins and carbohydrates and performs several fundamental functions [67]. Some examples are structural support, biomechanical signaling, biochemical signaling, dynamic remodeling and degradation of products. Each tissue has it own extracellular matrix with specific functions.

Through different processes called decellularizations, it is possible to produce printable hydrogels from extracellular matrices. The decellularization process consists in taking a tissue and remove both cells and cell debris. Decellularization processes can be divided in three groups: biological, chemical and physical [68]. Biological decellularization consists in exposing the tissue to enzymes. Chemical decellularization uses solutions. Examples of solutes are acids, alcohols and detergents. Physical decellularization is used complementarily or as pre-treatment to the other two. Examples of physical processes are mechanical agitation, pressure gradients and freeze/thaw cycles. After the decellularization protocol the decellularized extracellular matrix (dECM) retain the structure and the biochemical composition (proteins, proteoglycans and glycosaminoglycans) of the native tissue. To produce a printable hydrogel the dECM must be digested with an enzymatic agent. The process, usually carried out with pepsin, homogenize the solution but unfortunately destroys the architecture and topology of the ECM [69]. Not every dECM is suitable to become a printable hydrogel. Some factors like printability, cell viability, mechanical properties and remodeling capability must be considered.

The dECM derive hydrogels have a great potential in bioprinting due to the possibility to provide cells with the proteins of their natural environment [70]. Furthermore, they are in liquid form at cold temperature and gel at 37°C allowing a three-dimensional structure to be maintained at body temperature.

There are some things to take into consideration while making dECM. Firstly, the freshness of the tissue is essential for the successful completion of the procedure. Secondly, the amount of dECM that is obtained is extremely less than the starting tissue. Thirdly, residues of native DNA or toxic chemical can jeopardize the correct cellular activity. Nevertheless, despite some solvable issues, dECM could be the most promising hydrogel source in bioprinting [71].

For this thesis a hyaline cartilage dECM was used.

1.4 Applications

Additive manufacturing is increasing its application in many fields such as automotive, aerospace, pharmacy, industry and biomedical. Especially in the biomedical field, where every patient is different, the achievable high degree of customization and the ability to easily obtain complex geometries are important and fundamental features. Speed of production and good precision are additional important characteristics [72]. All these elements have made possible the ever-increasing use of additive manufacturing in the biomedical field. Nowadays, application of AM in the biomedical fields can be grouped into five different groups. (I) medical models, (II) implants and scaffolds, (III) tools, instrument and parts for medical devices, (IV) medical aids, guides, splints and prosthesis, (V) biomanufacturing [73].

Medical models are fabricated by directly scanning the affected body part. In this way, a faithful reproduction of the patient's anatomy can be obtained. Medical models are used for pre and postoperative planning, training. They can also serve as an information tool for patients and their families. Training models, in addition to geometry, must also provide feedback as close as possible to the real tissue. For example, model for bone drilling training must provide a resistance and a feeling similar to real bone.

Implants are designed to physically replace defective or missing tissue to take over its functions. They may stay inside the patient body for a long period so they must be biocompatible and not degradable. Examples of implants are hip or knee joints and dental crowns. Implants are often fabricated through PBF techniques. Scaffolds, instead, are non permanent implants. They are more complicate than the permanent

ones because, other than the structural requirements, they must also degrade inside the body. They need to provide a porous network for cell attachment and spreading. The degradation rate and cell replacement rate should also match.

Tools, instruments and parts form medical devices are designed to improve and facilitate clinical operation. They can be customized based on the patient dimensions and shapes. Some examples are surgical instruments or drilling guides.

Medical aids, supportive guides, splints and prosthesis are supports external to the body that can help in the postoperative or trauma recovery. Motion guides, fixators, external prosthesis and customized splint belong to this class of application.

Biomanufacturing combine AM with cell culture. Porous structures are designed for a three-dimensional culture of cells. Cells can be either seeded inside the material or added subsequently. The gaal is to fabricate real body tissues for medical and clinical testing, studying disease and analyze antidote response [74]. However, the ultimate objective of biomanufacturing and tissue engineering is the realization of fully functional organs.

1.4.1 Examples

In this section some practical examples of additive manufacturing application in the biomedical field are presented.

Wang et al. [75] fabricated a template to precisely inserts screws during a spinal surgery. The template was designed on the scan of the vertebra and fabricated through PBF. The fitting of the template was investigated with a 3D printed model of the vertebra. Finally, the template was used during the surgery and allowed a precise and easier insertion of the screws (Fig. 11).

Fig. 11 Template fitted on the printed model of the vertebrae (left). Positioning of the template during surgery (righ)

Arabnejad et al [76] designed a high strength fully porous hip implant (Fig. 12). The lattice architecture allowed the fine tuning of the mechanical properties to match the bone tissue. Thus, the bone loss due to stress shielding is reduced by 75% compared to a fully solid implant. Furthermore, the implant respected the bone ingrowth requirements at the implant interface.

Fig. 12 Printed implant.

Höhne et al. [77] designed and printed a training and educational model for crown preparation (Fig. 13). The tooth model presented different layers for enamel and dentin. The model was judged by dental students and experienced dentists through a questionnaire. Both groups valuated good the training effect of the model.

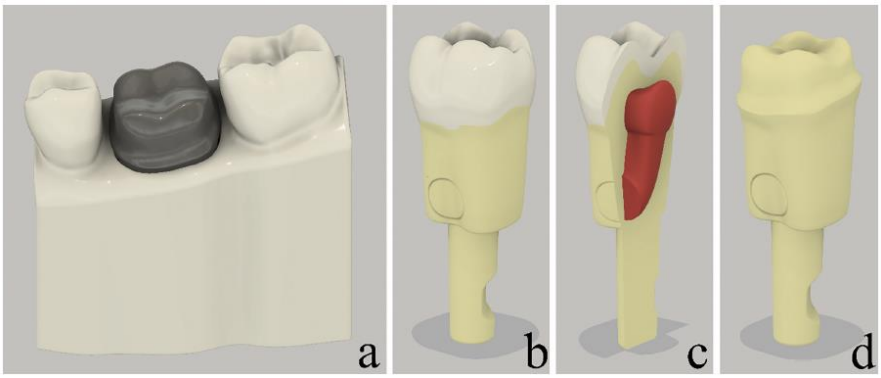

Fig. 13 tooth model with prepared tooth in grey for viewing crown preparation (a); complete tooth with enamel part in with and dentin in yellow (b); cross-section of tooth with pulp in red (c); tooth after preparation with removed enamel (d).

Xie et al. [78] fabricated a life-size eye model for fundus range viewing research (Fig. 14). The 3d printed structures was assembled with a PMMA aspherical cornea, variable iris and IOLs. When assembled the model resulted a useful tool for the fundus viewing studies.

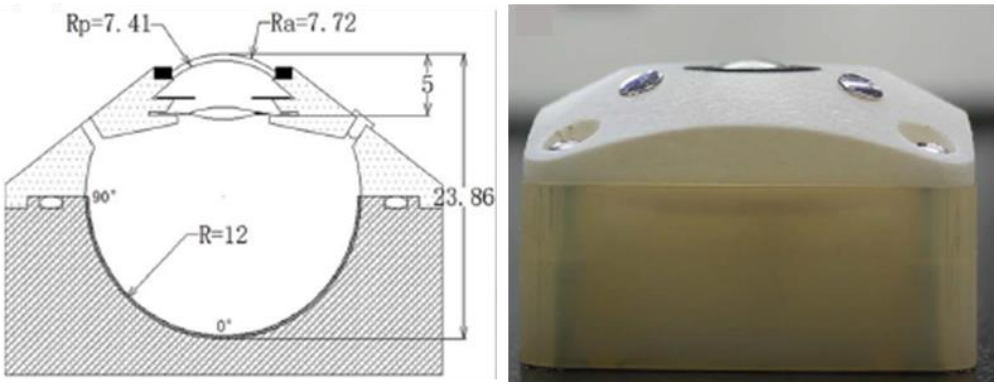

Fig. 14 Scheme of the model (left); assembled model (right).

Isaacson et al. [79] studied the feasibility of the production of an artificial cornea using a collagen based bioink containing corneal keratocytes cell (Fig. 15). The keratocytes cell showed high cell viability highlighting the potential of bioprinting for cornea substitutes developments.

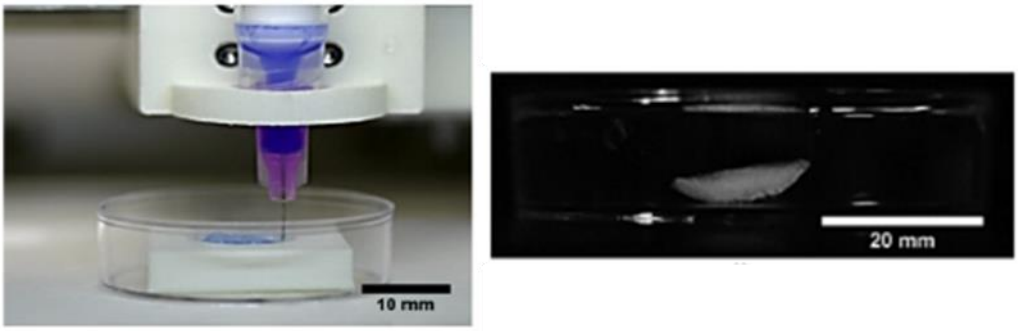

Fig. 15 Printing process of the cornea(left); printed cornea (right).

Finally, Heinrich et al. [80] bioprinted mini-brains to study the interaction between glioblastoma cells and macrophages (Fig. 16). The model was able to show that the glioblastoma cells interact with the macrophages increasing their progression and invasiveness in the mini-brain. The biomodel resulted useful in the understanig of tumor biology and evaluating of novel cancer therapeutics.

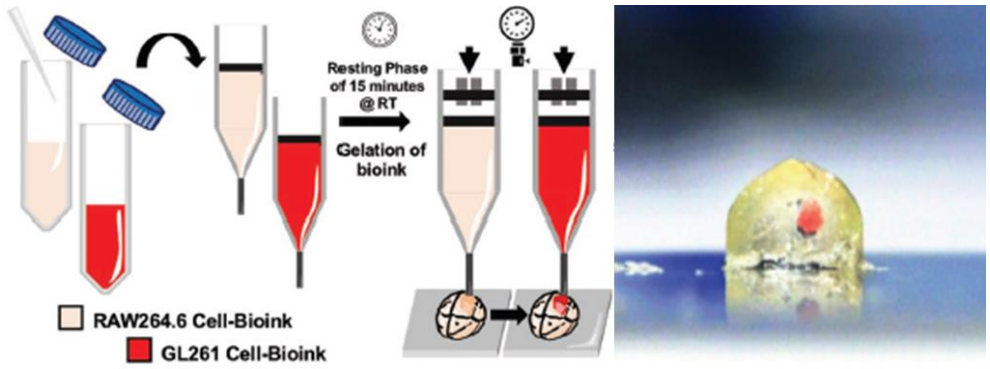

Fig. 16 Printing process of the mini-brains (left); cross-section of the printed mini-brain, glioblastoma area highlighted in red (right).

Chapter 2

Laser Based Powder Bed Fusion (LB-PBF) for bone application

In this chapter the works focused on the testing and characterization of lattice structures produced via Laser Based Powder Bed Fusion (LB-PBF) are presented. Firstly, an intensive review of the most used parameters to mechanically characterize metal lattice structure is reported. Secondly, the compression tests of 17-4 PH Steel lattice samples with radially oriented cells are analyzed. The published papers related to these topics are listed below:

- L. Riva, P.S. Ginestra and E. Ceretti, "Mechanical characterization and properties of laser-based powder bed–fused lattice structures: a review", Int J Adv Manuf Technol 113 (2021), pp. 649–671.
  In this work, the candidate was responsible of the literature search, data collection and organization, and writing and editing of the draft.

- P.S. Ginestra, L. Riva, G. Allegri, L. Giorleo, A. Attanasio and E. Ceretti, "Analysis of 3D printed 17-4 PH stainless steel lattice structures with radially oriented cells", Ind. 4.0 – Shap. Futur. Digit. World (2020), pp. 136–141.
  In this work, the candidate was responsible of the production of the specimens and subsequent testing and investigations. Furthermore, he analyzed the collected data.

2.1 Mechanical characterization and properties of Laser-Based Powder Bed Fused lattice structures: a Review

2.1.1 Introduction

Additive Manufacturing (AM), commonly known as 3D printing, have faced an extraordinary growth during the last years [1-3]. AM is defined by ASTM F2792 as "the process of joining materials to make objects from 3D model data, usually layer upon layer, as opposed to subtractive manufacturing methodologies" [4]. Briefly, a CAD model of the parts is divided in cross-sectional layers by a slicer software and uploaded into the printer that proceeds to build the object adding the material only where it is needed following the cross-section sequence [5]. AM was originally used for rapid prototyping purposes but in the last few years the quality and performances of the produced samples made it spread globally. This expansion is intended to continue in the next years, in fact if the value of the AM market in 2016 was around 7 billion of dollars, it is estimated to reach about 27 billion in 2022 [6]. Polymers are the most used material in AM but in the last few years metals have had the biggest growth rate. Among the technologies able to 3D print metals, laser-based powder bed fusion (PBF-LB) is one of the most used. PBF-LB is a powder bed fusion system in which a laser beam is used to locally melt metallic powder. More specifically, an PBF-LB system consists in a roller, two platforms and a laser [5]. The roller pushes a thin layer of metallic powder on the building platform, then the laser melts the powder following a filling strategy of the cross section of the designed object [7]. Once the layer has been completely melted and solidified the building platform moves down, the feeding platform rises and the roller spreads another layer of powder (Figure 1). The laser melts the second layer of powder that will adhere to the lower layer. Once the process is completed the unmelted powder is typically collected with a vacuum cleaner to be reused. PBF-LB allows the fabrication of almost fully dense metallic parts with the advantage of a high degree of precision and freedom of design [8,9]. In fact, it is possible to produce porous structures not obtainable with the traditional technologies [10]. These structures, called lattice, are composed by struts and nodes, where nodes are the meeting points of the struts' end. Lattices can be either stochastic or made by the repetition in different direction of a unit cell with a defined geometry [11]. Stochastic lattice structures have not fully predictable mechanical properties due to the random distribution and orientation of their struts and nodes, limiting their actual use. Unit cell lattice structures instead, are the most studied due to their repeatable mechanical properties that can match the properties of bulk parts but with significant lower weight. Furthermore, they have demonstrated good energy absorption as well as good thermal and acoustic insulation [12]. Lattice structures can be classified based on their deformation behavior, typically divided into two different deformation mechanism: bending dominated and stretch dominated. Bending dominated structures have lower mechanical strength and higher energy absorption properties while stretch dominated structure have opposite characteristics [13]. Moreover, it is possible to predict the deformation behavior of the structure based on the geometry of the cell. Metal lattice structures have several possible applications but the aerospace, automotive and biomechanical fields are the main ones for lattices design and evaluation. The aerospace and automotive research is always looking for light weight components with optimal mechanical properties to reduce fuel consumption and carbon emissions while maintaining the structural integrity and safety of the part [14]. Mines et al. [15] and Chantarapanich et al. [16] studied the mechanical properties of sandwich lattice panels as impact absorbers and load carrier. Bici et al. [17] investigated a novel wing leading edge that serves both as an impact absorber and an anti- ice system. Miller et al. [18] patented a new system to protect a flight recorder. Büşra et al. [19] after topology optimizing a suspension arm infilled it with lattice obtaining both strength improvement and weight reduction. On the other hand, in the biomedical field, the lattice structures are of particular interest for the production of bone scaffolds [20,21]. Dr.

Joseph became the first surgeon to use a lattice spinal implant during a surgical operation [22]. Many other researchers investigated the feasibility and mechanical properties of porous femoral, hip and knee implants. Limmahakhun et al. [23] studied a graded femoral stem that controls the micromotions in an acceptable range for bone ingrowth with a flexural stiffness similar to the human bone. Hazlehurst et al. [24] developed a femoral stem 48% lighter and 60% more flexible than a traditional one. España et al. [25] built an implant with a Young modulus matching the cortical bone reducing the stress shielding effect and increasing the *in-vivo* life. Moreover, Wang et al. [26] designed a hip prosthesis able to increase the stability of the bone-implant interfaces. Arabnejad et al. [27] developed a systematic approach to design hip implants with a considerable decreasing of resorption secondary to stress shielding. Murr et al. [28] demonstrated a biocompatible, customized knee implant with comparable bone stiffness to the natural tissue. Furthermore, Wathule et al. [29] observed no cytotoxicity and good bone ingrowth on a lattice tantalum implant in an in vivo experiment on a rat femur.

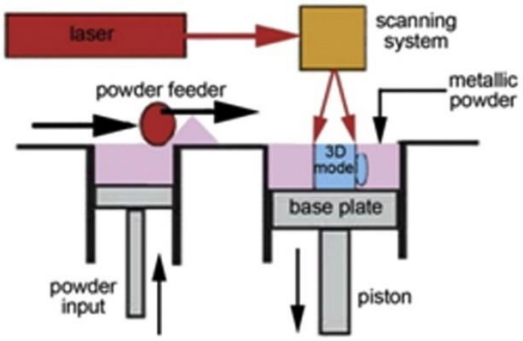

Fig. 1 Scheme of the laser-based powder bed fusion process [7].

For both the application fields mentioned above the most studied material is Ti-6AL-4V alloy due to its high mechanical properties and excellent biocompatibility, however many other materials such as 316L stainless steel, CoCr and Al-10Si-Mg have been studied.

Lattice structures have been deeply tested to characterize and validate their mechanical performances. Considering the overarching context of application, the compression test is the most used to characterize these structures but in the last few years, tensile, fatigue and bending tests have been carried out to broaden the knowledge of lattices mechanical response. The compression test is usually carried out following the ISO 13314 (related to compression tests for porous and cellular metals) that, although it is not specific for additively manufactured samples [30], provides good indications on which parameters to use during the test. For other characterization tests, there is not a standard for porous or cellular samples. In the absence of a specific international standard regarding the mechanical characterization of these structures, this review aims to point out which are the methodologies, instrumentations and parameters most used by the researchers around the world to provide a possible useful guideline for further developments in design, evaluation and applications of PBF-LB metal lattices. The review is intended to report the focal points of the PBF-LB process involving the design, material and process parameters of the PBF-LB technology leading to the mechanical tests parameters and outputs collected by several studies with different purposes and application objectives. Although many 3D technologies enable the production of metal lattice structures, the author decided to focus on PBF-LB due to the several number of papers that report mechanical tests data on PBF-LB lattice samples.

2.1.2 Production process

In this section, the fundamental aspects for the production of lattice structures will be illustrated, in particular cells geometries, materials used and printing parameters applied for the PBF-LB process.

2.1.2.1 Cell geometry

Cellular structures are available in nature to optimize energy consumption, such as honeycombs, bones and wood. These structures, despite their light weight and high porosity, have a great load capacity and high functionality [31]. Many manufacturing techniques as investment casting, deformation forming and metal wire approaches were used to produce these structures, but the processes were complex and with several drawback [32]. Only the recent development of 3D printing made the production of these structures, called lattice, really possible. Lattice structures consist of a base unit cell with a defined geometry repeated periodically in space [33]. Lattices can be categorized in different ways, 2D or 3D, random or periodic, open or closed [31], homogeneous or heterogeneous [34] but the most particular ones are strut-based or triply-periodic-minimal-surfaces (TPMS). Within the strut-based lattice, the unit cell is composed by a group of crossbars (s) interconnected with each other in points called nodes (n). The most significant lattice structures are shown in Figure 2 where the most used strut-based are the body-centered-cubic (BCC), the face-centered-cubic (FCC) and the diamond.

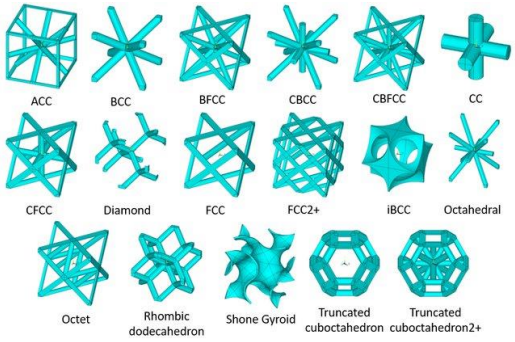

Fig. 2 Examples of lattice structures unit cells [35].

The number of struts (s) and nodes (n) of the unit cell is crucial to predict its deformation mechanism. In fact, they can influence the degree of connectivity and freedom of the unit cell that can be quantified with the Maxwell number (M) (Eq. 1):

$$M = s - 3n + 6 \quad (1)$$

Where M is the Maxwell number, S is the number of struts and n is the number of nodes inside the unit cell. If M < 0 the structure is *under-stiff*, the struts are unable to equilibrate the external forces, moments are transferred to the nodes and the deformation behavior is bending dominated. If M >= 0 the structure is *over/just stiff*, the moments are not transferred to the nodes and the deformation behavior is stretch dominated [36]. Stretching dominated structures are characterized by higher modulus and yield strength [37]. The higher the number of the struts and nodes, the higher the Maxwell number and the higher will be the mechanical strength and cell stiffness. Although the Maxwell number is a good method to predict the deformation behavior of the structure, it is not always a reliable coefficient since the strut configuration and alignment cannot improve the cell stiffness but increase the Maxwell number [36]. The unit cells of strut-based lattice structures cannot exceed 5 mm size due to manufacturability problems of overhanging struts [38], however the majority of the application requires smaller sizes.

As cited above, the other type of lattice structures are the triply-periodic-minimal-surfaces, porous structures with zero mean curvature of the surface [39]. TPMS are generated by algorithms [31] and can be represented by mathematical equations. The main TPMS structures are the gyroid and the diamond represented by these equations (Eq. 2 and 3) [39]:

$$\text{Gyroid: } F(x,y,z) = \cos x * \sin y + \cos y * \sin z + \cos z * \sin x + a \quad (2)$$

$$\text{Diamond: } F(x,y,z) = \sin x * \sin y * \sin z + \sin x * \cos y * \cos z + \cos x * \sin y * \cos z + \cos x * \cos y * \sin z + a \quad (3)$$

Anyhow, the most used TPMS structure is the gyroid (Fig. 3), without straight lines [41] but a spherical core and smooth struts, being self-supporting [38]. Contrarily to the strut-based structures, TPMS structures have an inferior limit on the unit cell size to allow the powder removal from the voids [38].

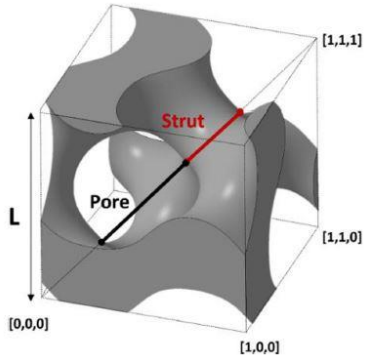

Fig. 3 Geometry and characteristics of the gyroid unit cell [40].

Regarding the general behavior of lattice structures, the deformation process usually is composed by three regions: elastic, yielding and post yielding where the stress reaches a maximum before dropping to a plateau related to the densification of the material [42]. The mechanical behavior is influenced by many factors including the printing process and the microstructure [42], but the material, topology and relative density of the sample are the main aspects that control the structural properties [43]. Generally, if the relative density decreases, the stiffness and the strength decrease as well [44]. In particular, this relationship can be linear in case of a stretching dominated structure or in form of a power law for a bending dominated structure [45]. Typically, the relative density increases with the decreasing of the unit cell size while the stiffness and strength decrease when the unit cell size increases [38]. For these reasons, the excessive reduction of the strut size can have an unexpected effect on the mechanical properties.

The design of a lattice structure is a two steps process: design of the unit cell and design of the pattern. There are three ways to design a unit cell: a primitive base method, based on a Boolean operation of geometric primitives, an implicit surface based method, based on equations that describe the surface of the unit cell in space, and topology optimization, based on algorithms that optimize the distribution of the material.

On the other hand, there are three methods for the pattern design: direct patterning, where the unit cell is repeated along the three dimensions (the most common technique), conformal patterning, where the unit cells are positioned in order to match a specific shape or a topological optimization [32].

Lattice structures can be designed with conventional CAD systems with limits related to the cell repetition in large scale to obtain the structure. Alternatives are MATLAB® [11] or specialized tools. However, the printers supporting software is typically equipped with an integrated library of the unit cells geometries, for example the 3DXpert modules of the 3D systems© printers.

2.1.2.2 Materials

The most common materials used for the fabrication of lattice structures are Ti-6Al-4V, 316L Stainless Steel, CoCr, Al-Si alloys and Ni alloys.

Ti-6Al-4V is the most used type of Titanium around the world and holds alone almost half of the global Titanium market [46]. It is an excellent material to be processed by PBF-LB, because in liquid state is very reactive to elements like oxygen and nitrogen and the controlled atmosphere inside the printers limits this reaction [47]. However, the fast heating and cooling rates can generate thermal expansions and residual stresses in the fabricated Titanium parts. To obtain a more stable melting [48] and a lower

porosity, that can reduce the anisotropy [49], a correct set of parameters should be chosen. Ti-6Al-4V has high strength, corrosion resistance and biocompatibility combined with low density and thermal conductivity making it suitable for application in fields like aerospace and biomedical, however it is used also in automobile, energy, marine and chemical industries [46,50]. Concept Laser developed a topology optimized Titanium bracket connector with a weight reduction of more than 30 % that has been installed on the Airbus A350 XWB [51]. Bugatti, in collaboration with Fraunhofer IAPT and Bionic Production AG, built the volumetrically largest functional component, consisting in a brake caliper meeting the requirements for a sport car production [52].

316L Stainless Steel is one of the most used material due to its high welding performance, good durability, anti-corrosion properties [53]. It also has good PBF-LB processability [54] nevertheless it still presents some processing challenges. For example, the energy density must be between a certain range in order to avoid pore formation and vaporization of alloying elements that affect the mechanical properties [55]. 316L is an austenitic steel with an elevated resistance to creep and oxidation up to 900 °C [56]. 316L is also biocompatible, used to produce plates, screw and nails but also temporary low-cost cemented implants [57]. Fraunhofer ILT, built a helicopter part with a 50% weight reduction due to the internal 316L lattice structures [32]. Wang et al. [58] printed a customized guide to precisely tighten screws in backbone surgeries.

Just like Titanium and Stainless Steel, Cobalt-Chromium alloys have been extensively used in biomedical [59], automotive and aerospace fields [60]. CoCr alloys are widely used for the fabrication of dental devices due to corrosion resistance, ductility and strength suitable for this purpose [61]. The high hardness and melting point make this material difficult to process in dental laboratories so the PBF-LB process became a good technology to process CoCr. Lastly, CoCr does not present any allergic or carcinogenic hazard in comparison with other metals like Nickel and Beryllium [62]. Averyanova et al. [63] stated that PBF-LB is a suitable technique to build dental crowns and bridges with good geometrical accuracy and adequate mechanical properties. Revilla Leon et al. [64] printed and implanted a CoCr maxilla framework on an edentulous patient.

Aluminum alloys are difficult to process via PBF-LB due to poor powder fluidity, laser reflectivity and oxidation [65]. The PBF-LB process induces a non-equilibrium solidification that increases the solid solution limit of the alloy in the matrix, making it harder to obtain the desired mechanical properties [66]. Nevertheless, Aluminum alloys have low density and high strength making this material the most used structural material with iron and steel [66], moreover, when processed, some alloys can present a better corrosion resistance than the wrought [67]. The majority of the alloys used in PBF-LB are based on commercial grade alloys [66], the most studied Aluminum alloys for PBF-LB are Al-Si alloys, in particular AlSi10Mg [68], a near eutectic alloy mostly used for aerospace and automotive applications [69]. For example, Bugatti installed a PBF-LB AlSi10Mg bracket with integrated cooling system on the Chiron to reduce the heat transmission [70]. Ho et al. [71], instead, produced airfoil heat sinks with different fins' shapes.

Nickel based alloys are another group of materials suitable for PBF-LB. They can reach a relative density near to 100% and often present a UTS higher than the cast. Nickel alloys have high corrosion resistance, high fatigue resistance, good weldability [72] and a good surface finish with a roughness below 10 µm. It has been observed that different scanning strategies can generate different grain structures and that microstructural anomalies result from localized shrinkages and stresses, so the proper process parameters must be chosen [73]. The most studied family is Inconel, super alloys used in high temperature application [47]. For example, Soller et al [74] developed an Inconel 718 injector for liquid rocket engines, while Caiazzo et al [75], with the same material, studied the feasibility of producing a turbine blade.

2.1.2.3 PBF-LB – printers and parameters

Laser-based powder bed fusion is an additive manufacturing process for the production of objects through layers of metal powder locally melted following the cross-sections of the object obtained from a CAD model. Initially used as a rapid prototyping technique, it evolved quickly to a manufacturing process due to the possibility of producing complex geometries, not achievable with the conventional and traditional technologies [76], and almost fully dense parts with no need of further post-processing [38]. The success of the production process is influenced by the parameters set involving: laser power, scanning speed, hatch spacing and layer thickness [30]. The process parameters are linked by the equation (Eq.4) [77]:

$$E = \frac{P}{v * h * l} \quad (4)$$

Where E is the energy density (J/mm^3), P is the laser power (W), v is the scanning speed (mm/s), h is the hatch spacing (mm) and l is the layer thickness (mm). Generally, an increase of the energy density results in a decreased porosity [78, 79] thus enhancing the mechanical properties.

A typical gap between the CAD model and the as built structure, is related to the actual diameter of the strut that often results larger than the designed one [45]. This outcome is due to the presence of not fully melted powder particles attached to the strut. The dimension of the struts is influenced by the process parameters that determine the size of the melt pool but even more by the inclination of the strut in the designed structure [80]. In fact, inclined struts lean on loose powder with a lower thermal conductivity and consequently, the struts orthogonal to the building direction are the most affected ones [80]. Nonetheless, the top facing surfaces of the struts are also affected by this phenomenon, but in a less critical way [41]. Another factor influencing the strut size is the staircase effect, typical of the layer-by layer fabrication processes [30]. These phenomena are crucial for the success of a lattice structure printing and therefore must be taken into account during the design phase.

The majority of the printers used in the scientific papers included in this review are developed from four companies that held almost the 60% of the total amount of available printers. The most used printers and related companies are listed in Table 1.

Table 1: Companies and printers most cited in the reviewed works.

Company	Printers	Ref.
3D systems	ProX 200	8 111
	ProX 300	122
	ProX 320	90 97 100 102 103 106 125
SLM Solution	SLM 250 HL	82 83 85 95 99 101 117
	SLM 280 HL	81 121
EOS	M 270	91
	M 280	88 104 128
	M 290	111 128
Renishaw	AM 250	98 116 120
	AM 400	13 115

The process parameters used to fabricate lattice structures differ widely from a paper to another, even considering the same material. This, in addition to the great variety of cell geometries and dimensions and structure porosity and orientation, makes the comparison of different studies ambitious.

2.1.3 Mechanical characterization

In this section, the testing parameters and outputs of the mechanical characterization of lattice structures will be analyzed. The most significant data have been reported in the following Tables. The Tables have been designed in order to correlate the material, the cell geometry of the samples and the characterization parameters to allow a comprehensive comparison between the analyzed researches. Moreover, the Tables contain details about any type of further design configurations and treatments applied that may have a

direct influence on the mechanical performances. Moreover, the test parameters and the main outputs of the mechanical tests have been reported in order to allow a direct comparison between the test design and the relative outputs, in absence of a dedicated standard to unify the testing of the lattice mechanical performances. Finally, the most significant curves are graphically reported in order to show the main trends characterizing the behavior of lattices structures subjected to compression, tensile, bending and fatigue tests.

2.1.3.1 Compression tests

The compression test is the most used one to characterize lattice structures due to the majority of their applications where the structures are subjected to this type of load. For example, in the biomedical industry, the compression performance of implants, together with the fatigue life and biocompatibility, is the key factor for selecting the right material. The reference standard, although not specific for additive manufacturing specimens, is the ISO 13314 - *compression test for porous and cellular metals* [30]. This standard is specific for sample with a porosity higher than 50%. The cross-section of the specimen can be either cylindrical or rectangular although the cylindrical one is recommended. The dimensions of the specimen, diameter and height in case of cylindrical samples and length, width and height in case of a rectangular geometry, should be set at least 10 times the average pore size and over 10 mm in length. The ratio between the height and the diameter, or the edge length, should be between 1 and 2. The crosshead speed of the test should be kept constant and it should be set to obtain an initial strain rate between 10^{-3} and 10^{-2} s^{-1}.

The data collected from the reviewed papers are shown in the Tables below according to the materials used. Table 2 shows the material, geometry, process design and compression parameters for Titanium samples.

Table 2: data collected from the compression tests of Titanium samples.

Ref	Material	Cell	Process Design	Test Parameters	Output	Values
82	Ti6Al4V	Cubic Honeycomb	Graded cells orientations	100 kN load cell strain rate 0,05/min	Quasi elastic gradient (Gpa) Elastic gradient (Gpa) First maximum compressive strength (MPa) Energy absorption (50% strain) (MJ/M^3)	2,5-14 GPa 0,5-14 GPa 64-692 Mpa 19-203 MJ/m^3
83	Ti6Al4V	Cubic Honeycomb	Strut sizes Cells orientations	Strain rate 0,05 per minute	First maximum compressive strength (Mpa) Energy absorption (50% strain) (MJ/m^3)	14-244 Mpa 3,94-77,52 MJ/m^3
89	CP-Ti grade 1	Gyroid	Cell sizes Compression directions	50 kN load cell strain rate 10^-3 s^-1	E (MPa) Yield strength (Mpa)	1465-2680 Mpa 45-57 Mpa
90	Ti6Al4V	Diamond	samples orientations HIP (920 °C, 1000 bar, 2 hours)	30 kN load cell Constant displacement rate 0,9 mm/min	Quasi elastic gradient (Gpa) First maximum stress (Mpa) Energy absorption (30% strain) (MJ/m^3)	3,2-5,4 Gpa 91,2-133,9 Mpa 5,4-27,4 MJ/m^3
91	Ti6Al4V	Pillar texile	Heat treatment (650°C, 2 hours) cells sizes	200 kN load cell Constant speed 0,5 mm/min	Compressive peak stress (Mpa) Compressive collapse stress (Mpa)	130-310 Mpa 18-80 Mpa
93	Commerciall y pure porous titanium (CPPTi)	BCC	Cell sizes Compression directions	1000 kN load cell Loading rate 0,5 mm/min	Compression load (at 40%) (N)	49-8048 N
95	Home made Ti-Tantalum powder	Custom made	Printing parameters	50 kN Load cell constant speed 0,6 mm/min	Elastic constant (Gpa) Yield strength (Mpa)	1,36-6,82 Gpa 25-420 Mpa
97	Ti6Al4V	Gyroid	Cell sizes Sheets sizes Process parameters	50 kN load cell (+100 kN) Displacement rate 1 mm/min	Apparent E (Gpa) Yield strength (Mpa) Ultimate Compressive strength (Mpa)	3-16,9 Gpa 42,1-236 Mpa 50,9-345 Mpa
99	Ti6Al4V	Self-designed	HIP (1000°C, 150 MPa, 1 hour)	Compression rate 0,125 mm/min	Compressive yield strength (Mpa)	100-143 Mpa

101	Ti6Al4V	BCC	Heat treatment (1050 °C, vacuum, 2 hours)	15 kN load cell Displacement rate 10 micron/sec = strain rate 10^-3 s^-1	Graphically reported	
103	Ti6Al4V	Diamond	Heat treatment Etched	30 kN load cell Constant strain rate 0,9 mm/min	Quasi elastic gradient (Gpa) Yield stress (Mpa) Maximum stress (Mpa)	4,3-6,5 Gpa 79,1-118,9 Mpa 88,6-146,8 Mpa
104	Ti6Al4V	Diamond	Volume fractions Topological optimization Heat treatment (650°C, 3 hours)	100 kN load cell. Constant speed 2 mm/min	E (Mpa) Compressive peak stress (Mpa)	34-1403 Mpa 2-78 Mpa
106	Ti6Al4V	Primitive I-WP Gyroid Diamond	Sheets sizes	100 kN load cell Deformation rate 10^-2 s^-1 = 1,2 mm/min	Quasi elastic gradient (Gpa) Yield stress (Mpa)	3,2-6,4 Gpa 92-276 Mpa
107	Titanium	Octahedron Random	Heat treatment (1400 °C, 3 hours) Randomization	Speed 1 mm/min	Strength (Mpa) Stiffness (Gpa)	36,7-56,4 MPa 2-6,5 Gpa
108	Ti6Al4V	Regular Irregular Random	Heat treatment Randomization Voids sizes Struts sizes	Displacement rate 2 mm/min	E (Gpa) Offset compressive strength (Mpa)	1-16 Gpa 70-400 MPa
109	Ti6Al4V	Rhombic dodecahedron	Graded Heat treatment (600-850 °C, 2-4 hours; furnace cooling; 700-900 °C, 2 hours)	Strain rate 10^-3 s^-1	Initial collapse strength (Mpa) Nearly plateau stress (Mpa) Densification strain (%)	40 Mpa circa 35 Mpa circa 65%
110	Ti6Al4V	Gyroid Primitive	Graded	100 kN load cell Strain rate 2 mm/min	E (Mpa) Yield strength (Mpa) Peak strength (Mpa) Energy absorption (MJ/m^3)	1188-1699 Mpa 29,8-62,1 Mpa 33,1- 77,1 Mpa 31-54 MJ/m^3
127	Ti6Al4V	Cubic	Strut sizes Cell sizes Heat treatment Ultrasonic cleaning	100 kN load cell Speed 25 mm/min	E (Mpa) Stiffness (N/mm)	1810-2598 Mpa 56-79 N/mm
128	Ti6Al4V	BCC fcc-BCC	Densities Heat treatment (750 °C, 2 hours)	Compression rate 1 mm/min	Equivalent elastic modulus (Mpa) Ultimate compressive strength (Mpa)	25-2800 Mpa 1,6- 156 Mpa

Table 3 shows the material, geometry, process design and compression parameters for Steel samples.

Table 3: data collected from the compression tests of Steel samples.

Ref	Material	Cell	Process Design	Test Parameters	Output	Values
7	316L	Cubic	-	Initial strain rate 10^-3 s^-1	E (GPa) Yield strength (Mpa)	0,15 Gpa 3.01 Mpa
12	316L	Gyroid	Cells orientations	20 kN load cell Constant speed 0,4 mm/min	E (Mpa) Yield strength (Mpa)	250-300 Mpa 14-15,5 Mpa
13	316L	Rhombic-dodecahedron	Topological optimization	30 kN load cell Constant speed 0,9 mm/min = strain rate of 0,0005 s^-1	E (Mpa) Initial yield strength (Mpa) Energy absorption (J) Specific energy absorption (KJ/Kg)	110-1140 Mpa 3-25 Mpa 40-360 J 3-11 KJ/Kg
81	1,4404 SS	FCCZ Hollow spherical	Heat treatment (900 °C, 1 hour)	400kN load cell Constant strain rate 10^-3 s^-1	E (GPa) Specific energy absorption after 40% strain (J/g)	6,8-11 Gpa 12,1-26 J/g
86	316L CoCr	Simple cubic Crossing rod BCC	-	100 kN load cell. Strain rate 10^-3 s^-1. cross-head separation rate 1 mm/min.	Equivalent strength (Mpa) Stiffness modulus (Gpa)	25-175 Mpa 8-55 GPa
88	316L	FCC Vertex cube Edge centre cube	Porosities Topological optimization	100 kN load cell Constant speed 1 mm/min	E (Mpa)	240-3000 Mpa
94	316L	Hexagon-honeycomb	Cell sizes	Interrupted loading	Effective E (Gpa)	1,6-8,6 Gpa
96	316L	Tetrakaidecahedron Diamond BCC	Process parameters. strut sizes Volume fractions.	Deformation rate/speed of loading 6 mm/min	E (Mpa) Yield strength (Mpa)	20-1810 Mpa 1,66-81 Mpa
112	316L	BCC	Graded	Comp: speed 1 mm/s	Graphically reported	

126	CL50WC powder 18 Ni Marage 300	Pillar texile	Cell sizes	250 kN load cell Constant speed 0,5 mm/min	Peak stress (Mpa)	97-206 Mpa
124	316L	BCC BCCz	Cells orientations	Displacement rate 1 mm/min	Yield strength (Mpa)	0,4-1,4 Mpa

Table 4 shows the material, geometry, process design and compression parameters for CoCr samples.

Table 4: data collected from the compression tests of CoCr samples.

Ref	Material	Cell	Process Design	Test Parameters	Output	Values
86	316L CoCr	Simple cubic Crossing rod BCC	-	100 kN load cell. Strain rate 10^-3 s^-1. cross-head separation rate 1 mm/min.	Equivalent strength (Mpa) Stiffness modulus (Gpa)	25-175 MPa 8-55 GPa
87	CoCr (Praxair)	Circular Crossing rod	-	Strain rate 10^-3 s^-1	E (Gpa) Yield strength (Mpa) Ultimate compressive strength (Mpa)	33-34 Gpa 70-110 Mpa 235-365 Mpa
100	CoCrF75 (A), LaserForm	Diamond	HIP (1200 °C, 1000 bar, 4 hours) Etched Layer thickness	Constant displacement rate of 0,9 mm/min.	Quasi elastic gradient (Gpa) Offset stress (0,2%) (MPa) First maximus stress (Mpa)	1,37-2,34 Gpa 22,42-41,62 Mpa 35,6-62,8 Mpa
102	CoCr F75	Diamond	Etched Samples dimensions	30 kN load cell. Constant strain rata 0,9 mm/min	Quasi elastic gradient (Gpa) Yield stress (0,2%) (Mpa) Maximus stress (Mpa)	2,2-3,4 Gpa 53-74 Mpa 76-116,3 Mpa
105	CoCr (ASTM F75)	Pillar octahedral	Strut sizes Graded Heat treatment (1200 °C, 2 hours)	300 kN Load cell Loading rate 2 mm/min	E (Gpa) Yield strength (0,2%) (Mpa) Ultimate compressive strength (Mpa)	2,3-3,14 Gpa 36-130 Mpa 113-5523 Mpa

Table 5 shows the material, geometry, process design and compression parameters for Aluminum and Inconel samples.

Table 5: data collected from the compression tests of other metals samples.

Ref	Material	Cell	Process Design	Test Parameters	Output	Values
84	AlSi12Mg	BCC FCC BCCZ FCCZ FBCCZ	-	Strain rate 10^-3 s^-1	E (Mpa) Strength (Mpa) Volumetric energy absorption up to compressive strength (MJ/m^3)	130-950 Mpa 4-20 Mpa 0,03-0,14 MJ/m^3
92	AlSi10Mg	FCC	Struts sizes	5 kN load cell Speed 0,001 mm/s	E (Gpa) Yield strength (Mpa) Ultimate compressive strength (Mpa)	0,5-1,77 Gpa 3,2-7,5 Mpa 5,3-13,3 Mpa
98	AlSi10Mg	BCC	Graded Heat treatment (520 °C, 1 hour; quench; 160 °C, 6 hours)	50 kN load cell Displacement rate 0,03 mm/s	E (Gpa) Energy absorption (MJ/m^3)	0,64 Gpa 5,7-6,3 MJ/m^3
111	AlSi12	F2BCC	Graded	50 kN load cell Strain rate 0,005 mm/s	E x10^-2 (Gpa) Energy absorption (MJ/m^3)	0,5-0,7 2,6-3,2 MJ/m^3
85	Inconel 625	BCC FCC BCCZ FCCZ	Cell sizes	Strain rate 10^-3 s^-1	E (Mpa) Yield strength (Mpa)	25-230 Mpa 0,5-18 Mpa

The reported works have different purposes and demonstrate different results. Several researches compare the mechanical properties and deformation behavior of different cells geometries subjected to the same loads. For example, Kohnen et al. [81] found that the face-centered-cubic geometry with vertical struts (FCCZ) has higher strength and elastic modulus than the hollow spherical geometry, making it suitable for structural components. On the other hand, Choy discovered that honeycomb cells have better

mechanical performances than cubic cells, with higher space efficiency [82,83]. Furthermore, Leary concluded that the face-and-body-centered geometry with vertical struts (FBCCZ) has the highest absolute values of strength and modulus [84] while FCCZ geometry has the best specific strength and modulus compared to other samples [85]. Furthermore, the BBC geometry has been reported to have higher equivalent strength and specific strength than crossing rod unit cell [86], while crossing rod presents higher ultimate and yield strength than circular unit cell [87]. Topological optimization leads usually to cell geometries that often result in improved mechanical performances [88]. For example, Cao et al. [13] introduced a shape parameter in the cross section of the strut that resulted in an increase of the compressive modulus and of the initial yield strength by 79% and 55%, respectively. Some non-isotropic geometries, characterized by struts placed only in certain directions, have been studied to evaluate the effect of different orientations of print of both the whole specimen and the cell. Yan et al. [12] found that gyroid structures with struts at 0 and 90 degrees in relation to the building direction, offer better mechanical properties than the traditional ones with the struts oriented at 45 degrees. On the other hand, Ataee et al. [89] did not find any influence of the sample orientation on the compression properties of gyroid scaffolds. Besides, Cutolo et al. [90] reported that the load direction in relation to the unit cell orientation has a great effect on the properties of diamond structures, finding an optimal orientation to obtain the strongest samples. Rather than the geometry, some researchers focus on the effect of changing the porosity and volume fraction of the cell by varying the strut dimensions and cell sizes. For example, Campanelli et al. [91] and Amani et al. [92] both found that an increase in volume fraction, or relative density, results in increased mechanical properties. Similar results were achieved by Mager et al. [93] and Ibrahim et al. [94] that recorded a decrease in the compression load and the effective modulus with the increase of the cell size. The printing parameters influence the mechanical properties of lattice structures. Sing et al. [95] and Zhong et al. [96] found that an increase of laser power results in increased mechanical properties. Differently, Kelly [97] did not find great changes on the mechanical properties with refined and optimized parameters. The PBF-LB process can lead to complications such as undesired porosities, defects formation and residual stresses. Heat treatment and chemical etching have been studied to reduce these issues. Many scientists [98,99.100,101] found that a heat treatment reduces the strength of the samples and increase the ductility. On the other hand, Van Hooreweder et al. [102] reported that chemical etching has no influence on mechanical properties while, in another paper, Van Hooreweder et al. [103] found that the different densities of the samples have a strong influence on the mechanical properties making the study of the heat treatment and chemical etching effects hard. Several analyzed works in the biomedical filed aimed to obtain structures with properties similar to the natural bones reaching good results [7,104,105,106]. For example, cellular randomization techniques have been tested to study their effect on bone ingrowth and mechanical properties. Mullen et al. [107] found that certain level of randomization can improve the mechanical properties reducing the fault planes typical of cellular structures while Raghavendra et al. [108] reported lower values of offset compressive strength and Young modulus for fully random structures. Finally, graded lattice structures have been reported to have better energy absorption capacities [109,110,111] and higher rate of densification [112].

Examples of resulting compression curves are shown Figure 4. The curves show different shapes based on the deformation mechanism that governs the cell. Bending dominated structures show an elastic region reaching a linear plateau followed by a sudden rising of stress and force values due to densification (Figure 4a). The stretch dominated structures present an elastic region culminating in a peak and followed by a wavy post yielding plateau prior to densification (Figure 4b, c) [113]. Figure 4a shows the compression curves of 316L BCC samples with different graded patterns. The general trend is the same for all curves with some small differences. In particular, adding a gradient to the structure increases the relative density resulting in a shorter plateau and in an increased compression force. In fact, the gradient increasing pattern results in higher deformation force and energy. Figure 4b shows the compression curves of Ti6Al4V primitive samples with different porosities (φ). As shown, both the yield stress and the plateau stress increase as the porosity decreases. Also, by decreasing the porosity, the plateau becomes shorter and wavyer. This wavyness is generated by the development of shear lines and build up stresses.

Finally, Figure 4c shows the compression curves of Ti6Al4V vertically oriented cubic cells samples with different struts sizes. Smaller strut sizes lead to higher porosity resulting in a lower yield and plateau stress. By decreasing the porosity, the samples become more brittle resulting in deeper peaks and valleys shortening the plateau region followed by densification.

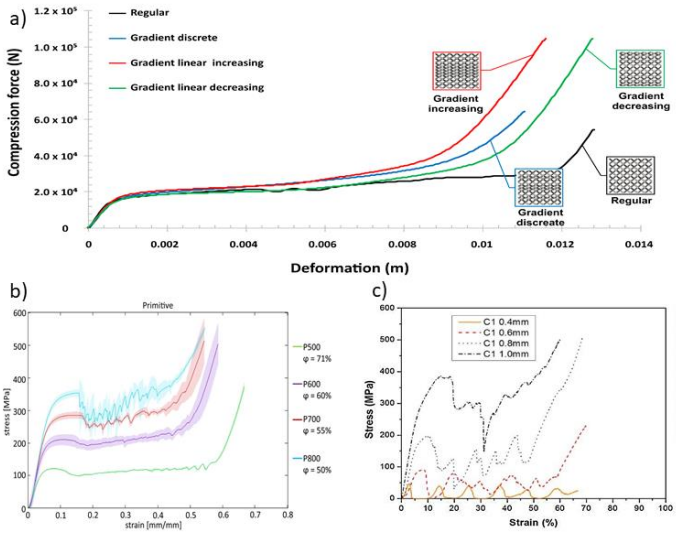

Fig. 4 Compression curves of: a) 316L BCC samples with different graded patterns [112], b) Ti6Al4V primitive samples with different levels of porosity φ, the color shades represent the standard deviation [106] and c) Ti6Al4V vertically oriented cubic cells samples with different struts sizes [83].

In conclusion, the most used load cells ranged from 5 kN to 400 kN, an indication that the mechanical properties of lattice structures can vary depending on the material, geometry, cell size and density. The speed of the moving crossbar is kept generally very low (mm/min), leading to a low strain rate as suggested by the ISO 13314 standard. The low strain rate is also suggested to allow the image acquisition to efficiently capture the deformation mechanisms. The most reported, and thus significant, outputs are the compressive Young's modulus, the quasi-elastic gradient and the yield stress. Moreover, the energy absorption is also often crucial due to the application of lattice structures as impact absorber.

2.1.3.2 Tensile test

To date, international standards for tensile tests of porous or cellular structures are yet to be developed. Although some of the test parameters like the low crossbar speed can be set by taking the compression test as an example, other parameters still remain undefined. For example, the size, the geometry and the minimum number of unit cell per side of the specimen are chosen arbitrarily without any reliable criteria. Moreover, the transition between the lattice section and the extremities of the samples that act as gripping points is not defined. For these reasons, an international standard regarding the tensile test of porous and cellular structures can lead to more uniform and reliable information. The most reported output of the tensile test is the tensile Young's modulus together with the yield stress and ultimate tensile strength. The analyzed data are reported in different tables divided by the target material: Table 6 for titanium, Table 7 for Steel and Table 8 for other metals.

Table 6 shows the material, geometry, process design, tensile parameters and results for Titanium samples.

Table 6: data collected from the tensile tests of Titanium samples.

Ref	Material	Cell	Process Design	Test Parameters	Output	Values
97	Ti6Al4V	Gyroid	Cell sizes Sheets sizes. Process parameters	50 kN load cell (+100 kN) Displacement rate 1 mm/min	Apparent tensile E (Gpa) Ultimate tensile strength (Mpa)	1,9-17,6 Gpa 23,9-121,1 Mpa
101	Ti6Al4V	BCC	Heat treatment (1050 °C, vacuum, 2 hours)	15 kN load cell Displacement rate 10 micron/sec = strain rate 10^-3 s^-1	Graphically reported	
107	Titanium	Octahedron Random	Heat treatment (1400 °C, 3 hours) Two levels of randomization	Speed 1 mm/min	Tensile strength (Mpa)	30,7-49,5 Mpa
108	Ti6Al4V	Simple cubic? Regular Irregular Random	Heat treatment Randomization Voids sizes Strut sizes	Displacement rate 2 mm/min	E (Gpa) Ultimate tensile strength (Mpa)	5-45 Gpa 50-275 Mpa
116	Ti6Al4V	BCC	Cell sizes. Samples dimensions Heat treatment (600 °C, 3 hours)	Strain rate 0,01 mm/s	E (Gpa) Ultimate tensile strength (Mpa)	7-20 Gpa 55-189 Mpa
118	Ti6Al4V	Diamond	HIP (920 °C, 1000 bar, 2 hours) Surface treatment (SILC cleaning)	Displacement rate 1 mm/min	Tensile E (Gpa) Tensile yield strength (Mpa) Ultimate tensile strength (Mpa)	10,4-14,1 Gpa 146,6-152 Mpa 194,9-195,5 Mpa
119	CP-Ti grade 2	Custom made	Sample dimensions Samples orientations	Constant strain rate 10^-3 s^-1	E (Gpa) Yield stress (Mpa) Ultimate tensile strength (Mpa)	1,5-3,7 Gpa 96,2-133,3 Mpa 129,8-143,6 Mpa
120	Ti6Al4V	Cubic	Heat treatment Eurocoating	Crosshead speed: 1 mm/min	E (Gpa) Yield strength (Mpa)	12,8 GPa 65 Mpa

Table 7 shows the material, geometry, process design, tensile parameters and results for Steel samples.

Table 7: data collected from the tensile tests of Steel samples.

Ref	Material	Cell	Process Design	Test Parameters	Output	Values
7	316L	Cubic	-	According to CSN EN ISO 6892-1	E (Gpa) Yield strength (Mpa) Ultimate tensile strength (Mpa)	0,12 Gpa 3,46 Mpa 14,55 Mpa
14	316L	Gyroid	Samples orientations	Constant rate 0,5 mm/min	Yield stress (Mpa) Ultimate tensile stress (Mpa) Elongation (%)	6-13 Mpa 19-29 Mpa 4-32 %
81	1,4404 SS	FCCZ Hollow spherical	Heat treatment (900 °C, 1 hour)	Constant strain rate 10^-3 s^-1	Ultimate tensile force (kN) Total elongation (%)	14,5-20,7 kN 4,9-14,8 %
86	316L	Simple cubic Crossing rod BCC	-	100 kN load cell. Strain rate 10^-3 s^-1. Cross-head separation rate 1 mm/min.	Equivalent strength (Mpa) Stiffness modulus (Gpa)	22-100 Mpa 4-22 GPa
96	316L	Tetrakaidecahedron Diamond BCC	Process parameters Struts sizes Volume fractions.	Deformation rate/speed of loading 6 mm/min	Plateau stress (Mpa) Energy absorption (J/cm^3)	2-80 MPa 1-31 J/cm^3
114	316L	Truss structure Octahedral BCC	-	Not reported	Strength (Mpa) Highest reached force (kN)	22,5-110 Mpa 1,45-7,05 kN
115	316L	Simple cubic BCC Tetragon vertex Tetragon edge	Struts sizes	Load speed 5 mm/min	E (Gpa)	0,84-9,07 Gpa
117	1.4404 steel	Custom made	Densities	50 kN load cell Testing speed 00,1-0,02 mm/s	Maximum force (N)	535-3800 N

Table 8 shows the material, geometry, process design, tensile parameters and results for other metals samples.

Table 8: data collected from the tensile tests of other metal samples.

Ref	Material	Cell	Process Design	Test Parameters	Output	Values
87	CoCr (Praxair)	Circular Crossing rod	-	Not reported	E (Gpa) Yield strength (Mpa) Ultimate tensile strength (Mpa)	21-27 Gpa 75-110 Mpa 80-150 Mpa
121	AlSi10Mg	Triangular prism Square prism Hexagonal prism	Cells sizes	250 kN load cell Deformation rate 1 mm/min	Tensile effective E (Gpa)	3,4-9,8 Gpa

One of the main focus of the evaluated works is the comparison of the performance of different geometries subjected to the tensile test. For example, Kohen et al. [81] reported, as in the case of compression, higher maximum tensile strength in the FCCZ geometry than in the hollow spherical geometry. Liverani et al. [86] compared the BCC, the crossing rod and the simple cubic geometries and the crossing rod geometry showed the highest specific strength and stiffness under tension. Again, Kessler et al. [114] reported a higher tensile strength in the truss structure geometry than in the octahedral or BCC geometries. Zhong et al. [96] studied the tensile properties of samples with different geometries and the same volume fraction, the tetrahedral geometry showed a higher ultimate tensile strength than diamond and BCC geometries. Finally, Hajinys et al. [115] compared the tensile properties of different geometries with three different strut sizes and the tetragon vertex unit cell with a strut diameter of 0,7 mm resulted the stiffest combination. The influence of the cell's parameters is also investigated by several authors. For example, Maskery et al. [116] tested BCC samples with two different cell dimensions and reported that the smallest cell size can maximize the stiffness of the sample. Kelly et al. [97] instead, studied gyroid samples with different wall and cell sizes and noted that these two variables have a direct and interdependent impact on the mechanical properties, determining the overall porosity of the sample. Similar results were reported by Lober et al. [117] who underlined how the maximum load tolerated by the structure has an exponential dependence from the density. Furthermore, a few works studied the effect of post processing on the tensile mechanical performances of the lattices. Brenne et al. [101] noted that heat treated samples bear higher maximum stresses and are able to sustain higher loads, while Kelly et al. [118] found that a surface treatment, such as SILC cleaning, can slightly improve the Young modulus of a Ti-6Al-4V diamond lattice. Other researches focused on the sample's building orientation. For example, Alsalla et al. [14] and Barbas et al. [119] found that vertical built samples have better mechanical tensile properties than horizontal ones. Furthermore, few studies investigated the effect of cell's randomization reaching contrasting results. Muller et al. [107] found that a certain level of randomization improves the mechanical properties while Raghavendra et al. [108] reported regular structures having higher values of strength. Other works tested lattice structures to compare their properties with the natural bone [7,87] or to validate the related FEM simulation [120,121].

Two significant examples of tensile stress-strain curves resulting from testing lattice structures are shown in Figure 5. The presence of a concave elastic region can be sign of good consolidation and absence of defects [14]. Figure 5a shows the tensile curves of 316L gyroid samples with two building orientation in relationship to the building platform. The axis of the sample with the horizontal orientation is parallel to the building platform while the axis of the sample with the vertical orientation is perpendicular to the building platform. Both curves represent the same trend with no sign of brittle failure. Although, the vertical oriented sample has enhanced mechanical properties with higher yield strength, ultimate tensile strength and elongation. Figure 5b shows the tensile curves of 316L samples with different unit cell geometries. Again, the curves show the same trend with an elastic region followed by a plastic elongation, sign of a ductile behavior. The crossing-rod geometry seems to show better properties both in

terms of strength and elongation. On the other hand, the BCC is stronger than the simple cubic but with lower elongation.

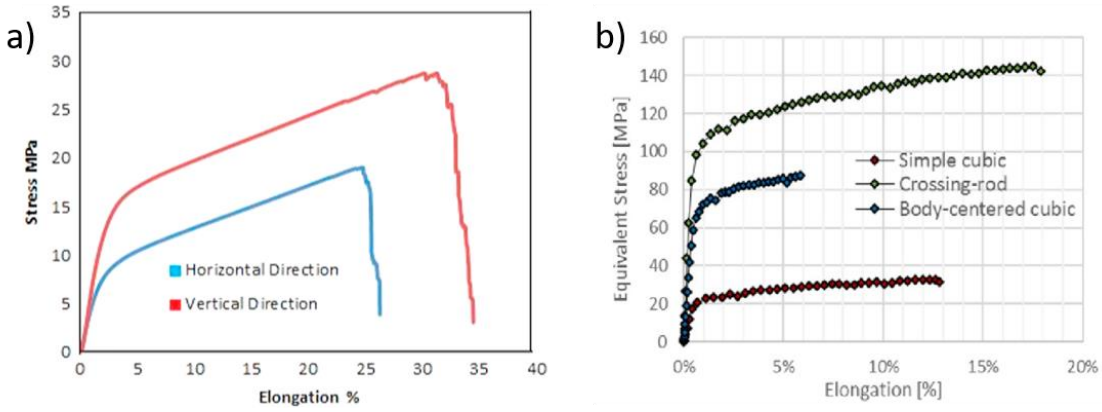

Fig. 5 Tensile curves of 316L samples with: a) gyroid unit cell and different building orientations in relation to the building platform. The horizontal direction has the axis parallel to the building platform, the vertical direction ha the axis perpendicular to the building platform. [14], b) different unit cell geometries [86].

2.1.3.3 Bending test

Although not the most studied property, flexural strength is important because in many applications parts are subjected to this type of load, for example components for the automotive industry, smart materials and tissue engineering fields. Bending tests are typically performed in a three points configuration with a lower span length between 60 and 80 mm and cylindrical shaped supports. The geometry of the sample is usually rectangular but with a wider range of chosen dimensions. It is also possible to find a thin layer of full bulk material, called "skin", on the upper and lower faces of the sample. These types of multilayered structures are often studied for aerospace applications and their blast absorbing capabilities. Similarly, to the other type of tests, the displacement rate is kept low. The most reported outputs are the flexural Young's modulus, the peak load and the flexural strength. The data are shown in Table 9.

Table 9: data collected from the bending tests.

Ref	Material	Cell	Process Design	test Parameters	Output	Values
7	316L	Cubic	-	According to CSN EN ISO 7438	E (Gpa) Yield strength (Mpa)	0,2 Gpa 3.82 Mpa
8	AlSi12	Circular (2D) Triangular(2D) Hexagonal(2D)	-	50 kN load cell Span length 70mm Loading rate 1mm/min	E (Gpa) Strength (Mpa) Load at break (kN)	4,3-5 Gpa 145-175 Mpa 15,5-19 kN
93	Commercially pure porous titanium (CPPTi)	BCC	Cells sizes Load directions	1000 kN load cell Loading rate 0,5 mm/min	Flexural load at tensile strength (N) Extension (mm)	87-1063 N 1,48-10 mm
94	316L	Double honeycomb	-	Interrupted loading	Effective E (Gpa)	5,6 Gpa
101	Ti6Al4V	BCC	Heat treatment (1050 °C, vacuum, 2 hours	15 kN load cell Displacement rate 10 micron/sec Strain rate 10^-3 s^-1 Rolls diameter: 16 mm Upper distance: 35 mm Lower distance 70 mm	Graphically reported	
122	17-4 PH (630 SS)	BCC Octet truss	Heat treatment (490 °C, 4 hours) Cleaning Graded	Lower distance 60 mm	Initial stiffness (kN/mm) Max load (kN) Deflection at max load [mm]	9,7-14,1 kN/mm 9,7-14,1 kN 0,98-1,74 mm
123	316L	BCC	Carbon fiber skin	Displacement rate 4,2x10^-6 m/s	Peak load (kN) Initial stiffness (kN/mm)	1,1 kN 1,77 kN/mm

124	316L	BCC	Carbon fiber skin	Displacement rate da 0,25 mm/min Lower distance 80 mm Diameter 10 mm	Load peak (N) Plateau load (N)	1100 N 800 N

Rashid et al. [8] found that the triangular geometry has both higher flexural strength and modulus compared to the circular and hexagonal geometries. Kang et al. [122] reported that the multi lattice model with relative density of 0,2 showed the highest stiffness and strength. Mager et al. [93] registered a decrease in the loading force and an increase in the bending extension for bigger cell sizes. Moreover, heat treatment can lead to higher ductility for a Ti-6Al-4V BCC sample with a 0,5 mm skin as reported by Brenne et al. [101]. Ibrahim et al. [94] performed the flexural test on a double honeycomb lattice structures finding an effective modulus similar to the one obtained from the compression test, suggesting an isotropic behavior of the structure. Finally, Shen et al. [123,124] studied the skin-core adhesion resistance of multilayered structures under flexural loads.

Two examples of stress-strain curves resulting from lattice structures bending tests are shown in Figure 6. As shown, the stress either reaches a peak followed by a drop almost to 0 indicating a brittle fracture (Figure 6a) [8] or by a plateau followed by a second increase due to localize compaction (Figure 6b) [124]. Figure 5a shows the bending curves of AlSi12 samples with different unit cell geometries. All geometries curves fail in a brittle way, circular and triangular geometries drop almost to zero, while hexagonal samples fail more gradually. The triangular geometry shows the highest properties while the circular and hexagonal are almost comparable. Figure 6b shows the bending curve of a 316L BCC sample with 4 layers of carbon-fiber reinforced plastic (CFRP) as skin. The curve represents a more ductile behavior with an elastic region culminating in a peak, a drop and an almost linear plateau. Despite no delamination of the carbon skin was observed after the application of the bending stress, it seems that the CFRP is not influencing the mechanical response of the BCCs.

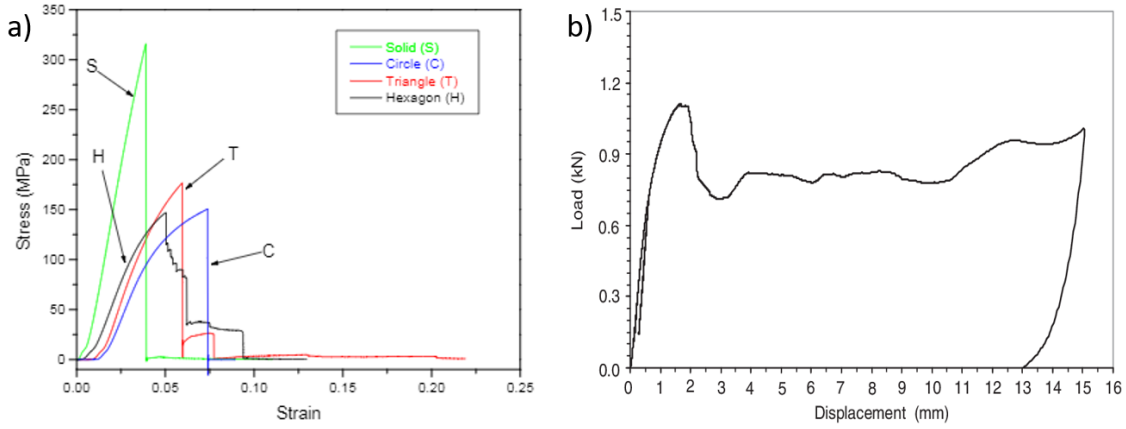

Fig. 6 Bending curves of: a) AlSi12 samples with different cell geometries [8], b) 316L BCC sample with carbon skin [124].

2.1.3.4 Fatigue test

The fatigue tests can be carried out under any stress condition: traction, compression and bending. The most commonly used is the fatigue test under compression because, as already stated above, several applications are subjected to this type of load. Fatigue performances are very important in the biomedical and aerospace fields where the limits associated with a cyclic loading are very strict [113]. Usually, the shape and size of the specimen follow the same rules as the static tests. The process parameters are quite similar within the considered papers, for example: the load is sinusoidal, the R is 0.1 and the number of cycles reaches 10^6. The frequencies vary in a range between 5 and 32 Hz, with 10 and 15 Hz being the most frequent. The data are shown in Table 10 and Table 11.

Table 10: data collected from the fatigue tests.

Ref	Material	Cell	Process Design	Fatigue	Test Parameters	Output	Valori
81	1,4404 SS	FCCZ Hollow spherical	Heat treatment (900 °C, 1 hour)	Tensile	32 Hz R ratio 0,1	Fatigue endurance limit (kN)	1,5 kN
97	Ti6Al4V	Gyroid	Cells sizes Sheets sizes Process parameters	Tensile Compressive	25 kN load cell 10 Hz R 0,1	Tensile fatigue strength stress amplitude (Mpa) Compressive fatigue strength stress amplitude (Mpa)	1,2-5,4 Mpa 5,3- 43 Mpa
99	Ti6Al4V	Self-designed	HIP (1000°C, 150 MPa, 1 hour)	Compressive	100 kN load cell 10 Hz R 0,1 Sinusoidal loading	Fatigue strength at 10^ 6 (Mpa)	43-55 Mpa
107	Titanium	Octahedron (30% random)	Heat treatment (1400 °C, 3 hours)	Compressive	10 kN load cell 6 Hz Haversine wave	Strength (30% random) (Mpa)	11,1-22,5Mpa
118	Ti6Al4V	Diamond	HIP (920 °C, 1000 bar, 2 hours) Surface treatment (SILC cleaning)	Tensile	5Hz R 0,1	Maximum stress applied (Mpa) Stress amplitude (Mpa)	40 Mpa 18 Mpa

As in the cases of compression and traction, also for the fatigue test Khonen et al. [81] reported better performances for the FCCZ geometry compared to hollow spherical geometry, failing to a higher load for the same number of cycles. Both Wu et al. [99] and Mullen et al. [107] noted an increase of the fatigue performances after heat treatment of Ti-6Al-4V self-design unit cell and gyroid unit cell, respectively. On the other hand, Kelly et al. [97,118] reported an increased fatigue life of a gyroid unit cell after process parameters optimization while no effect was observed by the same authors for a diamond cell after surface treatment.

Table 11: data collected from the fatigue tests that reported output only in graphical form.

Ref	Material	Cell	Process Design	Fatigue	Test Parameters
100	CoCr F75	Diamond	HIP (1200 °C, 1000 bar, 4 hours) Etched Layer thickness	Compressive	30 Hz R 10 Sinusoidal loading
101	Ti6Al4V	BCC	Heat treatment (1050 °C, vacuum, 2 hours)	Tensile Flexural	15 kN load cell Tensile: 10 Hz R -1 Load amplitude 210 N (80 Mpa) Flexural: 20 Hz R 0,1 Load amplitude 230 N Rolls diameter: 16 mm Upper distance: 35 mm Lower distance 70 mm
102	CoCr F75	Diamond	Etched Samples dimensions	Compressive	10 kN load cell 15 Hz R 0,1 Sinusoidal loading Fatigue life spectrum 10^3-6 cycles
103	Ti6Al4V	Diamond	Heat treatment Etched	Compressive	10 kN load cell 15 Hz R 0,1 Sinusoidal loading
106	Ti6Al4V	Primitive I-WP Gyroid Diamond	Sheet sizes	Compressive	15 HZ R 0,1 Sinusoidal waveform Max force 60% yield stress
125	Ti6Al4V CoCr	Diamond	Densities Heat treatment Etched	Compressive	10 kN load cell 15 Hz R 0,1 (constant amplitude sinusoidal) 10^3-10^6 cycles

Fatigue properties are not very suitable for a numerical and tabular representation, so many of the works reported the results only in graphical form. Van Hooreweder et al. [125,102,103] studied the fatigue properties (using a local method) of Ti6Al4V diamond unit cell samples subjected to hot isostatic pressing (HIP) and hot isostatic pressing followed by chemical etching. The study shows that the fatigue

life is improved by the HIP treatment, but an even better result is achieved when chemical etching is added (Figure 7).

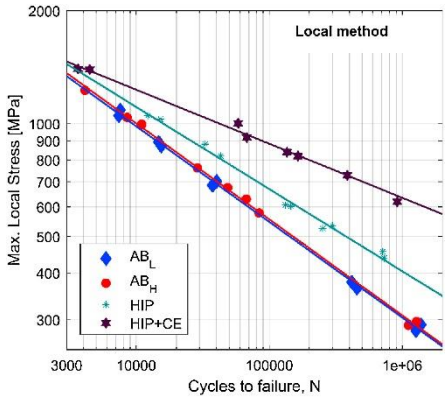

Fig. 7 Effect of heat and surface treatment on the fatigue performance of Ti6Al4V samples. AB are as built samples with low (L) and high (H) relative density, HIP are hot isostatic pressed samples and CE are chemically etched samples [125].

On the other hand, Cutolo et al. [100] reported an increasing of the fatigue performances of chemically etched CoCr samples on a local scale (Figure 8), while the HIP treatment seemed to be ineffective.

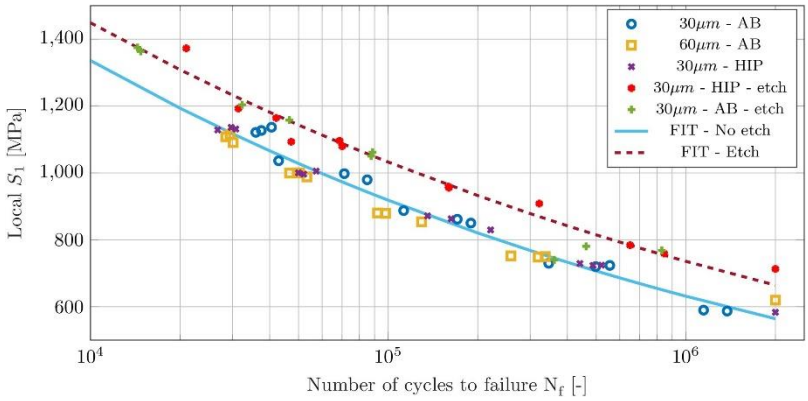

Fig. 8 Effect of heat and surface treatment on the fatigue performance of CoCr samples. AB are as built samples, HIP are hot isostatic pressed samples and etch are chemically etched samples. 30 and 60 µm are the layer thicknesses [100].

Brenne et al. [101] reported an improved fatigue life in Ti6Al4V samples after heat treatment with a significant increase in the number of cycles to failure at the same displacement amplitude (Figure 9).

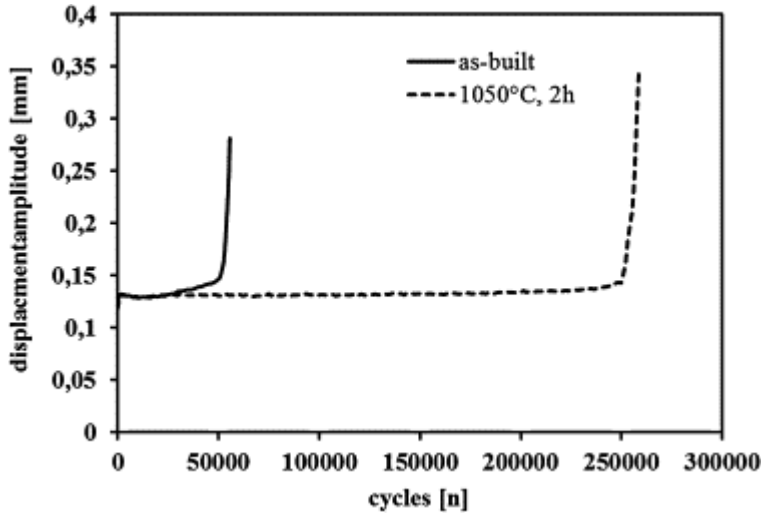

Fig. 9 Effect of heat treatment on the fatigue performance of Ti6Al4V BCC sample [101].

Bobbert et al. [106] studied the influence of apparent density of various Triply-periodic-minimal-surfaces geometries (Figure 10) on the fatigue properties of the samples. There are different trends as the apparent density increases. The performance of the primitive geometry increases as the apparent density increases, although this design results in the shortest fatigue life. The gyroid geometry shows a performance decrease as the apparent density increases, probably due to the geometry of the unit cell. The fatigue life of the I-WP geometry significantly increases with the increase of the apparent density, achieving high performances. Finally, the diamond geometry reaches the highest fatigue life with the lowest apparent density while for the other values the results are comparable.

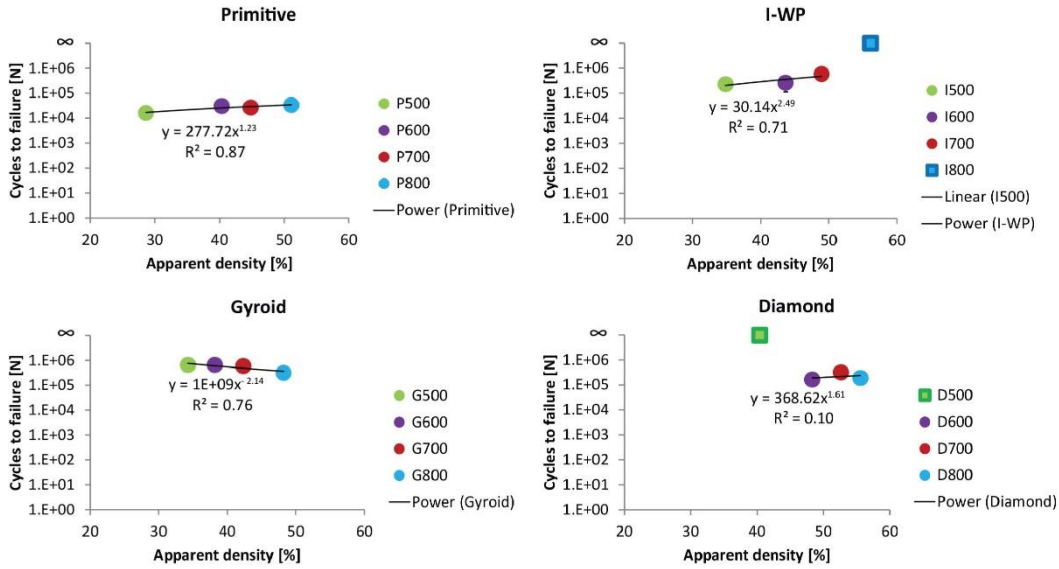

Fig. 10 Effect of different apparent densities on the fatigue performance of triply-periodic-minimal-surfaces Ti6Al4V samples. The squares in the graphs mean the samples reached 10^6 cycles without failing [106].

2.1.4 Conclusion

PBF-LB is an additive manufacturing powder bed fusion system for the production of lattice structures. Lattice structures have been intensively studied due to their low weight, good mechanical properties and energy absorption capabilities that make them suitable in fields such as aerospace, automotive and biomedical. Although the increasing interest in these type of structures, nowadays, the lack of a specified international standard regarding their characterizations, forces the researchers to rely on literature or on their experience. The introduction of an international standard would be very useful not only to provide a common procedure that would allow the comparison of results but also to certify the possible applications, without leaving the outcomes only to research porpuses. This review merged a large number of data concerning the production and testing of lattice structures. It gives a wide perspective on all the variables that must be taken into consideration when dealing with this type of structures. Furthermore, it gathers the parameters used by AM researchers to test lattice samples, providing a possible guideline to scientists and industries with different goals in the AM sector. The novelty of this review lays in the collection of a large number of data on the mechanical characterization of lattice structures to understand the presence of methodologies used transversely by various researchers, the outputs that are most collected and what are the target applications of the works focused on lattice structures. In addition, various information such as material, cell geometry and process design have been collected in order to relate them to the tests results. The main considerations are the following:

- Many researcher followed the ISO 13314- *compression test for porous and cellular metals*- for the compression test. Although it is not specific for additive manufacturing samples, it provides

good guidelines for the characterisation of lattice structures (i.e. the geometry of the sample with related proportions and recommended strain rate).

- The geometry of the samples chosen for tensile and bending varies arbitrarily: cyclic samples follow the shape of the quasi static tests. In this case, the strain rate is kept low, probably inspired by the compression tests.
- The most reported output for the quasi-static tests are the Young modulus, the yield stress and the ultimate stress, while for the fatigue test the graphical rapresentation is preferred and often the quantitative data are not reported.
- Different variables have been taken into account for the production of lattice structures: geometry, dimensions and post-production treatments. Therefore, several works studied their influence on the mechanical properties of different samples. A complete knowledge of these factors is fundamental to understand the full potential of these structures.
- It can be noted that an increase in samples density leads to an increase in the main mechanical properties. Further methods used to expand the range of obtainable values are heat treatment and grading of the sample, techniques that are quite effective on properties such as ductility and energy absorption.

The most common test parameters and outputs for every test used in the reviewed literature are listed in the Table 12.

Table 12: Most common parameters and outputs used in the reviewed literature.

	Sample	Load cell	Strain rate	Outputs	Frequency R-ratio Wave Form
Compression	Prismatic/Cylindrical	30-100 kN	10^-3 s^-1 0,5-2 mm/min	Young's modulus Quasi-elastic gradient Yield stress	-
Tensile	Prismatic/Cylindrical	50 kN	10^-3 s^-1 0,1-2 mm/min	Young's modulus Yield stress Ultimate tensile strength	-
Bending	Prismatic	15-1000 kN	10^-3 s^-1 0,25-1 mm/min	Young's modulus Peak load Flexural strength	-
Fatigue	Cylindrical/Prismatic	10-25 kN	-	Fatigue strength Graphical	10-15 Hz 0,1-10 Sinusoidal

This data can be considered as a starting point for a future study aiming to develop a new standard method. The presented tests parameters are all similar because they are inspired by the compression tests, but this strategy is not necessarily optimal for each type of test which can have a very different goal from the others. An additional point to focus on is the size and proportions of the samples, at the moment too different from each other and therefore with a different effect on the final result.

To conclude, the authors highlight that the number of works focusing on the tensile, bending and fatigue tests are relatively low compared to the ones focusing on the compression tests. A bigger number of studies is therefore needed to put a more solid base to allow a necessary comparison between different studies. Moreover, the authors suggest a critical evaluation of the mechanical test parameters to demonstrate their effectiveness and usefulness for the characterization of lattice structures and identify any possible modification to make the parameters more functional based on the final application.

2.2 Analysis of 3D printed 17-4 PH stainless steel lattice structures with radially oriented cells

2.2.1 Introduction

Additive Manufacturing (AM) of pure metals can be di-vided in different sub-categories according with the material charging method: powder bed fusion systems, where materials are added layer-by-layer and direct energy deposition systems, where materials are added through a nozzle or a wire fed system [1]. Cellular structures are usually divided in two major groups: stochastic porous structures and cellular lattice structures [2]. Stochastic porous structures are characterized by pores located randomly throughout the entire volume of the object, thus, the mechanical properties result not uniform and difficult to control. Cellular lattice structures consist in a unit cell repeated in all directions, making the mechanical properties controllable and repeatable. Consequently, lattice structures with a certain volume fraction present better mechanical properties than stochastic porous structures. As an example, in the aerospace field, the production of a component with the same level of performances but a reduced weight consists in a huge economical advantage. On the biomedical side, lattice structures can be advantageous enhancing the properties of implanted prostheses and functional orthoses [3]. Moreover, the surface properties of a metal lattice structure can improve the interaction with the physiological environment by stimulating cells through their morphology which was found to be a key factor for the biointegration of a scaffold [4-6]. Furthermore, an open cell structure makes a sample suitable even for non-structural applications like acoustic insulation, energy absorption and filtration.
Selective Laser Melting (SLM) of lattice structures is a relatively new process so there is no complete characterization of their performances in the literature yet. The properties of the lattice structures depend on several factors: cell geometry, material, struts dimension, loading directions and boundary conditions [7]. Although the lattice structures have a lot of advantageous properties there are some issues that have to be taken into account. The majority of the possible geometries is not isotropic, consequently the mechanical properties of an object show an anisotropic trend. Moreover, only few materials and geometries have been studied and the comparison between different results is often difficult due to the differences in tests procedures, process parameters and printing quality [8].

For example, the orientation of the cells within the sample changes the number of struts in the direction of compression causing a change in the strength of the sample. It also changes the thermal gradient that the part is subjected to, and consequently also the residual stresses within the structure. The study of different orientations is then fundamental for a complete analysis of the potential of lattice geometries. Moreover, considering the widespread use of lattice structures for load-bearing prostheses design in the biomedical field, a radial orientation of the cells within a lattice sample would replicate the structure of the Harvesian lamellae of the cortical bone [9]. In this work, 17-4 PH Stainless Steel was used to manufacture cylindrical lattice samples via SLM. The high tensile stress and hardness combined with a good corrosion resistance below 315°C make this material appealing for many applications [10]. The geometry of three different cells was chosen considering the most representative unit cells for cellular lattices available in the majority of the printers' design platforms and currently analyzed in literature [11-12]. The building orientation of the samples was modified to evaluate the effect of these parameters on the mechanical performances of the structures.

2.2.2 Materials and Methods

17-4PH stainless steel powder was used as printing material. All the powders were selected from the same batch to exclude the influence of the material. The powder exhibits spherical shape particles with a size in the range of 5-35 μm [13]. The chemical composition is reported in Table 1.

Table 1: Chemical composition of 17-4PH stainless steel powder.

17-4 PH	Cr	Ni	Cu	Mn	Mo	Nb	Si
Wt (%)	16.71	4.09	4.18	0.8	0.19	0.23	0.53

The low content of impurities is crucial to avoid side effects of embrittlement. The samples were manufactured using a laser based powder bed fusion machine (ProX 100, 3D SYSTEMS). The laser melting process occurred in a protective Nitrogen atmosphere with O2 content less than 0.1 vol.% and the processing parameters were set as reported in Table 2. Three replicas of each produced substrate have been analyzed for the compression tests. When the SLM process was finished, the samples were removed from the plate through a band saw.

Table 2: Process parameters used in the SLM process.

Process parameters	**Values**
Laser power (W)	50
Spot diameter (μm)	80
Scan speed (mm/s)	300
Hatch spacing (μm)	50
Layer thickness (μm)	30

2.2.2.1 Design and production of the lattice structures

The lattice structures studied in this work were generated by means of the integrated software 3DXpert. In particular, three different geometries were selected: diagonal, diamond and face centric cubic cells (FCC) (Fig. 1).

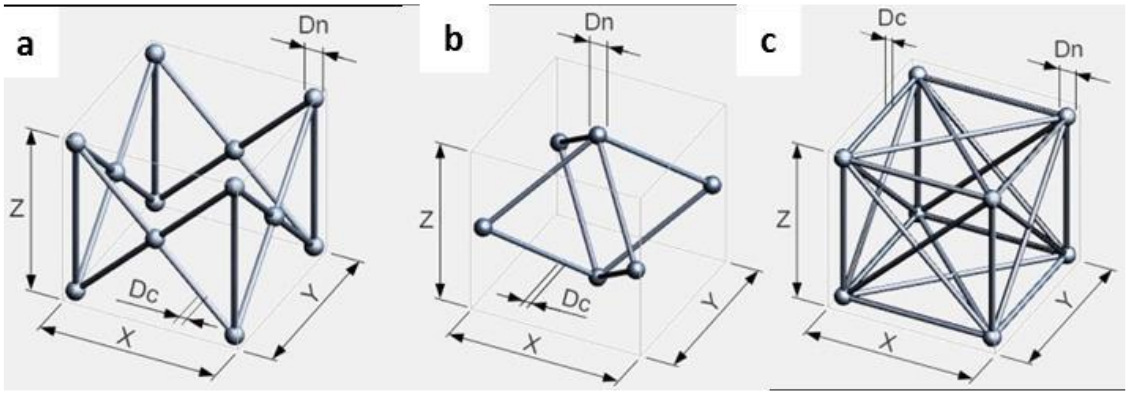

Fig. 1 Diagonal (a), Diamond (b) and FCC (c) unit cells

The dimensions of the unit cells were kept to 2(X) x 2(Y) x 2(Z) mm3. A diameter of struts (Dc) of 0,5 mm and spherical nodes (Dn) of 1 mm were selected. Following the ISO standard 13314, cylindrical samples with a 24 mm diameter and a 30 mm height were produced. Two building orientations were considered: 0° and 90° in relation to the building plate direction (Fig. 2).

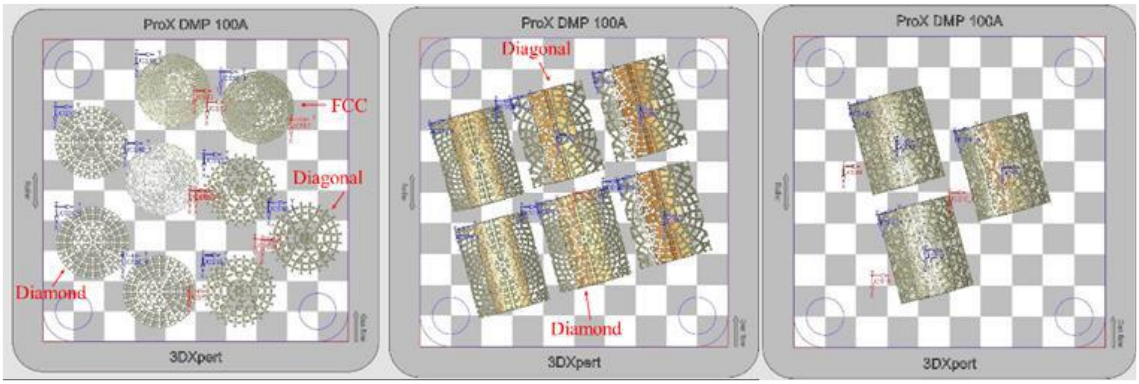

Fig. 2 Building plates design in 3DXpert. The direction of the roller is up-down.

In order to analyze the effect of the cells orientation on the mechanical properties of the samples, the cells were arranged with a radial distribution, in which the cells are not lined up one next to the other but form concentric features (Fig. 3).

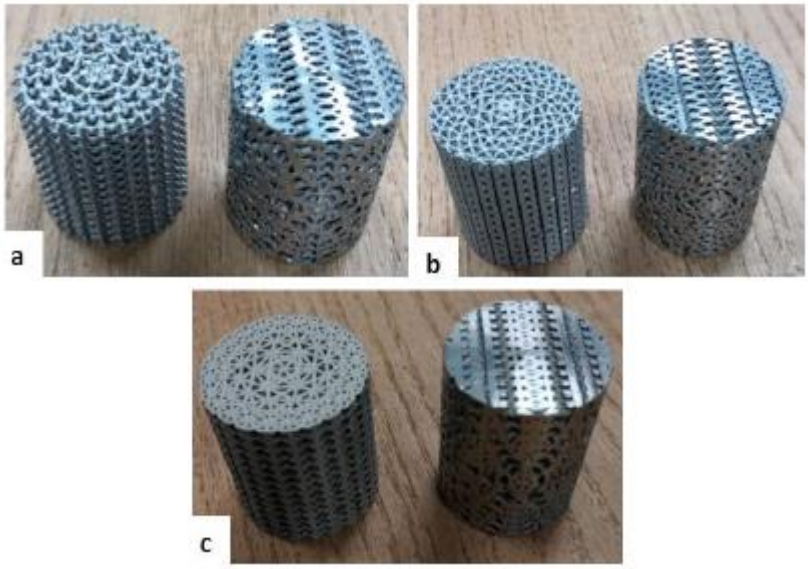

Fig. 3 Samples manufactured with 0° (left) and 90° (right) building orientation: Diagonal (a), Diamond (b) and FCC (c).

2.2.2.1 Characterization of the lattice samples

In order to obtain the relative density of the samples, the geometry and weight of the lattices were analyzed. The height and diameter of the cylinders were measured with a digital caliber while a microbalance was used to obtain the weight and calculate the relative density of the samples. The surface morphology of the samples was observed under an Hirox RH-2000 optical microscope.

The mechanical response of the lattice samples was evaluated by uniaxial compression tests carried out at 23° C by means of a hydraulic press equipped with a 1000kN load cell. The specimens were subjected to a compressive ramp under force control up to a displacement of 15 mm without intermittence. The samples oriented at 0° were subjected to a load parallel to the building direction while the samples built at 90° were subjected to a load perpendicular to the building direction. The results are reported as nominal stress vs. nominal strain curves, where the nominal stress is the force normalized on the overall specimen cross-section (about 452 mm2), while the nominal strain is the crosshead displacement normalized on the overall specimen thickness [14]. This representation allowed an easier comparison of the various

structures, avoiding effects ascribed to the differences in the cross-section of the samples. The elastic modulus (E) was considered as the slope of the linear fit of the stress-strain curve.

2.2.3 Results

2.2.3.1 morphology of the samples

The geometry of the samples was analyzed to evaluate the comparison between the designed models and the as-built samples and revealed a good consistency of the production process (Table 3).

Table 3: Geometry data of the as built samples.

Sample	Building angle (°)	Diameter (mm)	Height (mm)
Diagonal	0	23.8±0.06	29.4±0.07
	90	23.4±0.01	30.0±0.05
Diamond	0	24.1±0.04	29.4±0.06
	90	23.4±0.02	30.0±0.01
FCC	0	24.1±0.06	29.5±0.02
	90	23.8±0.01	29.9±0.01

The higher dispersion of data in relation to the diagonal cells is due to the geometry of the samples that may influence the right positioning of the caliber. As for the other cells geometries, the slightly higher standard deviation on the diameter of the samples built at 0° is probably due to the cutting edges. The relative density was analyzed considering that the volume fraction is one of the key parameters controlling the mechanical properties of porous parts (Table 4).

Table 4: Weight and density values calculated on the as built samples.

Sample	Building angle (°)	Weight (g)	Relative density (g/mm3)
Diagonal	0	27.3±0.37	2.1E-03
	90	29.6±0.04	2.3E-03
Diamond	0	30.0±0.07	2.2E-03
	90	29.5±0.16	2.3E-03
FCC	0	39.5±1.97	3.0E-03
	90	44.0±1.19	3.3E-03

The building orientation of the samples has a reduced impact on the relative density of the parts while the geometry of the cells, especially for the FCC configuration, may cause the presence of unmelted powder trapped inside the structure causing an increase of the relative density.

The surface morphology of the produced samples was observed to identify the presence of defects and collapsed struts (Fig. 4).

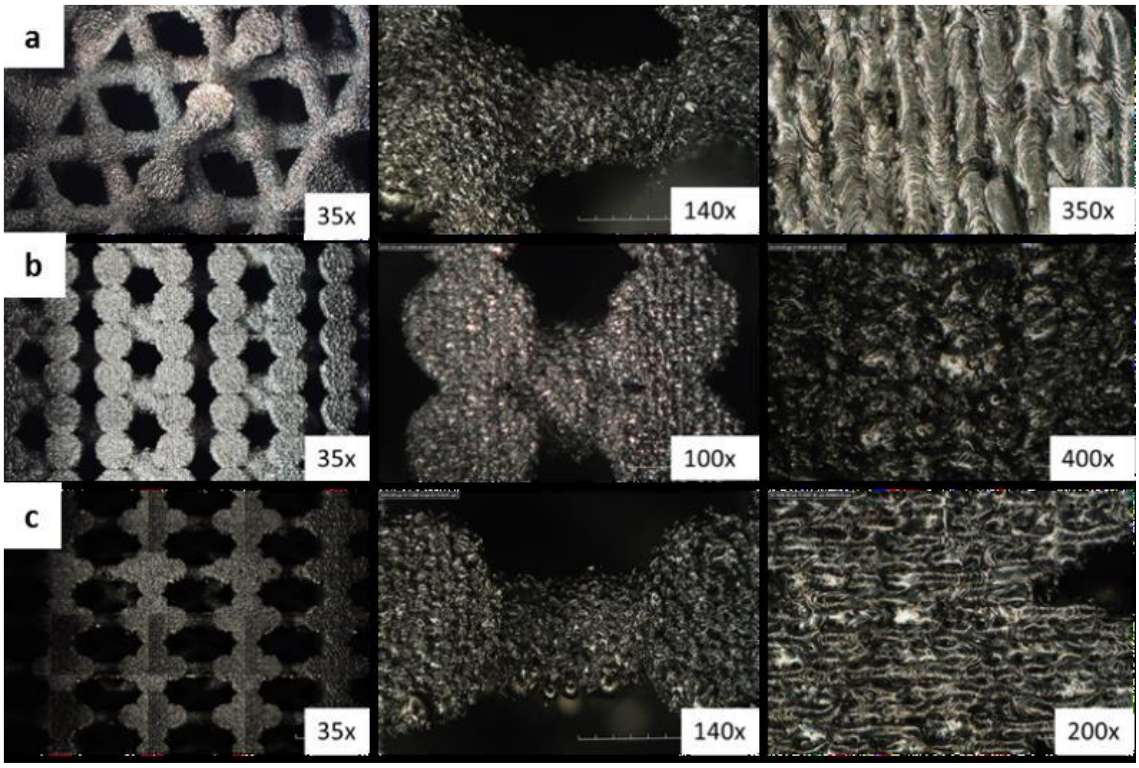

Fig. 4 Optical microscope images at different magnifications of the samples manufactured with 0° building orientation: Diagonal (a), Diamond (b) and FCC (c).

The struts and the nodes show the typical cylindrical and spherical shapes but their surfaces are covered with partially melted powder on the top layer.

At higher magnifications (Fig. 4), it is possible to see the path followed by the laser while scanning and melting the powder.

2.2.3.2 Mechanical response

The results of the compression tests are reported in terms of the nominal stress (i.e. stress over the initial section) vs. the engineering strain (i.e. the displacement over the overall specimen thickness) and are compared in Figures 5 and 6, as the most representative nominal stress vs. nominal strain curves for each material group. In this representation, the use of normalized force versus displacement allows the comparison between specimens with different cross sections and thickness.

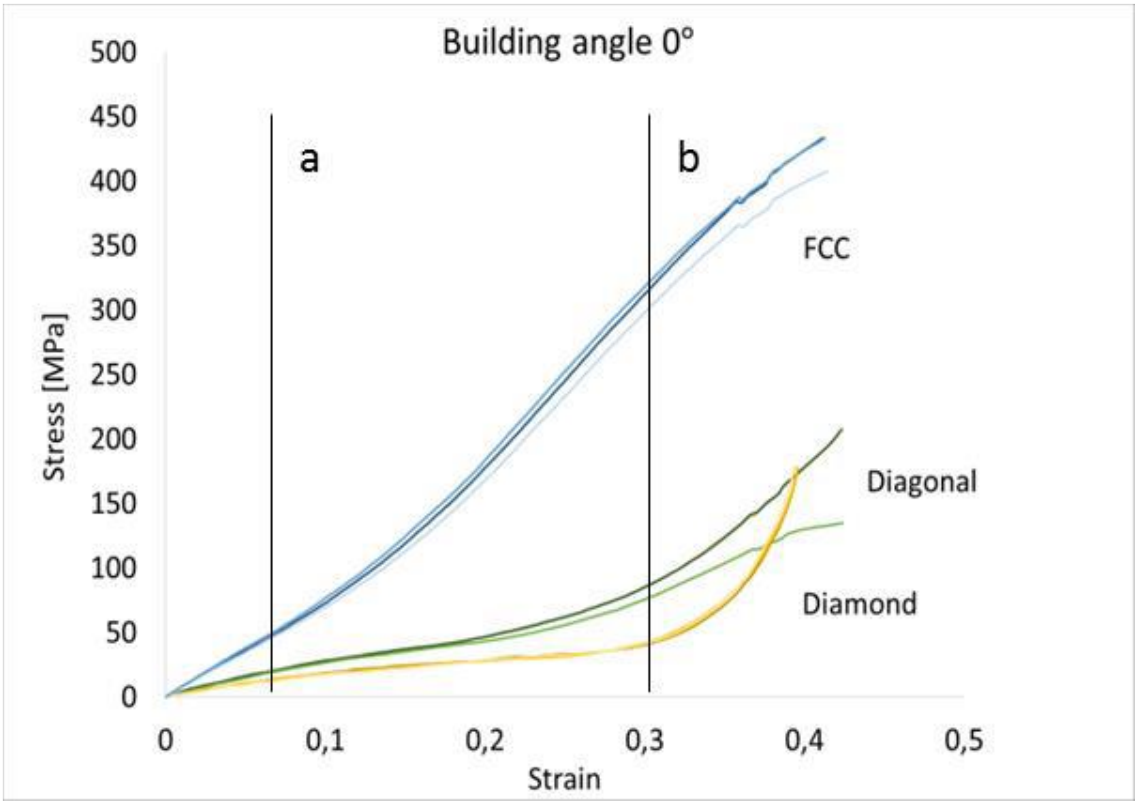

Fig. 5 Nominal stress vs. nominal strain curves obtained from the compression tests performed on the samples built at 0° of orientation.

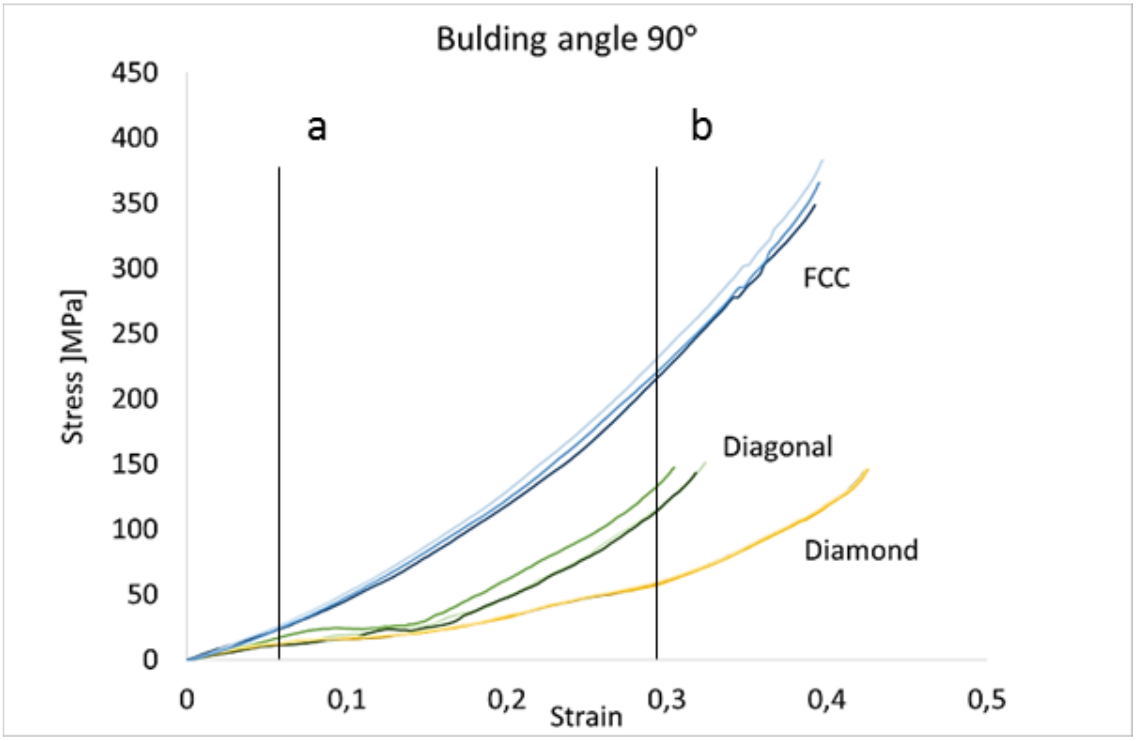

Fig. 6 Nominal stress vs. nominal strain curves obtained from the compression tests performed on the samples built at 90° of orientation.

All the curves show the occurrence of a multi stage compression history, as suggested by the three different slopes of the curves: the early deformation of the structure allows to evaluate the material stiffness at small strains (Fig. 7). This trend is followed by a reduction of the slope as a possible consequence of the collapse of the structure trough local collapses of the lattice layers. Finally, a subsequent increase of the slope is found after the collapsed structure has approached a more compact state. In particular, the early elastic deformation stage is followed by a plastic deformation region at higher values of strain (Fig. 5 and 6 line a), a subsequent collapse stage and a final hardening stage (Fig. 5 and 6 line b).

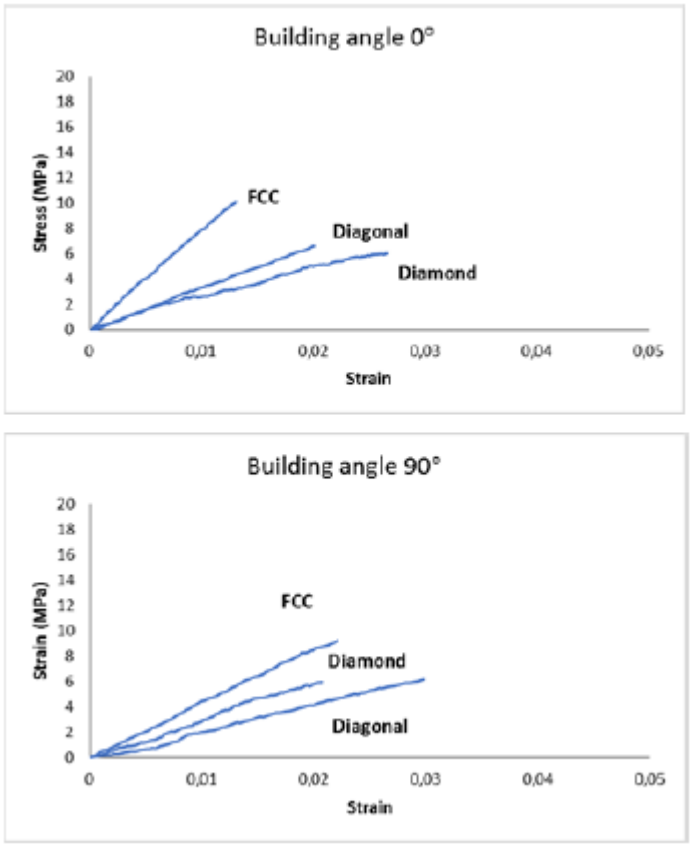

Fig. 7 Detail of the early elastic deformation stage on the samples built at 0° and 90° of orientation.

The difference in the performances between the two orientations for the diagonal and FCC samples are prob-ably caused by an anisotropy due to different number of struts in the direction of the compression, especially for the FCC configuration. In particular, the obtained curves for the samples oriented at 90° are influenced by an effect of densification of the structure that requires higher levels of stress compared to the other cells geometries. As for the diamond geometry, it can be observed that the building direction is not affecting the mechanical response in the same way, leading to a more isotropic behavior of these cells highlighted by the evident replicability of the compression trend. With regard to the diagonal geometry, the difference found between the trends observed at different building orientations is probably due to the less presence of struts parallel to the compression direction. The nominal stress vs. nominal strain curve stiffness (i.e. the slope of the curve in the linear initial trend) is reported in Table 5.

Table 5: Stiffness (E) calculated on the samples tested under compression.

Sample	Building angle (°)	E (MPa)
Diagonal	0	391.1±51.9
	90	261.9±36.1
Diamond	0	225.8±33.3

	90	286.0±29.3
FCC	0	782.5±35.6
	90	416.0±23.3

The reason of the observed difference between the stiffness calculated for the FCC configuration at different building orientations is probably the radial distribution of the cells that caused the two orientations to have very distinct internal structures and therefore different mechanical properties compared to the typical isotropic behavior of these cells.

The compressed samples are shown in Figure 8.

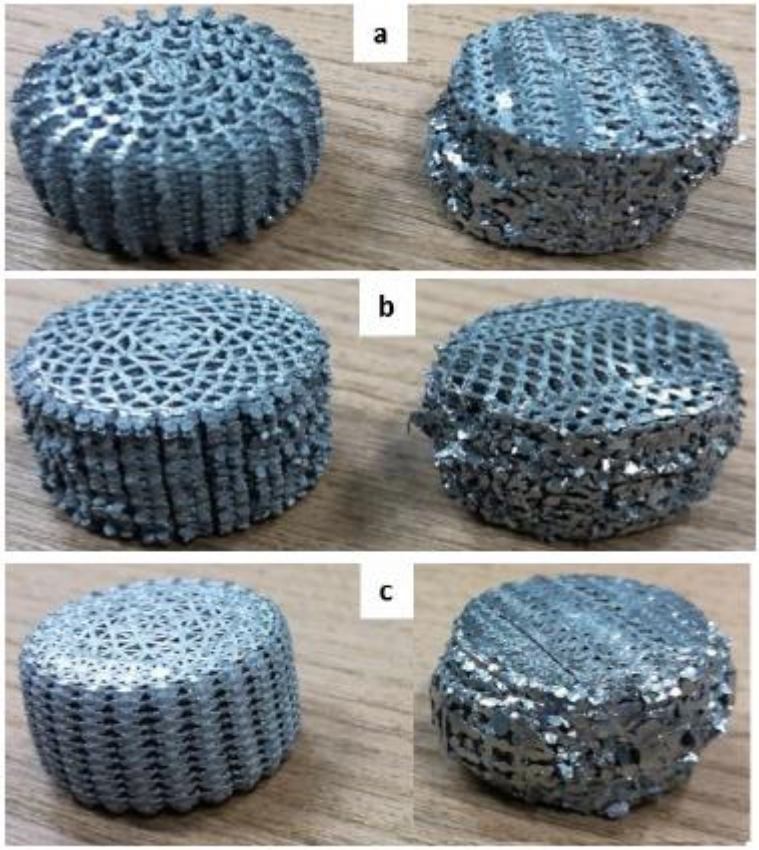

Fig. 8 Compressed samples: Diagonal (a), Diamond (b) and FCC (c).

The images of the compressed samples show the layer-by-layer buckling deformation, typical of the lattice structures, that was accompanied by a shear band (45°) clearly visible for the diagonal configuration as already observed for this type of geometry [15].

2.2.4 Conclusions

In this work, 17-4PH stainless steel lattice cylinders with a radial distribution of cells were built using a 3D printer. Three cell geometries, diagonal, diamond and FCC, and two different building orientations, 0° and 90°, were chosen. The 3DXpert software was used to design the samples, produced using the ProX100 printer (3D SYS-TEMS). The structures were characterized and subjected to compression tests by means of an hydraulic press. The geometry of the designed samples was reproduced by the process with an error of less than 1% and the geometries of the struts and nodes have been produced with-out defects. Regarding the mechanical performances of the samples under compression tests, the results suggested that when a diagonal geometry of the cells is used, the building orientation can strongly

influence the mechanical properties. In particular, the stiffness of the samples is higher in relation to a building orientation of 0° probably due to the higher number of struts along the compression direction. The diamond geometry showed isotropic mechanical properties almost independent from the building orientation of the structures. As for the FCC cells, the stiffness of the samples calculated in correspondence to a building orientation of 0° was significantly higher than the value calculated for the samples built at 90° with respect to the building plate. Although the geometry of the cells is isotropic, the performances resulted very different. Considering the relationship between the volume fraction and the mechanical properties of these samples, the results suggest that the radial orientation of the cells can influence the mechanical response of the lattice structures when the geometry of the cells can be varied by giving a radial distribution in relation to the building orientation.

The anisotropy of the mechanical properties found in SLM parts can be attributed to the oriented layer-by-layer growth process along the direction of the substrate. As expected, an increase of the overall system stiffness is found as the density increases. This suggests the possibility to easily tune the stiffness of the lattices, and to vary the object structure without significant changes in the overall stiffness. In particular, the optimization of the orientation of the cells can improve the mechanical properties of the lattice structures and enhance the performance efficiency of the produced cellular parts and, as a consequence, enhance the performances of the final product.

Chapter 3

Stereolithography (SLA) for eye model

In this chapter the research regarding the printing of a biocompatible scaffold for an eye model is presented. The scaffold should be biocompatible, transparent easy to handle and have geometry and dimensions similar to the eye. The chapter first focuses on the evaluation of the biocompatibility of different SLA resins, then on the effect of different sets of printing parameter on the properties of the scaffold. The samples are analyzed and evaluated based on the requirements. The published papers related to these topics are listed below:

- E.L. Mazzoldi, L. Riva, R.M. Ferraro, P.S. Ginestra, S.C. Giliani, "3D Printing of Biocompatible Scaffolds for Eye Tissue Engineering", Procedia CIRP 110 (2022): 214-219.
  In this work the candidate was responsible for the design and production of the samples, as well as their post-processing treatments.

- L. Riva, E.L. Mazzoldi, P.S. Ginestra, E. Ceretti, S.C. Giliani, "Eye model for floaters' studies: production of 3D printed scaffolds", Prog Addit Manuf (2022). https://doi.org/10.1007/s40964-022-00288-5.
  In this work the candidate was responsible of the samples design and fabrication. Moreover, he designed and carried out the testing. He collaborated in the data organization and analysis. Finally, he contributed to the writing and editing of the draft.

3.1 3D Printing of Biocompatible Scaffolds for Eye Tissue Engineering

3.1.1 Introduction

Several pathological conditions of the eye involving the vitreoretinal interface (*e.g.*, macular hole, macular pucker, retinal detachment, diabetic retinopathy, floaters) may require the vitreous body removal through a surgical procedure called vitrectomy [1,2]. The vitreous body is a viscoelastic, transparent gel made up of water, collagen fibers, hyaluronic acid, and other proteins and glycosaminoglycans [3]; moreover, it is rich in ascorbic acid, an important antioxidant which prevents cataract formation [4]. The vitreous body is an almost completely acellular tissue, except for a layer in the cortex where rare cells reside, mostly macrophage-like cells called hyalocytes [5]. During the surgery, the vitreous body is temporarily replaced with a variety of tamponade agents, such as gases, salt solutions, perfluorocarbon liquid, semifluorinated alkanes, or silicone oil, in order to prevent the eyeball from collapsing and to keep the retina in position [6]. Tamponade agents used nowadays are later either absorbed by the surrounding tissues or must be removed after some weeks due to their long-term toxicity; the vitreous cavity is eventually filled with the aqueous humor, a less viscous fluid secreted by the ciliary body, different from the vitreous humor for its physical, chemical, and biochemical properties. Indeed, the vitreous body does not regenerate [1,6].

To overcome the disadvantages of using temporary substitutes, novel materials are under investigation, including semi-synthetic polymers and hydrogels. Such experimental polymers should meet some requirements: they should be non-toxic, non-immunogenic, non-biodegradable to last over the time, and should have a refractive index and viscoelastic properties similar to the native vitreous humor. Moreover, they should allow the diffusion of electrolytes, oxygen, and nutrients [1].

An attractive future perspective is to culture the vitreous-resident cells, *i.e.* hyalocytes, either isolated from vitrectomized patients [7] or differentiated from patient-specific induced pluripotent stem cells (iPSCs) [8,9], in a three-dimensional environment constituted by hydrogels, in order to promote extracellular matrix deposition *in vitro* to lead to artificial vitreous production, and vitreous remodeling if implanted *in vivo* [1]. Pioneeristic studies on hyalocyte cultures have already been performed on human [10,11] and other mammalian cells [5,12,13], giving promising results, even though the realization of an artificial vitreous body *in vitro* still remains challenging.

To perform *in vitro* studies on hydrogels that have a consistency similar to the real vitreous body, *i.e.* not self-standing, highly hydrated gel-like structures, a rigid scaffold is necessary. Such scaffold must present appropriate features: it must be transparent to allow cell inspection under a microscope, it should resist high temperature and pressure to be sterilized by autoclave, it should confer a shape similar to the eyeball upon the hydrogel, it should be easy to handle to allow cell culture procedures and, above all, it must be biocompatible to keep viable cells in culture [14]. Some resins certified as biocompatible can be 3D-printed to produce transparent substrates. Therefore, different formulations were purchased and bowl-shaped specimens were 3D-printed by stereolithography (SLA). SLA is among the most popular technologies to print polymer substrates, since it allows the production of complex structure with defined mechanical properties [15,16].

In this preliminary work, the samples that showed the best dimensional accuracy after 3D-printing parameter optimization (layer thickness, exposure time and light blocker percentage added) were tested for long-term biocompatibility, and their transparency was evaluated at a microscopic level.

3.1.2 Materials and Methods

3.1.2.1 Substrates fabrications

Bowl shaped samples (D_{ext} = 24 mm) have been produced by SLA (Prusa SL1 printer) with a layer of 0.025 mm, an exposure time of 30 s and 1% of Light Blocker to assure the transparency of the resin. Details on the fabrication procedure have been previously described by Riva *et al* [17].
Three specimens have been fabricated for each resin type that has been tested. Clear and Tough resin (3DResyns©, Barcelona, Spain) have been purchased in different blind formulas (#3, #4, #5, and #6) as requested by the company while the Dental LT resin and the Elastic 50A resin (both from Formlabs©, Somerville, MA) have been tested as the commercially available variation. All the samples have been sterilized by autoclave before use.

3.2.2.2 Cell culture

MS5 cells were cultured in Dulbecco's Modified Eagle Medium (DMEM, Euroclone, Milan, Italy) completed with 10% fetal calf serum (FCS, Euroclone), 1% L-glutamine (Euroclone), 1% penicillin/streptomycin (Euroclone). Cultured cells were maintained at 37 °C, 5% CO_2 in a humidified incubator.

3.1.2.3 Biocompatibility tests: ATP cell viability assay

3D printed, round resin samples have been let to release into 10 mL complete cell culture medium, in 100 mm-diameter Petri dishes, for one week in incubator. For each resin formulation, three samples were tested. As control, 10 mL complete DMEM were maintained in a Petri dish in the same conditions.

MS5 cells were seeded in 96-well plates, 1,000-3,000 cells/well, in triplicate for each experimental point. Medium was changed the following day with resin-conditioned medium prepared as described before. After 1, 3, and 6 days, cell morphology was checked by observing them under an inverted microscope (EVOS™ XL, Thermo Fisher Scientific, Waltham, MA), then cells were subjected to an ATP cell viability assay (CellTiter-Glo® 3D Cell Viability Assay, Promega, Madison, WI), as per manufacturer's instructions. An ATP standard curve was set up in parallel for absolute quantification. Luminescence was acquired using a Tecan Infinite® M200 microplate reader (Tecan, Männedorf, Switzerland).

3.1.2.4 Biocompatibility tests: Annexin V/PI apoptosis assay

MS5 cells were seeded in 12-well plates, 25,000-50,000 cells/well. The day after, medium was changed with resin-conditioned medium, as performed for ATP cell viability assay. After 1, 3, and 6 days, cells were detached and stained with Annexin V-FITC/Propidium iodide (PI) apoptosis detection kit for flow cytometry (BD Bioscience, Franklin Lakes, NJ), and acquired on a FACS Canto II cytometer (BD Bioscience). Data were collected from at least 1x104 events/sample and analyzed with a FlowJo software (TreeStar, Ashland, OR). Cell viability was expressed as the percentage of Annexin V/PI double negative cells.

3.1.2.5 Cell visualization

MS5 cells were detached by tripsinization and immediately observed through the bottom of bowl-shaped resin samples under an inverted microscope (EVOS™ XL). Resin samples were used either as built or after grinding with wet sandpaper (500 and 2000 grit). Pictures were taken at 20X magnification.

3.1.2.6 Statistical analysis

Data from replicates were expressed as mean ± standard deviation (S.D.). Comparisons between groups were performed by Student's t-test, using GraphPad Prism (San Diego, CA).

3.1.3 Results

3.1.3.1 Clear and Tough #3, #4, and #5 resins were demonstrated to be highly toxic

Since resin specimens are intended to be used as a support in cell culture, the biocompatibility of the formulations is the first feature to be assessed. In order to reduce the number of cells and the volumes of reagents to be used, indirect cell viability tests were performed, i.e. round resin samples were dipped in complete DMEM, then cells were put in contact with resin-conditioned DMEM. The first formulations tested were named #3, #4, and #5 (the numbers correspond to different formulas developed by the company for the Clear and Tough Resin, 3DResyns©). After one day of culture in the presence of resin-conditioned medium, MS5 cells were almost all dead or suffering, while control cells grew and appeared healthy (Fig. 1A).

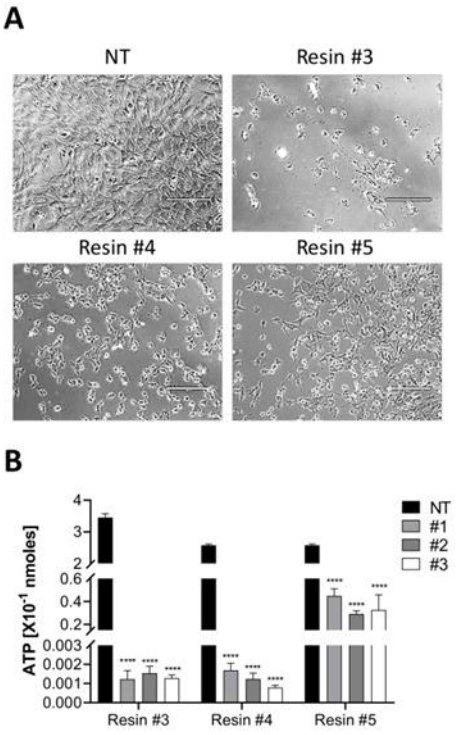

Fig. 1 A) Representative pictures of MS5 cells cultured for one day in complete DMEM conditioned for 7 days with resin #3, #4, end #5, or control DMEM (not treated, NT). Scale bar 200 µm. B) ATP concentration measurement in MS5 cells cultured for one day either in control DMEM (NT) or in DMEM conditioned for 7 days with resin #3, #4, end #5. The graph shows the mean ± S.D. (n = 3, **** $p < 0.0001$).

This result was confirmed by both ATP cell viability assay (Fig. 1B) and Annexin V/PI apoptosis assay (Fig. 2A and B). ATP cell viability assay is an enzymatic assay that exploits the ATP produced by the cells to convert luciferin into oxyluciferin, which generates a light signal. Thus, the signal detected is a measure of the number of metabolically active cells in culture. A decreased luminescence can be caused

by either cell death or metabolic quiescence due to over-confluence or medium exhaustion. In this experiment, luminescence generated by the cells cultured in the presence of resin #3 and #4 was negligible in comparison to not treated cells (NT). The signal was higher in the presence of resin #5, but still about one tenth of NT (Fig. 1B). The decrease in luminescence was due to increased cell death, as demonstrated by Annexin V/PI apoptosis assay.

In this test, cells that underwent apoptosis (*i.e.*, programmed cell death) are stained positive for Annexin V and/or PI, depending on the apoptosis phase they are. On the contrary, living cells are double negative. In this experiment, cells cultured in the presence of resin #3 resulted almost all dead; with resin #4, about 5% of cell survived, while with resin #5 cell viability was about 30%, still too low in comparison to NT cells (Fig. 2A and B).

Since cell viability was severely affected already after one day of culture, it was not useful to go on with longer timepoints with these formulations.

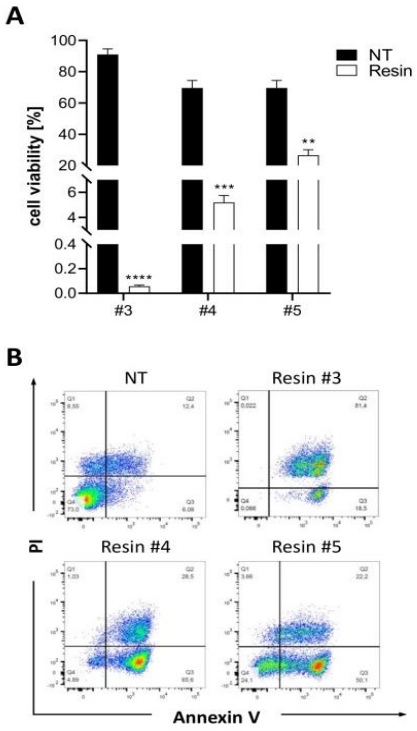

Fig. 2 A) MS5 cell viability (expressed as percentage of Annexin V^-/PI^- cells) after one day of culture either in control DMEM (NT) or in DMEM conditioned for 7 days with resin #3, #4, end #5. The graph shows the mean ± S.D. (n =3, ** p > 0.01, *** p > 0.001, **** p > 0.0001). Representative dot plots are shown in panel B.

3.1.3.2 Dental LT resin slightly impaired cell growth without affecting cell viability

The next formulation to be tested was named Dental LT (Formlabs©). After one day, cells appeared alive at microscope inspection, displaying a monolayer comparable to NT (Fig. 3A). The ATP content measured in resin-conditioned medium treated cells was slightly, yet significantly, reduced compared to NT (Fig. 3B). However, this difference was not due to increased cell death, since the percentage of Annexin V/PI double negative cells (*i.e.*, living cells) was similar between the two groups (Fig. 4A and B). Since promising results were obtained after one day, it was worth proceeding with longer timepoints. After 3 days, both treated and not treated cells were still alive (Fig. 3A) and increased in number, as pointed out by ATP assay; however, the difference between the two groups was still present (Fig. 3B).

Nevertheless, no difference in the percentage of living cells was observed following FACS staining (Fig. 4A and B).

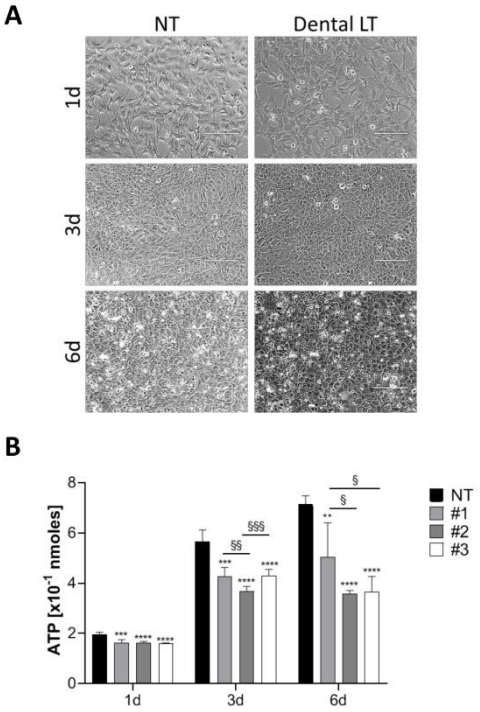

Fig. 3 A) Representative pictures of MS5 cells cultured for 1, 3, and 6 days in complete DMEM conditioned for 7 days with Dental LT resin, or control DMEM (not treated, NT). Scale bar 200 μm. B) ATP concentration measurement in MS5 cells cultured for 1, 3, and 6 days either in control DMEM (NT) or in DMEM conditioned for 7 days with Dental LT resin. The graph shows the mean ± S.D. (n = 3, § p > 0.05, ** and §§ p > 0.01, *** and §§§ p > 0.001, **** p < 0.0001).

After 6 days, both treated and NT cells still appeared alive at microscope inspection, although overcrowded, with some detached round cells, observed in both groups (Fig. 3A). Again, ATP content increased in NT cells; instead, ATP content in resin exposed cells was stable as compared to day 3 (Fig. 3B). However, FACS analysis of living cells did not highlight differences in the two groups, even though the percentage of living cells decreased to about 50% also in NT cells, probably due to overconfluence (as seen in Fig. 3A) and nutrient starvation for medium exhaustion (Fig. 4A and B).

We can speculate that some component released by Dental LT resin could impact either on cell growth rate or metabolism starting from early timepoints, without causing a massive cell death.

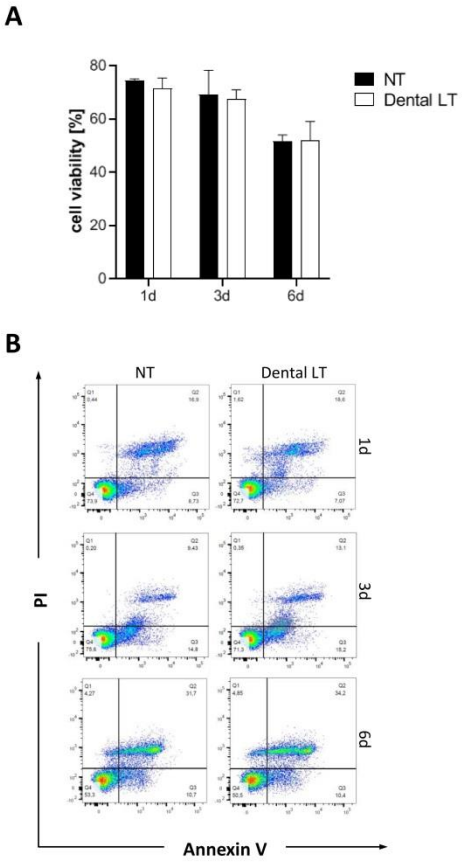

Fig. 4 A) MS5 cell viability (expressed as percentage of Annexin V^-/PI^- cells) after 1, 3, and 6 days of culture either in control DMEM (NT) or in DMEM conditioned for 7 days with Dental LT resin. The graph shows the mean ± S.D. (*n* =3). Representative dot plots are shown in panel B.

3.1.3.3 Elastic 50A and Clear and Tough #6 resins showed the best biocompatibility among the tested ones

The same biocompatibility evaluations were carried out on Elastic 50A resin (Formlabs©) and Clear and Tough #6 resin (3DResyns©).

ATP content in Elastic 50A resin-treated cells was comparable to the NT group at day 1; at day 3, it increased in NT cells and in resin-treated cells, but to a lower extent. At day 6, ATP content was reduced compared to the previous timepoint, probably due to metabolic quiescence for overconfluence or nutrient deprivation, but no significant difference between the two groups was highlighted (Fig. 5A). However, Annexin V/PI staining did not point out any difference in cell viability at any timepoint (Fig. 5B).

Analogously to Elastic 50A resin, MS5 cells treated with Clear and Tough #6 resin showed an ATP content similar to NT cells at any timepoint. Even though a tiny reduction was observed, especially at 3 and 6 days, it was not significant, except for the third specimen tested at day 1 and day 6 (Fig. 6A). Moreover, a gradual increase was observed over the time for each group, meaning that the resin did not significantly impair cell growth and metabolism (Fig. 6A).

Also, cell viability was not compromised, as assessed by Annexin V/PI staining (Fig. 6B).

Overall, the last two formulations tested, Elastic 50A and Clear and Tough #6, proved to be the best ones in preserving cell viability, having only a negligible impact on cell growth.

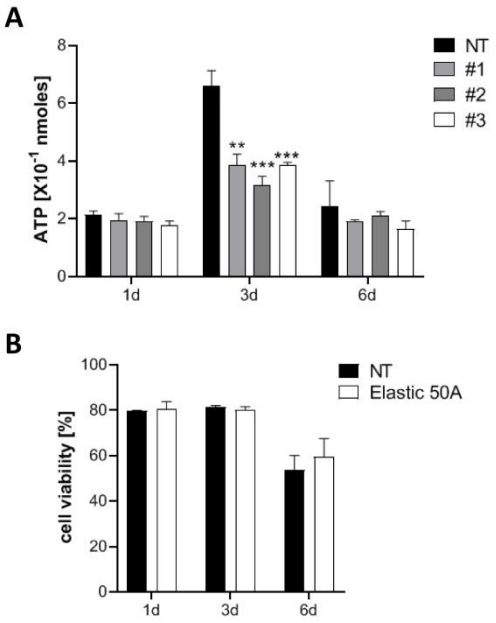

Fig. 5 A) ATP concentration measurement in MS5 cells cultured for 1, 3, and 6 days either in control DMEM (NT) or in DMEM conditioned for 7 days with Elastic 50A resin. The graph shows the mean ± S.D. (n = 3, ** p > 0.01, *** p > 0.001). B) MS5 cell viability (expressed as percentage of Annexin V$^-$/PI$^-$ cells) after 1, 3, and 6 days of culture either in control DMEM (NT) or in DMEM conditioned for 7 days with Elastic 50A resin. The graph shows the mean ± S.D. (n =3).

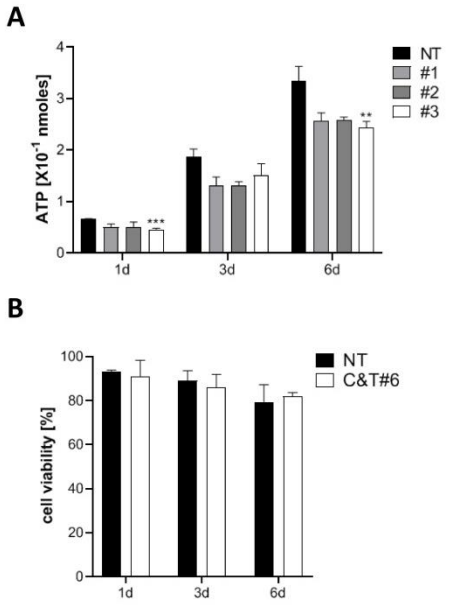

Fig. 6 A) ATP concentration measurement in MS5 cells cultured for 1, 3, and 6 days either in control DMEM (NT) or in DMEM conditioned for 7 days Clear and Tough #6 resin. The graph shows the mean ± S.D. (n = 3, ** p > 0.01, *** p > 0.001). B) MS5 cell viability (expressed as percentage of Annexin V$^-$/PI$^-$ cells) after 1, 3, and 6 days of culture either in control DMEM (NT) or in DMEM conditioned for 7 days with Clear and Tough #6 resin. The graph shows the mean ± S.D. (n =3).

3.1.3.4 Post-processing with 2000 grit wet sandpaper increased cell visibility

Another important requirement of resin specimens used in cell culture is transparency: indeed, the operator constantly needs to check the status of the cultured cells, by using an inverted optical microscope. Thus, we wondered if the resin specimens produced in the present work allowed microscope observation. To this end, we detached MS5 cells and put the floating cells into bowl-shaped scaffolds made up with Clear and Tough #4 resin. As shown in Figure 7A, it was impossible to visualize cells beyond the printing layers. In order to reduce the interference and improve resin transparency, the samples were post-processed by grinding with sandpaper (500 and 2000 grit); to do this, the sandpaper was previously wetted with water. Transparency was remarkably improved only with 2000 grit grinding (Fig. 7A). Since resin #4 resulted to be non-biocompatible, the same post-processing protocol was applied to Clear and Tough #6 and Dental LT resins. Also, as-built #6 resin did not allow cell visualization; however, grinding with 2000 grit wet sandpaper improved cell observation (Fig. 7B). Finally, Dental LT resin was tested as built or grinded with 2000 grit sandpaper wetted either with water or with isopropanol; moreover, as built, printed scaffold was wetted with some drops of liquid resin in order to smooth the roughness. Grinding with sandpaper clearly increased cell visibility; however, the printing layers were still visible, yet faintly, after grinding with sandpaper wetted with isopropanol. On the other hand, wetting the printed resin with liquid resin did not increase transparency enough: indeed, in this way cell could be seen, but the printing layer interference was still present and disturbing (Fig. 8). We can conclude that post-processing with 2000 grit sandpaper wetted with water proved to be the best method to increase cell visibility through the bottom of 3D printed resin scaffolds.

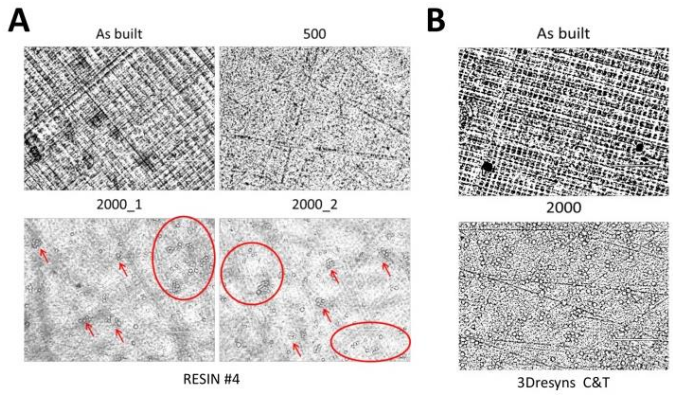

Fig. 7 Representative images of floating MS5 cells observed under an optical microscope through the bottom of the printed resin samples. A) Clear and Tough #4 resin samples were used either as built or post-processed by using 500 and 2000 grit wet sandpaper. Circles and arrows highlight visible cells in samples grinded with 2000 grit sandpaper. B) MS5 cell visualization through Clear and Tough #6 resin printed samples, either as built or grinded with 2000 grit sandpaper. Scale bar 200 µm.

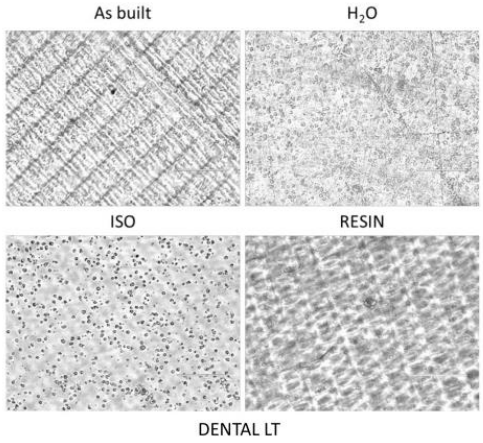

Fig. 8 Representative images of floating MS5 cells observed under an optical microscope through the bottom of the printed resin samples. Dental LT resin samples were used either as built of after post-processing with 2000 grit sandpaper, wetted either with

water (H_2O) or with isopropanol (ISO). Resin samples, as built, were also spread with some drops of liquid resin to improve cell visualization. Scale bar 200 µm.

3.1.4. Conclusions

To set up a 3D cell culture for eye tissue engineering, a resin scaffold is needed to be loaded with a cell-containing hydrogel. Several commercial formulations are available from different companies: all of them are certified as non-toxic at 24h. We further tested six resins by performing two different biocompatibility analyses (ATP assay and Annexin V/PI staining for flow cytometry) on the MS5 cell line, not only at day 1, but also at longer timepoints (3 and 6 days), since we expect to maintain cell in culture for at least one week. Surprisingly, Clear and Tough #3, #4, and #5 resins did not pass the test already at 24h: these formulations are not suitable for our purposes. Dental LT resin gave better results: indeed, resin-treated cells survived also at longer timepoints, even though slowed down in their growth rate. Also, Elastic 50A and Clear and Tough #6 resins gave satisfactory results: both did not impair cell viability and only had a little, usually not significant, impact on cell growth rate.

For these reasons, we can conclude that Clear and Tough #6 resin is the best for our purposes among the ones tested: it could be used in cell culture without concerns of cell death induction. However, since some detrimental effects on cell growth persist, we are still looking for better solutions.

Another feature to be considered when using resin samples in cell culture is their transparency. The as-built resin samples did not allow cell visualization because of the interference of the printing layers; post-processing with 2000 grit sandpaper, wetted with water, highly increased cell visibility. However, we still need a more standardized method to make 3D printed resin specimens more transparent, even if at the moment we consider our achievements acceptable for our purposes.

3.2 Eye model for floaters studies: production of 3D printed scaffolds

3.2.1 Introduction

Floaters are opacities of the vitreous body that are responsible for visual field distortions that appear as lines, circles or spots [1]. Floaters, as the name states, float around the eyes but do not exactly follow eye and head movements due to the damping characteristic of the internal structure of the vitreous body. The cause of their formation can be either endogenous or exogenous [2]. The endogenous cause is a liquefaction of the vitreous body that causes an aggregation of collagen in fibrils that move inside the eye. Floaters generated by this type of phenomenon are called primary floaters. On the other hand, secondary floaters are of exogenous causes such as preretinal or vitreal hemorrhages. To this day, a proper way to measure the severity of floaters has yet to be reported [3]. Moreover, this research is made more complex by the fact that the influence floaters have on a patient quality of life is highly subjective [4]. In fact, people with a higher vitreal opacity may suffer less floaters than people with a lower opacity, and vice versa [5]. Nevertheless, in some cases the floaters are so severe that they require to be treated. There are two possible treatments: vitrectomy and laser vitreolysis [6]. Vitrectomy consists of removing floaters by suctioning them through a needle that is inserted into the eye, while laser vitreolysis is a closed eye procedure where the laser breaks down floaters in smaller pieces. Vitrectomy seems to be more efficient, even if surgical complications may occur [7].

Technological advances in recent years have made it possible to develop new tools for the study and research of diseases [8]. Among these, a prominent place is held by 3D printing, which has enabled the production of bio-models. Bio-models are systems that aim to replicate the shape and the structure of a specific body part, usually to study or test a treatment for a pathology in vitro. Currently, bio-models main applications are: implants and prosthesis fabrication, preoperative practicing, surgical training and teaching, device testing and research purpose [9]. For example, Sedlak et al. [10] printed an eye prosthesis with aesthetic qualities comparable to hand-crafted ones, although with high production costs. Xie et al. [11] developed a physical eye model able to replicate the optical performance of the human eye for fundus range viewing research. Again, Phan et al. [12] fabricated a blinking eye model to study the release of ophthalmic drugs through contact lenses. Finally, Yap et al. [9] printed a multi material ophthalmic model with different tactile properties and flexibility for surgical simulations.

A further possibility related to 3D printing is bioprinting. Bioprinting consists in printing a bioink containing living cells inside [13]. The cells are then treated and cultured to survive and replicate within the structure [14]. In this way, it is possible to generate models that not only replicate the geometry and structure but also the biology of the desired tissue, allowing a dynamic and 3D culture of cells [15]. Scaffolds and substrates for tissue engineering must be biocompatible [16], have adequate mechanical properties [17] to be suitable for mechanical stimulation during cell culturing, and sustain the sterilization process (autoclave or UV). A further specific characteristic is transparency because it allows to visually inspect the cells through microscopy and to stimulate them with light for research purposes. One of the most used technologies to print polymer substrates is Stereolithography (SLA) [18]. SLA allows the fabrication of complex structures with different types of resins with different mechanical properties [19]. Resins labeled as biocompatible by the manufacturers may however be toxic as important effects may appear later than the standard observation time (24h according to ISO 10993-5) [20]. It is therefore useful to carry out biocompatibility tests with an observation time as long as the time of the target investigation.

This work aims to optimize the printing parameters to produce a transparent and biocompatible resin eye model. The scaffold, in addition to providing the necessary support, will also need to have a geometry

similar to the physiological eye, as already demonstrated for cardiac applications [14]. The investigated printing parameters are layer thickness, exposure time and light blocker percentage added to the resin. The selected samples were then tested for biocompatibility and the cells were visualized under optical microscope. The visualization of the cells is essential for the right evaluation of cells state, proliferation and differentiation. The development of a 3D printed eye bio-model, then, will allow a better understanding of the etiology and formation mechanisms of eye floaters.

3.2.2 Materials and Methods

3.2.2.1 Sample production

The designed geometry of the sample is visible in Fig. 1. It consists in a bowl shape with an internal diameter of 24 mm, as the medium diameter of the human eye, a height of 12 mm and a thickness of the wall and the bottom of 1 mm and 0.2 mm, respectively. This configuration has been chosen combining the biological analysis, the 3D printing process and testing requirements. Specifically, a flat and transparent bottom surface allows microscope inspections, and an open top could facilitate a 3D cell culture maintaining a semispherical shape. The samples were fabricated by SLA technology with a Prusa SL1 3D printer (Prusa©). The material used was Clear and Tough Resin, labeled biocompatible by the supplier (3Dresyns©). Different printing parameters were used to determine their effect on the final properties of the samples. Three different parameters were taken into account. In particular, the layer thickness, the exposure time and the percentage of Light Blocker (LB1 Bio, Fine Tuner, 3Dresyns©) added to the resin. Furthermore, three levels for each parameter were investigated. Particularly, a layer thickness of 0.025-0.05-0.1 mm, an exposure time of 10-20-30 s and a LB1 percentage of 0.5-1-1.5 % for a total of 27 combinations of parameters. A summary of the factors and levels is visible in Tab. 1. The parameters combinations were used randomly in order to avoid any error propagation (Tab. 2). The Test Name identifies the actual order of execution of the tests (run order), while the Standard Order lists the tests by increasing parameters. The tests will be named with the numbers related to the test name (run order). Each print test includes 3 samples. After printing the samples were washed in isopropyl alcohol for 4 minutes and then dried and cured for 5 minutes. Both these steps were completed with the Prusa Curing and Washing Machine (CW1, Prusa©).

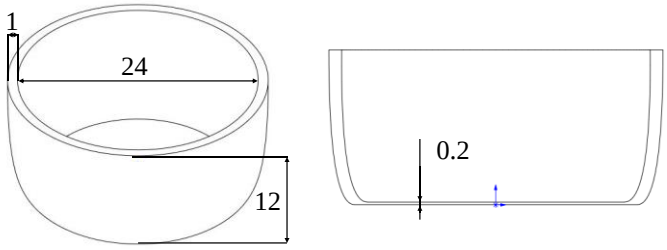

Fig. 1 Scheme of the geometry and dimensions of the printed scaffolds. Measures in mm.

Table 1: Tested parameters and levels.

Factors	**Levels**		
Layer thickness [mm]	0.025	0.05	0.1
Exposure time [s]	10	20	30
LB1 percentage [%]	0.5	1	1.5

Table 2: Printing combinations.

Test Name	**Layer [µm]**	**Exp. Time [s]**	**LB1 [%]**	**St. Ord.**

13	0.025	10	0.5	1
23	0.025	10	1	2
1	0.025	10	1.5	3
19	0.025	20	0.5	4
7	0.025	20	1	5
17	0.025	20	1.5	6
5	0.025	30	0.5	7
11	0.025	30	1	8
2	0.025	30	1.5	9
26	0.05	10	0.5	10
16	0.05	10	1	11
9	0.05	10	1.5	12
15	0.05	20	0.5	13
6	0.05	20	1	14
25	0.05	20	1.5	15
4	0.05	30	0.5	16
21	0.05	30	1	17
3	0.05	30	1.5	18
8	0.1	10	0.5	19
18	0.1	10	1	20
24	0.1	10	1.5	21
22	0.1	20	0.5	22
12	0.1	20	1	23
20	0.1	20	1.5	24
10	0.1	30	0.5	25
27	0.1	30	1	26
14	0.1	30	1.5	27

3.2.2.2 Sample characterization

Three characterization steps were carried out in succession, each with different tested properties. The steps are defined as: qualitative, quantitative and biological characterization. Qualitative characterization was performed on every sample. Quantitative examination was carried out only on the samples that passed the qualitative ones. Biological characterization was performed on the best samples chosen after quantitative characterization.

Qualitative investigations

The qualitative analyses were bases on a pass-fail selection system. The samples were subjected to the next test only if they already passed the previous one. The first two tests relay on the process: the failing parameters combinations (fabrication fails) and excess support defects (supports residual region). Once the failed and defective samples have been rejected, the following step was to verify the transparency of the bottom side, which is necessary for microscopy evaluations. Finally, the walls transparency/clarity was evaluated, as needed for cell culture inspection and light stimulation.

Printing failures

The samples were visually inspected for good printing and structural integrity. The ability to perform the required function of containing cells was evaluated.

Printing support residual region

The size of the region containing the printing support residuals was visually observed. The excessive deformation of the geometry was considered to be unfunctional.

Transparency

The transparency of the bottom of the sample was investigated by placing the sample on a reference image. Clarity, opacity and blurriness were visually evaluated.

Color

The samples were compared and divided in three groups, rejected, acceptable and optimal, based on their color, from darkest to clearest, respectively. A dark color was considered unsuitable for the final application.

Quantitative investigations

The samples that passed all the qualitative analyses were further investigated with quantitative analyses. These investigations were carried out in order to have a more complete understanding of the performance and quality of the process. The results were statistically analyzed with ANOVA analysis, providing a deeper insight on the effects of the printing parameters on printing accuracy and process stability.

Roughness

Roughness measures were carried out using a Mitutoyo Surftest Sj-301 profilometer in accordance with UNI EN ISO 4288:1997. Three measures were taken for each sample. The roughness values of the tests were obtained by the average of all measurements.

Wall thickness and external diameter

Wall thickness and external diameter measurements were carried out using a digital caliper. One measure was taken for each sample of the same test (three samples). The thickness and the diameter values were obtained by the average value of the three samples.

Layer accuracy

The thickness of the printing layer was measured with Hirox RH-200 digital microscope. One measure was taken for each sample of every test (three samples). The thickness value was obtained by the average value for each test.

Biological characterization

The samples selected after qualitative and quantitative analyses were subjected to biological tests: biocompatibility test and microscope cell visualization test. The samples were firstly subjected to the biocompatibility tests after the washing and curing protocol mentioned above: samples were washed in isopropyl alcohol for 4 minutes, left drying and then cured for 5 minutes. The protocol was modified later to achieve acceptable results in terms of cytotoxicity. Specifically, the washing and curing steps were increased to 3 cycles each, for a total of 12 minutes of washing and 15 minutes of curing.

Biocompatibility test.

Samples were sterilized by autoclave (Alfa Junior, VWR International PBI,Radnor, PA) prior to use in cell biology context.

Biocompatibility was assessed using the stromal cell line MS5 (kindly provided by Dr. Anna Villa, San Raffaele Telethon Institute For Gene Therapy, Milan, Italy). MS5 cells were cultured in Dulbecco's Modified Eagle Medium (DMEM, Euroclone, Milan, Italy) supplemented with 10% fetal bovine serum (FBS, Euroclone), 1% penicillin/streptomycin (Sigma-Aldrich, St. Louis, MO), and 1% L-glutamine (Sigma-Aldrich) (complete media), and passaged by trypsinization twice a week, when reaching confluence.

Samples were placed in 100 mm-diameter cell culture dishes and have been let to release any potential component into 10 mL of complete media, for one week in a humidified incubator at 37 °C, 5% CO2. As a control, 10 mL of complete DMEM were put in a dish in the incubator in the same conditions.

The day before the test, MS5 cells were seeded either in flat bottom 96-well plates (3,000 cell/well) or in 12-well plates (50,000 cells/well). Three replicates were set up for each condition. The day after, cell supernatant was removed and replaced by either resin sample conditioned medium or control medium. Cell health status was firstly checked by observing cell morphology under an inverted optical microscope (EVOS™ XL, Thermo Fisher Scientific, Waltham, MA). Cells seeded in the 96-well plates were subjected to an ATP cell viability assay (CellTiter-Glo® 3D Cell Viability Assay, Promega, Madison, WI), as per manufacturer's instructions, after 24h, 72h, and 6 days of treatment. To perform an absolute ATP quantitation, a standard curve was generated in parallel by preparing serial dilutions of a standard ATP disodium salt (Promega). Luminescence was acquired by using a Tecan Infinite® M200 microplate reader (Tecan, Männedorf, Switzerland).

In parallel, cells seeded in the 12-well plates were collected after 24h, 72h, and 6 days of treatment, stained with an Annexin V-FITC / Propidium iodide (PI) apoptosis detection kit for flow cytometry (BD Bioscience, Franklin Lakes, NJ), and analyzed on a FACS Canto II cytometer (BD Bioscience). Data were collected from at least 1x104 events/sample and elaborated with FlowJo software (TreeStar, Ashland, OR).

Data from replicate tests were expressed as mean ± standard deviation (S.D.). Comparisons between treatments were performed by Student's t-test, using GraphPad Prism (San Diego, CA).

Microscope cell visualization tests

MS5 cells were detached by trypsinization, moved into the printed samples, and immediately observed under an EVOS™ XL inverted optical microscope through the bottom of the samples, when still floating into the medium. Pictures were taken at 4X and 20X magnifications.

3.2.3 Results and discussion

3.2.3.1 Qualitative analysis

Fabrication Fails

The first step was the verification of the printing process to produce the samples without any defect that would compromise the proper functioning. Six tests were not able to successfully complete the printing process, precisely, tests number 26, 16, 9, 8, 18 and 24. The failures can have different causes: the samples did not print at all (Fig. 2a), the samples were printed with a distorted geometry (Fig. 2b), and the samples were printed with the correct geometry but incomplete (Fig. 2c). From Tab. 2 it can be observed that all the failure tests have in common a low exposure time (10 s) associated with a thick layer (0.05 mm; 0.1 mm). These combinations resulted in an insufficient polymerization of the material that did not allow the formation of the desired geometry.

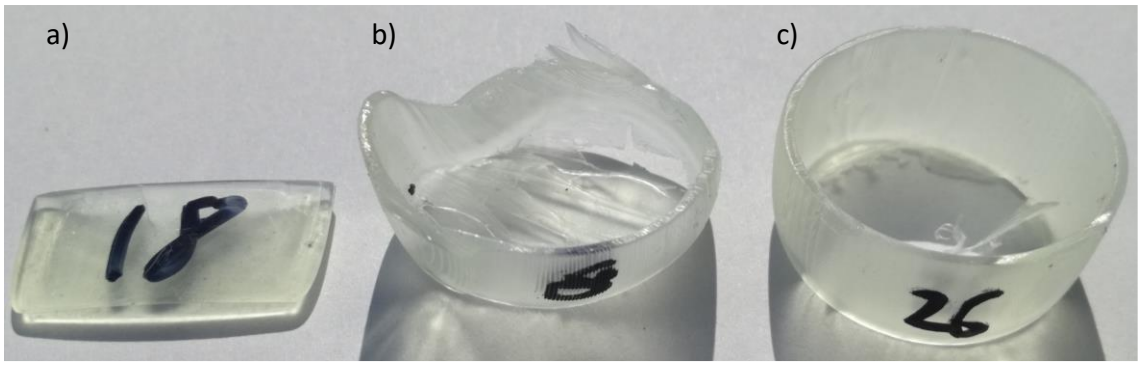

Fig. 2 Printing failure types: geometry not formed (a), distorted geometry (b), incomplete bottom (c).

Printing support residual region

The second evaluation step was to inspect the region where the supports were generated during the printing process. The printed parts were not considered suitable if the supports generated during the manufacturing process left largely deformed areas compromising the final geometry. Four tests did not pass this examination. In particular, tests number 7, 5, 11, and 4. Examples of failed support region are visible in Fig. 3. The accumulated material located on the support region area is probably due to an overexposure of the resin caused by a thin layer (0.025 mm; 0.05 mm) and an excessive exposure time (20 s; 30 s) associated with a low content of LB1 (0.5 %; 1%).

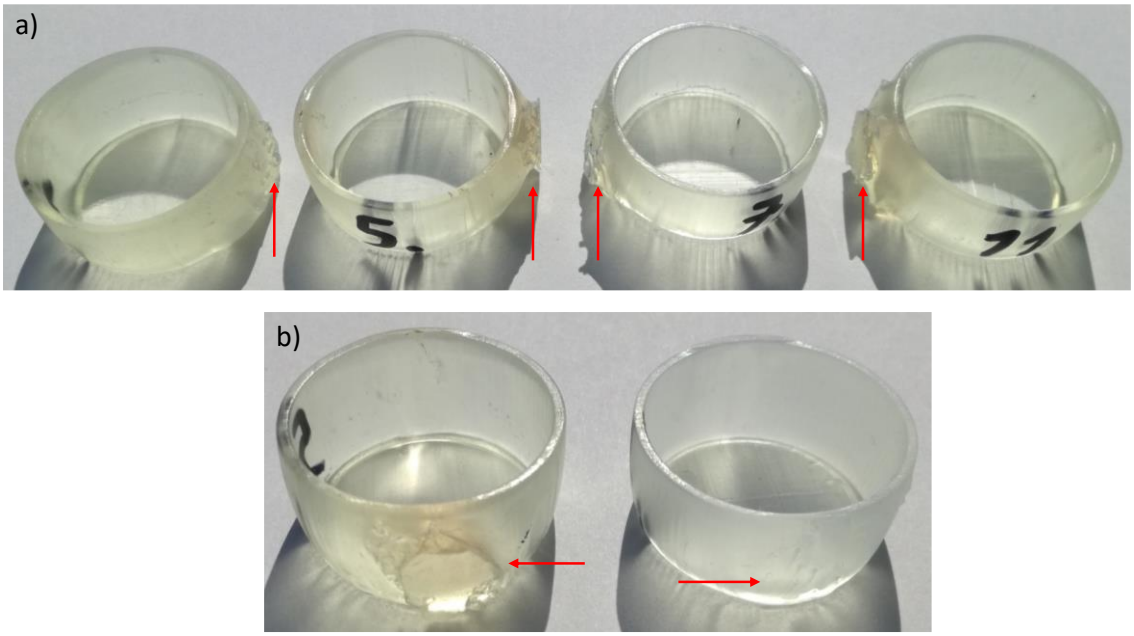

Fig. 3 a) Tests with support region failure. From left to right: test n. 4, 5, 7, 11. b) Comparison between tests n. 5 (failure) and test n. 1 (ok). The red arrows point to the support regions

Transparency

The ability to see the cells through the printed structure is fundamental for the final application. In order to test the transparency, the samples were placed on top of a printed logo of our university. If the logo details were clearly visible, the test was considered passed. Fig. 4 compares two tests, the one on the left met the requirements (test n. 3), the sample on the right did not pass (test n.12). It is possible to note that both of the tests are transparent, in fact the logo is visible through both of the samples, probably due to the small thickness of the bottom side (0.2 mm). However, test n.12 presents a more opaque and slightly blurred logo. Tests number 12, 20 and 22 reported the same visualization issues and failed the transparency test. These tests are characterized by the same printing parameters. In fact, they were all printed with a layer thickness of 0.1 mm and an exposure time of 20 s. Probably, the exposure time

was not enough to guarantee the full polymerization of the thick layer of resin causing a more irregular internal structure that resulted in increased opacity and blurriness.

Figure 4: Comparison between test n.3 that passed the transparency test (left) and test n.12 that did not (right).

Color

The last visual investigation is based on the color of the samples. Since the cells that will be held inside the eye models will probably be subjected to light stimulation, the samples need to be as clear as possible. We divided the samples in 3 groups, optimal, acceptable and rejected, based on their color. The tests of the optimal and acceptable groups were considered suitable for the final application. Fig. 5 shows the samples divided in the three groups. The samples with the red cross on them are the samples that failed the previous tests, they have been added to allow a proper comparison of the colors. It is possible to note how the rejected group shows a more dark-orange color while the other two groups are more clear-yellow. Tests number 19, 21 and 2 were then rejected, tests number 15, 17, 25, 27, 3, 6 and 13 were considered acceptable, while tests 10, 14, 23 and 1 were considered the optimal ones. It is possible to identify some trends based on the process parameters of the samples. As the layer becomes thinner (0.025 mm; 0.05 mm) the color gets darker and orange. The same effect is given by increasing the exposure time (20 s; 30 s). For example, tests number 4 and 21, with an exposure time of 30 s, were placed in the rejected group while all the others samples with a layer thickness of 0.05 mm were considered acceptable. Again, test number 27 is the only test placed in the acceptable group while all the other tests with a layer thickness of 0.1 mm were considered optimal. From these observations it can be concluded that excessive polymerization will darken the color of the resin. It is also interesting to note that tests number 23 and 1 both belong in the optimal group. In these cases, the effects of the layer thickness and exposure time seem to balance each other. Furthermore, an influence of the percentage of LB1 present in the samples cannot be excluded although has been considered negligible for this investigation.

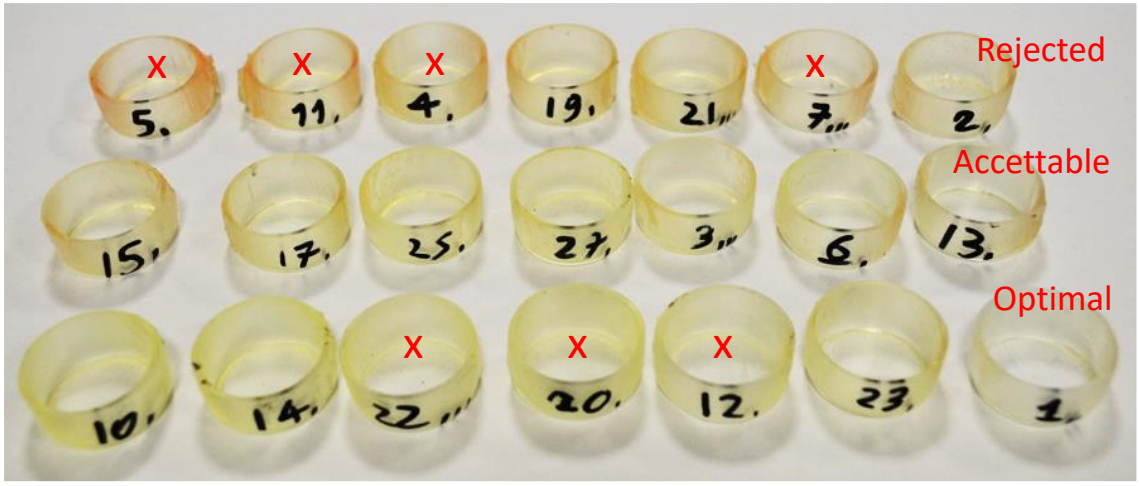

Fig. 5 Tests divided in groups by color. The red x indicates samples that failed the previous examinations.

Selection based on the qualitative investigations

The tests that passed all the qualitative investigations are visible in Tab. 3. A general linear relationship between layer thickness and exposure time can be noted. In fact, the tests that passed the qualitative investigation are characterized by a layer thickness of 0.025 mm printed with an exposure time 10 s; a layer thickness of 0.05 mm printed with an exposure time 20 s; a layer thickness of 0.1 mm printed with an exposure time 30 s. The light blocker influence may be seen in the two exceptions tests number 17 and 3 where the 0.025 mm layer is associated with the 20 s exposure time and the 0.05 layer is associated with the 30 s exposure time, respectively. In these cases, the high percentage of LB1 may have reduced the polymerization of the resin enough to avoid darkening.

Table 3: Samples that passed the qualitative investigations.

Test Name	Layer [µm]	Exp. Time [s]	LB1 [%]	ST. Ord.	Building	Support	Transparency	Color
13	0.025	10	0.5	1	✓	✓	✓	✓
23	0.025	10	1	2	✓	✓	✓	✓
1	0.025	10	1.5	3	✓	✓	✓	✓
19	0.025	20	0.5	4	✓	✓	✓	×
7	0.025	20	1	5	✓	×	×	×
17	0.025	20	1.5	6	✓	✓	✓	✓
5	0.025	30	0.5	7	✓	×	×	×
11	0.025	30	1	8	✓	×	×	×
2	0.025	30	1.5	9	✓	✓	✓	×
26	0.05	10	0.5	10	×	×	×	×
16	0.05	10	1	11	×	×	×	×
9	0.05	10	1.5	12	×	×	×	×
15	0.05	20	0.5	13	✓	✓	✓	✓
6	0.05	20	1	14	✓	✓	✓	✓
25	0.05	20	1.5	15	✓	✓	✓	✓
4	0.05	30	0.5	16	✓	×	×	×
21	0.05	30	1	17	✓	✓	✓	×
3	0.05	30	1.5	18	✓	✓	✓	✓

8	0.1	10	0.5	19	✗	✗	✗	✗
18	0.1	10	1	20	✗	✗	✗	✗
24	0.1	10	1.5	21	✗	✗	✗	✗
22	0.1	20	0.5	22	✓	✓	✗	✗
12	0.1	20	1	23	✓	✓	✗	✗
20	0.1	20	1.5	24	✓	✓	✗	✗
10	0.1	30	0.5	25	✓	✓	✓	✓
27	0.1	30	1	26	✓	✓	✓	✓
14	0.1	30	1.5	27	✓	✓	✓	✓

3.2.3.2 Quantitative analysis

Roughness

The roughness can have a significant influence on the transparency of the samples. A low roughness allows the light to better pass through the material without being reflected back, making the object clearer. Three roughness measurements were taken for each of the three samples of every test. The measurements were taken on the back of the bottom side and perpendicular to the building direction. The average value of the measurements was considered the roughness of the test. The results are visible in Fig. 6.

The results show that the roughness is relatively low and uniform despite different parameters combinations used, as expected for this process. In particular, the lack of influence of the layer thickness is also confirmed by the ANOVA analysis that gives a p-value of 0.382. On the other hand, it is possible to note how the measurements corresponding to the 0.1 mm layer thickness are more scattered in relation to the others.

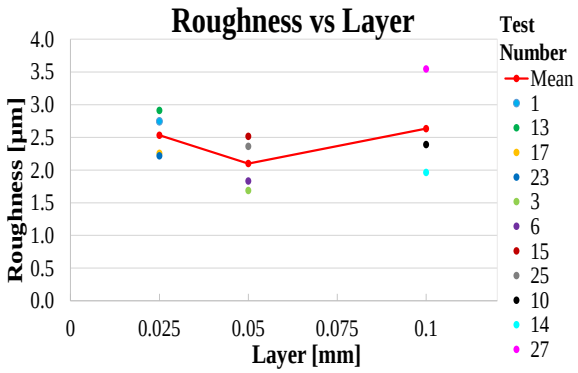

Fig. 6 Results of the roughness measurements. Tests grouped by layer thickness.

Wall thickness

In order to evaluate the capacity of the process to accurately reproduce the given geometry, the wall thicknesses of the samples were measured with a digital caliper. The results are shown in Fig. 7.

It is possible to note how the process tends to increase the thickness of the wall by an amount ranging from 0.05-0.35 mm. As confirmed by the ANOVA analysis, that presents a p-value lower than 0.01, the wall thickness is affected by the layer thickness. Higher layer thicknesses result in greater increments. However, despite the worse construction accuracy, it can be seen that the 0.1 mm layer has much less data scattering than the thinner layers. The ANOVA analysis highlighted that also the exposure time

influences the wall thickness. For example, exposure times of 20 s and 30 s result in thicker walls (1.24 mm; 1.27 mm) compared to the ones built with an exposure time of 10 s (1.08 mm). However, this could probably be deduced by the previously mentioned almost linear relationship between the layer thickness and exposure time in the selected tests.

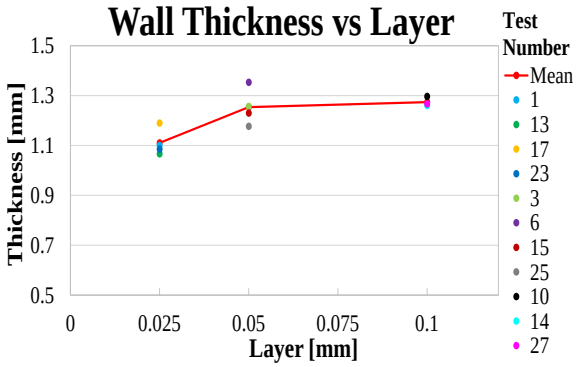

Fig. 7 Results of the wall thickness measurements. Tests grouped by layer thickness.

External diameter

Another dimension measured to evaluate the quality of the print was the outer diameter of the samples. Two different outer diameters were measured: one not containing the printing support residual region and one containing it. The measures were carried out using a digital caliper. The results for the diameters not containing the support region are shown in Fig. 8. The graphs show that the process is accurate. The samples differ less than 1 % of difference from the CAD measure. The reported results show that the process tends to reduce the dimensions of the external diameter in relation to all the parameters combinations. Once again, the 0.1 mm layer thickness presents the smallest scattering of the data, confirming itself as the most repeatable. In this case, the ANOVA analysis showed an influence of the exposure time (p-value 0.002) and not of the layer thickness (p-value 0.179).

The largest diameters in the printing supports residuals regions were evaluated and compared to those previously measured. Fig. 9 shows how the support region can increase the diameter by a factor of 1 to 4 %. Moreover, the percentage of LB in the solution influences this increment (p-value 0.006). The best results are obtained with a LB percentage of 1 % that leads to an average diameter increase of around 1.5%.

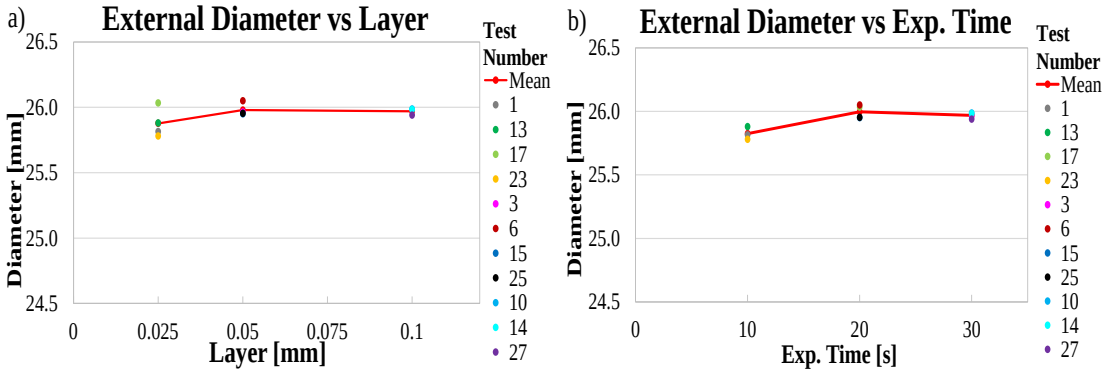

Fig. 8 Results of the external diameter measurements. Tests grouped by layer thickness (a) and tests grouped by exp. time (b).

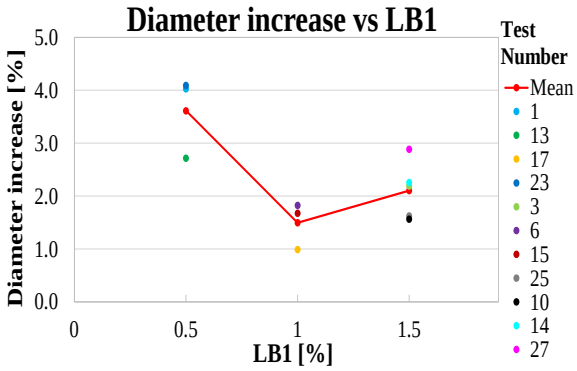

Fig. 9 Results of the diameter increase in the support region. Tests grouped by LB1 percentage.

Layer accuracy

A final test was carried out to evaluate the accuracy of the printer along the printing direction. The layer thickness of the samples was measured with Hirox RH-2000 optical microscope (Fig. 10). Fig. 11 shows the difference (Δl) between the experimental and the theoretical layer thicknesses. The process results very accurate considering the extremely reduced (< 1.5 µm) variance of data from the target values. However, it is possible to note that as the layer thickness increases (0.05 mm) the Δl becomes more equally distributed around the zero line. In fact, all the samples with a layer thickness of 0.025 mm present positive values of Δl while the other tests resulted in variable values around zero (including negative values). Moreover, as the layer thickness increases (0.05 mm) the scattering of the values increases. Nevertheless, these deviations are really small (*i.e.* σ = 0.58 for a layer of 0.1 mm) and have a negligible effect on the accuracy of the process.

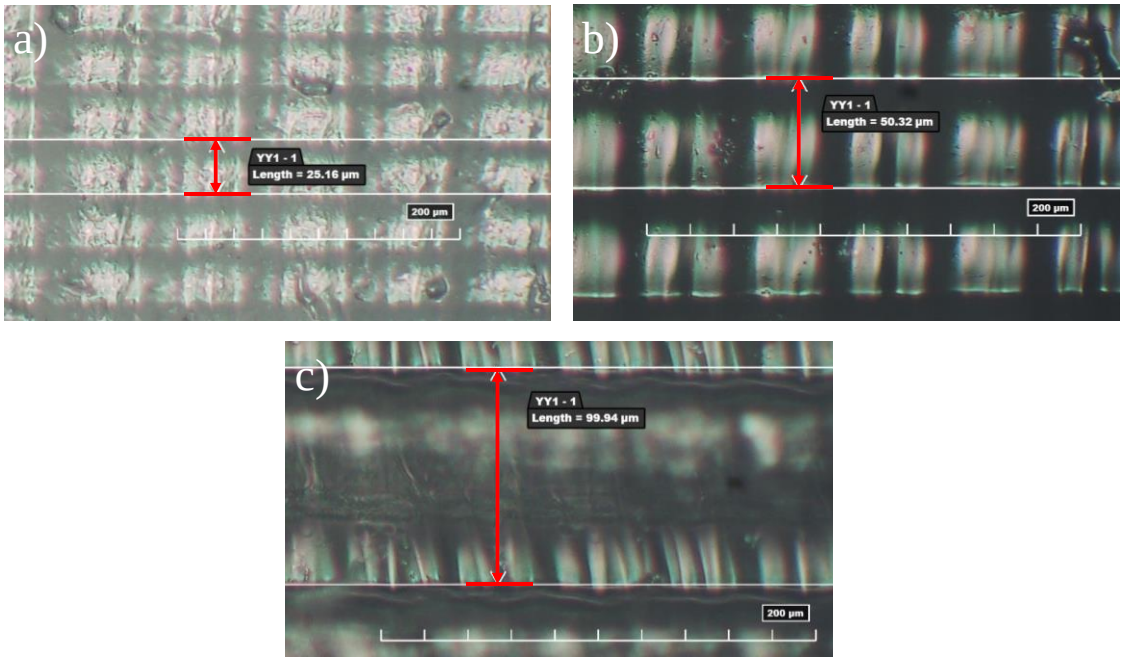

Fig. 10 Results of the layer thickness through Hirox microscope. a) 0.025 mm layer, b) 0.05 mm layer, **c)** 0.1 mm layer.

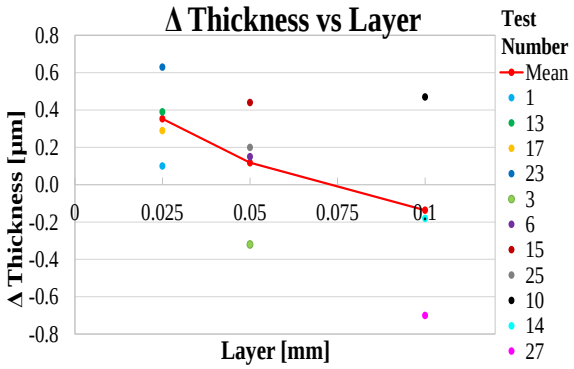

Fig. 11 Difference between the experimental and theoretical layer thicknesses. Tests grouped by layer thickness.

3.2.5 Selection based on the quantitative investigations

Quantitative investigations demonstrated a stable process within the tested range of process parameters, with only minor influences on some outputs. Quantitative investigations produced comparable results across all tests. Consequently, the choice of the optimal samples for our purposes was made mainly on the basis of the results of the qualitative investigations. In particular, the transparency and the color tests were the most significant for the choice, considering that the final application is an eye model for the study of vitreous cells under different stimulations Finally, the sample test number 1 was selected as the clearest of all the specimens (Fig. 5). Specifically, four replicas of the samples printed with a layer of 0.025 mm, an exposure time of 10 s and a LB1 percentage of 1.5% were used for the biological analysis.

3.2.3.3 Biological analysis

Biocompatibility test

Since resin samples were printed with the aim of culturing the vitreous body cells in, their non-toxicity is crucial and had to be verified. To this end, we took advantage of a fast-growing stromal cell line, named MS5, as cells isolated from the vitreous body are few and really precious. In order to reduce the number of seeded cells, the volumes of reagents, and the variability related to cell-to-resin adhesion, four printed resin samples had been allowed to release any component that could affect cell viability into MS5 culture medium, *i.e.* complete DMEM, for 7 days. Then, appropriate volumes of either control medium or resin-conditioned medium were put on previously seeded MS5 cells. After 24h, cells in resin-containing DMEM appeared almost totally dead at a first inspection under the microscope, while cells in control medium formed a healthy monolayer (Fig. 12a).

The detrimental effects of the resin were confirmed by performing an ATP assay. This is an enzymatic assay, in which the substrate luciferin is converted into oxyluciferin by the enzyme luciferase. To work, the enzyme takes advantage of the ATP produced by cell metabolism. As a result, luminescence is generated, that is proportional to the number of metabolically active cells present in culture. Thus, ATP assay can be exploited as an indirect measure of cell viability.

While ATP content in cells kept in control medium was easily measurable, the luminescence produced by cells in resin-conditioned medium was negligible, thus suggesting the presence of very few living cells (Fig. 12b).

In such conditions, it appeared useless to proceed with further assays and with longer treatment timepoints.

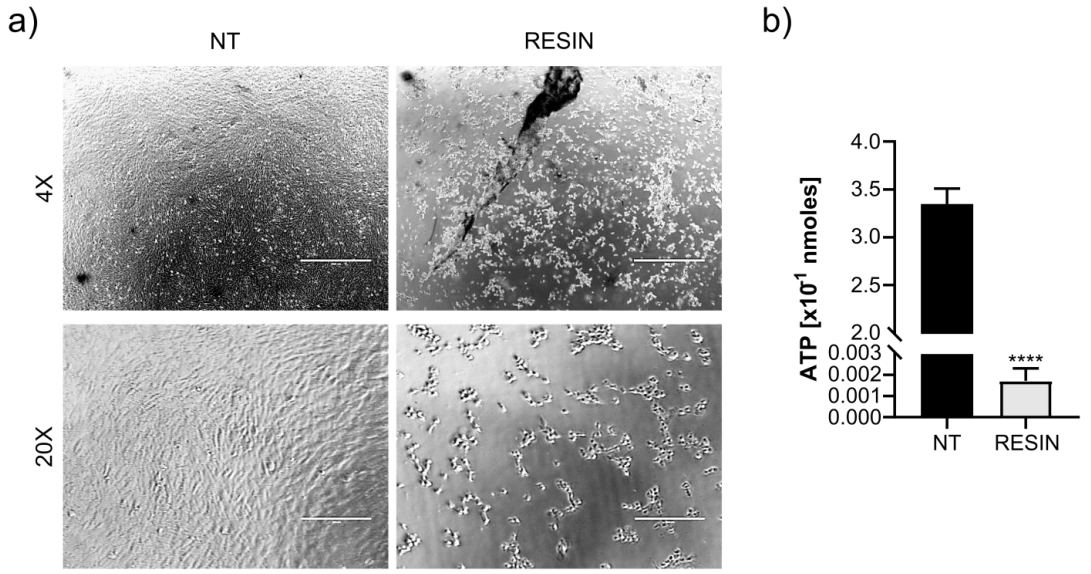

Fig. 12 a) Representative pictures of MS5 cells after 24h of culture either in control DMEM (NT) or in resin conditioned DMEM medium (RESIN). Scale bar = 1000 µm in 4X magnification, 200 µm in 20X magnification. b) ATP concentration in MS5 cells after 24h of culture either in control DMEM (NT) or in resin conditioned DMEM medium (RESIN). The graph shows the mean ± S.D. (n = 4, **** $p < 0.0001$).

The washing and curing protocol resulted unsuitable for the complete removal of unpolymerized resin on the samples. Unpolymerized resin can have a toxic effect on cells, thus compromising the biocompatibility. The protocol was then modified to achieve acceptable biocompatibility results, as specified in *Materials and Methods* section.

Three new resin samples, treated with prolonged washing/curing steps after printing, were put in complete DMEM medium, as described previously, and cell viability assays were repeated.

After 24h, MS5 cells maintained in resin-conditioned medium formed a monolayer comparable to the one formed by non-treated cells (Fig. 13a). ATP cell viability assay gave comparable results in non-treated and resin-treated cells (Fig. 13d). Similarly, flow cytometry annexin V/PI apoptosis assay demonstrated that the differences in percentage of annexin V/PI double negative cells between treated and non-treated cells were not significant (Fig. 14a and b). In this test, early apoptotic cells are stained positive for annexin V and negative for PI, cells in mid phase apoptosis are double positive, while cells negative for annexin V and positive for PI are in late apoptosis or already dead. Living, healthy cells are double negative.

Thus, we proceeded with later timepoints. Since resins are guaranteed as biocompatible by the manufacturers if toxic effects are not highlighted over a 24h observation time, we cannot exclude a later onset of cytotoxicity. To this reason, it is recommendable to carry out biocompatibility tests over longer culture periods.

After 72h, cells still appeared living and healthy when observed under the microscope, even more crowded than two days before, as a sign that cells had replicated (Fig. 13b).

Even though ATP content in treated cells resulted slightly lower than in non-treated ones, the result of this assay suggests that cells were viable and metabolically active in both the groups; moreover, ATP content in both the groups increased in comparison to the results obtained after 24h, thus demonstrating that cells were healthy enough to increase in number (Fig. 13d). Annexin V/PI apoptosis assay confirmed that there was no statistically significant difference between the percentage of living cells in resin-treated and non-treated cells (Fig. 14a and c).

We maintained MS5 cells in culture in the two different kinds of media until day 6. Even though cells appeared alive, but overcrowded, when their morphology was observed under the microscope (Fig. 13c), the results of the ATP assay were highly variable even among technical replicate wells. Moreover, the

ATP content measurement dropped down if compared to the results at 24h and 72h (Fig. 13d). The reason could be that ATP assay is just an indirect measure of cell viability, as stated above. It works well when cells are metabolically active and have nutrients and room enough to grow; on the contrary, results are not reliable when cells are metabolically quiescent, as a consequence of overconfluence or nutrient starvation due to medium exhaustion. Actually, cells were confirmed to be alive by annexin V/PI staining, that is a more specific assay to assess cell viability and death (Fig. 14a and d).

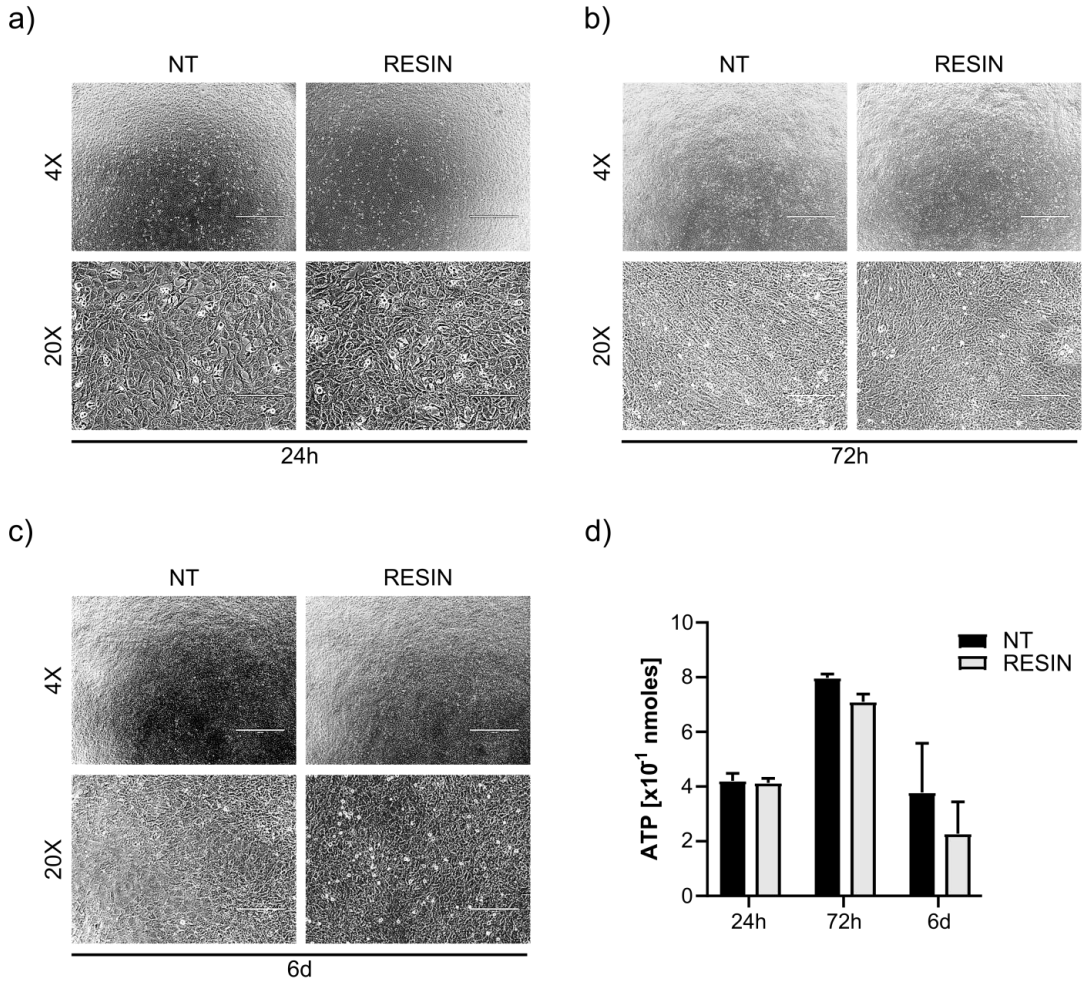

Fig. 13 Representative pictures of MS5 cells after 24h (a), 72h (b), or 6days (c) of culture either in control DMEM (NT) or in resin conditioned DMEM medium (RESIN). Scale bar = 1000 µm in 4X magnification, 200 µm in 20X magnification. d) ATP concentration in MS5 cells after 24h, 72h, or 6 days of culture either in control DMEM (NT) or in resin conditioned DMEM medium (RESIN). The graph shows the mean ± S.D. (*n* =3).

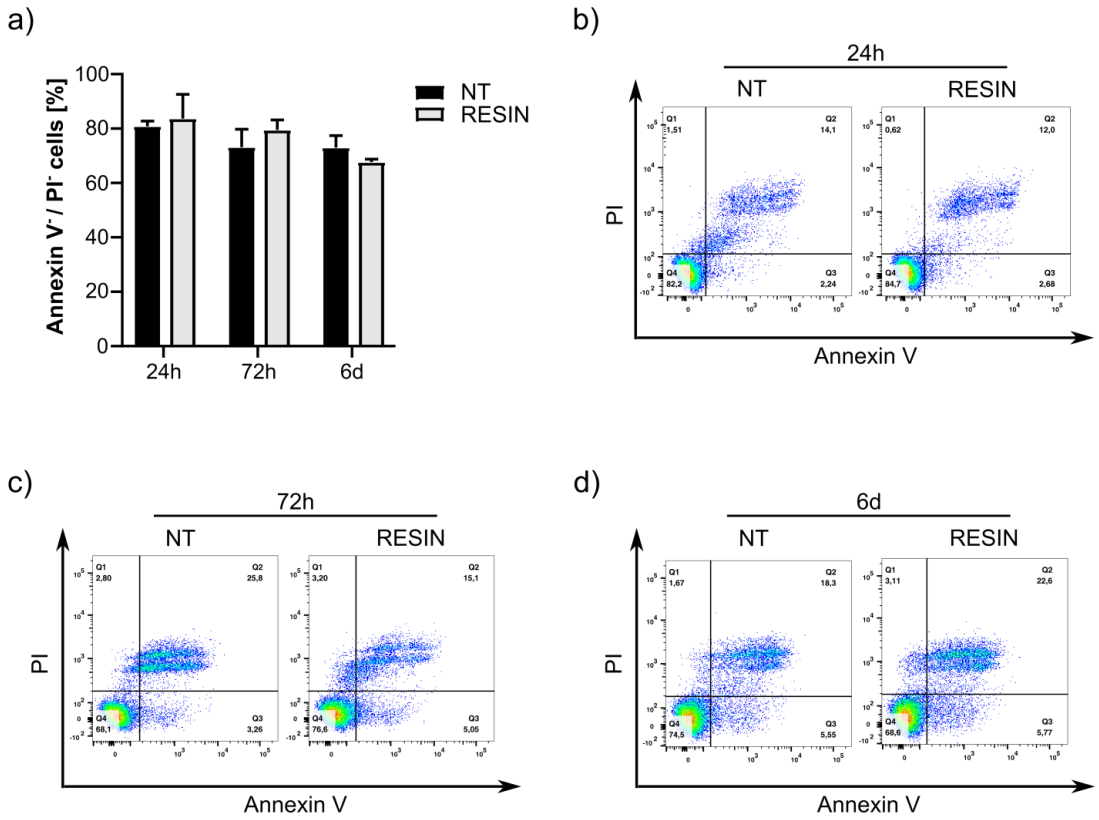

Fig. 14 a) Percentage of living cells (expressed as annexin V^-/PI^-) after 24h, 72h, or 6 days of culture either in control DMEM (NT) or in resin conditioned DMEM medium (RESIN). The graph shows the mean ± S.D. (*n* =3). Representative dot plots are shown in panels b), c), and d).

Microscope visualization

To see adequately cells through the bottom of the resin samples, is one of the most important requirements for their final biological applications. To verify whether the printed samples met such requirement, we performed a visual test putting some MS5 cells into the resin samples as printed, and immediately observing them under an inverted microscope when still in suspension, just waiting that cells settled on the bottom. Unfortunately, it was impossible to clearly distinguish cells beyond the printing layers; we could just perceive some moving shadows (Fig. 15, left panel). Thus, resin samples were post-processed, to minimize the printing layer interference and this allowed us to see the cells clearly on the bottom (Fig. 15, right panel). The post processing consisted in progressive grinding starting from 240 to 2000 grit.

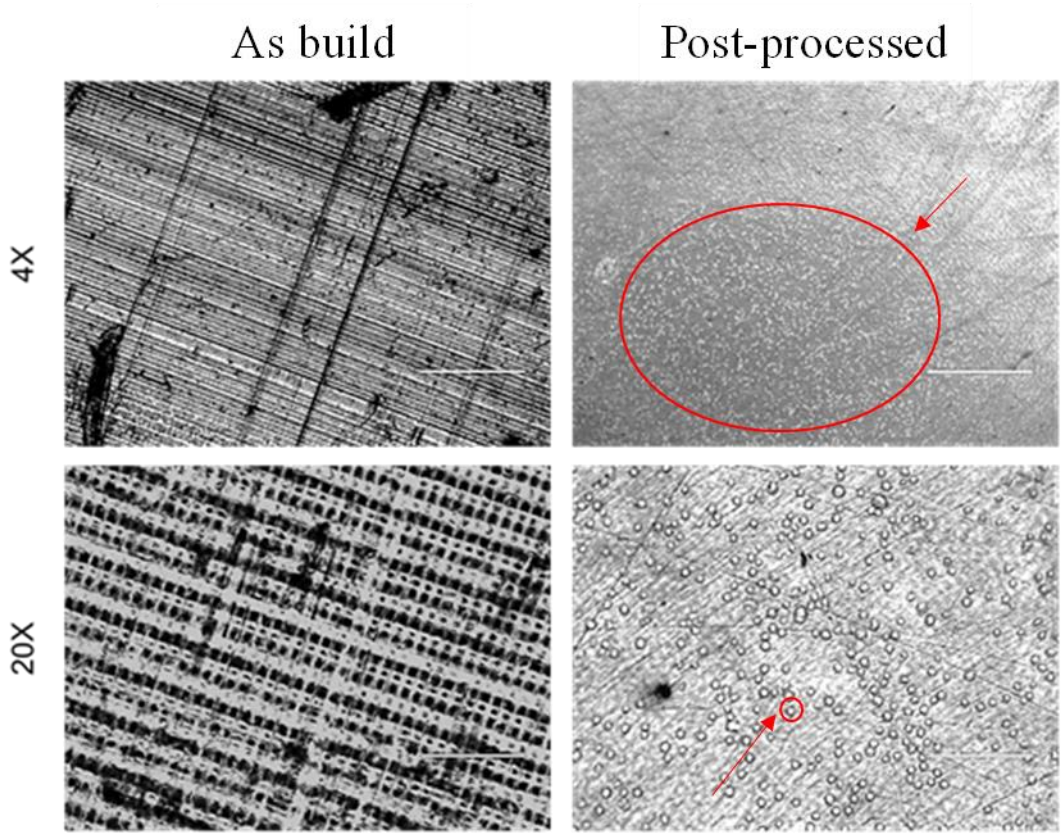

Fig. 15 Representative pictures of floating MS5 cells observed under an inverted microscope through the bottom of the printed resin samples. On the left, samples were used as printed; on the right, samples were post processed progressive grinding. Arrows and circles are showing the observed cells on the samples under microscope evaluation. Scale bar = 1000 μm in 4X magnification, 200 μm in 20X magnification.

3.2.4. Conclusions

3D printing has opened up new frontiers in the medicine field, especially with regard to the development of bio-models through biomanufacturing for the study of certain pathologies. Stereolithography is one of the main technologies for the realization of the necessary supports for bio-models. This work optimizes the printing parameters for the production of a substrate acting as a bio-model of an eye, with the study of vitreal floaters as ultimate future goal. The required characteristics of the model are: three-dimensional geometry as similar as possible to the eye, biocompatibility and transparency. Moreover, the model should be easy to handle and appropriate for microscopic evaluation. Three different printing parameters were investigated, namely: layer thickness, exposure time and fine tuner percentage mixed within the resin. The printed samples were subjected to 3 different types of analysis: qualitative, quantitative and biological. The qualitative tests allowed the evaluation of the printing quality in terms of transparency, color and geometry. The quantitative tests were referred to the accuracy of the printing in relation to the designed model. Finally, the biological tests were carried out to verify the cytotoxicity of the samples. The quantitative tests produced comparable results for all the specimens on which they were performed, so it was decided to carry out the biological tests on the samples with the optimal results in the qualitative tests, especially considering transparency requirements. Both the qualitative and quantitative analysis clarified the direct dependence between the layer thickness and exposure time, while the fine tuner percentage had a limited effect on the geometrical precision of the process. Specifically, a layer thickness of 0.025 mm requires an exposure time of 10 s, a layer thickness of 0.5 mm requires an exposure time of 20 s and a layer thickness of 0.1 mm requires an exposure time of 30 s to assure the best combinations of transparency and process accuracy. The samples selected for the biological evaluation were printed with

the following printing parameters: layer thickness 0.025, exposure time 10 s and fine tuner percentage of 1.5%. Despite the declared biocompatibility of the purchased resin, the samples resulted toxic, probably due to the presence of residual unpolymerized resin on the surface after only one cycle of washing and curing. The printing parameters do not have any influence on the biocompatibility of the resin. Therefore, the washing and curing process was modified to include 12 minutes of washing and 15 minutes of curing. The new protocol allowed achieving a long-term biocompatibility; in fact, the cells remain alive even after a time point of 6 days. On the other hand, the as built samples were not sufficiently transparent to allow a proper observation of the cells under the optical microscope, in fact the printing layers were widely visible and prevented a good view of the cell bodies. Therefore, a progressive grinding process has been used on the surfaces of the samples to achieve a better surface finishing and allowed a correct visualization of the cells.

Finally, the samples resulted adequate to accommodate a bioink containing living cells. The next steps will be carried out for bioprinting of the bioink inside the support. The bioink should mimic the vitreous body properties and should contain hyalocytes to simulate the extra-cellular matrix formation typical of the eye. The cells will then be stressed in two different ways: mechanically and by light pulses. The influence of these stresses on the cells, in terms of collagen fibrils release and rearrangement, will be investigated. This will allow studying the causes and the processes that lead to floaters formation inside the vitreous body of the eye.

Chapter 4

Bioprinting for 3D cell culture

This chapter focuses on the printing of a biocompatible hydrogel, The results regarding the hydrogel formulation and characterization and 3D structure realization are reported. The hydrogel is obtained from a decellularized extracellular matrix (dECM) derived from porcine hyaline cartilage.

In this work, the candidate was responsible of the design and production of the samples. He contributed also in hydrogel formation and preparation, in conducting the live/dead, swelling ratio and rheology tests, as well as in analyzing the results.

.

4.1 Preliminary study of a decellularized extracellular matrix hydrogel as vitreous substitute for eye model application

4.1.1 Introduction

The vitreous humor comprises about 80% of the eye volume and fills the space between the lens and the retina [1]. It consists in a transparent and fragile hydrogel composed of around 99% water [2]. Other major constituents are collagen fibrils, hyaluronic acid, hyalocytes, inorganic salts and lipids [3]. The vitreous humor absorbs and dampens external forces, reduces mechanical deformation of the eye, acts as a metabolic buffer, and allows light to reach the retina while maintaining transparency [4]. All these features make it an active player in the physiology of the eye and not only a space filler [5]. However, the vitreous body undergoes natural aging due to biochemical changes occurring inside it. These changes affect the collagen and the viscosity of the vitreous and result in a gradual liquefaction of the gels [6]. Vitreous liquefaction occurs because hyaluronic acid separates from the collagen fibers. The fibers then aggregate together and the aqueous medium entrapped in them is released [7]. Liquefaction of the vitreous can lead to a posteriori vitreous detachment (PVD), where the vitreous detach from the retina [8]. PVD is one of the main causes of vitreous opacities, or floaters. Floaters are a very common eye complaint and usually are described as bubbles, dark spots or bugs in the visual field [9]. Floaters are generally benign but, in some cases, can interfere with vision causing physiological stress [10] and a negative impact on quality of life.

Hyalocytes are mononuclear cells situated in the posterior vitreous cortex [6] that derives from a monocyte/macrophage lineage [11]. Hyalocytes perform various functions within the eye, including the synthesis of the extracellular matrix (ECM) [12]. In fact, hyalocytes are reported to be responsible for the synthesis of the vitreous collagen and hyaluronic acid [13,11]. Furthermore, they can stimulate cell migration, proliferation and gel contraction [14]. For these reasons, it can be hypothesized that hyalocytes play a role in the formation of floaters.

The great expansion of additive manufacturing in recent years has enabled the development of new methods and tools to study and research various pathologies [15]. Bioprinting is a branch of additive manufacturing that involves printing biomaterials, cells and biomolecules [16]. Its aim is to develop structures that can mimic the human body [17]. Extrusion based printing is one of the most common bioprinting methodologies. It consists in the extrusion of a cell-laden hydrogel through a nozzle by means of compressed air or a plunger.

Many hydrogels, both natural and synthetic, have been tested as vitreous substitutes [5,7,18]. More recently a new type of hydrogels has been developed. Decellularize extracellular matrix (dECM) hydrogels, as the name states, are hydrogels based on decellularized biological tissue. Although, they may have poor printability due to the low viscosity caused by the removal of the proteins during the decellularization process, they can provide the ideal conditions of native matrix [19].

The purpose of this work was to study the suitability of a dECM hydrogel as a vitreous substitute for an eye model to study the formation and development of floaters. The dECM was derived from porcine cartilage since the natural composition of the cartilage matrix is similar to the one of the vitreous [20]. A 3D structure was developed after a printing parameter study. Biocompatibility, transparency, rheological and swelling tests were performed to investigate the suitability of the hydrogel for the desired application.

4.1.2 Materials and Methods

4.1.2.1 dECM formation and hydrogel preparation

The cartilage was dissected from porcine bones acquired at a local market. The cartilage was then washed in 1X PBS for an hour in DW and chopped in small pieces. After that, six cycles of freeze (-80 °C) and thaw (37 °C) were carried out. The cartilage was then treated with 0.25 % (w/v) trypsin/PBS solution for 24 hours in a 37 °C incubator, washed with hypertonic buffer (1.5 M NaCl + 50 mM Tris-HCL, pH 7.6) for 12 hours and treat with nuclease solution (50 U ml−1 DNAse and 1 U ml−1 RNAse A in 10 mM Tris–HCL, pH 7.5) with agitation at 37 °C for 4 hours. To remove the enzymes a 10mM hypotonic Tris-HCL solution was used for 24 hours, followed by an incubation in 1% Triton X-100 (v/v, in PBS) for 24 hours. Finally, the dECM was washed in 1X PBS for 6 cycles of 8 hours each and then freeze dried.

Different concentrations of dECM were investigated. Specifically, 0.5%, 1% and 1.5 %. The designed amounts of dECM, together with pepsin (10% of the dECM weight) were dissolved in a 0.5M acetic acid bath (80% of the final volume). The solution was left to stir at 550 rpm at room temperature for 2 days until complete dissolution, then 10M NaOH was gradually added until the pH reached a value of 7. Finally, 10X PBS was added to reach final volume.

Finally, an additional dECM-collagen hydrogel was tested. A 1.5% dECM hydrogel was mixed together with a 1.5% collagen hydrogel in a 7:3 ration to obtain a final hybrid hydrogel.

4.1.2.2 Supporting bath preparation

The supporting bath is a solution of 1% gelatin, 2% alginate, 1.25% PVA and 0.2% Calcium Chloride ($CaCl_2$) in DW. Briefly, gelatin, sodium alginate and PVA are added without mixing to half of the required DW, left in oven at 60 °C for 4 hours and sterilized in autoclave. While the solution is still warm, the $CaCl_2$, diluted in the remaining DW, is added and mixed thoroughly. The solution is then left at 60 °C until completely settled.

4.1.2.3 Bioprinting

The printing was carried out with a 3DX Printer (T&R Biofab). An investigation on the printing pressure (P), speed (s) and layer thickness (lt) was carried out and the final 3D structures were built with the optimal set (P = 20 kPa; s = 300 mm/min; lt = 0.75mm). The hydrogel was kept at 15 °C during the printing while the building plate was set to 30 °C. A 25G needle (0.25 mm; Musashi Engineering, Inc.) was used for printing. The printing was carried out inside petri dishes containing the supporting bath.

The final 3D structures have a dome shape with a diameter of 10 mm and a height of 5 mm. Two different types of structures have been built, porous and bulky. The building path is a 2 mm grid for porous structures and 0.68 mm grid for bulky structures. After printing the samples were placed in incubator to crosslink. Once crosslinked the supporting bath was removed with a scoop and washes in PBS.

4.1.2.4 Macrophages differentiation and culture

Macrophages cells were differentiated from THP-1 monocytes following a dedicated protocol. Briefly, THP-1 cells with a concentration of $1x10^5$ cells/ml were placed in RPMI media + 10% FBS for 2-3 days. After that RPMI media+10%FBS+ 100ng/mL of Phorbol 12 Myristate 13 Acetate (PMA; P8139, Sigma aldrich, USA) treatment was performed for 48 hours. After PMA treatment the adherent cells were differentiated to macrophages, the non-adherent cells were removed by washing with 1xPBS and the medium was replaced with fresh RPMI media + 10% FBS for 72 hours.

The macrophages were then cultured in high glucose media + 10% FBS. The media was changed once every two days, after washing two times with 1XPBS.

4.1.2.5 Biocompatibility tests

Biocompatibility was evaluated through live/dead assay and CCK 8 assay. $3x10^6$ cells/ml were mixed with the hydrogel. The hydrogel was then let crosslinked in incubator or printed in a 3D structure and then crosslinked. After crosslinking culture medium was added.

Live/dead. At day 1, 4 and 7 the medium was removed from the well and the hydrogel was washed two times with 1xPBS. Then 1ml of l/d solution was added in each well and the samples were left in incubator for 30 min to react. The samples were then analyzed with an Axio-observer AX10 (Zeiss, Oberkochen, Germany) microscope.

CCK8. At day 1, 4 and 7 the medium was removed from the well and the hydrogel was washed two times with 1xPBS. Then 500µl of CCK8 solution was added in each well and the samples were left in incubator for 3 hours to react. Then 2x100µl of media was taken for each sample and pipetted in a 96 well. The analysis was then performed with a microplate reader (Elisa reader) with a wavelength of 450 nm.

4.1.2.6 Rheology tests

Rheology tests were performed using a Discovery HR-2 hybrid rheometer (TA instruments). Flow sweep, gelation kinetic and dynamic modulus were investigated.

The flow sweep was performed with a temperature of 4 °C and a shear rate from 0.1 to 1000 1/s.

The gelation kinetic was carried out with a starting and finishing temperature of 4 °c and 37 °C, respectively. The ramp rate was set to 5 °C/min, the strain to 2% and the angular frequency to 10 rad/s.

The dynamic modulus was measured with a starting temperature of 37 °C a strain % of 2% and angular frequency from 0.1 to 100 rad/s.

4.1.2.7 Transparency test

Transparency tests were performed both qualitatively and quantitatively.

The qualitatively test were performed spreading 150 µl of hydrogel in a petri dish, let it crosslink and placing it over a printed text.

The quantitative test consisted in a transmittance test. 150 µl of hydrogels were placed inside a 96 well, crosslinked and analyzed with a well plate reader. The wavelengths investigated ranged from 300 nm to 800 nm.

4.1.2.8 Swelling ratio

The swelling ration has been measured through the formula:

$$Swelling\ ratio = \frac{Ws-Wd}{Wd}\ x\ 100 \quad (1)$$

Where Wd is the weight of the dried sample and Ws is the weight of the swelled sample. To measure the wights 500 µl of hydrogel were placed in previously weighted conical tubes. After crosslinking in incubator, the samples were freeze dried. The tubes containing the dried hydrogel were weighted again and the Wd was obtained as a difference between the two weights. 1 ml of PBS was added in each tube for the hydrogel to absorb and left at 37 °C for 24 hours. The Ws was measured in 2 different ways. Firstly, after the removal of the excess PBS the tubes were weighted a third time; again, the Ws was obtained from the difference in wight between the filled and the empty tubes. The swelled samples were then removed from the tubes by adding new PBS and weighted after removing the excess PBS with a paper towel.

4.1.3 Results and discussion

4.1.3.1 Hydrogel formulation and printing of 3D structure

The choice of the hydrogel formulation was made based on its ability to make a 3D structure capable of self-sustaining. A low dECM percentage hydrogel should guarantee a better biocompatibility, so the first tests were carried out with low dECM percentages. For every formulation, tuning tests were previously performed to find the set of parameters that allows a uniform and defined line. The 0.5% dECM hydrogel resulted to be too fragile to produce a stable structure. In fact, the structures shattered in many pieces during the removal of the supporting bath (Fig. 1). The dECM percentage was too low and the crosslinking resulted too weak. The

Fig. 1 0.5% dECM structure shattered after the washing of the supporting bath.

The dECM percentage in the hydrogel has been increased to 1%, however, once again the structure resulted too fragile and broke down during the removal of the supporting bath. To further increase the mechanical properties of the hydrogel the dECM percentage has been increased and collagen has been added. Two different hydrogels were formulated, a 1.5% dECM hydrogel and a 1.5% collagen hydrogel. The two hydrogels were then mixed together in a 7:3 ratio. The hybrid hydrogel was able to endure the washing protocol and allowed a 3D structure.

The lines obtained from the best set of parameters from the printing tuning are visible in Fig. 2 The pressure was set to 20 kPa and the speed to 300 mm/min. The lines resulted defined and stable with an average thickness of 0.78 mm.

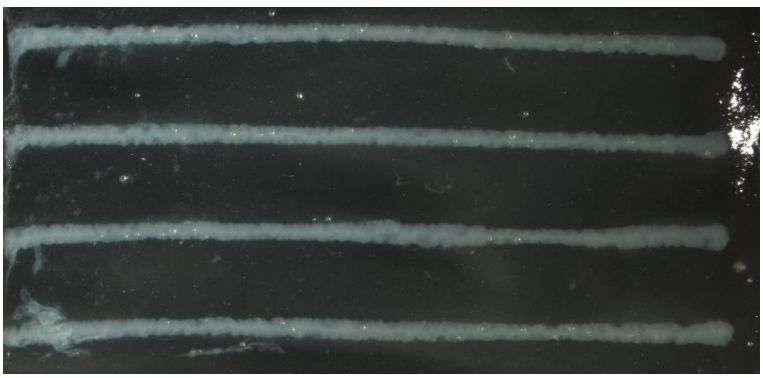

Fig. 2 Hybrid hydrogel best parameter tuning test line. Obtained wit a pressure of 20 kPa and a speed of 300 mm/min

These parameters allowed the fabrication of two different dome shaped 3D structures, a porous one and a bulky one. Both structures have a designed diameter of 10 mm, a height of 5 mm, a layer thickness of 0.75 mm and a grid like printing path. The distances between the lines are 2 mm for the porous one and 0.68 mm for the bulky one. Even with the design of a bulky structure, the structure still shows small pores. This may be caused by the material, which biologically behaves slightly differently each time, or by the design, which involves many short patterns and does not allow the pressure to work in a steady state.

Fig. 3 shows the porous and bulk structures. The structures maintained the designed geometry even after the washing of the supporting bath. They present a well defined shape with regular and uniform lines.

a) 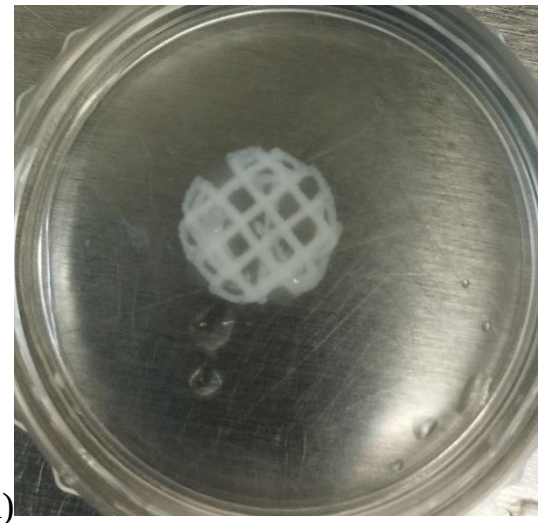 b) 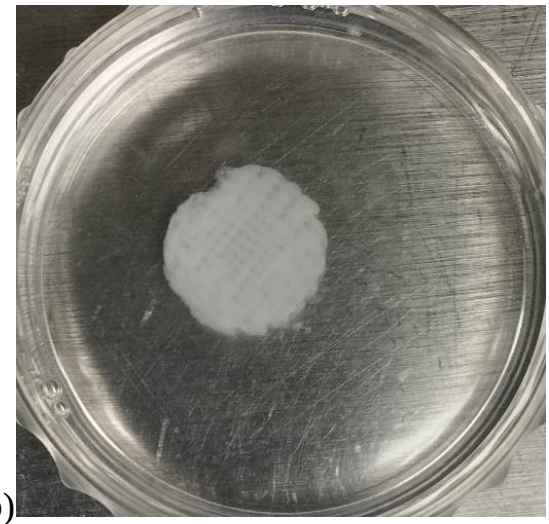

Fig. 3 printed 3D strucutures. Porous (a) and bulky (b).

4.1.3.2 Biocompatibility tests

Live/dead assay and CCK8 assay were performed both on the not printed hydrid hydrogel and on cell laden 3D printed structures. A 1.5% collagen hydrogel has been used as control sample. The results of the biocompatibility tests on the not printed hydrogel are visible in Fig. 4. The live/dead results show that the cells are alive after 7 days. Furthermore, they grow in number and form clusters. Compared to collagen 1.5% the hybrid hydrogel present less dead cells. The CCK8 results show how the viability of the cells increases over time, reaching almost 100% at day 7. With respect to the 1.5% collagen hydrogel the hybrid hydrogel presetns higher values and a slightly bigger increase over time. Overall the hybrid hydrogel shows good biocompatibility results.

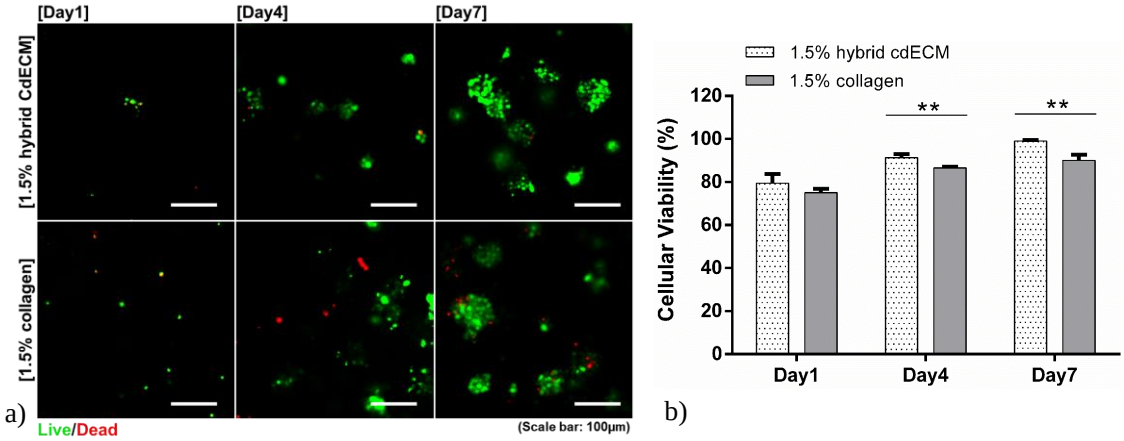

Fig. 4 Biocompatibility tests results on not printed hybrid hydrogel. Live/dead assay (a), CCK 8 assay (b).

The results of the biocompatibility tests on the cell laden 3D structures are visible in Fig. 5.

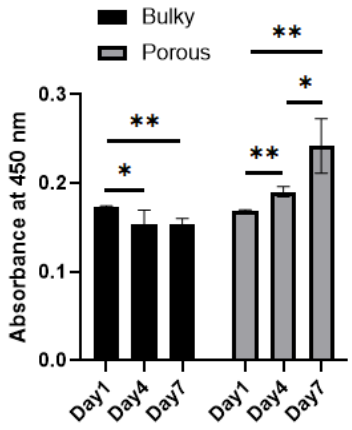

Fig. 5 Biocompatibility tests results on cell laden 3D structures, CCK 8 assay.

The CCK8 results show a different behavior between the bulky and the porous samples. The bulky samples do not proliferate and the absorbance decrease over the time span. On the contrary, presents an increase of the absorbance over time, indicating a small but constant proliferation of the cells. This different behavior may be due to the structures of the samples (Fig. 3). The dense structure of the bulky specimens may have prevented the complete runoff of the support bath during washing, causing it to remain anchored internally to the grid. This could have prevented the nutrients in the culture medium from easily penetrating the hydrogel and reaching the cells. On the contrary, the loose grid of the porous samples facilitated the outflow of the supporting bath during washing, allowing a better interaction between culture medium and cells.

4.1.3.3 Rheological analysis

The results of the rheological analysis are visible in Fig. 6. The hybrid hydrogel, at small flow rate, has a lower viscosity compared to the collagen hydrogel. As the flow rate increases, the reduction in hybrid hydrogel viscosity is less pronounced and follows a less inclined line, reaching a final value higher than the collagen hydrogel. However, the decrease in the viscosity underlines the shear thinning behavior important for extruded hydrogels.

Regarding the gelation kinetics, the graph shows the thermoresponsive behavior of the hydrogels with a high increase in complex moduli (G*) after a certain temperature. The hybrid hydrogel gels at a slightly

higher temperature than the collagen hydrogel. Furthermore, after peaking and the subsequent small drop, the complex moduli of the hybrid hydrogel follows a small but steady increase in value, indicating that the gelation process slowly continues over time for some time.

Both hydrogels present a storage modulus higher than the loss modulus for every frequency tested, this underlines the presence of a strong hydrogel network. The loss modulus curves of both hydrogels have a steeper increase towards higher frequencies compared to the respective storage modulus curves. Finally, the hybrid hydrogel present overall higher storage and loss modulus than the collagen hydrogel that, together with a bigger difference in value between the two curves, makes it him more suitable for a 3D structure.

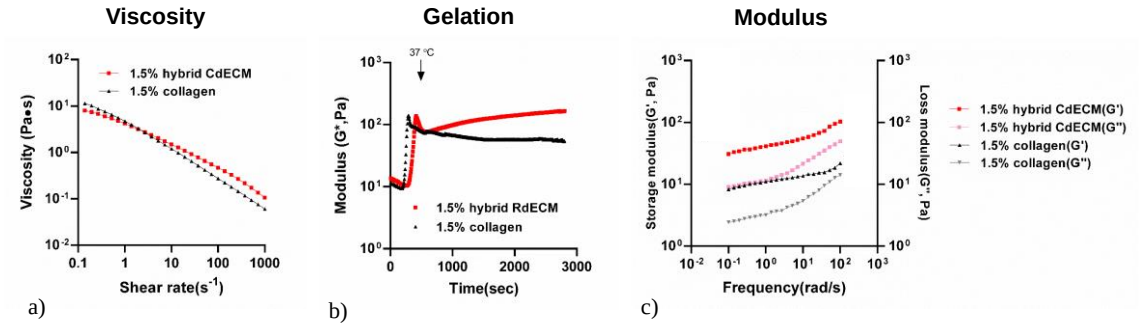

Fig. 6 Rheological analysis: flow rate- viscosity (a), gelation kinetic (b), dynamic modulus (c).

4.1.3.4 Transparency tests

The results of the transparency tests are visible in Fig. 7. Both the 1.5% collagen hydrogel and the hybrid dECM hydrogel were found to be nontransparent. In fact, in the qualitative analysis, the text is barely visible for the collagen hydrogel and completely covered by the dECM hydrogel. This result is also confirmed by the quantitative analysis where the transmittance is lower than 20% for every wavelength investigated. The crosslinking process produces a whitening of the hydrogel that compromises its transparency. This could complicate a future cell stress process using light pulses, however, being the bars of the grid very thin, it is possible for a portion of light to still penetrate inside the structure. Finally, a decrease in thickness could increase the transparency of the samples. However, the stability and robustness of the whole structure could be compromised.

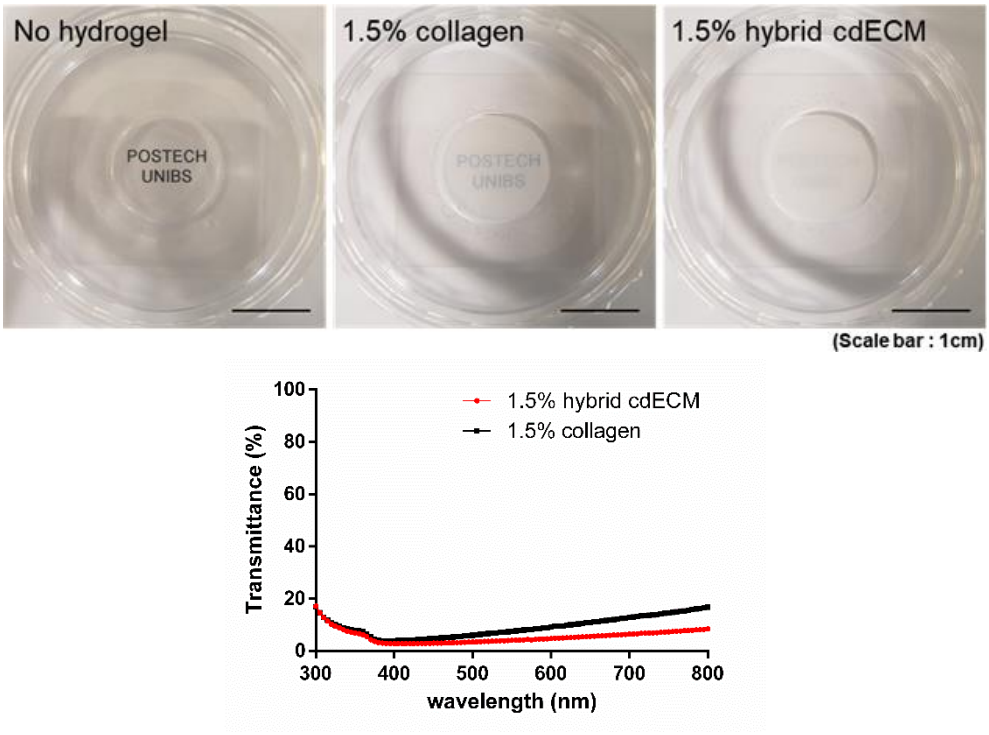

Fig.7 Transparency tests results. Qualitative analysis (top), transmittance test (bottom).

4.1.3.5 Swelling ratio

The swelling ration results are visible in Table 1. Even if the two methods of measuring the swelled weight give different values, the overall results are the same. The hybrid dECM hydrogel presents more water compatibility, helpful for cell activity. Furthermore, a aqueous environment results more similar to the vitreous body, as it is composed of about 98-99% water.

Table 1: swelling ratio values

Hydrogel	Sweling ratio (tubes)	Sweling ratio (no tubes)
dECM	689.64	569.85
Collagen	523.72	488.56

4.1.4 Conclusion

Vitreous humor is a gel like substance that fills most of the eye. it dampens the external forces and have a significant role in the physiology of the eye. However, the vitreous undergoes natural aging in the form of liquefaction that can results in the appearance of floaters, visual disorder that can impact the quality of life. Hyalocytes are macrophage lineage cells residing in the vitreous that may play a role in the liquefaction of the vitreous due to their role in the synthesis of collagen and hyaluronic acid.

In this work a cartilage dECM-collagen hybrid hydrogel was investigated as a possible vitreous substitute for an eye model for the study of the formation and development of floaters. The goal was to obtain a printable hydrogel with adequate mechanical and biological properties. A tuning of the printing parameters was performed in order to obtain a well defined line. The chosen set allowed the fabrication of a self sustainable 3D structure. The hydrogel resulted biocompatible both in the non printed and printed form, allowing the viability of the cells up to 7 days. The rheological analysis underlined a shear thinning behavior, important for extruded hydrogels, while the swelling test presented an high water compatibility.

The hydrogel resulted not transparent after crosslinking with a transmittance below 20%. These preliminary analyses provided satisfactory results regarding the final application. further optimizations such as increased transparency and improved biocompatibility will be the subject of further studies.

Chapter 5

Fused Filament Fabrication (FFF) for dental devices

In this chapter the preliminary research regarding the development of an autonomous system for assisted dental surgery is presented. However, this work mainly focuses on the thrust force generated during the drilling of the samples. Samples fabricated through FFF with different infill percentage and starting materials have been analyzed. Furthermore, an evaluation on collaborative robot has been carried out. The published papers related to these topics are listed below:

- L. Riva, R. Pagani, A. Fiorentino, A. Borboni, and E. Ceretti, "Preliminary study for the development of an autonomous system for emulating mandibular bone drilling", *Int. J. Mechatronics and Manufacturing Systems* (2022), Vol. 15, Nos. 2/3, pp.185–202.
  In this work, the candidate was responsible of the samples fabrication. He collaborated in performing of the tests and data analysis. Finally, he took part in the writing and editing of the draft.

5.1 Preliminary study for the development of an autonomous system for emulating mandibular bone drilling

5.1.1 Introduction

Robotic systems have recently developed a lot, particularly for applications related to human activities. Robots began to spread in significant numbers in the mid-1970s, especially in the industrial field [1], but only in recent years, a strong expansion of the service robotics market has taken place, particularly in the field of robotics where service robots [2] are adopted for professional and domestic use. The main applications for service robots are logistics, mobility, defense, agriculture, cleaning, entertainment, personal assistance, and medical robotics.

Medical robotics is a broad discipline that encompasses systems for surgery, diagnosis, rehabilitation, prosthetics, and medical care [3]. Rehabilitation robots are mainly used in rehabilitation clinics and are usually exploited for the recovery of motor function in the patient's upper [4] and lower [5] limbs. Diagnostic robots [6,7], on the other hand, typically consist of robotic arms for moving sensors in contact with the patient's skin. Surgical robots, instead, can fill a variety of roles in the operating room [8].

Robot-assisted surgery can incorporate real-time stereoscopic viewing of the surgical field, compensating natural or essential tremor of the hand, furthermore, enabling functional motions with enhanced dexterity and accuracy. As a result, a robotic system provides an easy-to-use platform that increases surgeon maneuverability and improves the working environment for the entire surgical team [9,10].

Recently, cases of using collaborative robots in the field of dental implant surgery were studied to increase the quality of the operation [11]. Dental implantology is the study of surgical techniques that aims to restore physiognomy, functionality, aesthetics, phonetics, comfort, and health to a patient subject to edentulism [12]. Several devices, called dental implants, are surgically inserted into the mandibular or maxillary bone, allowing the connection of fixed or removable dental prostheses [13]. In this type of surgery, the positioning of the implant is one of the factors that most influence the success of the operation. Due to this reason, the first commercial robotic dental system that assists the surgeon during the operation was developed in 2017 [9,14].

The purpose of a dental implant is to fill the space left by one or more missing teeth, either in the upper or lower dental arch. The most difficult phase of the operation is the drilling of the mandibular bone [15]. In fact, a human being is not able to exert a constant drilling force throughout the entire period of the operation and this could lead, in the case of using too high forces, to the onset of osteonecrosis of the bone tissue due to the abnormal rise in bone temperature [16]. For manual drilling, it is therefore essential to reduce the feed force required by choosing the correct drill and adopting a drilling technique that suits the type of operation. The most commonly used materials for dental tool tips are steel, stainless steel, tungsten carbide, and zirconium dioxide whose diameter sizes range from 2 mm to 4.3 mm [13].

Nowadays, the use of computerized solutions for scheduling surgery is becoming increasingly common [17]. Typically, the phases of dental implant surgery are: diagnosis, acquisition of radiographs, virtual implant planning, design and fabrication of drill guides, and finally the surgery.

The present work is part of a larger research which aims at developing a robotic system that will support dental surgery. The system will perform a surgical procedure similar to the one mentioned before but robot aided (Figure 1). Specifically, through a CT scan, it is possible to obtain the geometry of the oral cavity of the patient. Subsequently, the design of the various operations and the handling of the robot, taking into account anatomical obstacles. The robot must maintain the correct orientation and positioning

throughout the operation. To do so, some sensors, fixed or mobile, will be necessary to provide a reference system, both in the case of an awake patient, therefore with the possibility of small movements, and in the case of a sedated patient. Finally, the robot will be programmed and the surgery will take place. For its development, it is necessary to build a simulacrum that can be used to train the system. This work focuses on the bone drilling issues during the surgical procedure with the main objective of developing specimens capable of emulating the bone behavior of the mandible and maxilla during dental implant operations. Therefore, specimens were designed, fabricated, and drilled according to the standard dental procedure.

Fig. 1 Phases of dental implant surgery supported by a robot.

This work focuses on the replication of the thrust force which represents the axial resistance of the bone during drilling. In particular, attention was given to the thrust force when drilling the external compact structure of the cortical bone and the inner porous structure of the trabecular bone [18-21].

To fabricate the bone for the simulacrum additive manufacturing was considered. In fact, additive manufacturing is having great growth as engineering tool [22]. Within the dental industry with several different technologies such as Laser Powder Bed Fusion (LPBF), Stereolithography (SLA), Material Jetting (MJ), and Fused Filament Fabrication (FFF) [23] are being employed. Despite the spread of these technologies, studies to understand their full potential are still ongoing [24, 25, 26, 27]. Compared to the other technologies, FFF does not require post-processing, reducing time and costs [28]. Moreover, one of the most used materials in FFF for biomedical applications is PLA [23, 29].

In literature, there are some studies on bone models in oral and cranio-maxillofacial surgery [30]. For example, Favier al. [31] compared the force required to drill samples of different 3D printable materials, such as Polycarbonate (PC), resins and Polyamide (PA), with respect to a thin wall of bone. The obtained values (75-200 N) resulted higher than those of the bone. Hochman et al. [32] developed a 3D printed temporal bone model, however the work focused on the vibrations generated during drilling rather than the thrust force. Regarding PLA drilling, the literature reports studies about fiber-reinforced PLA obtained by injection molding [33, 34]. Finally, all the cited studies focus on the drilling of bulk samples. As the use of PLA to emulate the entire structure of bone (cortical and trabecular) has not been adequately investigated, this work aims to fill this gap.

Accordingly, a set of sample geometries of the mandible was identified, designed, and fabricated. In particular, additive manufacturing was used to realize the samples thanks to its versatility and cost-effectiveness for the production of small batches or geometrically complex shapes, as in the case of the medical industry [35-37]. Accordingly, in this work, bone samples were printed in PLA taking into account the infill pattern and the infill density process parameters. Drilling tests were performed using a CNC milling, the Kern Nano micro-milling machine, and two different collaborative robots, the Sawyer from Rethink Robotics and the UR10 series E from Universal Robot. In particular, the robots were required to perform only the drilling operation without performing the complex handling required to operate with a real patient. The dental drill was attached to the robot using a grasping system developed specifically for this project. Thrust drilling force was measured during the tests and the hole positions were measured on the drilled samples. As a result, the effects of the printing parameters on the drilling force were outlined and they were calibrated in order to match the experimental force. Moreover, the behavior of the collaborative robots was evaluated in terms of accuracy and precision.

5.1.2 Experimental setup

5.1.2.1 Samples fabrication

The samples were fabricated using FFF technology. In particular, the Ultimaker 3 extended 3D printer was used together with Ultimaker White Pearl White PLA filament. The sample's geometry consists of a 30x10x12 mm^3 prism. Three different types of samples (Figure 2) were designed: shell sample, infill sample, and full sample (combination of shell and infill).

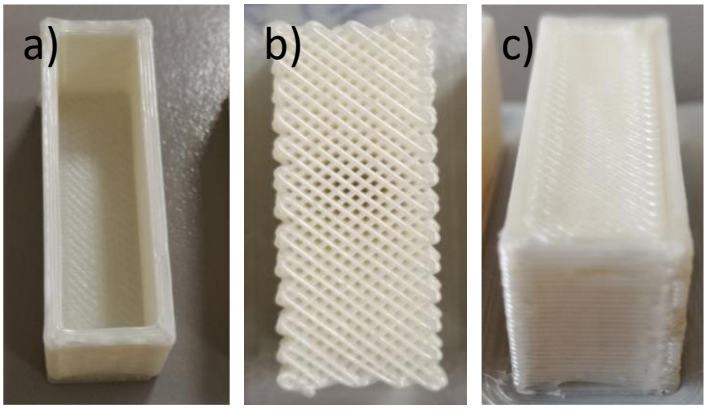

Fig. 2 Types of samples. a) Shell, b) infill (50%), c) full

Shell samples present only the top surface and the outer walls. The thickness of the top surface and the walls is 1.2 mm. The infill samples show a bottom surface 1.2 mm thick while the rest of the volume is filled at different infill densities with different infill strategies. The infill densities are varied from 25% to 87.5% while the infill strategies are linear and gyroid (Figure 3). The full samples are a combination of the previously described designs. In particular, they present the walls, the top-bottom surfaces, and the internal infill. Samples were printed with two different layer thicknesses, more precisely a layer thickness of 0.4 and 0.1 mm. A summary of the characteristics of each sample is reported in Table 1.

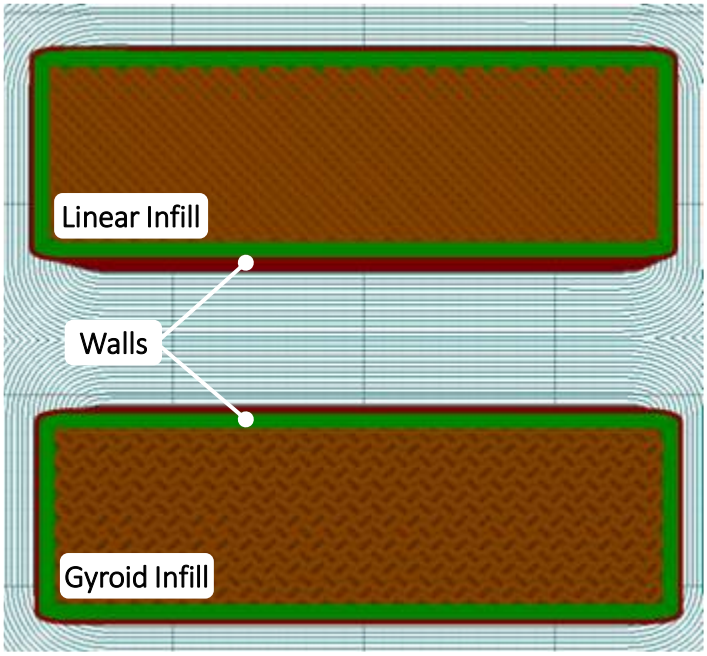

Fig. 3 Infill strategies: linear (upper) and gyroid (lower). Sections of Full samples.

Table 1: PLA bone samples that were tested.

Sample Type	Infill [%]	Top/Bottom Surfaces	External Walls	Layer Thickness [mm]	Filling Type
Shell	0	Yes / No	Yes	0.4 – 0.1	None
Infill	25 – 50 – 62.5 75 – 87.5	No / Yes	No	0.4 – 0.1	Linear - Gyroid
Full	25 – 50 – 62.5 75 – 87.5	Yes / Yes	Yes	0.4 – 0.1	Linear - Gyroid

5.1.2.2 Drilling procedure

All the drilling tests were performed with a dental drill tip of 2.2 mm in diameter. On each specimen, 8 mm deep holes were drilled following the drill tapping surgical approach. In particular, each hole was drilled in two steps: the drill first descended 4 mm into the sample, then ascended to allow the chip to escape and the temperature to cool down, and then descended again to reach the final depth. The drilling speed was set to 1 mm/s and parallel to the building direction of the samples (i.e. layers were drilled along their orthogonal direction). During the tests, the samples are mounted on a support positioned on a strain gauge load cell LCS-1 (max load 50 kg), with an accuracy of 0.1 N (Figure 4). The signals of the load cells were acquired and elaborated using the LabView software.

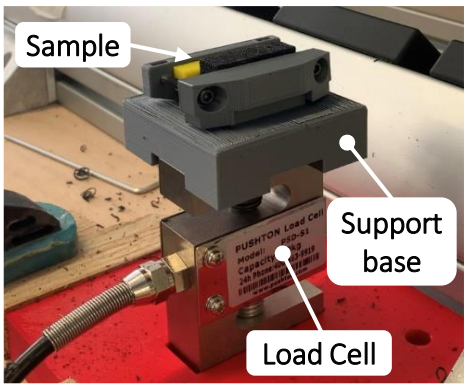

Fig. 4 Gauge load cell LCS-1 with a sample mounted on the support base

The drilling tests were performed both on collaborative robots and a CNC precision machine. In particular, preliminary tests were conducted on the two robots (Sawyer and UR10e) to compare their performance during drilling. Then, the drilling process was investigated on a CNC machine to focus on the calibration of the drilling thrust force and exclude external noise factors, such as the robot stiffness. Further experimental tests on a limited set of selected samples were performed on the more performant robot (UR10e) to evaluate its precision during the emulated surgical procedure when the thrust force is comparable with the experimental values.

5.1.2.3 Collaborative robots

Two different collaborative robots were tested: a Sawyer robot and a UR robot. The drilling tip was set in motion at the highest possible speed by the dental drill DEC 100 equipped with an INTRA matic 20 CB handpiece connected to the robots by a clamping system.

Anthropomorphic robotic manipulator

The Sawyer robot (Figure 5) is a robot manufactured by Rethink Robotics. It is a 7-degree-of-freedom (DoF) anthropomorphic manipulator which is included in the category of collaborative robots because it is able to work in direct and safe contact with a human operator. In particular, Sawyer is classified in the category of "Power and force limited by inherent design" [38]. The payload of the robot is 4 kg and it has nominal repeatability of ± 0.1 mm. To increase safety, there are protective elements of soft material on

the joints and it is also equipped with both electrical and mechanical brakes, which, combined with torque sensors on each joint, allow the motion to stop in case of accidental impact.

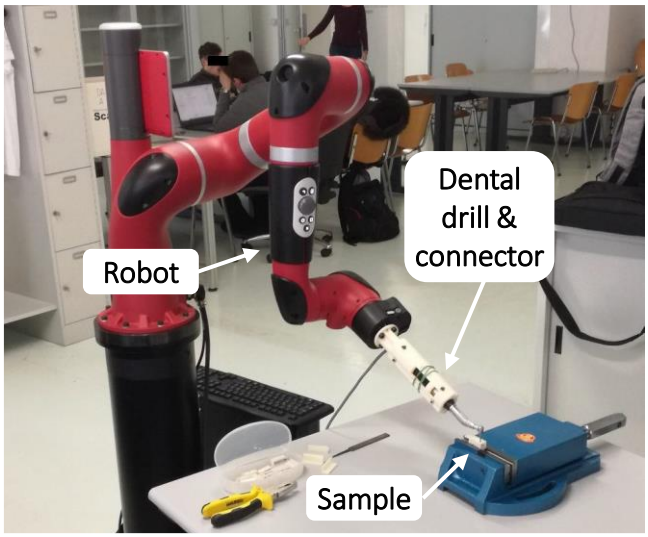

Fig. 5 Sawyer robot with the mounted dental drill.

Articulating robotic system

The UR10e (Figure 6) is a 6-DoF collaborative robot manufactured by Universal Robots. It has a force sensor at the wrist with a range of 150 N and 10 Nm. The robot joints are plastic coated for safety reasons, while the links are made of steel. The nominal repeatability of the robot is ± 0.05 mm, making it suitable for precision applications. These features, together with simplified programming using the supplied teach-pendant, make the robot particularly suitable for collaborative applications.

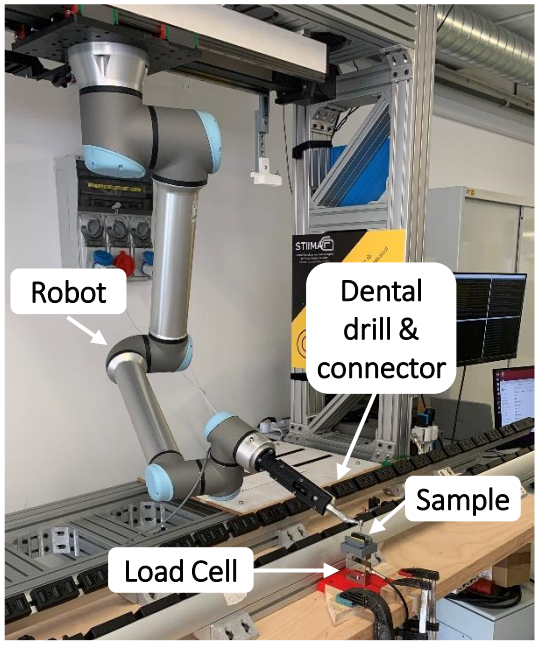

Fig. 6 UR10e robot with the mounted dental drill

5.1.2.4 Precision machining center

The drilling tests on the CNC machine were performed with a Kern Pyramid Nano (Figure 7), an ultra-precision 5 axes machining center. The drillings were performed by inserting the drilling tip directly into the machine's spindle. The rotation speed was set to 1000 rpm.

Fig. 7 CNC machine Kern Pyramid Nano

5.1.3 Experimental tests

5.1.3.1 Preliminary tests

Preliminary tests were conducted to evaluate which of the two collaborative robots better met the requirements for the drilling procedure and to optimize the parameters of the sample.

Robot evaluation

The preliminary tests were conducted both on the Sawyer and the UR robots (Table 2).

Table 2: Summary of the Preliminary test performed on the robots.

	Sawyer	**UR10e**
Layer thickness [mm]	0.4	0.4
Infill [%]	25 – 50 – 75	50 – 62.5 – 75 – 87.5
Infill pattern	Linear	Linear
Sample type	Shell – Infill – Full	Shell – Infill – Full

The tests conducted with the Sawyer robot used samples that were built with a layer thickness of 0.4 mm and a linear infill pattern. The infill and full samples have an infill density of 25%, 50%, and 75% for the Sawyer robot. The tests were replicated 3 times. These experiments produced two main results: the first one was that the robot was not adequate to conduct the drilling due to the lack of rigidity given by the springs in its joints. The second was that an infill of 25% with the linear pattern was too low, with the drill tip entering the voids of the grid (Figure 8). As a consequence, the drilling is more likely to deform the grid rather than cut it. For these reasons, the Sawyer robot was discarded due to its lack of rigidity and the levels of the infill density were varied.

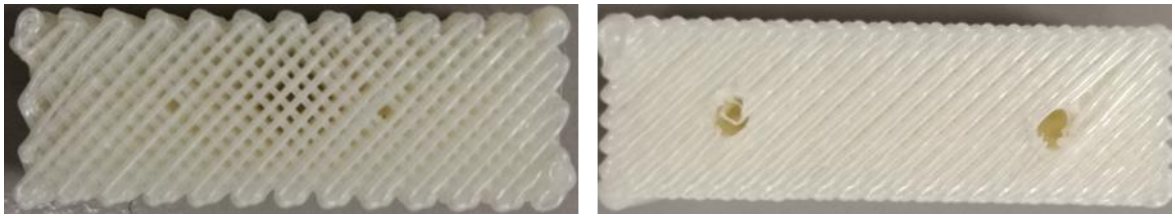

Fig. 8 Drilling holes on the samples with a density of 25% (left) and 87.% (right).

The tests conducted with the UR10e robot focused on a higher range of infill densities, in particular 50%, 62.5%, 75%, and 87.5%. The typical thrust force profile when drilling a full (shell with filling) sample is reported in Figure 9. In particular, it shows the two taps of the drilling, the Peak and Plateau Forces which correspond respectively to the drilling of the shell (i.e. cortical bone) and of the infill (i.e. trabecular bone). When shell or infill type samples are considered, Plateau or Peak force is missing respectively.

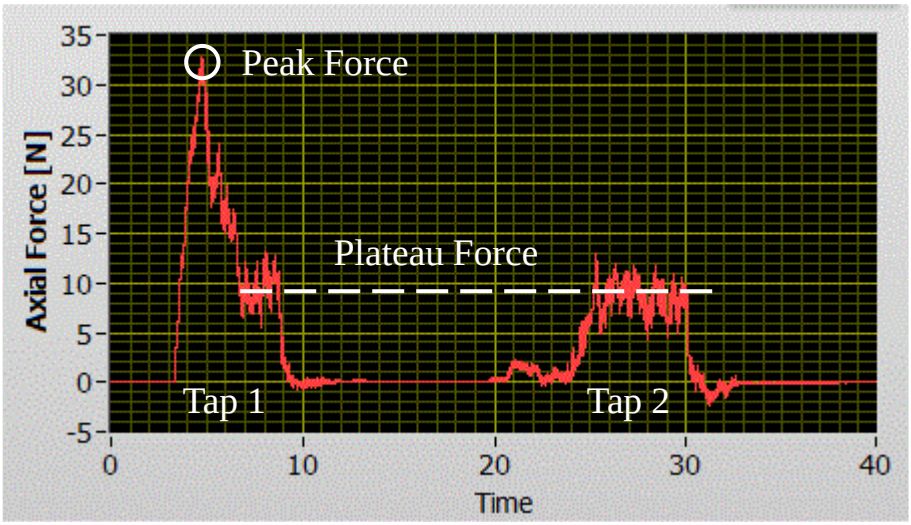

Fig. 9 Typical force profile during drilling (full sample).

Figure 10 reports the results of the drilling thrust force in the UR robot Experiments. The results of the Plateau forces are grouped in the left area of the graph (data named from 50% to 87.5%) while the results of the Peak forces are grouped in the right area (data named from Shell + 50% to Shell + 87.5%) samples. The results of the samples with no filling (data named Shell) can be assigned to both groups being at the same time samples having a shell with 0% filling or a 100% filling with no shell.

The Plateau force (force needed to drill the infill) slightly increases for low infill values (50% to 75%) while it increases for rapidly high infill values (from 75% to shell). The Peak force values show that it is stable and, in particular, it is not influenced by the presence of the underneath infill. Finally, the extension of the boxes in the figure shows that the variability of the results is almost uniform amongst the groups and relatively low when compared to the difference between the groups.

Based on these considerations, it is possible to state that the shell and the infill can be treated as two separate variables in the investigation. Moreover, the values of the Peak forces (21.8-26.4 N) are comparable but a little higher than the ones found in literature for the drilling of the cortical bone (10-12 N) [19-21]. With regards to the Plateau force (3.3-20.8 N), it is comparable with the one of the trabecular bone (5-6 N) [19-21].

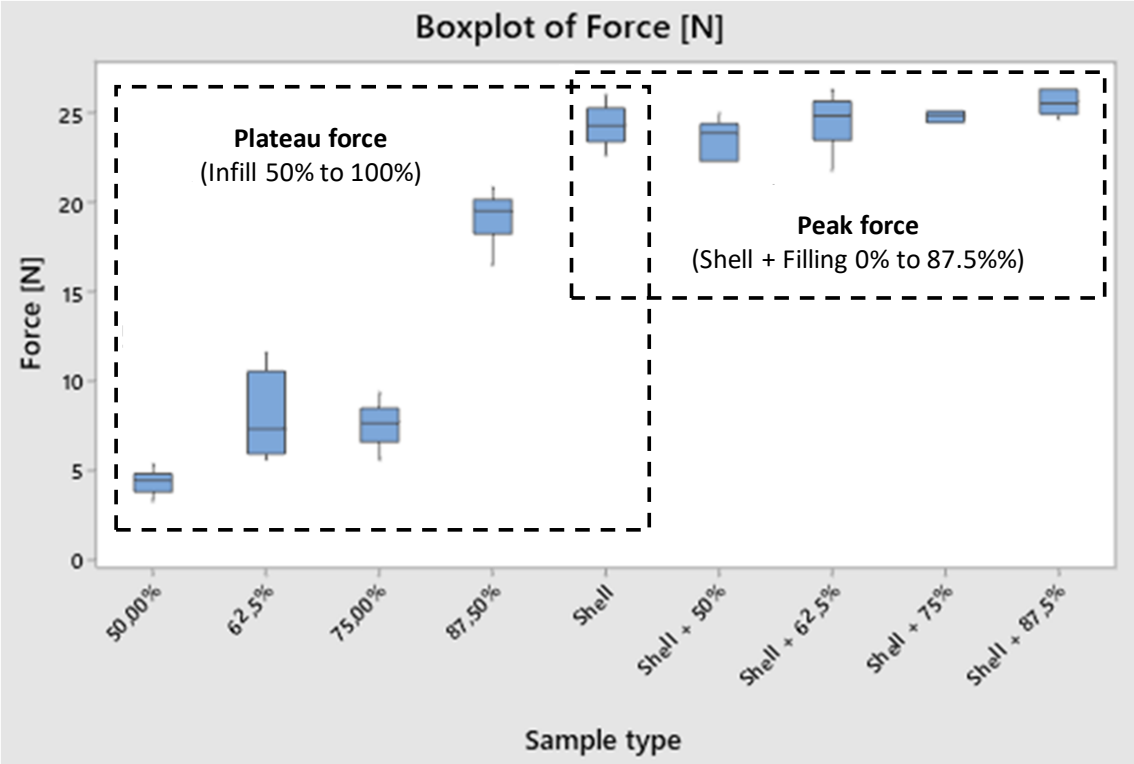

Fig. 10 Thrust forces results of drilling test on UR robot

Precision milling center

In order to characterize the samples on a stiff system, drilling tests were performed on a KERN CNC milling center. In this way, it is possible to remove the variabilities induced by the joint gaps of the robots and achieve a more precise evaluation of the forces.

Two different campaigns were performed to investigate the effects of the layer thickness and infill strategy (Table 3). The first campaign was performed on samples with a layer thickness of 0.4 mm, infill values of 50%, 62.5%, 75%, 87.5%, and a linear infill pattern. The second campaign was carried out on samples with a layer thickness of 0.1 mm and the same infill densities. The two campaigns slightly differ in the infill pattern and the sample type. This is because the resolution of a 0.4 mm layer thickness is too poor for the fabrication of a Gyroid pattern which becomes almost a linear pattern. Therefore, a linear pattern was tested in both campaigns while the Gyroid pattern was excluded in the first one. Moreover, the results of the first campaign (layer thickness 0.4 mm) confirmed, as described below, that Peak force is not influenced by the underneath infill density. Therefore, the Full samples (shell with infill) were excluded in the second campaign (layer thickness 0.1 mm) and the Shell and Infill types were only tested. In both campaigns, all tests were replicated 3 times.

Table 3: Summary of the experimental tests performed on the CNC machine.

	First campaign	**Second campaign**
Layer thickness [mm]	0.4	0.1
Infill [%]	50 – 62.5 – 75 – 87.5	50 – 62.5 – 75 – 87.5
Infill pattern	Linear	Linear – Gyroid
Sample type	Shell – Infill – Full	Shell – Infill

The results of the first and second campaigns are reported in Figure 11 and Figure 12 respectively.

The results on the Peak force (Figure 11a and Figure 12a) show that there are no significant variations as the tested parameters change. In fact, in the case of 0.4 mm layer thickness (Figure 11a), the results are independent of the presence of the filling or its density. This confirms what was observed in the Robot evaluation tests. Moreover, the Peak force in the case of a 0.1 mm layer thickness (Figure 12a) is lower than the case of 0.4 mm, but it remains close. Therefore, the layer thickness or the presence of the infill does not significantly affect the thrust force when drilling the compact shell of the sample.

For what concerns the Plateau force (Figure 11b and Figure 12b), it is possible to see that it increases with the infill density and, unlike the data obtained with the robot, the trend is almost linear in both campaigns. Moreover, the layer thickness has a double effect. First, the increase in force due to the infill density is much less steep as the layer thickness decreases. In particular, differences in the force are more evident as the infill density is reduced, while they become negligible as density reaches 100% (as the Shell). Second, the variability within the tests is significantly lower. These effects are probably related to the material bonding cavities that are less and smaller when lower layer thicknesses are adopted. Therefore, the sample structure is more uniform and the actual infill density is higher. This is in agreement with a more uniform and higher thrust force. Finally, Fig. 11b shows how the Plateau force does not vary in the presence or absence of the shell layer, confirming the absence of interaction between the two areas of the sample with respect to the thrust force. Furthermore, it underlines the capability of the measurement system to perceive the change in density and resistance.

When the infill pattern is considered, the Gyroid one is less resistant than the linear one, but its benefits are visible in the case of 50% infill where it significantly reduces the variability of the force concerning the linear pattern. This can be explained by the fact that the linear pattern consists of lines deposited in the layer in pre-imposed directions that are alternated along the build direction. This gives a structure with passing through holes along the building direction. Since drilling is parallel to the building direction and the drill position to the holes is random, the thrust force randomly varies on the base of the alignment of the drill to the holes. Moreover, the lower the density, the larger the holes. Therefore, the material distribution of the infill is less uniform. This can lead to the higher variability of the thrust force observed for lower infill densities (Fig. 12b). Accordingly, a minimum infill density of around 62.5% should be adopted in the case of a linear infill. On the contrary, the Gyroid pattern avoids the presence of passing through holes and, therefore, allows a more uniform thrust force on the whole range of densities considered.

a)

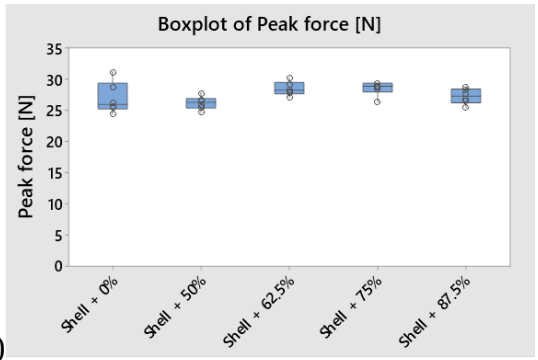

b)

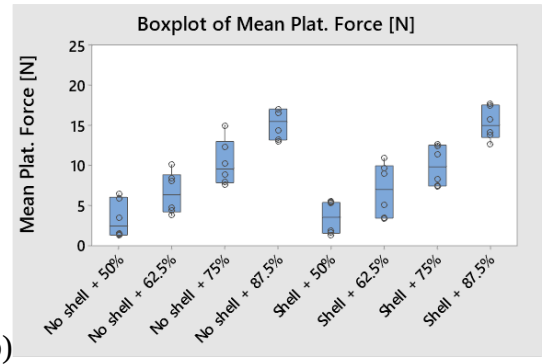

Fig. 11 Results of first campaign (0.4 mm Layer thickness) on CNC machine. a) Peak force. Values obtained for the Shell samples (0%) and Full samples (other %). b) plateau force. Values obtained for the Infill samples (no shell) and Full samples (yes shell)

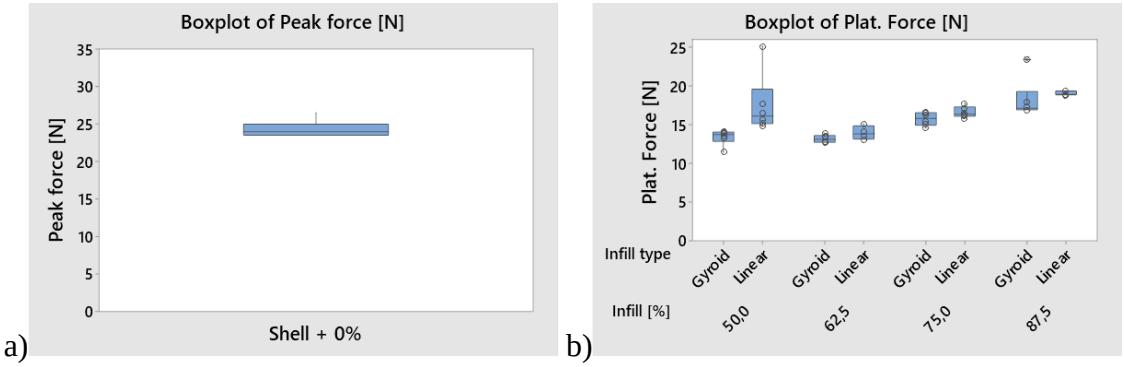

Fig. 12 Results of second (0.1 mm Layer thickness) campaign on CNC machine. a) Peak force. Values obtained for the Shell samples. b) plateau force. Values obtained for the Infill samples.

5.1.3.2 Experimental work

The main objective of this campaign is to characterize the behavior of the complete system composed of the robot and the samples. Therefore, the more stable and repeatable conditions identified in the preliminary tests (section 5.1.3.1) were considered. Accordingly, the UR10e robot was chosen within samples having a layer thickness of 0.1 mm and a Gyroid infill pattern.

Full samples (shell with infill) using three levels of infill density, respectively 0%, 50%, and 87.5%, were used. For each type of sample, 5 replicates were 3D printed and 3 drills on each sample were performed following the tap drilling procedure described before. The results of the Peak and Plateau forces are reported in Figure 13 and grouped accordingly to the infill density. The trends are in accordance with the results on the CNC machine, even though some differences are present. In particular, the Peak force shows a slight influence from the infill density. In fact, its values range from 19-23 N for the 0% (i.e. Shell) samples to 23-28 N for the 87.5% infill full samples. However, the mean value is comparable with the previous tests. The plateau forces, instead, result lower than the one found in the CNC machine tests. In fact, for the 50% infill, the value is about 5 N while for the 87.5% the value is around 11 N. The differences in the forces are probably due to the lower stiffness of the robot which can be influenced by the sample structure and so leading to a change in the position of the drill and, hence, to the cutting mechanism.

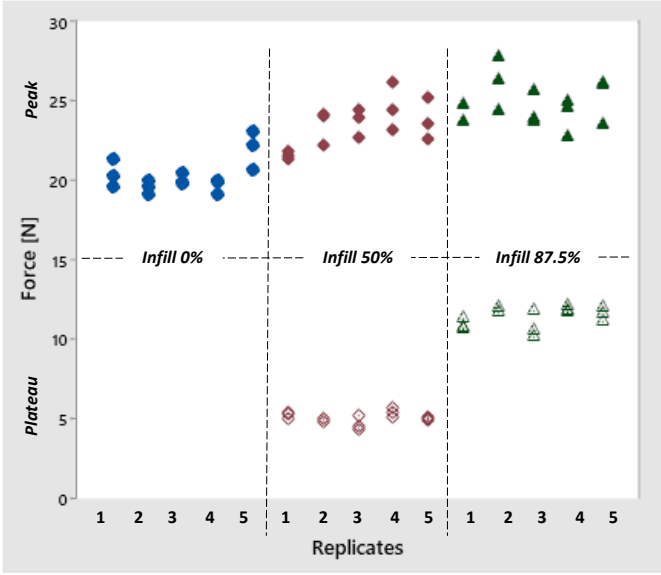

Fig. 13 Thrust drilling force of the tests conducted with the robot UR.

To evaluate the adequacy and precision of the robot in performing the operation, the relative positions of the second and third holes were measured with respect to the first hole, held as a reference point. The holes were drilled in a straight line at a spacing of 9 mm. The x and y deviations of the holes from the ideal position were evaluated using a microscope. The results are visible in Figure 14.

The graphs show that along the x-axis, the axis perpendicular to the direction of movement, the robot is really stable (Figure 14a). In fact, the errors are centered in zero with a maximum deviation of 0,15 mm. Along the y axis, the axis parallel to the direction of movement, almost all the errors present a positive value, indicating that the robot usually performs a greater displacement than the nominal one (Figure 14b). This kind of behavior can be generated by a small initial sliding of the drilling tip on the samples surface caused by the joint flexibility of the robot and clamping system. The resulting total error, however, has an average deviation of less than 0.5 mm from the nominal position (Figure 14c). An error of this magnitude can be considered acceptable and adequate, especially with respect to manual positioning [39].

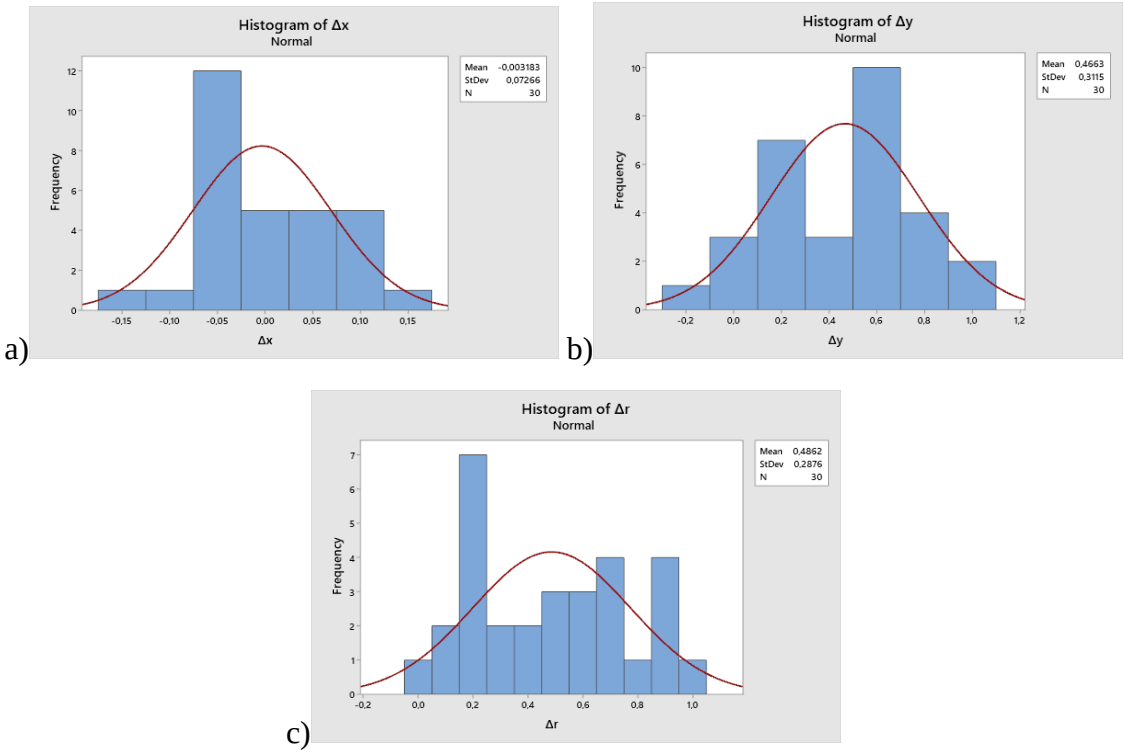

Fig. 14 Measure of the deviations of the holes with respect to the original position: a) deviation along the x axis, b)deviation along the y axis, c) total deviation.

5.1.4 Conclusions

In the present work, Additive Manufacturing was investigated to replicate the thrust force of the bone during drilling. In particular, samples characterized by an external compact shell and an infill with a lower density were fabricated to emulate the cortical and trabecular bones respectively. Moreover, different manufacturing parameters and drilling systems were considered and compared.

The investigation on the process parameters showed that:

- The thrust force when drilling the compact shell of the sample is not affected by the layer thickness or the presence and density of the infill.

- The thrust force when drilling the infill of the sample almost linearly increases with its density. Moreover, it is more uniform, higher, and less dependent on the density as the layer thickness is reduced. Finally, the use of a Gyroid infill pattern further reduces the force variability with respect to a Linear one.

The investigation on the Robots showed that:

- The use of collaborative robots for dental drilling applications is possible after a preliminary analysis of the mechanical behavior of the manipulator (i.e. a structure that is too elastic can negatively affect the performance of the machine).
- The precision and accuracy achieved by a robotic system are extremely better than that achievable by the hand of a surgeon.

Moving the focus to the dental surgery application, the choice of the more suitable parameters set should be made considering the objective that is followed:

- Uniformity of the samples. Low values of the Layer thickness should be adopted, a Gyroid infill pattern is preferred and the infill density can be varied for a moderate calibration of the trabecular thrust force. The cortical thrust force is constant.
- Customization of the samples. The Layer thickness should be high, a Gyroid infill pattern is preferred and the infill density can be varied for a strong calibration of the trabecular thrust force in order to replicate a wider range of bone densities. The cortical thrust force is constant.
- Choice of the robot. The UR10e robot is a potential solution for bone drilling when the positioning accuracy is considered, especially compared to the manual procedure.

Overall, the bone emulators made of PLA fabricated through the FFF technology guarantee a drilling thrust force that has uniform repeatability and is comparable with the values reported by the literature. Moreover, it is possible to calibrate the thrust force of the infill by varying its value to replicate different bone conditions (i.e. different bone mass densities).

Future works will investigate other materials for the bone to evaluate whether and how the thrust force can be calibrated to match different bone densities. Other sample geometries will be considered as cortical thickness or infill pattern. Moreover, a more complete evaluation of the drilled holes, such as depth of drilling and orientation, will be carried out. Finally, a working 3D printed model of the patient oral cavity will be fabricated in order to replicate clinical cases.

Regarding the robotic system, future developments will include the study of other collaborative robots to compare their effectiveness and the use of advanced control techniques, such as Force control or Impedance control, to further improve the results obtained. Furthermore, optimized movement trajectories will be investigated for the feasibility study of drilling in confined spaces like the oral cavity. Another interesting development could be to realize a customized dental drilling system by exploiting the knowledge gained through the use of different cobots.

Chapter 6

Post processing of biocompatible surfaces

In this chapter the research regarding the finishing processes of biocompatible material and surfaces is presented. Specifically, the smoothing 3D printed ABS samples through two different acetone protocols. The first consisting in directly dipping the specimens into an acetone bath, the second in which hot acetone vapor hit the target surface. Finally, an evaluation of different finishing technique on cells and bacteria colonization of 3D printed titanium surfaces is carried out. The published papers related to these topics are listed below:

- L. Riva, A. Fiorentino and E. Ceretti, "Characterization of the Chemical Finishing Process with a Cold Acetone Bath of ABS Parts Fabricated by FFF", In: Carrino, L., Tolio, T. (eds) Selected Topics in Manufacturing (2022). Lecture Notes in Mechanical Engineering. Springer, Cham.
  In this work the candidate was responsible of sample fabrication, test performing and data collection. He took part in writing and editing of the draft.

- L. Riva, A. Fiorentino and E. Ceretti, "Characterization of chemical surface finishing with hot acetone vapours on ABS parts fabricated by FFF", Prog Addit Manuf 7 (2022), 785–796.
  In this work the candidate collaborated in the writing and the editing of the draft.

- P.S. Ginestra, L. Riva, E. Ceretti, D. Lobo, S. Mountcastle, V. Villapun, S. Cox, L. Grover, M. Attallah, O. Addison, D. Shepherd and M. Webber, "Surface finish of Additively Manufactured Metals: biofilm formation and cellular attachment", Paper presented at ESAFORM 2021. 24th International Conference on Material Forming (2021), Liège, Belgique.
  In this work the candidate collaborated in the writing and the editing of the draft.

6.1 Characterization of the Chemical Finishing Process with a Cold Acetone Bath of ABS Parts Fabricated by FFF

6.1.1 Introduction

The demand of low cost, customized and aesthetic products is increasing in recent years [1]. Additive manufacturing (AM) comprehends a series of technologies able to meet these new needs. Some of the major advantages of these technologies are low material waste, high resource efficiency, complex geometries and production flexibility [2]. Between the AM technologies, Fused Filament Fabrication (FFF) is certainly one of the most diffused [1]. It consists in a filament of material being extruded through a nozzle moving in XY direction. Once the layer is completed the building plate moves in z direction and a new layer begins. The object is then fabricated in a layer-by-layer method [3]. The most used materials in FFF are polylactic acid (PLA), Acrylonitrile butadiene styrene (ABS), polycaprolactone (PCL) and polypropylene (PP) [2]. FFF has many applications in a wide range of fields like automotive, biomedical, orthodontics and casting [3,2]. However, as other technologies, FFF presents also some drawbacks. One of the most limiting is a low surface finish [4]. To address this problem, it is possible to act in two ways: pre-process or post-process [1]. Pre-process solutions optimize the process parameters such as layer thickness [5] and build orientation [6] even though a residual stair case effect remains. Post-process solutions are divided in mechanical and chemical finishing techniques. Possible mechanical techniques are manual sanding, CNC grinding [7], abrasive milling [8] and barrel finishing [9]. CNC grinding is probably the most effective mechanical technique to surface finish FFF components however it works only on simple geometries. Chemical finishing offers some advantages with respect to mechanical finishing like the ease in treating undercuts or internal surfaces, the absence of the contact tool-object and a lower cost [1]. Possible chemical finishing techniques are manual painting and coating, vapour smoothing and dipping. Manual painting is very fast and cheap however it leaves an irregular surface due to an uneven application [1]. Vapour smoothing and dipping are usually carried out using dimethyl ketone (acetone) as solvent. Vapour smoothing has been fairly studied by scientists [10-12]. In [13] the authors studied two different sample configurations at various vapour exposition times. The process was able to reduce roughness up to 98%. Similar results were found by Kuo et al [14] where both linear and curved profiles were studied. Bathia Sing et al [10] investigated different vapour exposure times associated with different process temperatures and found out that the finishing temperature plays a major role in the final roughness. In order to speed up the process it is also possible to dip the object directly in the acetone bath. However, it is necessary to control the process in order to avoid too aggressive treatments. In literature few researches have been published on this topic, therefore this work focuses on a larger characterization of the process by studying its capability and the effects of the main process parameters. In particular, ABS 3D printed parts were considered. Moreover, the initial roughness of the surface, its orientation to gravity during dipping, treatment time and solvent degradation were investigated. The work is divided into two steps. The first aims at identifying the optimal test procedure. In particular, it identifies the time window of the treatment where the process is more controllable. Moreover, the possibility to reuse the solvent without a loss in the process capability is investigated. The second one investigates the effectiveness and the robustness of the process by testing the whole range of possible initial roughness together with the orientation to gravity of the surface and the treatment time. The results show that the process is stable, repeatable and it allows to strongly reduce the surface roughness down to the 97% on average.

6.1.2 Experimental setup

6.1.2.1 Samples fabrication

The samples geometry is represented in Fig. 1, in particular it consists in a 60x10x6 mm^3 prism. In order to fabricate samples with different initial roughness, they can be 3D printed using different building angles. Since overhangs requires support material, chamfers are present on the samples to distinguish between the upper free surface (used as reference for the tests) and the bottom one which is fabricated in contact with the support material. The samples also present two holes for the mounting on the treating chamber (Fig. 2).

Samples were fabricated using the Stratasys Dimension bst 1200es FDM printer. ABS filament was used to fabricate the samples and polystyrene was used as support material. The layer thickness was set to 0.254 mm while the nozzle temperature was 300 °C. In order to control the shrinkage of the material during the process, the printing chamber has a controlled temperature of 75 °C.

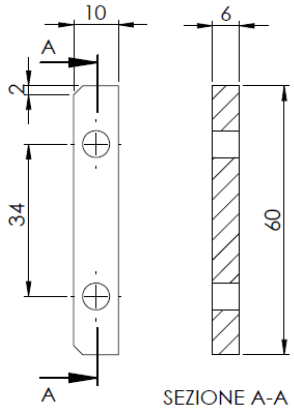

Fig. 1 Sample geometry.

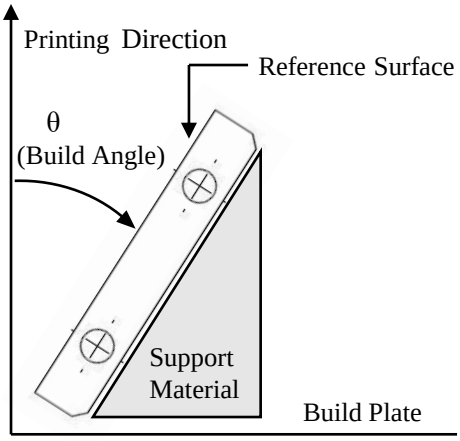

Fig. 2 Sample orientation during manufacturing.

6.1.2.2 Testing procedure

The test set up (Fig. 3) consists in a treating chamber made by a glass jar filled with acetone at room temperature. The samples are fully immersed in the bath and held by stainless steel wire hooks which are inserted in the mounting holes. In order to avoid the release of acetone vapours, the jar is sealed with aluminium foil. The samples are immersed in the acetone bath and different orientations and treating times can be adopted. Once extracted, the specimens are dried at room temperature for at least 48 hours in the same orientation adopted for the treatment.

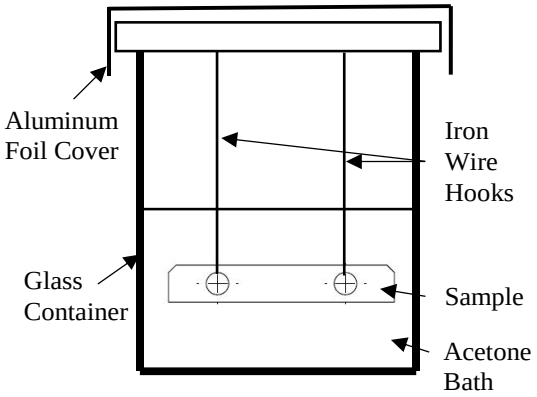

Fig. 3 Test set up.

6.1.2.3 Roughness

The surface roughness was measured on the samples before and after the treatment using a Mitutoyo Surftest Sj-301 profilometer. Measures were repeated 3 times for each sample.

6.1.3 Experimental tests

The experimental tests were conducted to evaluate the capabilities of the chemical post-process on the surface finishing as the initial roughness changes. Moreover, different process parameters were investigated: surface orientation to gravity, treatment time and acetone bath condition (Tab. 1 and Tab.2).

Table 1: Process parameters used in the preliminary tests.

Time [s]	Build Angle [°]	Configuration	Solution
5-15-30	0	A	Pure
60-120-240	70	B	Reused
480		C	

Table 2: Process parameters used in the experimental campaign.

Time [s]	Build Angle [°]	Configuration	Solution
60 - 120	0 - 35 - 60	A - B - C - D	Reused
240 - 480	70 - 80 - 90		

Fig. 4 reports the trend of the roughness of the samples as a function of the building angle. For low angles (approx. 0÷50°) the curve increases gently starting from a building angle of 0°, in which the roughness is around 20 µm. Then (approx. 60÷70°) both values and scattering increase in a marked way until the roughness reaches its peak around 70° with a value of approximately 65 µm. Then (approx. 80÷90°) the curve rapidly lowers again reaching (at 90°) a value of about 18 µm similar to the one at 0°. The difference between the two cases is in the surface pattern which is stair-cased in the case of 0° while it depends on the layer filing in the case of 90°. Accordingly, experiments were conducted on samples covering the whole range of roughness using build angles equal to 0°, 35°, 60°, 70°, 80° and 90°.

During the finishing treatment, ABS is partially solved by acetone and the surface of the samples comes into a semisolid state. Therefore, surface orientation to gravity was included in the experiments to evaluate whether the sample materials could flow and influence the results of the treatment. In particular,

different sample orientations were considered, namely A to D. In configuration A, the samples are immersed with the target surface facing upwards, in the B configuration the target surface faced laterally and, finally, in the C configuration the target surface faced downward (Fig. 5). Configuration D is a variant of configuration B since the treated surface is faced laterally, but the printed layers are horizontal instead of vertical. Therefore, they are oriented one transversally and the other parallel to gravity respectively.

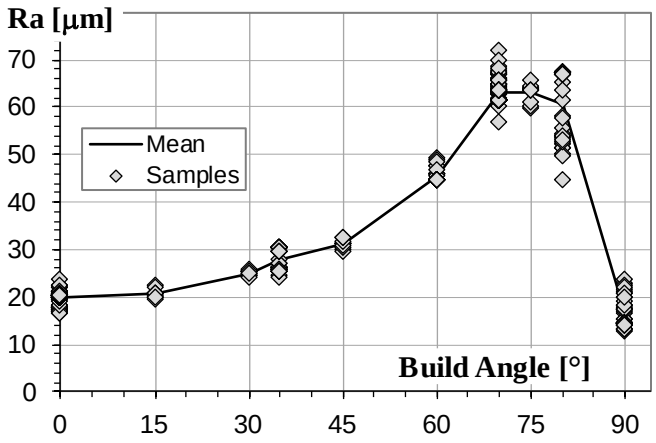

Fig. 4 Roughness trend in relation to the building angle.

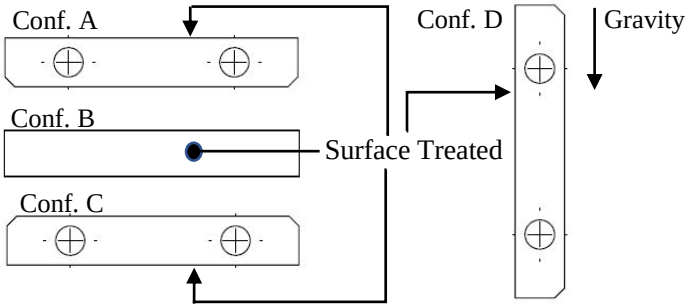

Fig. 5 Immersion orientations.

The treatment times were chosen in the range of 5s to 480s. This range was chosen to evaluate the effects of the treatment from short to long duration cases. The intermediate values were chosen on the base of the slope of the process results. In particular, they were thickened where the gradient of the results is higher.

During the treatment, part of the sample is solved by acetone which, at the end of the process, is contaminated by the sample material. Therefore, the solvent bath should be replaced by new and Pure acetone (P) at every treatment to ideally reproduce the same treating conditions. On the other hand, the use of raw material influences the cost of the process. For this reason, the experimental campaign investigated whether Reused solvent (R) could affect the process.

The experimental tests were conducted in two steps: preliminary tests and experimental campaign respectively focused on the test procedure and the process characterization. Moreover, the tests are named using codes that derive from the process parameters (i.e. code 80°-B-30s-P refers to a sample with a build angle of 80°, treated in the B orientation for 30s using Pure acetone). In the case a code does not include one or more parameters, it refers to a set of tests that were performed with the same parameters (i.e. code 70°-C refers to all the test that used samples with a build angle of 70° and treated in C orientation).

6.1.3.1 Preliminary test

Preliminary tests were performed to define a testing procedure able to make the process more stable and controllable. In particular, the focus was set on the treatment time window and the acetone solutions that were tested together with a subset of values for the building angle (i.e. surface roughness) and orientation to gravity (Tab. 1).Accordingly, treatment times were chosen to be spread almost uniformly in the tested range and then they were locally thickened to better catch the slope of the process results. Consequently, 5 - 15 - 30 - 60 - 120 - 240 and 480s were tested. Moreover, samples were immersed in Pure and Reused acetone baths. Furthermore, samples having the maximum and minimum surface roughness corresponding to the building angle of 0° and 70° respectively were used. In this way, the procedure is investigated in the least and most severe initial roughness. Finally, the configuration named A, B and C were considered.

Fig. 6 reports the results of the preliminary tests in terms of Ra_f/Ra_i that expresses the ratio between the roughness of the samples after the treatment (Ra_f) and before (Ra_i) as treatment time, surface orientation and solvent state change.

The results on the treatment time show that for small durations (5s to 30s) a rapid reduction of the roughness occurs even though trends are dissimilar. In fact, the curve progressively decreases in some cases (0°-B, 70°-A, 70°-B and 70°- C) while it suddenly drops in others (0°-A and 0°-C). For longer treatments (30s to 480s), the slope of the roughness reduction is more stable and similar amongst the tests. Even though in some cases (0°-A and 70°-C) a slight raise in the surface roughness occurs from 120s of treatment, the process reaches a plateau in the range 60÷480s. Accordingly, below 60s of treatments the process is uncontrollable because of the high speed and dissimilitude of the treatment. On the contrary, the presence of the plateau after 60s indicates that the process has probably entered a phase of stability.

The results on the solvent state (Fig. 6) do not show significant differences between treatments conducted using Pure or Reused acetone. In fact, the curves are almost overlapped except for few sporadic and not systematic cases that are attributed to randomness.

On the basis of these results, the preliminary tests indicated that the experimental campaign should be performed using a treatment time from 60s to 480s where the process is more stable and controllable. Moreover, Reused acetone can be used in order to save material. On this point, particular attention was paid to monitor any possible change in the solvent efficiency. In fact, Reused acetone gradually evaporates and gain more and more sample material as the treatments are conducted. Therefore, Pure acetone was added before each test to recover the initial volume of the solvent. Moreover, reference tests were carried out at the beginning and at the end of each test session to outline a control chart for the solvent and to identify possible drifts in the experimental procedure. The check tests that were chosen for the experiments are: 70°-A-60s, 70°-B-60s and 70°-A-480s and include the highest initial roughness (70°), two opposite sample orientations (A and B) and short and long treatment times (60s and 480s).

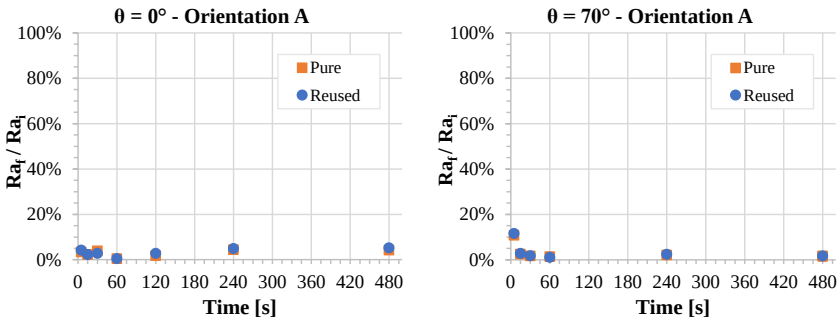

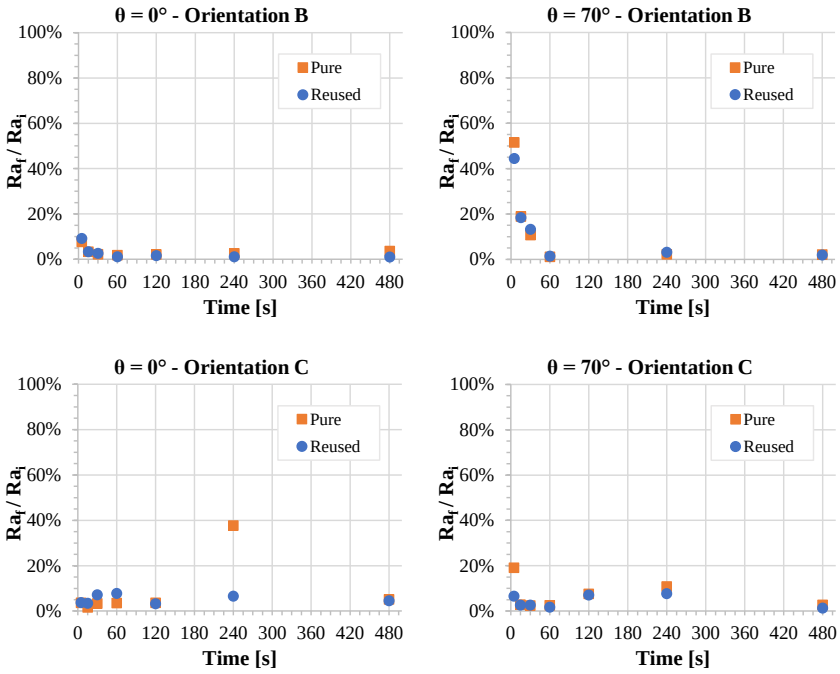

Fig. 6 Preliminary tests result.

6.1.3.2 Experimental campaign

The experimental campaign focused on the evaluation of the process capability and robustness with respect to the initial roughness of the surface, its orientation to gravity during treatment and the duration of the process. Therefore, a larger number of build angles and orientations to gravity were tested. Moreover, according to the results of the preliminary tests, treatment times from 60s were considered and Reused acetone was adopted. A summary of the experimental campaign is reported in Table 2.

The effect of the surface treatment on the roughness reduction was evaluated through the ratio Raf/Rai and its absolute value Raf. In particular, the results (Fig. 7) show that the process is almost stable and uniform as the build angle, the treatment time and the orientation to gravity vary within the tested ranges. Moreover, the overview of the data (Fig. 8) shows that the final achieved roughness is about 1.2 µm on the average which corresponds to the 3% of the initial one. In order to evaluate and quantify the robustness of the process, the results were elaborated using regression analysis and ANOVA to investigate whether the tested parameters have a statistical effect on the roughness reduction.

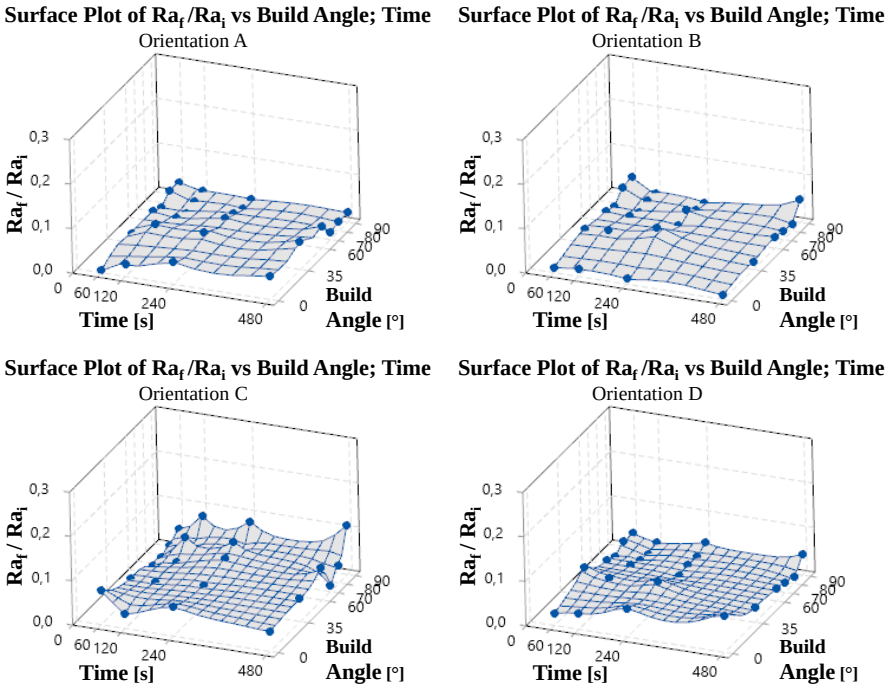

Fig. 7 Experimental campaign results.

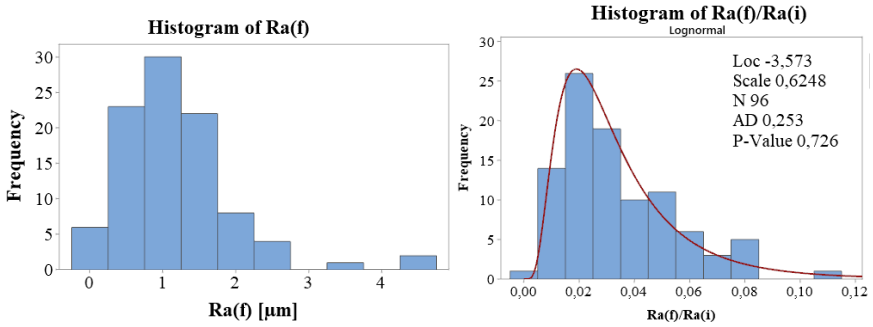

Fig. 8 Frequency distributions of the final roughness.

The regression analyses performed on the ratio Raf/Rai lead to a non-normal distribution of the residuals. Therefore, it was not possible to determine which factors influence the process on the base of their p-value. Consequently, it was decided to perform a Box-Cox analysis to identify a suitable transformed function of the response for the statistical analysis. The Box-Cox analysis suggested a logarithmic function as reported in Fig. 9.

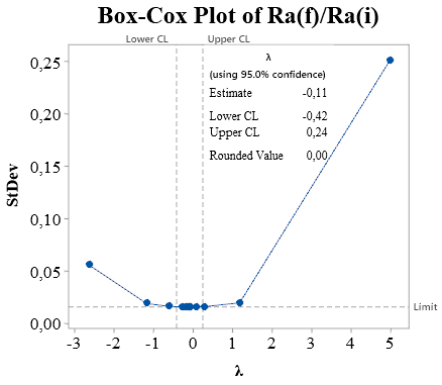

Fig. 9 The Box Cox analysis.

The analysis on the transformed response provided residuals with normal distribution, ensuring the reliability of the p-values of the factors. In particular, starting from a regression model which includes all the tested factors (Fig. 10a) and gradually removing the non-influential parameters, the orientation to gravity of the surface resulted the only factor that influences the process (Fig. 10b).

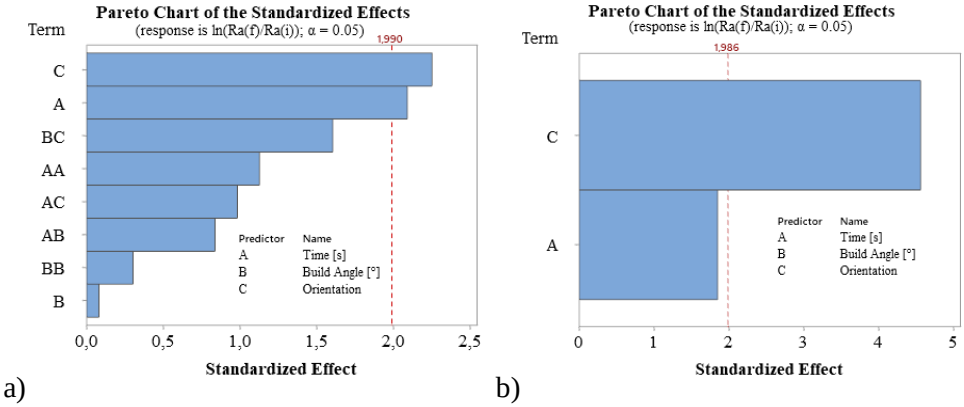

Fig. 10 Analysis of the transformed function.

Accordingly, the effect of the surface orientation was investigated. In particular, Fig. 11 shows that the impact of the orientation on the roughness reduction varies from about 2% to 5%, which implies a variability of 3% on the result of the process. This low impact is confirmed by a very low value of the correlation coefficient of the regression model (R-sq = 23.7%).

The results of the previous analysis show that the process is independent from and very robust with respect to the build angle of the part surfaces and the treatment time. Since a 3D part has surfaces that are fabricated with different build orientations, the robustness of the treatment with respect to the build angle allows to achieve a relative reduction of roughness which is uniform on the whole part. Moreover, the independence from the treatment time allows to use the shortest treatment in the tested range so reducing the duration of the process to 60 seconds. With regard to the part orientation to gravity, a light influence on the process was highlighted. This is probably due to the gravitational force that may deform the surface material when it is in semi solid state with unpredictable effects. Anyway, the impact of the gravity on the process capability is negligible (<3%).

Overall, the process is capable to strongly reduce the surface roughness of ABS 3D printed parts fabricated through FFF. In particular, it allows to achieve a reduction of the initial roughness of about 97% on the average within a treatment time of 60s.

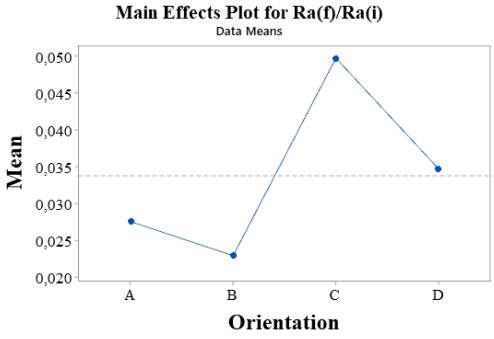

Fig. 11 Impact of surface orientation to gravity on the roughness.

6.1.3.3 Check in-out tests.

As previously discussed, the acetone solvent was reused in the test. Since it is not afore known for how long it can be reused, control tests were performed during the entire experimental campaign. The results of the control tests are reported in Fig 12. where no significant changes or drifts over time of the process

are present. This confirms that the results of the experimental campaign are not affected by the adoption of Reused acetone.

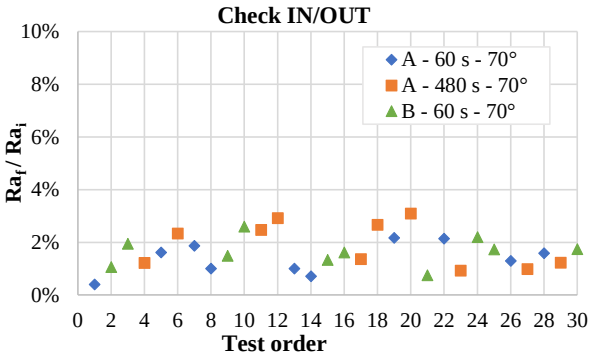

Fig. 12 Results of the Check IN/OUT tests.

6.1.4 Conclusions

Additive manufacturing is a technology with the biggest growing rate and its freedom of design makes it suitable for many applications like rapid prototyping or high customization. Fused Filament Fabrication is probably one of the most famous additive technologies. However, it comes with some drawbacks, one of which is the poor surface finishing of the parts.

This work investigated the effects of a surface treatment consisting in the immersion of ABS parts in acetone baths. The results show that for short treatment of times (below 30 s) the process is not really controllable (Fig. 6) while from 60 seconds the process reaches a plateau becoming stable and repeatable (Fig. 7). The process is able to reach a good quality of surface finish. In particular, with a roughness percentage reduction about 97% on the average corresponding to Ra = 1 μm can be achieved regardless of the initial roughness (Fig. 8). Moreover, the orientation to gravity of the treated surface affects the process but with a negligible impact. Furthermore, no differences were found between new and used acetone solutions, making this process interesting also from an industrialization point of view.

Future researches will focus on analysing how this process can affect the dimensional stability of the specimens and how it behaves on more complex and three-dimensional surfaces. Moreover, data on the solvent reusability will be collected in order to evaluate costs and environmental aspects. Finally, this study is part of a larger one that aims at developing and evaluating different treatment methodologies based on acetone (hot and cold vapours together with direct contact). Once the whole study will be performed, an overall comparison amongst the different methods will be conducted.

6.2 Characterization of chemical surface finishing with hot acetone vapours on ABS parts fabricated by FFF

6.2.1 Introduction

Additive Manufacturing (AM) allows great flexibility in the production of components with complex shapes and geometries [1]. Furthermore, the customization of the final product is easily reached [2]. AM was originally born as a method to rapid prototyping but, in the last years, its properties made it spread across several fields such as automotive, electronics and medical [3, 4]. Other applications are the fabrication of functional tools and molds for casting to reduce manufacturing costs and time [5]. Fused Filament Fabrication (FFF) is one of the most used AM technologies for producing parts made of thermoplastic materials [6]. In FFF, the STL geometry of the part is processed by the 3D printer software to generate the G-Code [7]. A spool of thermoplastic filament is then extruded through a heated nozzle which moves along the path defined in the G-Code [8]. Usually, the print is performed on a heated print bed [9] that is lowered when a layer is completed to extrude the following layer until the part is finished [10]. FFF is adopted in various fields such as aerospace, automotive, biomedical and tooling thanks to its low operating, fabricating and maintenance costs [11-12]. However, FFF is characterized by anisotropy and poor surface quality [13] due to surface texture and staircase effect. In particular, the texture originates from a coarse STL file which approximates the curved surface of the part using too few triangles [14]. This defect can be overcome by reducing the dimension of the triangles so enhancing the definition of the geometry. On the contrary, the staircase effect is intrinsic to the process and therefore cannot be totally solved. It is because a continuous surface is approximated by layers having a finite height along the build direction. Therefore, the printed surface will have a stepped profile. Many researchers focused on different methods to overcome these issues [15], and the influence of process parameters on surface quality was studied by several authors [16, 17]. In particular, layer thickness and part orientation are the most influencing factors [18, 19]. However, it is not possible to completely reach a very smooth surface only by optimizing the process parameters, therefore a post-process [20-22] is needed to achieve a higher roughness reduction [23]. Surface treatments can be either mechanical or chemical. The most common mechanical treatment is CNC machining but other processes like barrel finishing or abrasive flow can be used [24-25]. However, these treatments present some disadvantages such as the difficulty in reaching some regions of the part thus increasing the process cost or the risk of damaging the less resistant parts. Being not able to obtain a homogeneous surface with no part properties modification and low cost [26], mechanical treatments are not the ideal solution for roughness reduction.

Chemical treatments reach very good results without the aforementioned limitations. One of the main treatments is carried out using Dimethyl ketone (acetone), especially for Acrylonitrile Butadiene Styrene (ABS) [27], one of the most used FFF materials. Moreover, the part can be treated with different approaches: dipped in the solvent bath or exposed to cold or hot solvent vapours. Dipping an ABS part in an acetone solution results in an aggressive reaction, the concentration of the solution and immersion duration must be carefully chosen in order not to generate undesired effects like deformation or dimensional changes [28]. Surface treatments using acetone vapours are instead more gradual and can be carried out without any significant dimensional change [29]. Vapours can be either cold or hot [30, 31]. Cold vapour treatments result in a more gradual finishing since the heat accelerates the reaction kinetic. Hot vapours then, speed up the treatment making it a little less controllable with possible not uniform surfaces [32]. Besides some commercial systems (as Polymaker Polysher, Zortrax Apoller or 3D Dipsmooth) are available and some studies are present in the literature on the chemical treatments [33, 34], few is reported on the process optimization and its robustness and stability as the process parameters or the initial part roughness change. Moreover, there is not a wider analysis that compares the different

approaches. For instance, the literature does not provide a comprehensive investigation on the surface finish obtainable with the FFF process, particularly for the worst roughness (corresponding to build angles of 70° and 80°), which are often unaddressed. Furthermore, the current data in literature lacks on the replicability of the treatment. Finally, a robust set of process parameters able to smooth the surface independently from the initial roughness has yet to be demonstrated. In particular, this latter is a fundamental topic since a 3D printed component presents many surfaces with different build orientations, thus different starting roughness. For these reasons, the authors are conducting an extensive investigation of this process. In particular, cold vapours [31] and dipping [35] approaches have been investigated and their capability and robustness were identified in previous researches.

To consider and, in the end, compare a wide range of alternatives, this study focuses on a treatment based on hot vapours. Differently from the works already present in the literature, this research aims to find a set of process parameters able to be effective on whatever initial roughness of the samples. Doing so the process is applicable for every possible printable geometry. The parameters investigated are acetone concentration, treatment time, and distance between the samples and the bath. Moreover, the set of parameters has to be repeatable and robust, consequently a different approach is proposed. In particular, previous works were based on a full characterization of the processes within the entire range of the process parameters. Differently, the present research is based on incremental experiments that progressively reduce the parameters window to find an optimum set of parameters that allows a stable, robust and repeatable method. The experimental plan was designed with the DOE technique and the effect of the treatment were statistically analysed. The results show the existence of an optimal combination of parameters for the hot vapour smoothing process that leads to a high smoothing effect on every starting roughness with high uniformity and replicability. Furthermore, the process can reduce the roughness of the sample with negligible effect on its dimensions and at a low cost.

6.2.2 Experimental set-up

The samples were fabricated with a Stratasys Dimension BST 1200es FFF 3D printer using ABS (namely ABSplus-P430) using Polystyrene (namely P400R) as breakaway support material. The materials were extruded through nozzles at the temperature of 300°C, the printing chamber was kept at 75°C and the layer thickness was set at 0.254 mm.

The geometry of the samples is reported in Fig. 1. In particular, the surface considered in the experiments (target surface) is a plane 60 mm long and 6 mm wide. This geometry was chosen because a curved surface has a variable orientation with respect to the build direction and, therefore, it has a roughness that locally varies. In contrast, the evaluation of the roughness according to UNI EN ISO 4288:1997 [36] requires a fixed minimum sampling length of 0.4 to 40 mm depending on the actual roughness of the sample. Therefore, if the surface finish varies along the sampling length, the measured roughness is an averaged value and does not fully characterize the surface of interest. For this reason, a 60 mm flat target surface was chosen. Moreover, samples with different build angles were printed so to test different starting roughness, they were packed on titanium support (Fig. 2) and then treated.

The test set-up is visible in Fig. 3. It consists of a glass beaker (105 mm in diameter and 1 L capacity) containing the solvent. The backer is placed on a heating magnetic stirrer to bring the solvent to boiling temperature. After the bath has reached boiling point, the samples pack is placed on the top of the beaker with the target surfaces facing down. When the treatment time is reached, samples are removed and dried for 24 hours. The entire equipment was placed under a laminar flow hood.

To keep the tests under control, some precautions were taken. In particular, the titanium sheets were placed inside the solution to reduce the boiling turbulence and prevent any splash of the solvent on the samples. Moreover, the level of the solvent was refilled at the beginning of each test to keep under control the distance from the target surface of the samples. Furthermore, the loss of solvent due to evaporation

was strongly reduced by an aluminium foil used to seal the beaker. Finally, the use of vapours at boiling point guarantees a repeatable temperature for all the tests.

Roughness (Ra) measurements were performed before and after treatment with a Mitutoyo Surftest Sj-301 profilometer following the standard UNI EN ISO 4288:1997 [36]. The effects of the treatment on the dimension of the sample were evaluated with a micrometer.

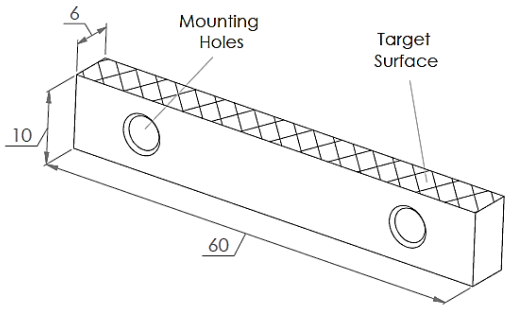

Fig. 1 Scheme of the ABS samples dimension and geometry.

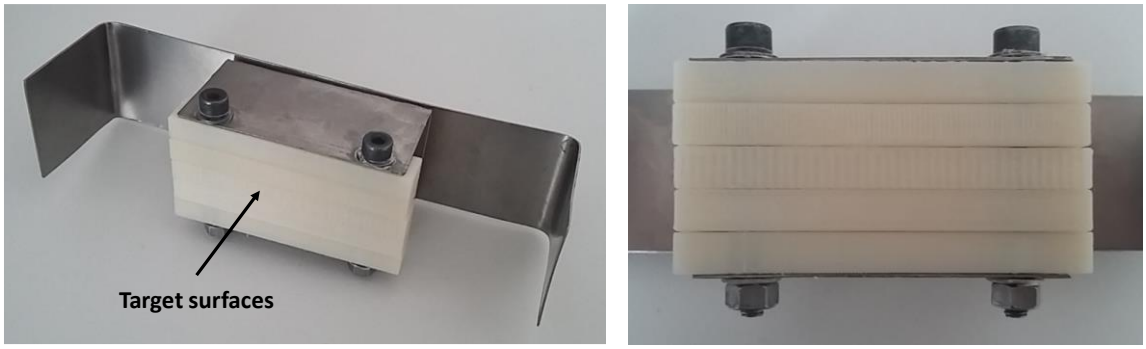

(a) (b)

Fig. 2 (a) Set of samples packed and mounted on the titanium support and (b) detail on the target surfaces.

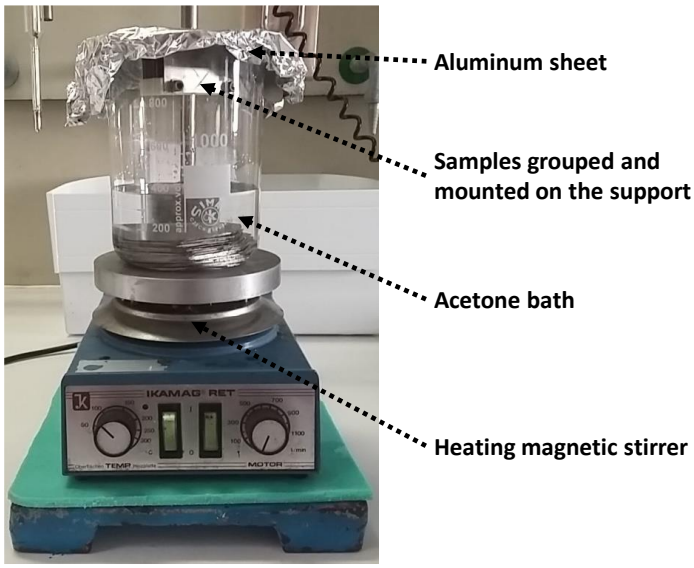

Fig. 3 Experimental set-up used for the surface treatment.

6.2.3 Experimental campaign

The experiments were conducted adopting a step by step approach. Initially, samples were characterized to evaluate their initial roughens as the build angle changes and to select the ones that mostly represent the finish of a printed part. Then, an explorative experimental campaign was conducted to identify a technological window (i.e. ranges of parameters) where the process is repeatable. A Central Composite Design (CCD) experimental plan investigates the parameters on 3 levels with a low number of experiments [37]. In particular, it focuses on the main effects of the parameters and neglects the higher grade interactions. For these reasons, it is suitable for preliminary tests. Accordingly, the explorative campaign was conducted and, in particular, a subset of the parameter ranges that guarantees an effective and stable process was identified. Finally, a 3k experimental plan was conducted within the technological window to characterize and optimize the process.

Experimental tests were conducted grouping and treating together samples with different roughness (Fig. 2). In particular, each pack contained a set of samples fabricated with a different build angle accordingly to the ones selected in the sample characterization phase. Moreover, the position of the samples in the pack was randomized for each test to avoid any systematic effect on the results. Each test was repeated 3 times and the run sequence was randomized. After the sample treatment, 6 measures of roughness were taken on each sample (2 in the central region and 2 for both external regions). Then, the average final roughness (Ra) and the standard deviation (σ) were calculated to evaluate process efficacy and surface uniformity. Furthermore, dimensional measurements were taken to evaluate the effect of the process on part precision.

6.2.3.1 Samples characterization

A preliminary characterization of the samples was performed. In particular, the influence of the build angle on the surface roughness was evaluated. Nine different orientations that cover the entire range from 0˚ to 90˚ with respect to the printing direction have been considered (Fig 4a). Ten samples for each orientation were printed. During printing, samples were positioned to keep the target surface not in contact with the support material to avoid any interaction. Surface roughness measurements were taken on the target surface orthogonally to the pattern of the staircase effect (Fig. 4b). Fig. 4c shows the results of the characterization of the sample roughness. In particular, both average values and their dispersion increase from 0° to 70°-80° and then fall when approaching to 90°.

The present research focused on 5 different build angles selected to consider the whole range of starting roughness. In particular, 0° and 90° (low values), 70° and 80° (highest value and scattering respectively), 35° (intermediate values) were considered.

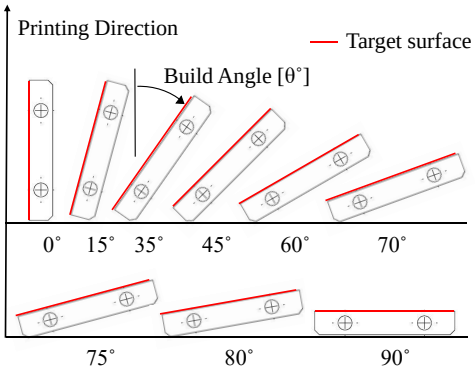

(a)

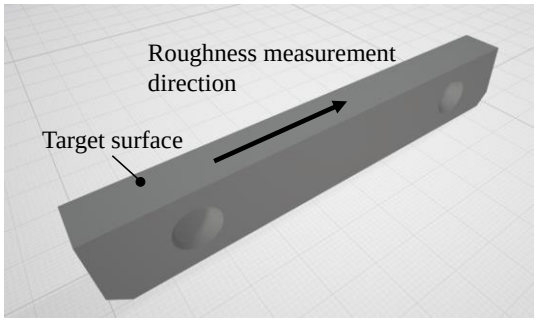

(b)

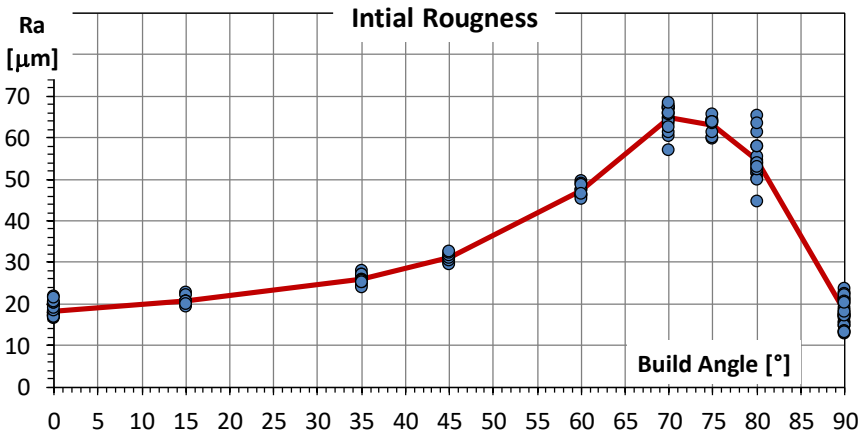

(c)

Fig. 4 Samples characterization – Build angle and initial roughness: (a) representation of build angle and direction; (b) slicing with model and support materials; (c) untreated samples roughness as a function of the build angle (the line connects the average value of the groups).

6.2.3.2 Feasibility ranges – Preliminary tests

The preliminary tests were conducted to define the ranges of the process parameters where the post-processing is feasible. In particular, the focus was set on the acetone concentration, the distance target surface to acetone bath and the treatment time. The tests showed that an acetone concentration lower than 90% generates cracks and discontinuity on the sample surface, probably due to the excessive accumulation of water moisture that locally shields the surface from the treatment. Furthermore, tests showed that a treatment time higher than 12 minutes does not improve the smoothing but, on the contrary, the surface starts to over-dissolve and drip.

Starting from these observations, ranges and levels of the process parameters were selected for the following experiments. In particular, tests were conducted using 90 to 100% of Acetone concentration, 50 to 100 mm for the distance between the target surface and acetone bath within 3 to 12 min of treatment time (Tab. 1). Since the boiling temperature of a solution varies with concentration, it was measured and the results are reported in Tab. 1 together with the acetone concentrations. Except for the preliminary tests, the temperature of the solution is almost constant within a variation of 56 ± 1 °C.

Table 1: Tested parameters and levels.

Factors	**Feasibility Ranges (Preliminary Tests)**	**Explorative Tests (CCD plan)**	**Characterization & Optimization (3^K)**
Acetone concentration [%]	50 ÷ 100	90 – 95 – 100	90 – 95 – 100
(Boiling Temperature [°C])	(69 ÷ 55)	(57 – 56 – 55)	(57 – 56 – 55)
Distance surface-acetone bath [mm]	75	50 – 75 – 100	50 – 75 – 100
Treatment time [min]	0 ÷ 15	3 – 7.5 – 12	7.5
Replicates	2	3	3

6.2.3.3 Explorative tests – Central composite design

Explorative tests were conducted using Central Composite Design (CCD). In particular, the Face Centred Design ($\alpha = 1$) was adopted to keep the parameters within the feasibility ranges (Tab. 1). Results were evaluated using visual inspections and roughness measurements.

Fig. 5 reports an example of the visual inspection. In particular, it shows the sample treated with a low acetone concentration (90%) and a high distance of the sample surface (100 mm) at different treatment times (0 to 12 minutes). The treatment time of 3 minutes (Fig.5b) is insufficient to smooth the surface for each build angle. In particular, the printing layers are still clearly visible in the specimens that have the highest initial roughness (build angle of 70° and 80° accordingly to Fig.4c). A treatment time of 7.5 minutes (Fig. 5c) can produce a more homogeneous smoothing on all the samples, even if the printing layers are still visible on the 70° and 80° samples. After 12 minutes (Fig. 5d) the printing layers are not visible anymore on the 70° and 80° samples, but the process is more unstable. In fact, phenomena like material dripping and bubble formation start to take place resulting in a non-homogeneous surface. This is due to an excessive softening of the material.

Fig. 6 shows the typical behaviour of the roughness measures in terms of average and standard deviation values. In particular, it represents the values found for the 35° samples. By visual examination (Fig. 5), the lowest value of roughness and scattering were found for a treatment time of 7.5 minutes (Fig. 6b and 6e) that results in a more uniform smoothing effect. This is more evident in Fig. 7 where the average Roughness and scattering are overall lower for a treatment of 7.5 minutes. Similar results were obtained with other build orientations.

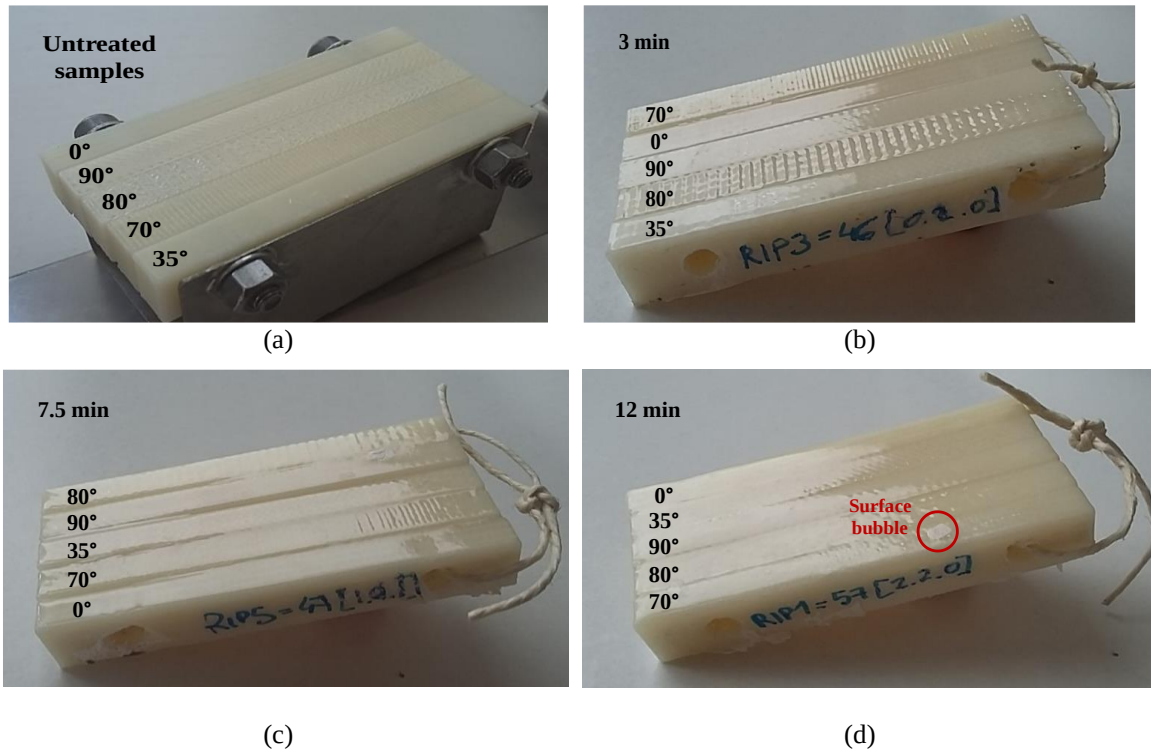

Fig. 5 Explorative tests (build angle of 35°) – Typical appearance of the target surface under various treatment durations (acetone concentration 90%, distance 100 mm): (a) untreated samples and results of the treatment after (b) 3 minutes, (c) 7.5 minutes and (d) 12 minutes.

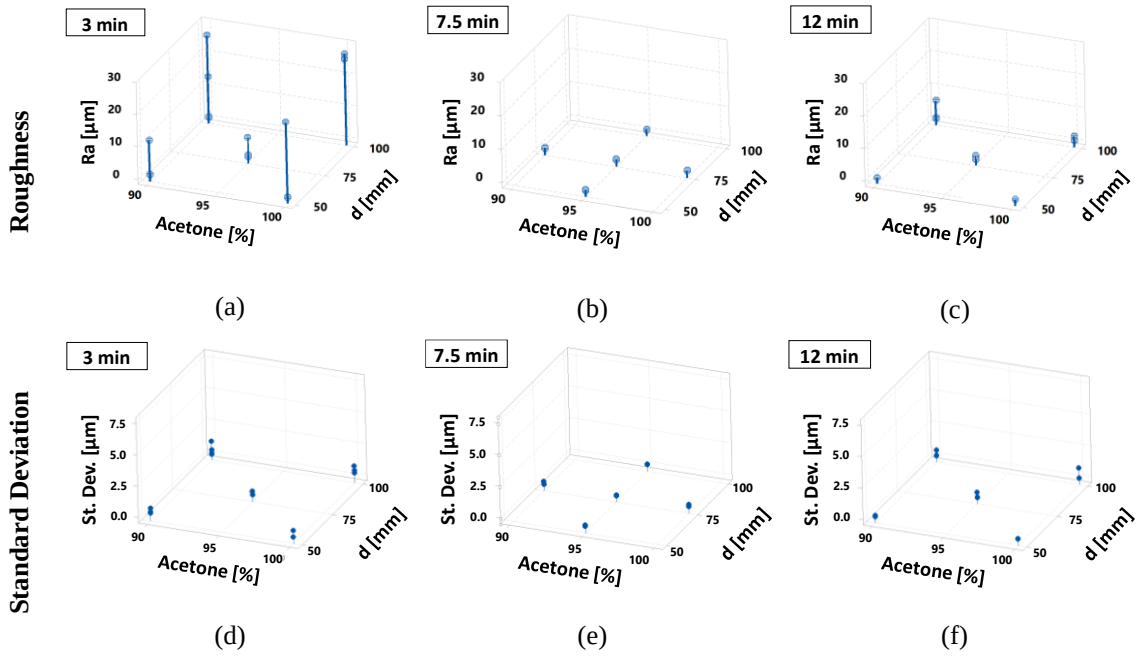

Fig. 6 Explorative tests (build angle of 35°) – Typical results of the treatment as a function of the exposure time: roughness (a, b, c) and standard deviations (d, e, f).

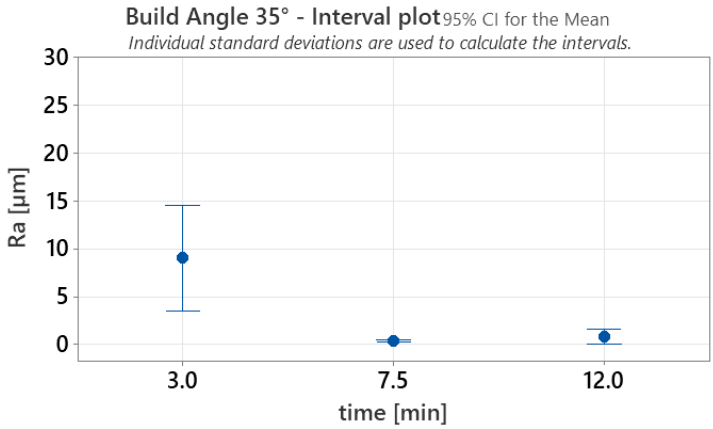

Fig. 7 Explorative tests (build angle of 35°) – Influence of treatment time on the surface Roughness (data are grouped for same times values)

6.2.3.4 Process characterization and optimization – 3k design

The treatment time of 7.5 minutes was found to be the one that furnishes good and uniform smoothing. Therefore, another experimental campaign was carried out to fully characterize the process considering the effects of the process parameters given a fixed treatment time of 7.5 minutes. Tests were performed extending the CCD to obtain a 3k experimental plan (Tab. 1) and the results are shown in Fig. 8 and Fig.9. The process shows to be stable when the initial roughness of the samples is low (0°, 35° and 90°) reaching an almost constant roughness and low scattering. Results from samples with higher initial roughness (70° and 80°) are less uniform. Besides these differences, there are some configurations where the process reaches similar results in all cases (acetone 95% with distance 75mm; acetone 100% with distance 50mm).

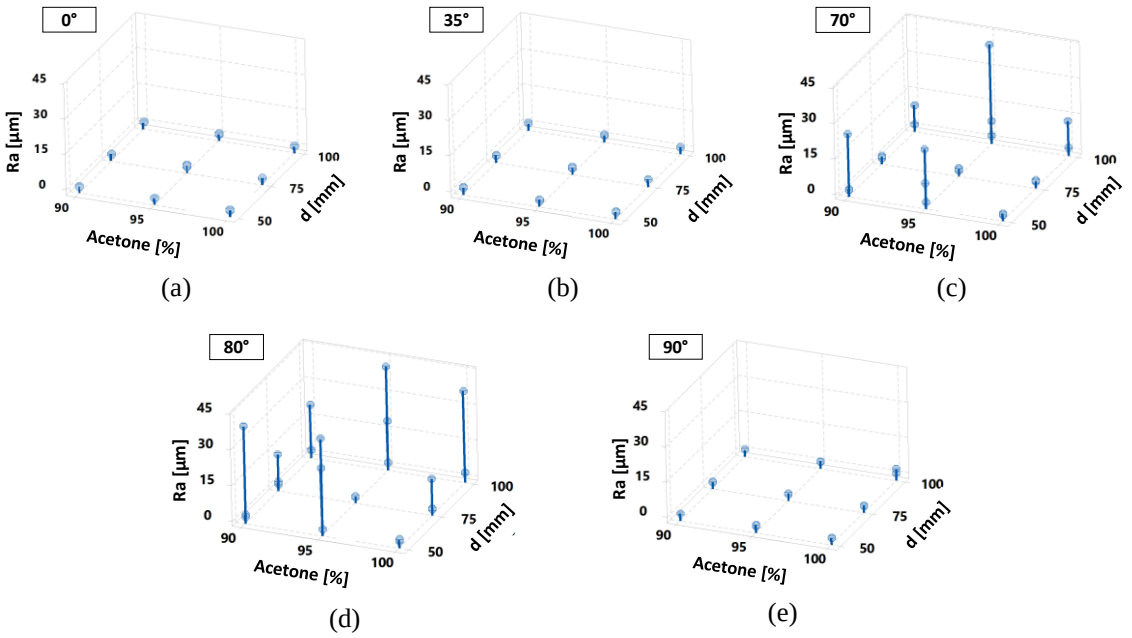

Fig. 8. Process characterization – Average roughness on the samples for each build angle (treatment time = 7.5 minutes).

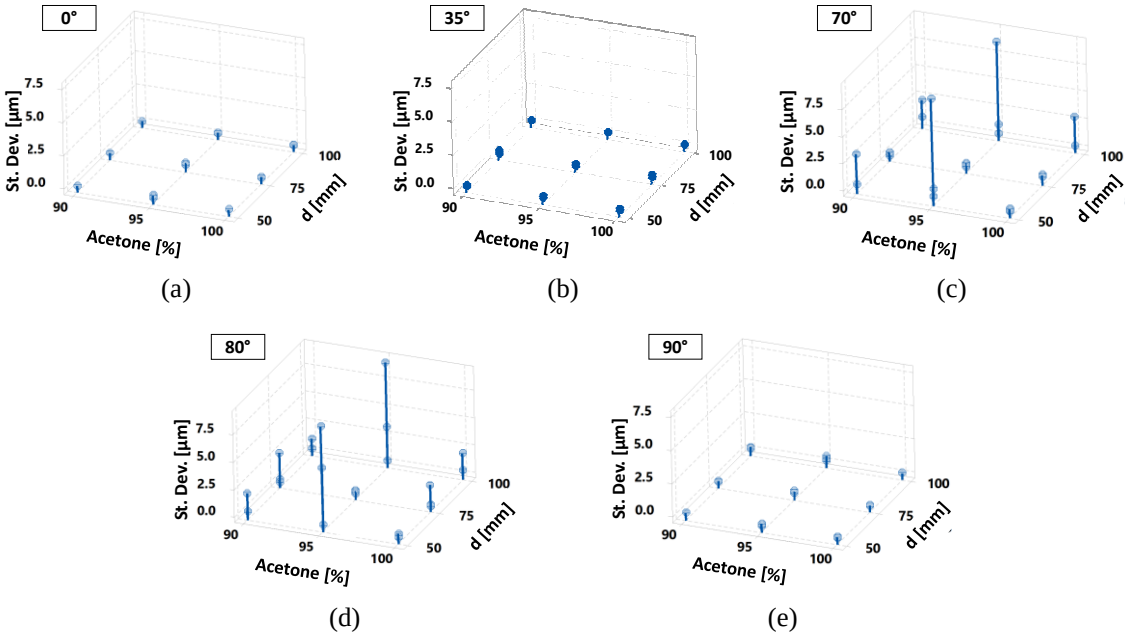

Fig. 9 Process characterization – Standard deviations of the roughness for each build angle (treatment time = 7.5 minutes).

To investigate the robustness of the process with a treatment time of 7.5 minutes, the experimental results were statistically analysed with ANOVA. Initially, the equal variance hypothesis [37] was evaluated using Levene's tests. The test showed that the results of the experiments at 0°, 35°and 90° are uniformly distributed, while 70° and 80° experiments have a non-uniform dispersion. Therefore, the first group of results (0°, 35° and 90°) was analysed by ANOVA, while the second group (70° and 80°) was analysed by direct comparison with the first one. In particular, the ANOVA results were compared in terms of the correlation coefficient of the regression model (R2) and the probability of the null hypothesis (p-value). The R2 coefficient estimates the percentage of variability between the results due to the process parameters. The p-value evaluates the probability that a parameter influences the process (if lower than

the threshold value of 0.05). Therefore, high R2 and low p-values indicate a high influence of the parameters. Conversely, low R2 and high p-values indicate independence of the treatment from the process parameters. Consequently:

- The ANOVA results on the first group (0°, 35°and 90°) are reported in Tab. 2. In particular, the analysis on the average surface finish (Tab. 2, Ra – Average) shows low R2 coefficients (0.156 to 0.452) and high p-values (over 0.137). Similar results are given by the analysis of the surface uniformity (Tab. 2, Ra – St. Deviation) with low R2 coefficients (0.166 to 0.481) and high p-values (over 0.164). Therefore, no parameter statistically influences the process in a 7.5 minute treatment for the build angles 0°, 35°and 90°.

- The direct comparison of the second group (70°and 80°) with the first one was carried out considering 7.5 minutes of treatment, 95% concentration and 75 mm of distance. In particular, within this set of parameters, the final roughness and its scattering are both low and uniform for all the build angles (Fig. 9). This is highlighted in Fig. 10 that shows that the build angle does not influence the final achievable roughness. Similar results can be obtained by choosing the set of parameters 7.5 minutes, 100% of concentration and 50 mm of distance, but the previous set is economically preferable as it requires less acetone.

Overall, the surface treatment with hot vapours of acetone considerably reduces the roughness of ABS surfaces made with FFF technology. In particular, the following comments can be drawn:

- The process is not uniform within the ranges of the tested process parameters, particularly when the build angle changes. This can be correlated with the scattering of the initial roughness which is not uniform and, particularly, greater for 70° and 80° (Fig. 4). Moreover, the distance of the sample from the acetone causes variability in the final roughness. This is more evident when the initial roughness is greater (i.e. 70° and 80° build angles) and the sample is closer to the acetone bath (distance of 50 mm) or the top of the chamber (distance of 100 mm). On the contrary, in the middle position (distance of 75 mm) the process is more stable. This can be explained by the presence of turbulence or gradients of acetone (temperature and concentrations) which may be more intense where the acetone evaporates or condenses (at the bottom and top of the chamber respectively).

- There are conditions in which the process is uniform, independent and therefore robust, to the process parameters. In particular, when the initial roughness is low to medium (i.e. 0°, 35°and 90° build angles), a treatment of 7.5 minutes is statically robust to the other parameters (concentration and distance). Furthermore, the treatment is independent of the initial roughness (i.e. all build angle) at 7.5 minutes of treatment, 95% concentration and 75 mm distance. In this case, the final average roughness of the surface is 0.11 ÷ 0.41 □m which corresponds to an average reduction of 98% of the initial roughness (Fig. 10).

- The presence of stable conditions of the process is in accordance with other papers that show how these treatments reach a steady-state [31, 34].

- The surface of a 3D object can be oriented along any build angle. Therefore, the identification of a robust process condition with respect to the initial surface roughness is of great importance for the treatment of fabricated parts.

Table 2: Results for correlation coefficients (R^2) and p-values in the ANOVA analysis.

	Ra - Average	**Ra - St. Deviation**

Build Angle	0°	35°	90°	0°	35°	90°
	R^2			R^2		
Regression	0.223	0.156	0.452	0.442	0.166	0.481
	p-values			p-values		
Factor						
distance [mm]	0.698	0.955	0.137	0.414	0.552	0.164
Acetone [%]	0.744	0.901	0.237	0.183	0.627	0.613
distance [mm]*distance [mm]	0.302	0.403	0.273	0.502	0.855	0.514
Acetone [%]*Acetone [%]	0.688	0.945	0.255	0.196	0.620	0.642
distance [mm]*Acetone [%]	0.565	0.944	0.155	0.468	0.529	0.179
distance [mm]*distance [mm]*Acetone [%]	0.328	0.397	0.244	0.559	0.818	0.543
distance [mm]*Acetone [%]*Acetone [%]	0.460	0.837	0.193	0.522	0.504	0.203

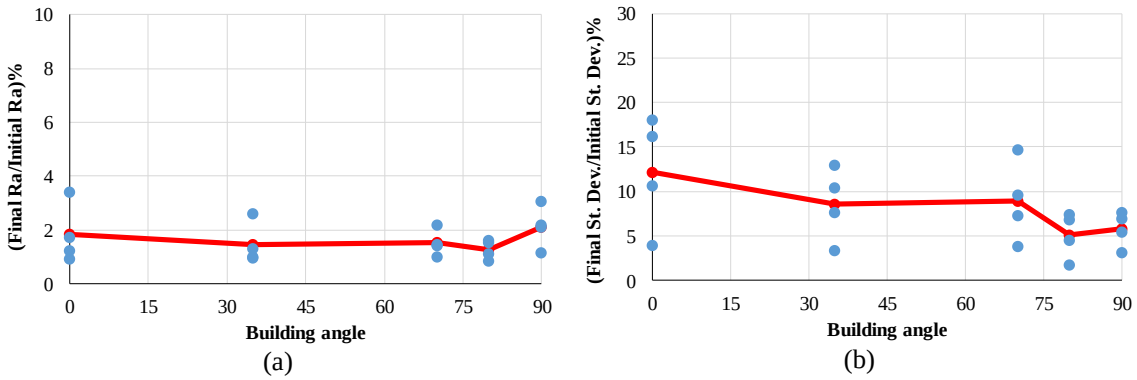

Fig. 10 Results with acetone concentration of 95%, a distance of 75 mm and an exposure time of 7.5 minutes in terms of (a) percentage roughness reduction and (b) percentage standard deviation reduction.

Sample dimensions

The chemical process uses acetone as a solvent to treat the surface. Therefore, the geometry of the samples was measured before and after the treatment to evaluate its impact on the final dimension of the samples. In particular, the samples were measured in height (Fig. 1) since it is orthogonal to the target surface and therefore it is representative of the global effect of the treatment.

According to the results on the robustness of the process described in the previous section, the sample treated with 95% of acetone concentration, 75 mm of distance and 7.5 minutes of treatment was considered. Fig. 11 reports the results in terms of variation in height (Δh). In particular, it shows that it is about 1% in the worst case which is negligible when compared to the precision of the FFF process (from 0.7 to 3.75 % [38]). Therefore, the process turns does not influence the global dimensional stability when the printing precision is also taken into account. Again, the results match those of other researchers who found no influence of the chemical smoothing process on the samples' dimensions [28]. To investigate whether this variation is due to material loss or not, the sample profiles were probed. The results (Fig. 12) show that the original profile of the surfaces is characterized by a periodic sequence of peaks and valleys. Moreover, considering the samples with the highest and lowest starting roughness (70° and 90° build angles), the distance of the peaks (as well as the valleys) from the average profile is about 0.08 mm and

0.03 mm respectively. The loss in height in the same samples is 0.09 mm and 0.01 mm and comparable with the previously mentioned height of peaks (as well as the depth of the valleys). Considering the fact that only the target surface is affected by the treatment (while the opposite one is not) and that peaks and valleys are almost not recognizable after the treatment, it can be concluded that the process does not significantly remove material but it changes the topography of the surface by filling the valleys of the profile with the material of the peaks which is softened by the hot acetone vapours (Fig. 12).

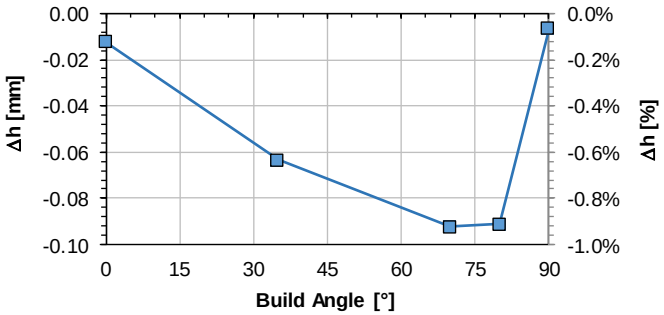

Fig. 11 Height variation of the samples treated with a 95% concentration of acetone at 75 mm of distance for 7.5 minutes.

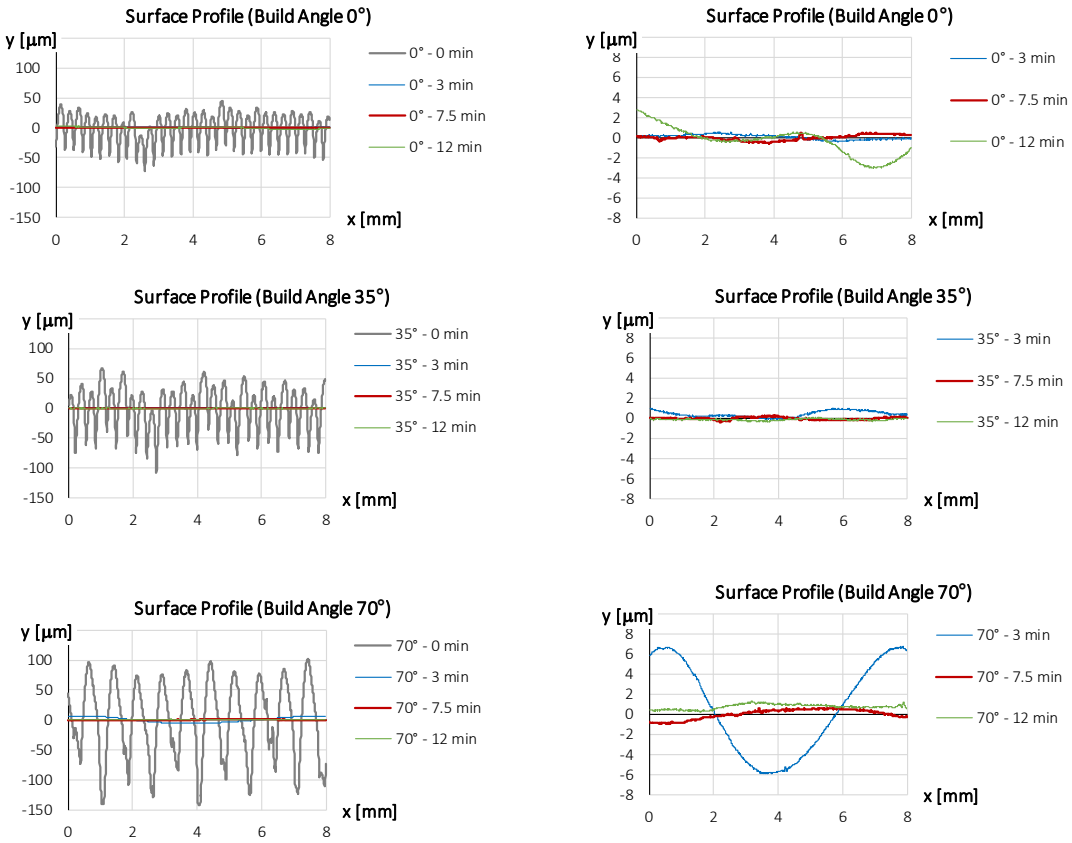

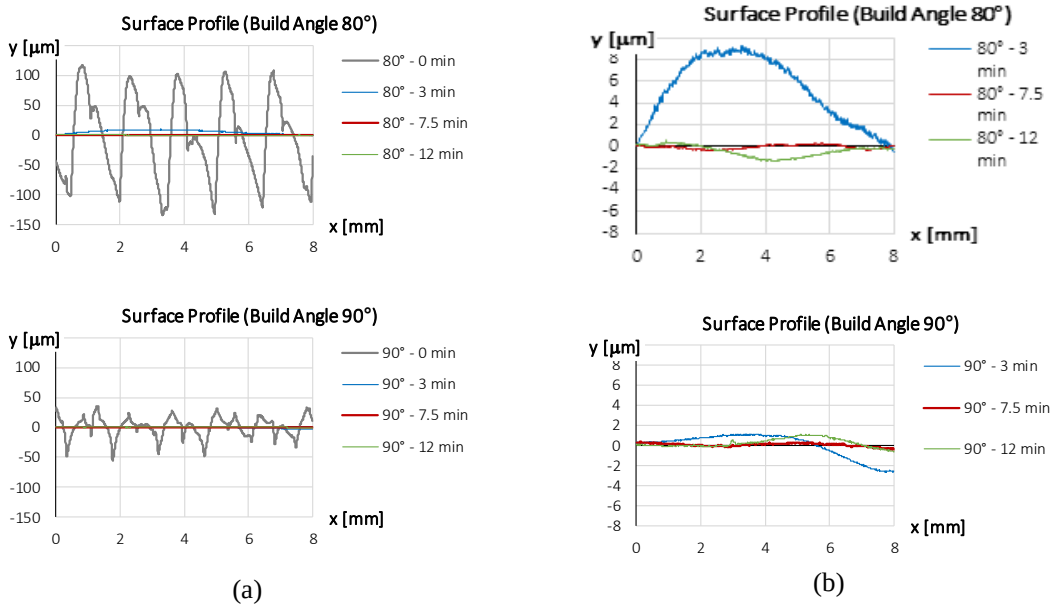

Fig. 12 Surface profiles at different treatment times (0 to 12min) and build angles using an acetone concentration of 95% and a distance of 75 mm. a) All data b) details.

6.2.4 Conclusions

FFF is one of the most widespread AM technologies. However, the surface roughness of the printed parts can represent a limit for the applicability of the technology, especially in applications as casting moulds, couplings or fluidics.

This work investigated a chemical post-process treatment based on the exposure to hot acetone vapours, able to smooth the surface of ABS samples fabricated through FFF. The investigation focused on different process parameters (acetone concentration, the distance between the treated surface and the acetone bath and the treatment time). Tests were conducted along 3 experimental campaigns and the results were statistically analysed. The first campaign identified the ranges of the process parameters that guarantee the feasibility of the process. The second campaign investigated the process within the feasibility ranges and identified the best treatment time, namely 7.5 minutes. A shorter or longer time would result in a poor or not uniform surface finish. The third campaign was performed using a fixed treatment time of 7.5 minutes and identified the range of the other parameters where the process is more stable. The final results show that, for low and intermediate values of starting roughness, the acetone concentration and the distance between the target surface and the acetone bath do not statistically influence the process, making it robust and repeatable. For higher starting roughness instead, the same robustness is achievable only for a limited number of combinations of the process parameters. By comparing the data for all the initial roughness, the third experimental campaign revealed the optimal parameter combinations are: 95%, 75mm and 7.5 minutes together with 100%, 50mm and 7.5 minutes (in terms of acetone concertation, the distance between target surface bath, treatment time respectively). These combinations can guarantee an average repeatable and uniform reduction of the roughness equal to 98%. In particular, the identified parameters are able to treat a 3D printed component having different surface orientations and roughness. The research showed that the treatment changes the topography of the surface without significantly removing material. Moreover, the effects on the overall dimensions of the part are negligible when compared to the precision of the FFF process. Local effects, as the dimensional variations of edges and corners (as visible in Fig. 5), will be investigated in future researches.

Finally, a comparison of the main surface finish processes is visible in Table 3. Compared to the previously investigated cold vapours [31] and dipping [35] treatments, the present process enhances the final finishing in a relatively low time. Moreover, the present hot vapours process, compared to the other methods present in the literature, reaches overall better results. About CNC [24] and barrel [25] finishing, it can easier treat the surfaces of the part, especially the ones located in undercuts, and without the risk of damaging it as a consequence of cutting forces.

Table 3: Comparison between finishing processes.

Process	**Samples**		**Outcomes**			**Ref.**
	Build Angles [°]	**UNI EN ISO 4288:1997 compliance**	**Treatment time**	**Final Ra [µm]**	**Process Robustness**	
Hot vapours	0 ÷ 90	Yes	7.5 min	0.11 ÷ 0.41	Tested	(present)
Cold vapours	0 ÷ 90	Yes	60 min	0.3 ÷ 0.96	Tested	[31]
Dipping	0 ÷ 90	Yes	1 min	0.09 ÷ 4.72	Tested	[35]
Hot vapours	0 ÷ 85	Partial	0.75 min	< 3	n.a.	[34]
Cold vapours	0	No	50 min	0.12	Tested	[33]
CNC	0	Partial	n.a.	2	Tested	[24]
Barrel	0 ÷ 30	No	120 min	3	Tested	[25]

Future activities will focus on the comparison between the different acetone treatments that were investigated by the authors: hot vapours (the present one), cold vapours [31] and direct dipping [35]. In particular, the optimal process conditions identified in the three researches will be used to tread 3D parts with more complex geometries including small features (as thin walls, narrow holes and groves together with edges and corners). As a result, more comprehensive knowledge of the acetone smoothing capabilities will be achieved. Moreover, the pros and cons of the analysed process will be discussed and highlighted providing guidelines for the post-processing of printed ABS parts.

6.3 Additively Manufactured Metals: biofilm formation and cellular attachment

6.3.1 Introduction

The demand for implantable devices is expected to rise consistently over the next two decades. Longer life expectancy and an increase in population will raise the volume of medical implantable devices, while the higher mobility demanded by younger patients may outliving such devices. This increase in demand is linked to the inherent complexity of the required implant which paired with the differences between patients makes difficult their standardization, originating the challenge to manufacture high quality and vastly different implantable devices to modern engineering [1,2]. Additive manufacturing (AM) techniques allow the production of highly customized implants meeting the final application specifications. Powder bed fusion processes offer the possibility of fabrication of complex and bespoke metal parts usually characterized by scarce surface finishing [3]. The surface quality of 3D printed parts is extremely important for the biological outcomes of both cells and bacteria colonization during in vivo conditions [4,5]. Infection of implantable devices is, still today, a great healthcare concern. Each year 1 to 5 % indwelling prosthetics became infected [6] where an attempt of salvaging the prosthetics through debridement of the infected site and long term antibiotic treatment are preferred over replacement, but literature shows that this procedure success rates range can be as low as 30 to 50% [7,8,9]. Antimicrobial coatings, photocatalysis antibodies and antibiotics can be applied to titanium surfaces to add an active mechanism of defence against bacteria colonization [10], but they are time consuming and complicate the part processing and supply chain. Polishing, etching and sandblasting finishing are commercially available treatments implementable with relatively easy application [11]. Their low cost, practicality and simplicity make them ideal candidates to treat additive manufactured parts. Biofilm formation, cell adhesion and differentiation had been shown to be heavily influenced by the aforementioned treatments, with substantial increases in osteogenesis and hindering of biofilm formation. This demonstrates a real possibility of tailoring the healing response of an implantable device with simple post processing techniques, but optimization of both cell adhesion and biofilm hindering remains a challenge while its impact on untreated additive manufacturing parts its mostly unknown. In this work, AM samples are produced by Selective Laser Melting (SLM) and the effect on bacterial and cells adhesion of post-processing techniques such as polishing, passivation and sandblasting followed by passivation are demonstrated.

6.3.2 Manufacturing and post processing

6.3.2.1 SLM samples fabrication and treatment

The Ti6Al4V (Ti64) atomized powder was fully characterized before processing as reported in [12]. Briefly, the morphology of the powder particles and particle size distribution have been analyzed to assess the homogeneity of the powder before the printing and the flow properties have been examined to verify the dynamic properties and consequently the flow ability under low stress conditions.

For this research, cubical samples of 10 mm3 were printed with a M2 Cusing SLM system (Concept Laser, Germany). An island pattern was chosen and the parameters for the fabrication were set as: 20 μm layer thickness, 75 μm hatch spacing, 1750 mm/s scanning speed and 150 W laser power.

As fabricated (AF) parts were then processed by polishing (PO), passivation (PA) and sandblasting followed by passivation (SP). All the post-processing techniques were applied to both the top and the side surfaces of the specimens and selected as commonly used in industrial standard operations to modify the

surface finish of as built parts. The polishing process was performed using a centrifugal disc finishing machine (Finishing Techniques Ltd., FINTEK) with multiple stages. The whole process was carried out firstly using a G240 grinding disk, then a G1200 and finally a G4000 grinding disk followed by a polishing cloth with aluminum oxide balls (6−10 mm) to deburr and polish the parts, with total process duration of 8 h. All parts were cleaned using compressed air, an ultrasonic bath, and isopropyl alcohol. Passivated samples were obtained by etching in NHO3 for 30 minutes. Sandblasting was performed in an Air Blast cabinet (CBI Equipment Ltd., UK) for 2 min with a speed of 100 m/s as previously reported [12]. Sandblasted samples were also passivated afterwards. Both the top surface and the side surface have been treated and analyzed.

6.3.3 Microstructural and biological characterization

6.3.3.1 Surface characterization of the samples

Micrographs of Ti-6Al-4V specimens were obtained using a XL30 FEG environmental SEM (Philips, UK) at 20 kV. Energy-dispersive X-ray spectroscopy (EDS) was used to evaluate the presence of contaminants due to the postprocessing. The surface roughness of the as built and treated parts was analyzed using a Bruker Contour GT-K 3D Optical Microscope at 20× magnification.

The chemical properties of the surfaces were characterized by measuring the contact angle (CA) using a Attension® Theta tensiometer (Biolin Scientific). A droplet of deionized water (5 μm) was pipetted onto the top and side surfaces of the samples. Three measurements of the roughness and contact angle were obtained on representative areas of the overall surface for three different sample variants.

6.3.3.2 Biological tests

Staphylococcus epidermidis (gram-positive) and Pseudomonas aeruginosa (gram-negative) were used to evaluate the adhesion of two bacterial strain on Ti64 surfaces as previously shown [12]. The crystal violet assay provided non spatially specific quantification of bacterial adhesion across the surfaces of the samples. Briefly, the samples were sterilized and 300μm of Lysogeny broth (LB - Sigma-Aldrich, UK), inoculated 1:100 of an overnight culture of Staphylococcus aureus and Pseudomonas aeruginosa was added. After incubation, the samples were removed from the media and then prepared for the SEM and for the crystal violet staining for bacteria quantification. The samples were then observed under Scanning Electron Microscopy (ZEISS, USA). Samples were then immersed in 1 mL of 1% (w/v) crystal violet (CV) solution for 10 min to bound the dye with the bacteria. Overnight cultures in LB were diluted to an optical density 600 nm. Three absorbance readings were obtained from each replicate using a FluoSTAR Optima plate reader (BMG Labtech).

Human osteosarcoma cells (SAOS-2) were cultured in a proliferation medium composed by McCoys media (Thermo Fisher Scientific) supplemented with 10% FCS (fetal calf serum) and 100 units/ml of pen/strep in a humidified incubator at 37°C and 5% CO2. The mineralization medium was prepared by adding 50 μg/ml ascorbic acid (Sigma- Aldrich, UK),10-8M dexamethasone (cell culture tested) (Sigma-Aldrich, UK) and 10 mM β-glycerophosphate (Sigma- Aldrich, UK) into the cell culture medium. Cultures are incubated for up to 21 days with media changes every 3 days initially then daily as the cells become more confluent.

6.3.4 Results

6.3.4.1 SEM and EDS results

Scanning electron micrographs of AF samples highlighted the presence of the island scanning as already reported [12].

Figure 1 reports the micrographs of the as fabricated and treated samples on both top and side surfaces.

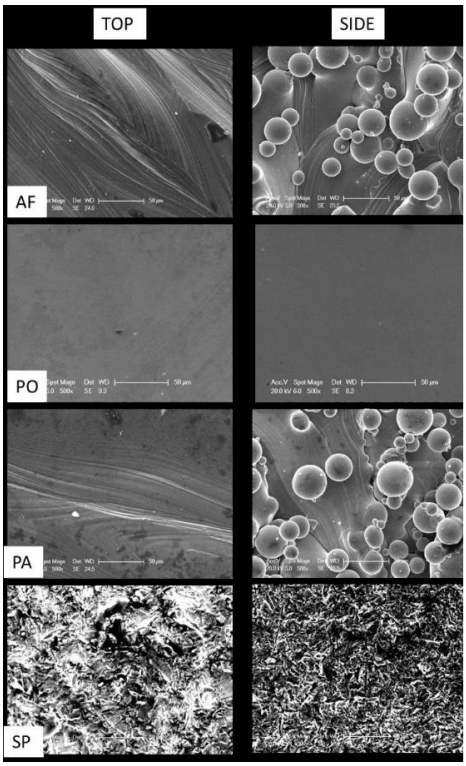

Fig. 1 SEM images of the top and side regions of as fabricated (AF), polished (PO), passivated (PA) and sandblasted and passivated (SP) samples. Scale bars are 50 μm

The laser track scans patterning are still visible on the top faces of the passivated samples while are not distinguishable anymore on the polished and sandblasted samples. No partially melted powder particles are observed after polishing while a greater number of partially melted particles are still visible on the passivated side face. The sandblasted samples report the presence of an irregular surface on both the top and the side surfaces as expected for the application of this treatment.

Table 1,2 and 3 show the chemical composition of the surfaces after the post processing treatments.

Table 1: Chemical composition of the Polished samples quantified from the EDS spectra

Polished					
Top			**Side**		
Element	**Weight %**	**Atomic %**	**Element**	**Weight %**	**Atomic %**
Al K	6.38	10.82	Al K	6.29	10.67
Ti K	89.62	85.59	Ti K	89.62	85.66
V K	4.00	3.59	V K	4.09	3.68

Table 2: Chemical composition of the Passivated samples quantified from the EDS

Passivation					
Top			**Side**		
Element	**Weight %**	**Atomic %**	**Element**	**Weight %**	**Atomic %**
Al K	6.22	10.56	Al K	5.45	9.30
Ti K	89.85	85.91	Ti K	89.94	86.52
V K	3.92	3.53	V K	4.62	4.18

Table 3: Chemical composition of the Sandblasted and Passivated samples quantified from the EDS spectra

Sandblasted and Passivated					
Top			Side		
Element	**Weight %**	**Atomic %**	**Element**	**Weight %**	**Atomic %**
O K	6.72		O K	11.12	22.07 ± 3.4
Al K	3.78		Al K	3.94	5.07
Si K	23.73		Si K	18.23	22.54
Ti K	63.11		Ti K	63.77	46.25
V K	2.66		V K	2.95	2.01

As expected, no contaminants are observed on polished and passivated samples while the sandblasting treatment leads to the presence of Si and oxygen. The Si presence is more evident on the top surface due to the possible presence of more adhesion sites for the contaminants while the oxidation level of the side surface is demonstrating a higher oxide layer resulting on the side face of the samples. In this case, the oxidation is not causing any presence of Fe on the treated samples.

6.3.4.2 Surface roughness results

The results of the roughness analysis on the surface of the samples are presented as mean and standard deviation of the mean (Fig. 2).

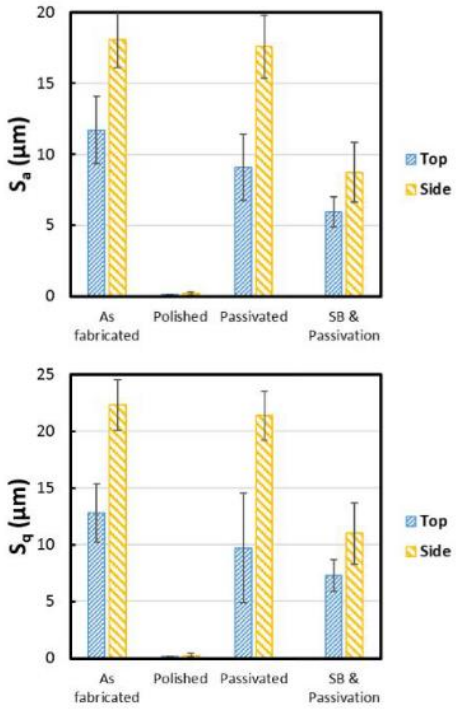

Fig. 2 Histograms of the Sa and Sq of the top and side faces of the as fabricated, polished, passivated and sandblasted and passivated samples

No significant difference between measurements of samples as fabricated and after passivation in relation to the Sa was highlighted. The passivated samples demonstrated a slightly lower surface roughness in relation to the as fabricated on the top surface while on the side surface the surface topography is similar. Notably, the SP samples demonstrated a reduction of the surface roughness in relation to the AF on both top and side surfaces probably depending on the final quantity of partially un-melted powder on each sample. On the other hand, the polished samples reported an extremely low surface roughness on both top and side faces, as expected. The high variance of the data observed for all the post-processing techniques, excepting the polishing, demonstrated the inner stability of these processes. Generally, the lower values of roughness calculated for the top and side faces of the SP samples are highly related to the morphology

of the surfaces after this treatment compared to the PA ones that is characterized with higher peaks similar to the AF surfaces.

6.3.4.3 Contact angle results

The contact angle of the top and side surfaces of the as fabricated and processed samples is reported in Figure 3 as mean and standard deviation of the mean.

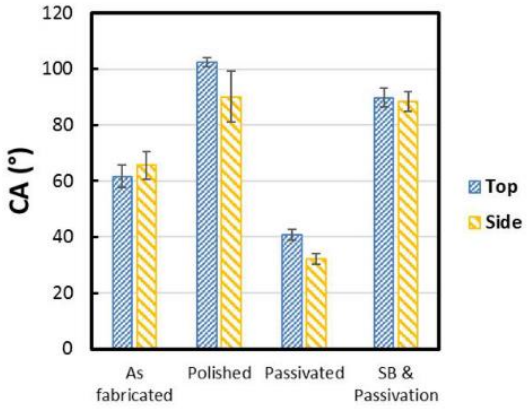

Fig. 3 Histograms of the CA of the top and side faces of the as fabricated, polished, passivated and sandblasted and passivated samples

Notably, the contact angle measurements on the top and side surfaces of the passivated samples are comparable and show substantially lower values in relation to the as fabricated parts. As expected, the polished samples report higher values of contact angles in relation to all the other samples especially in comparison with the passivated parts. It is interesting to highlight that the contact angle of the sandblasted samples is not lowered by the following passivation process.

Generally, the post processing treatments are increasing the contact angle of the surfaces enhancing the hydrophobicity of the faces with the exception of the passivated samples, as expected. The variability of the data observed for the side faces of the polished samples is probably due to the surface morphology of the as fabricated samples where an higher presence of spherical particles was reported.

6.3.4.4 Bacterial adhesion and staining

The S. epidermidis (Fig. 4) and P. aeruginosa (Fig. 5) images show the different adhesion of the bacterial strains on the as fabricated and treated samples.

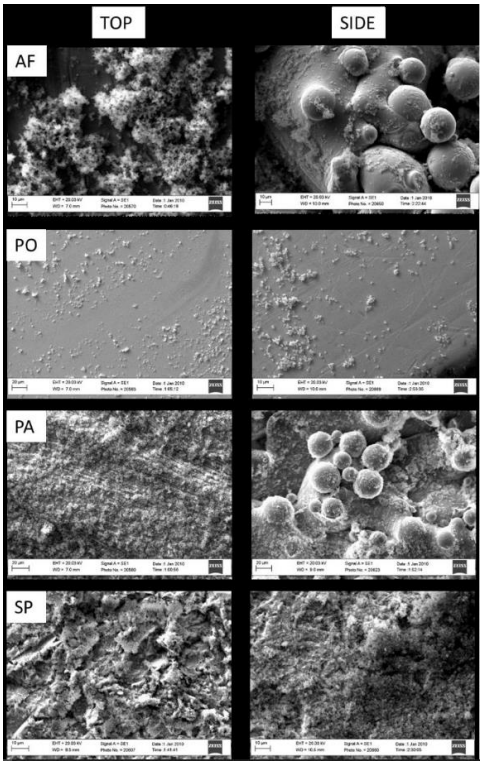

Fig. 4 SEM images of S. epidermidis biofilms formed on the top and side regions of AF, PO, PA and SP parts

As reported, the S. epidermidis is colonizing the as fabricated samples forming clumps especially on the top surface while on the side surfaces of both AF and PA samples, the bacteria are filling the gaps between the partially melted particles. On the top surface of the PA and SP samples instead, the S. epidermidis spreads onto the surface demonstrating that either the hydrophobicity or the topography of the surface can have a strong effect on the adhesion and proliferation of bacteria. On the other hand, despite the presence of fewer bacteria, it is notable a certain number of S. epidermidis on the top and side faces of the polished samples demonstrating that the treatment is effective in controlling the spreading of the bacteria preventing the formation of a biofilm in the short-term.

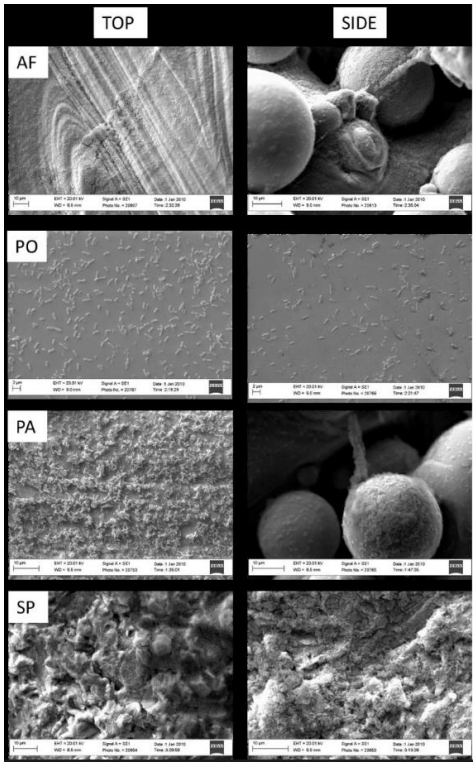

Fig. 5 SEM of P. aeruginosa biofilms formed on the top and side regions of AF, images PO, PA and SP parts

The P. aeruginosa spatial location on the AF top surface is similar to the SP ones due to the similar morphology of the two faces that allow the formation of a uniform layer of biofilm. The AF side surfaces show a similar trend of bacterial spreading compared to the SP side faces due to the presence of spherical particles that enable the communication of the gram negative bacteria from an unmelted powder to another. Notably, the spreading of bacteria on the top surface of PA samples seems disconnected and less homogeneous. As expected, on the polished surface no biofilm formation is visible unless the typical beam shape of the P. aeruginosa is still distinguishable due to the presence of few bacteria on the top and side surfaces.

The results of the Crystal violet staining are reported in Fig. 6.

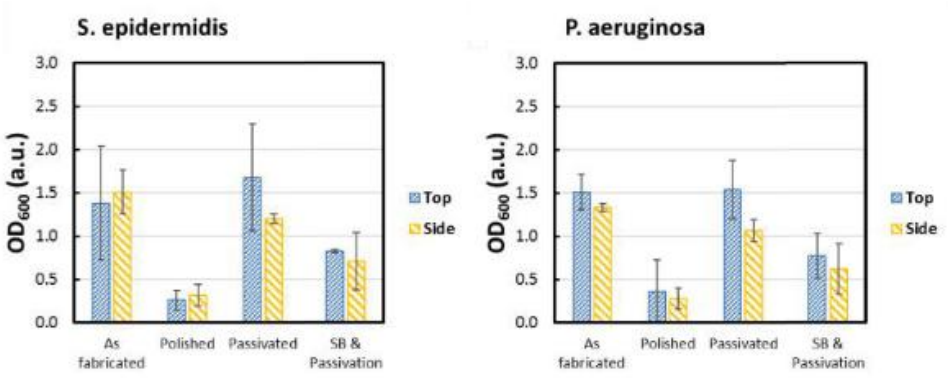

Fig. 6 CV absorption of S. epidermidis and P. aeruginosa bacteria on the AF, PO, PA and SP samples

The results show that the bacteria, both S. epidermidis and P. aeruginosa, are adhering on the different samples. In particular, the trends reported are confirming the impact of the surface roughness and contact angle of passivated samples on the bonding sites available for the bacteria to attach.

Notably, the staining shows that the bacteria are equally located on the top and side surface of the as fabricated and treated samples. Both strains quantifications show the lower level of colonization on PO samples while AF and PA report no significant difference on the bacteria presence. The quantitative results identify the PA samples as exposed as the AF ones to the bacterial colonization while the PO samples are the most effective against the microorganisms adhesion. The SP treatment is demonstrated to reduce the bacteria attachment in comparison with AF and PA samples.

6.3.4.5 Cells adhesion

The cells have been observed after 21 days of differentiation. The results are shown in Figure 7. As shown, the cells demonstrate to adhere on the top and side surfaces of all the analyzed samples. Notably, on the polished samples the cells are present in colonies with clusters caused by a limited mineralization of the cells. In this case, the differentiation of the cells has been compromised by the reduced adhesion due to the high hydrophobicity of the surface. The adhesion and mineralization of the osteoblasts seems to have the same trend on PA and SP samples. In particular, the chemical difference of the surfaces causes a more uniform spreading and thus the presence of scattered mineralization areas on the SP samples while the cells seem to be organized in agglomerations on the PA samples, especially on the side face. This trend is probably induced by the high roughness of the surface related to an enhanced hydrophilicity. Notably, the cells are spreading on the top and side surfaces of the AF samples with the formation of connected clumps on the side surface surrounding the spherical particles. In this case, the proliferation of the cells and the mineralization sites are less visible in comparison with the PA and SP treated samples.

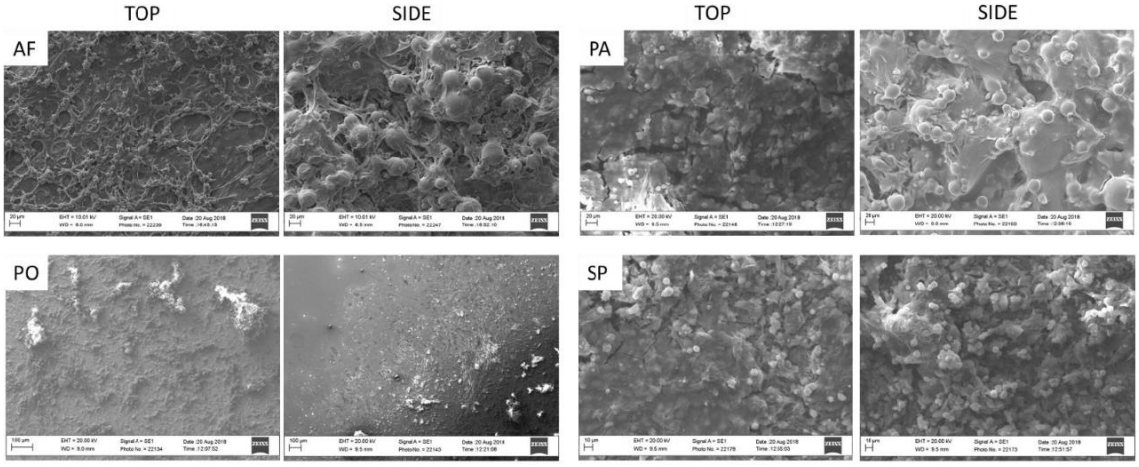

Fig. 7 SEM images of SAOS-2 cells on the top and side regions of AF, PA, PO and SP samples. Scale bars are 20 μm for the AF, PA; 10μm for SP and 100μm for PO samples. The white spots visible on the micrographs are indicating the presence of mineralized areas

6.3.5 Discussion

The powder bed fusion processes allow the production of complex samples with bespoke properties but usually result in inadequate surface quality that can prevent the osseointegration of the parts. Typically, these manufacturing technologies are followed by one or more post-processing of the samples to modify the surface finishing and meet the application requirements. This research demonstrated how specific treatments of the samples surfaces result in different outcomes in terms of chemical and topographical properties of the processed parts. The main effect of each treatment is related to the modification induced

on the scanning track of the top surface and on the partially melted particles characterizing the side face of SLM samples.

The roughness of the surfaces has been modified more effectively with polishing and sandblasting while the final roughness of the passivated samples is demonstrated very similar to the roughness values measured for the as fabricated parts. On the other hand, the hydrophobicity of the samples has been deeply increased by the polishing process while the treatment that generated hydrophilic surfaces in relation to the as fabricated ones was the etching followed by the passivation of the metal samples. Notably, the sandblasting followed by passivation decreased the roughness of the samples especially on the side surface, confirming the uniformity of the surface with the majority of partially melted particles reached by the sandblasting. Contrarily, the passivation of the surfaces obtained after sandblasting did not cause a strong effect on the contact angle of the treated surfaces that resulted more hydrophobic than the as fabricated ones. This effect demonstrated that, despite the passivated samples resulted more hydrophilic than the as fabricated ones, when the passivation is combined with sandblasting, the samples are still showing higher contact angle in relation to the passivated surfaces. As expected, the polished surfaces resulted more hydrophobic not only compared to the as fabricated but also to the PA and SP surfaces. The sandblasting and polishing treatment introduced an increased uniformity between the top and the side faces of the samples, reducing the impact of the metal particles on the side surface. Differently, the passivation process resulted in a visible difference between the roughness of the top and the side surfaces, as reported for the fabricated specimens, while this distinction is less evident on the contact angle analysis due to the chemical changes introduced on the samples. The chemistry and topography of the surfaces are reflected on the biological results. In particular, the used bacterial strains showed the formation of a spreading biofilm on all the samples except for the polished ones where the number of microorganism is undoubtedly lower. The presence of spherical particles on the side surfaces of as fabricated and passivated is causing the formation of uncontrollable adhesion sites that would make these samples difficult to treat in case of infection. Furthermore, the sandblasted samples, despite showing a uniform spread of both the gram positive and gram negative bacteria, exhibited a proper adhesion and mineralization of the cells. The passivated surfaces instead, showed the adhesion and partial mineralization of cells in agglomerated state as on the as fabricated samples. As expected, the polished surfaces prevented the attachment of a proper amount of cells that result isolated and unable to properly colonize the samples. The same behavior was shown by the bacteria on the polished surfaces that prevented the formation of a homogenous biofilm.

6.3.6 Conclusions

The work reports the effects on bacteria and cells adhesion of modifying the surface chemistry and topography of additively manufactured implants by the most used postprocessing processes: polishing, etching and sandblasting. The presented approach offers the opportunity to analyze the differences of antimicrobial and osseointegration properties of 3D printed implants for orthopedic applications. This work highlighted the necessity of minimizing the presence of particles on Ti6Al4V SLM specimens that could prevent a proper adhesion of the cells and promote the S. epidermidis and P. aeruginosa colonization of the surfaces. The polishing treatment of the parts, typically performed on parts before implantation, has been demonstrated effective for reducing the bacterial presence. Although, the presented preliminary study on cell adhesion and mineralization showed that surface polishing can impede the attachment of the cells.

The proposed methodology highlights the necessity of combining physical, chemical and mechanical approaches to properly promote osseointegration reducing the effect of a short-term bacterial infection.

Conclusions

In this thesis, additive manufacturing technologies were used for the study and realization of biomedical devices. The work focused on several topics like lattice structures, 3D models for the study of eye diseases or surgical training and surface finishing methods.

The main mechanical characterization tests of lattice samples made by LB-PBF were reviewed. The work pointed out that lattice structures are being increasingly investigated because of their properties, but also that the research is not yet at a sufficient level and there is a need for more deep knowledge. The main reason is undoubtedly the absence of a specific standard for the characterization of lattice structures. In this way, researchers choose test parameters that may be also very different from each other, making the comparison between the results difficult. Regarding compression, which is s the most studied characterization, many researchers rely on ISO 13314, standard for the compression test for porous and cellular metals. However, it is also true that the standard is not specific to AM lattice specimens, which have both very different properties from ordinary porous metal and a totally different manufacturing process. Moreover, this standard does not cover other tests such as tensile and flexural, where there are no guidelines and the choice of parameters is left to the researcher. Finally, pending the development of international standards, this research paper sought to group and identify the parameters most used by researchers for different characterizations of lattice structures, providing a guideline for anyone wishing to approach this topic. The work continues with a study on compression tests of lattice samples with radial cell distribution. The geometry and size of the unit cell are among the most investigated variables of lattice samples. However, the majority of the paper focuses on the orthogonal distribution, while a radial distribution is almost never taken into consideration. The study of different distributions, instead, can lead to a more complete understanding of the structures and a possible expansion of the obtainable properties, making lattice even more attractive.

The realization of a 3D model for the study of the development of black floaters within the vitreous body of the eye was then addresses. Usually floaters, when they become an excessive impediment to vision, are surgically removed by vitrectomy. The removed vitreous is then replaced by a substitute. However, the replacements, in addition to the risks related to surgery, are not yet long-term and other complications may arise. Research in recent years has focused on finding better performing substitutes but little has been done to discover the genesis of floaters. Hence, the decision to develop a model that could help discover the causes of its formation and development. The model is composed of two elements, a scaffold and a hydrogel. The scaffold requires some fundamental characteristics such as biocompatibility and transparency. Optimization of the printing process and post-processing resulted in a scaffold with the needed properties. A cartilage dECM-based hydrogel was developed for the fabrication, by material extrusion, of a self-sustaining 3D structure for ocular cells culture. The results showed that the hydrogel allows cell viability and proliferation for at least 7 days. It also has good printability, with the geometry maintained for the required time. However, this work is still in its preliminary state and many things are yet to be investigated. For example, the transparency of the hydrogel could be improved and the biocompatibility with the actual eye cells must be evaluated. Nevertheless, this work can provide a good basis for the further development and improvement of the model. For example, the dECM hydrogels are still relatively new and their full potential has not yet been exploited. With further tuning on the composition, even better results could be achieved mechanically, process-wise and biologically. Finally, this work focused on the development of a 3-D eye model for studying the genesis and development of floaters. Preliminary results are encouraging for further development of the model, which could provide information on how to prevent floaters formation and improve people's quality of life.

A model for emulating the behavior of mandibular bone during the drilling operation for dental implant installation was developed. The sample was designed to emulate both the compact outer layer and the

lamellar inner layer of the bone. The different densities and internal filling strategies studied allows for a wide range of achievable responses. Despite this, the model still has some issues to be resolved. For example, the peak forces, despite being close, are still greater than those of the bone. Likewise, the plateau forces also resulted to be slightly greater than the desired ones. In the second case a possible solution could be decreasing the density by lowering the infill percentage. In the first case, however, this solution cannot be applied because the shell must be full to emulate the cortical layer of the bone. A possible solution then could be a change in material. Possible future developments are therefore testing of new samples of both monomaterial and multimaterial. Also, the geometry of the samples should be modified to match the real shape of the jaw. Nevertheless, the system used allowed for the development of a model with customizable responses, which, once optimized, will be able to allow the surgeons to practice at will on different conditions.

Finally, surface finishing studies on biocompatible materials and surfaces are presented. The surface finish of biomedical devices such as earmolds or casts is very important because it affects the ergonomics and consequently the well-being of the patient. Two different finishing processes using acetone were investigated to reduce the roughness of ABS samples. The first consisted in directly dip the samples in the acetone bath, the second consisted in treating the samples with hot acetone vapors. Both methods provided good results with a roughness reduction greater than 95%. The vapor method, however, might be preferred because being slower it allows for more control, including the preservation of geometry. Then, the effects of different surface treatments on cell adhesion and bacterial proliferation were analyzed on specimens made by LB-PBF. The results show that it is necessary to combine physical, chemical, and mechanical approaches to promote osseointegration and reduce bacterial infection.

This thesis work involved working with various additive technologies for the fabrication of biomedical devices, each with its own characteristics and peculiarities. However, we could identify optimization of process parameters as a common goal of the various topics addressed. Optimization was done by trying to follow a rational and logical method, whether the goal was a compromise between printability and biocompatibility of the hydrogel or finding the best exposure time to the smoothing agent. As a result, the various problems that arise during the fabrication of biomedical devices were faced and the knowledge of the different additive technologies was deepened.

In conclusion, additive manufacturing includes various processes that are very different from each other but have many common points such as flexibility, freedom of design, and customization. By exploiting these properties, it is possible to make tailored objects, especially important in fields such as the biomedical one, where customization and specificity are a great added value.

References

Chapter 1

[1] Wohlers Associates, "What is additive manufacturing?", 2010, https://wohlersassociates.com/additive-manufacturing.html

[2] M. Anni, Tesi di Laurea Magistrale in Ingegneria Gestionale, "3D Printing: analisi della tecnologia e studio delle potenzialità del mercato", Politecnico di Milano, A.A. 2015-2016.

[3] T.D. Ngo, A. Kashani, G. Imbalzano, et al., "Additive manufacturing (3D printing): A review of materials, methods, applications and challenges", Composites Part B (2018), Vol. 143, pp. 172-196.

[4] M. Mobaraki, M. Ghaffari, A. Yazdanpana, et al. Bioinks and bioprinting: A focused review, Bioprinting 18 (2020) e00080. https://doi.org/10.1016/j.bprint.2020.e00080.

[5] W. Sun, B. Starly, A.C. Daly, et al. The bioprinting roadmap, Biofabrication 12 (2020) 022002. https://doi.org/10.1088/1758-5090/ab5158.

[6] https://learn.bios4you.infoproject.eu/mod/url/view.php?id=101

[7] S. L. Sing, W. Y. Yeong Laser powder bed fusion for metal additive manufacturing: perspectives on recent developments, Virtual and Physical Prototyping (2020), 15:3,359-370. DOI: 10.1080/17452759.2020.1779999.

[8] C.Y. Yap, C.K. Chua, Z.L.Dong, et al. Review of selective laser melting: Materials and applications, APPLIED PHYSICS REVIEWS 2 (2015), 041101. doi: 10.1063/1.4935926.

[9] https://learn.bios4you.infoproject.eu/mod/url/view.php?id=101.

[10] J.P. Oliveira, A.D. LaLonde, J.Mac, Processing parameters in laser powder bed fusion metal additive manufacturing, Materials and Design 193 (2020) 108762. https://doi.org/10.1016/j.matdes.2020.108762.

[11] D. Dev Singh, T. Mahender, A.R. Reddy, Powder bed fusion process: A brief review, Materials Today: Proceedings 46 (2021) 350–355. hhttps://doi.org/10.1016/j.matpr.2020.08.415.

[12] T. Wholers, T. Gornet, History of additive manufacturing, Wohlers Report 2016.

[13] F.P.W.Melchels, J. Feijen, D.W. Grijpma A review on stereolithography and its applications in biomedical engineering, Biomaterials 31(2010)6121e6130. doi:10.1016/j.biomaterials.2010.04.050.

[14] J.Z. Manapat, Q. Chen, P. Ye, et al. 3D Printing of Polymer Nanocomposites via Stereolithography, Macromol. Mater. Eng. (2017), 302, 1600553. DOI: 10.1002/mame.201600553.

[15] O. Santoliquido, P. Colombo, A. Ortona Additive Manufacturing of ceramic components by Digital Light Processing: A comparison between the "bottom-up" and the "top-down" approaches, Journal of the European Ceramic Society 39 (2019) 2140–2148, https://doi.org/10.1016/j.jeurceramsoc.2019.01.044.

[16] J. Huang, Q. Qin, J. Wang A Review of Stereolithography: Processes and Systems, Processes 2020, 8, 1138. doi:10.3390/pr8091138.

[17] R. Singh, H.K. Garg Fused Deposition Modeling – A State of Art Review and Future Applications, Reference Module in Materials Science and Materials Engineering. doi:10.1016/B978-0-12-803581-8.04037-6.

[18] G.D. Goh, Y.L. Yap, H.K.J. Tan, et al. Process–Structure–Properties in Polymer Additive Manufacturing via Material Extrusion: A Review, Critical Reviews in Solid State and Materials Sciences, 45:2 (2020), 113-133, DOI: 10.1080/10408436.2018.1549977.

[19] B. Banjanin, G. Vladić, M. Pál et al. PRODUCTION FACTORS INFLUENCING MECHANICAL AND PHYSICAL PROPERTIES OF FDM PRINTED EMBOSSING DIES, (2018). https://doi.org/10.24867/GRID-2018-p28.

[20] M. Ahmadifar, K.vBenfriha, M. Shirinbayan et al. Additive Manufacturing of Polymer-Based Composites Using Fused Filament Fabrication (FFF): a Review, Applied Composite Materials (2021) 28:1335–1380. https://doi.org/10.1007/s10443-021-09933-8.
[21] A. Dey, I.N. Roan Eagle, N. Yodo A Review on Filament Materials for Fused Filament Fabrication, Manuf. Mater. Process. 2021, 5, 69. https://doi.org/10.3390/jmmp5030069.
[22] S. Ramesh, O.L.A. Harrysson, P.K. Rao, et al. Extrusion bioprinting: Recent progress, challenges, and future opportunities, Bioprinting 21 (2021) e00116. https://doi.org/10.1016/j.bprint.2020.e00116.
[23] S. Boularaoui, G. Al Hussein, K.A. Khan et al. An overview of extrusion-based bioprinting with a focus on induced shear stress and its effect on cell viability, Bioprinting 20 (2020) e00093. https://doi.org/10.1016/j.bprint.2020.e00093.
[24] Z. Fu, S. Naghieh, C. Xu, et al. Printability in extrusion bioprinting, Biofabrication 13 (2021) 033001. https://doi.org/10.1088/1758-5090/abe7ab.
[25] A.C. Daly, M.E. Prendergast, A.J. Hughes, et al. Bioprinting for the Biologist, Cell 184 (2021). https://doi.org/10.1016/j.cell.2020.12.002.
[26] L.E. Murr, E. Martinez, J. Hernandez et al. Microstructures and Properties of 17-4 PH Stainless Steel Fabricated by Selective Laser Melting, J. Mater. Res. Technol. (2012), 1(3):167-177.
[27] Z. Sangari Motlagh, B. Tolaminejad, A. Momeni Prediction of Hot Deformation Flow Curves of 1.4542 Stainless Steel, Metals and Materials International (2021) 27:2512–2529. https://doi.org/10.1007/s12540-020-00627-7.
[28] S. Sabooni, A. Chabok, S.C. Feng, et al. Laser powder bed fusion of 17–4 PH stainless steel: A comparative study on the effect of heat treatment on the microstructure evolution and mechanical properties, Additive Manufacturing 46 (2021) 102176. https://doi.org/10.1016/j.addma.2021.102176.
[29] M. Mahmoudi, A. Elwany, Aref Yadollahi, et al. Mechanical properties and microstructural characterization of selective laser melted 17-4 PH stainless steel, Rapid Prototyping Journal 23/2 (2017) 280–294. DOI 10.1108/RPJ-12-2015-0192.
[30] T.H. Hsu, P.C. Huang, M.Y. Lee, et al. Effect of processing parameters on the fractions of martensite in 17-4 PH stainless steel fabricated by selective laser melting, Journal of Alloys and Compounds 859 (2021) 157758. https://doi.org/10.1016/j.jallcom.2020.157758.
[31] P. Ponnusamy, B. Sharma, S.H. Masood, et al, A study of tensile behavior of SLM processed 17-4 PH stainless steel, Materials Today: Proceedings 45 (2021) 4531–4534. https://doi.org/10.1016/j.matpr.2020.12.1104.
[32] S. Vunnam, A. Saboo, C. Sudbrack, et al. Effect of powder chemical composition on the as-built microstructure of 17-4 PH stainless steel processed by selective laser melting, Additive Manufacturing 30 (2019) 100876. https://doi.org/10.1016/j.addma.2019.100876.
[33] https://it.3dsystems.com/sites/default/files/2017-06/3D-Systems_17-4_PH_%28B%29_DMP_DATASHEET_US_A4_2017.06.21_WEB.pdf
[34] L. Tonelli, I. Boromei, E. Liverani, et al. Microstructural evolution induced by heat treatment in the Co28Cr6Mo alloy produced by Selective Laser Melting, Metall. Ital., 113(2), pp. 22–3.
[35] F. Cantaboni, P.S. Ginestra, M. Tocci, et al. Compressive behavior of Co-Cr-Mo radially graded porous structures under as-built and heat-treated conditions, Frattura ed Integrità Strutturale, 62 (2022) 490-504. DOI: 10.3221/IGF-ESIS.62.33.
[36] J. Chen, Y. Yang, S. Wu, et al. Selective laser melting dental CoCr alloy: microstructure, mechanical properties and corrosion resistance, Rapid Prototyping Journal 27/8 (2021) 1457–1466 . DOI 10.1108/RPJ-09-2019-0252.
[37] B. Konieczny, A. Szczesio-Wlodarczyk, J. Sokolowski, et al. Challenges of Co–Cr Alloy Additive Manufacturing Methods in Dentistry—The Current State of Knowledge (Systematic Review), Materials 2020, 13, 3524; doi:10.3390/ma13163524.
[38] S. Acharya, R. Soni, S.Suwas, et al. Additive manufacturing of Co–Cr alloys for biomedical applications: A concise review, Journal of Materials Research, (2021) Vol. 36, Issue 19. DOI:10.1557/s43578-021-00244-z.
[39] C. Yan, L. Hao, A. Hussein, et al. Advanced lightweight 316L stainless steel cellular lattice structures fabricated via selective laser melting, Materials and Design, 2014, Vol. 55, pp. 533-541.

[40] L. Yuan, S. Ding, Wen C Additive manufacturing technology for porous metal implant applications and triple minimal surface structures: a review. Bioactive Mater (2019) 4:56–70. https://doi.org/10.1016/j.bioactmat.2018.12.003.
[41] A. Nazir, K.M. Abate, A. Kumar, et al. A state-of-the-art review on types, design, optimization, and additive manufacturing of cellular structures. Int J Adv Manuf Technol (2019) 104:3489–3510. https://doi.org/10.1007/s00170-019-04085-3.
[42] I. Echeta, X. Feng, B. Dutton, et al. Review of defects in lattice structures manufactured by powder bed fusion, The International Journal of Advanced Manufacturing Technology (2020) 106:2649–2668. https://doi.org/10.1007/s00170-019-04753-4.
[43] F. Marbury Characterization of SLM Printed 316L Stainless Steel and Investigation of Micro Lattice Geometry, 2017.
[44] M. Leary, M. Mazur, H. Williams, et al. Inconel 625 lattice structures manufactured by selective laser melting (SLM): Mechanical properties, deformation and failure modes, Materials and design, (2018), Vol. 157, pp. 179-199.
[45] B.B. Babamiri, H. Askari, K. Hazeli Deformation mechanisms and post-yielding behavior of additively manufactured lattice structures. Mater Des (2020), 188:108443. https://doi.org/10.1016/j.matdes.2019.108443.
[46] L. Sartore, slides from the course "Polimeri industriali e riciclo", University of Brescia, A.A 2020.
[47] G. Kakabadze ANISOTROPIC BEHAVIOUR ANALYSIS OF 3D PRINTED STRUCTURES, 2020.
[48] T. Swetham, K.M. Mohan Reddy, A. Huggi, et al. Critical Review on of 3D Printing Materials and Details of Materials used in FDM, IJSRSET (2017), Vol 3, Issue 2.
[49] P. Zur, A. Kolodzieij, A. Baier, et al. Optimization if ABS 3D-Printing Method and Parameters, European Journal of Engineering Science and Technology (2020), 3 (1):44-51.
[50] K. Deshmukh, M. Basheer Ahamed, R.R. Deshmukh, et. al. Biopolymer Composites With High Dielectric Performance: Interface Engineering, Biopolymer Composites in Electronics (2017). http://dx.doi.org/10.1016/B978-0-12-809261-3.00003-6.
[51] E.H. Tümer, H.Y. Erbil Extrusion-Based 3D Printing Applications of PLA Composites: A Review, Coatings (2021), 11, 390. https://doi.org/10.3390/coatings11040390.
[52] H.O. Agu1, A. Hameed, G.J. Appleby-Thomas The Dynamic Response of Dense 3 Dimensionally Printed Polylactic Acid, Journal of Dynamic Behavior of Materials (2019). https://doi.org/10.1007/s40870-019-00198-8.
[53] V. DeStefano, S. Khan, A. Tabada Applications of PLA in modern medicine, Engineered Regeneration 1 (2020) 76–87. https://doi.org/10.1016/j.engreg.2020.08.002.
[54] A. Kausar A review of filled and pristine polycarbonate blends and their applications, Journal of Plastic Film & Sheeting (2018), Vol. 34(1) 60–97. DOI: 10.1177/8756087917691088.
[55] K Takeuchi 5.16 Polycarbonates, Polymer Science: A Comprehensive Reference (2012), Volume 5. doi:10.1016/B978-0-444-53349-4.00148-5.
[56] A.B. Balaji, H. Pakalapati, M. Khalid, et al. Natural and synthetic biocompatible and biodegradable polymers, Biodegradable and Biocompatible Polymer Composites (2018). http://dx.doi.org/10.1016/B978-0-08-100970-3.00001-8.
[57] S.A. Begum, A.V. Rane, K. Kanny Applications of compatibilized polymer blends in automobile industry, Compatibilization of Polymer Blends, chapter 20 (2020). https://doi.org/10.1016/B978-0-12-816006-0.00020-7.
[58] L.J. Tan, W. Zhu, K. Zhou Recent Progress on Polymer Materials for Additive Manufacturing, Adv. Funct. Mater. (2020), 30, 2003062. DOI: 10.1002/adfm.202003062.
[59] A. Andreu, P.C. Su, J.H. Kim, et al. 4D printing materials for vat photopolymerization, Additive Manufacturing 44 (2021) 102024. https://doi.org/10.1016/j.addma.2021.102024.
[60] Y. Li, L. Zheng, S. Peng, et al. Structure-Property Relationship of Stereolithography Resins Containing Polysiloxane Core-Shell Nanoparticles, ACS Appl. Mater. Interfaces (2020). DOI: 10.1021/acsami.9b20417.
[61] S. Van Vlierberge, G.J. Graulus, S. Keshari Samal, et al. Porous hydrogel biomedical foam scaffolds for tissue repair, (2014). DOI : 10.1533/9780857097033.2.335.
[62] F. Alihosseini Plant-based compounds for antimicrobial textiles, Antimicrobial Textiles (2016). http://dx.doi.org/10.1016/B978-0-08-100576-7.00010-9.
[63] M. Mohiti-Asli, E.G. Loboa Nanofibrous smart bandages for wound care, Wound Healing Biomaterials (2016) - Volume 2. http://dx.doi.org/10.1016/B978-1-78242-456-7.00023-4.

[64] K.Y. Lee, D.J. Mooney Alginate: properties and biomedical applications, Prog Polym Sci. (2012); 37(1): 106–126. doi:10.1016/j.progpolymsci.2011.06.003.
[65] Y. Zhang, W. Yu, G. Lv, et al. The Artificial Organ: Cell Encapsulation, Enabling Technologies (2011).
[66] L.A. Loureiro dos Santos Natural Polymeric Biomaterials: Processing and Properties, Reference Module in Materials Science and Materials Engineering (2017). doi:10.1016/B978-0-12-803581-8.02253-0.
[67] T. Hoshiba Cultured cell-derived decellularized extracellular matrix: future applications and problems -A mini review, Current Opinion in Biomedical Engineering, https://doi.org/10.1016/j.cobme.2020.100256.
[68] D.E. Heath A Review of Decellularized Extracellular Matrix Biomaterials for Regenerative Engineering Applications, Regenerative Engineering and Translational Medicine (2019) 5:155–166. https://doi.org/10.1007/s40883-018-0080-0.
[69] Y.S. Kim, M. Majid, A.J. Melchiorri, et al. Applications of decellularized extracellular matrix in bone and cartilage tissue engineering, Bioengineering & Translational Medicine (2019);4:83–95. DOI: 10.1002/btm2.10110.
[70] B.S. Kim, S. Das, J. Jang, et al. Decellularized Extracellular Matrix-based Bioinks for Engineering Tissue- and Organ-specific Microenvironments, Chem. Rev. (2020), 120, 10608−10661. https://dx.doi.org/10.1021/acs.chemrev.9b00808.
[71] B.S. Kim, H. Kim, G. Gao, et al. Decellularized extracellular matrix: a step towards the next generation source for bioink manufacturing, Biofabrication 9 (2017) 034104. https://doi.org/10.1088/1758-5090/aa7e98.
[72] B. Sun, Q. Ma, X. Wang, et al. Additive manufacturing in medical applications: A brief review, IOP Conf. Series: Materials Science and Engineering 1078 (2021) 012007. doi:10.1088/1757-899X/1078/1/012007.
[73] M. Salmi Additive Manufacturing Processes in Medical Applications, Materials (2021), 14, 191. https://doi.org/10.3390/ma14010191.
[74] A.J. Sheoran, H.Kumar, P.K. Arora et al. Bio-Medical applications of Additive Manufacturing: A Review, Procedia Manufacturing 51 (2020) 663–670. 10.1016/j.promfg.2020.10.093.
[75] D. Wang, Y. Wang, J. Wang, et al. Design and Fabrication of a Precision Template for Spine Surgery Using Selective Laser Melting (SLM), Materials (2016), 9, 608. doi:10.3390/ma9070608 www.mdpi.com/journal/materials.
[76] S. Arabnejad, B. Johnston, M. Tanzer, et al. Fully Porous 3D Printed Titanium Femoral Stem to Reduce Stress-Shielding Following Total Hip Arthroplasty, JOURNAL OF ORTHOPAEDIC RESEARCH (2017). DOI 10.1002/jor.23445.
[77] S.Y. Yoo, S.K. Kim, S.J. Heo, et al. Dimensional Accuracy of Dental Models for Three-Unit Prostheses Fabricated by Various 3D Printing Technologies, Materials (2021), 14, 1550. https://doi.org/10.3390/ma14061550.
[78] P. Xie, Z. Hu, X. Zhang, et al. Application of 3-Dimensional Printing Technology to Construct an Eye Model for Fundus Viewing Study, PLoS ONE (2014) 9(11): e109373. doi:10.1371/journal.pone.0109373.
[79] A. Isaacson, S. Swioklo, C.J. Connon 3D bioprinting of a corneal stroma equivalent, Experimental Eye Research 173 (2018) 188–193. https://doi.org/10.1016/j.exer.2018.05.010.
[80] M.A. Heinrich, R.Bansal, T. Lammers, et al. 3D-Bioprinted Mini-Brain: A Glioblastoma Model to Study Cellular Interactions and Therapeutics, Adv. Mater. (2019), 31, 1806590. DOI: 10.1002/adma.201806590.

Chapter 2

Section 2.1

[1] M.K. Thompson, G. Moroni, T. Vaneker et al, Design for Additive Manufacturing: Trends, opportunities, considerations, and constraints, CIRP Annals - Manufacturing Technology 65 (2016) 737–760. http://dx.doi.org/10.1016/j.cirp.2016.05.004.
[2] T. DebRoy, H.L. Wei, J.S. Zuback, et al., Additive manufacturing of metallic components – Process, structure and properties, Progress in Materials Science 92 (2018) 112–224.

[3] M. Yakout, M.A. Elbestawi and S.C. Veldhuis, A Review of Metal Additive Manufacturing Technologies, Solid State Phenomena Vol. 278 (2018) 1-14.
[4] Wohlers Associates, What is additive manufacturing?. https://wohlersassociates.com/additive-manufacturing.html , 2010.
[5] V. Bhavar, P. Kattire, V. Patil et al., A review on powder bed fusion technology of metal additive manufacturing, 4th International conference and exhibition on Additive Manufacturing Technologies-AM-2014 (2014).
[6] Soiel International, Produzione additiva: a che punto siamo. https://www.soiel.it/news/dettaglio/produzione-additiva-a-che-punto-siamo/ , 2017.
[7] J. Čapek, M Machová, M Fousová et al, Highly porous, low elasticmodulus 316L stainless steel scaffold prepared by selective laser melting, Materials Science and Engineering C 69 (2016) 631–639. http://dx.doi.org/10.1016/j.msec.2016.07.027.
[8] R.A. Rahman Rashid, J. Mallavarapu1, S. Palanisamy et al, A comparative study of flexural properties of additively manufactured aluminium lattice structures, Materials Today: Proceedings 4 (2017) 8597–8604.
[9] P.S. Ginestra, E. Ceretti, D. Lobo et al, Post processing of 3D printed metal scaffolds: A preliminary study of antimicrobial efficiency, Procedia Manufacturing 47 (2020) 1106-1112.
[10] T. J. Horn, O. L. A. Harrysson, Overview of current additive manufacturing technologies and selected applications, Science Progress (2012), 95(3), 255-282. doi: 10.3184/003685012X13420984463047.
[11] B.K. Nagesha, V. Dhinakaran, M. Varsha Shree, Review on characterization and impacts of the lattice structure in additive manufacturing, Materials Today: Proceedings 21 (2020) 916–919. https://doi.org/10.1016/j.matpr.2019.08.158.
[12] C. Yan, L. Hao, A. Hussein et al, Advanced lightweight 316L stainless steel cellular lattice structures fabricated via selective laser melting, Materials and Design 55 (2014) 533–541. http://dx.doi.org/10.1016/j.matdes.2013.10.027.
[13] X. Cao, S. Duan, J. Liang et al, Mechanical properties of an improved 3D-printed rhombic dodecahedron stainless steel lattice structure of variable cross section, International Journal of Mechanical Sciences 145 (2018) 53–63. https://doi.org/10.1016/j.ijmecsci.2018.07.006.
[14] H. Alsalla, L. Hao, C. Smith, Fracture toughness and tensile strength of 316L stainless steel cellular lattice structures manufactured using the selective laser melting technique, Materials Science &Engineering A 669 (2016) 1–6. http://dx.doi.org/10.1016/j.msea.2016.05.075.
[15] R.A.W. Mines, S. Tsopanos, Y. Shen et al, Drop weight impact behaviour of sandwich panels with metallic micro lattice cores, International Journal of Impact Engineering 60 (2013) 120e132. http://dx.doi.org/10.1016/j.ijimpeng.2013.04.007.
[16] N. Chantarapanich, A. Laohaprapanon, S. Wisutmethangoon et al, Fabrication of three-dimensional honeycomb structure for aeronautical applications using selective laser melting: a preliminary investigation, Rapid Prototyping Journal 20/6 (2014) 551–558, DOI 10.1108/RPJ-08-2011-0086.
[17] M. Bici, S. Brischetto, F. Campana et al, Development of a multifunctional panel for aerospace use through SLM additive manufacturing, Procedia CIRP 67 (2018) 215 – 220. doi: 10.1016/j.procir.2017.12.202.
[18] D. L. Miller, G. Kersten, W.A. Frost, SYSTEMS AND METHODS For PROTECTING A FLIGHT RECORDER, US 8,723,057 B2, 13 May 2014.
[19] A. Büşra and R.Y Ali, Optimum design of automobile components using lattice structures for additive manufacturing, Materials Testing 62 (2020) 6 633-639.
[20] A. Fiorentino, G. Zarattini, U. Pazzaglia et al, Hip prosthesis design. Market analysis, new perspectives and an innovative solution, Procedia CIRP 5 (2013) 310-314.

[21] P.S. Ginestra, E. Ceretti, A. Fiorentino, Potential of modeling and simulations of bioengineered devices: Endoprostheses, prostheses and orthoses, Proceedings of the Institution of Mechanical Engineers, Part H: Journal of Engineering in Medicine (2016) 230(7), pp. 607-638.
[22] 3D Printing Media Network, Joseph Spine surgeons implant world's first 3D printed Aries L Titanium Spinal Implant. https://www.3dprintingmedia.network/joseph-spine-surgeons-implant-worlds-first-3d-printed-aries-l-titanium-spinal-implant/ , 2019.
[23] S. Limmahakhun, A. Oloyede, N. Chantarapanich et al, Alternative designs of load−sharing cobalt chromium graded femoral stems, Materials Today Communications 12 (2017) 1–10. http://dx.doi.org/10.1016/j.mtcomm.2017.05.002.
[24] K. B. Hazlehurst, C. J. Wang, M. Stanford, An investigation into the flexural characteristics of functionally graded cobalt chrome femoral stems manufactured using selective laser melting, Materials and Design (2014). doi: http://dx.doi.org/10.1016/j.matdes.2014.03.068.
[25] F. A. España, V. K. Balla, S. Bose et al, Design and fabrication of CoCrMo alloy based novel structures for load bearing implants using laser engineered net shaping, Materials Science and Engineering C 30 (2010) 50–57. doi:10.1016/j.msec.2009.08.006.
[26] H.V. Wang, S.R. Johnston, D.W. Rosen, Design of a graded cellular structure for an acetabular hip replacement component, Proceedings of the The Seventeenth Solid Freeform Fabrication Symposium (2006).
[27] S. Arabnejad, B. Johnston, M. Tanzer et al, Fully Porous 3D Printed Titanium Femoral Stem to Reduce Stress-Shielding Following Total Hip Arthroplasty, JOURNAL OF ORTHOPAEDIC RESEARCH (2017). DOI 10.1002/jor.23445.
[28] L.E. Murr, K.N. Amato, S.J. Li et al, Microstructure and mechanical properties of open-cellular biomaterials prototypes for total knee replacement implants fabricated by electron beam melting, Journal of the Mechanical Behavior of Biomedical Materials 4 (2011) 1396–1411. doi:10.1016/j.jmbbm.2011.05.010.
[29] R. Wauthle, J. van der Stok, S. Amin Yavari et al, Additively manufactured porous tantalum implants, Acta Biomaterialia (2014), doi: http://dx.doi.org/10.1016/j.actbio.2014.12.003.
[30] S. L. Sing, Y. Miao, F. E. Wiria et al, Manufacturability and mechanical testing considerations of metallic scaffolds fabricated using selective laser melting: a review, Biomedical Science and Engineering (2016), doi:10.4081/bse.2016.11.
[31] A. Nazir, K. M. Abate, A. Kumar et al, A state-of-the-art review on types, design, optimization, and additive manufacturing of cellular structures, The International Journal of Advanced Manufacturing Technology (2019) 104:3489–3510. https://doi.org/10.1007/s00170-019-04085-3.
[32] W. Tao, M.C. Leu, D esign of lattice structures for additive manufacturing. DOI: 10.1109/ISFA.2016.7790182
[33] G. De Pasquale, M. Montemurro, A. Catapano et al, Cellular structures from additive processes: design, homogenization and experimental validation, Procedia Structural Integrity 8 (2018) 75-82. 10.1016/j.prostr.2017.12.009.
[34] F. Leonardi, S. Graziosi, R. Casati et al, Additive manufacturing of heterogeneous lattice structures: an experimental exploration, International Conference on Engineering Design, ICED19 (2019), DOI:10.1017/dsi.2019.71.
[35] K. Refai, M. Montemurro, C. Brugger et al, Determination of the effective elastic properties of titanium lattice structures, Mechanics of Advanced Materials and Structures (2019). DOI: 10.1080/15376494.2018.1536816.
[36] M. Mazur, M. Leary, M. McMillan et al, Mechanical properties of Ti6Al4Vand AlSi12Mg lattice structures manufactured by Selective Laser Melting (SLM), Laser Additive Manufacturing (2017). http://dx.doi.org/10.1016/B978-0-08-100433-3.00005-1.

[37] D. Qi, H. Yu, M. Liu et al, Mechanical behaviors of SLM additive manufactured octet-truss and truncated-octahedron lattice structures with uniform and taper beams, International Journal of Mechanical Sciences 163 (2019) 105091. https://doi.org/10.1016/j.ijmecsci.2019.10509.
[38] C. Yan, L. Hao, A. Hussein et al, Evaluations of cellular lattice structures manufactured using selective laser melting, International Journal of Machine Tools & Manufacture 62 (2012) 32–38. http://dx.doi.org/10.1016/j.ijmachtools.2012.06.002.
[39] L. Yuan, S. Ding, C. Wen, Additive manufacturing technology for porous metal implant applications and triple minimal surface structures: A review, Bioactive Materials 4 (2019) 56–70. https://doi.org/10.1016/j.bioactmat.2018.12.003.
[40] D. Mahmoud, M. A. Elbestawi, Selective laser melting of porosity graded lattice structures for bone implants, The International Journal of Advanced Manufacturing Technology (2019) 100:2915–2927. https://doi.org/10.1007/s00170-018-2886-9.
[41] E. Yang, M. Leary, B. Lozanovski et al, Effect of geometry on the mechanical properties of Ti-6Al-4V Gyroid structures fabricated via SLM: A numerical study, Materials & Design 184 (2019) 108165. https://doi.org/10.1016/j.matdes.2019.108165.
[42] B. B. Babamiri, H. Askari, K. Hazeli, Deformation mechanisms and post-yielding behavior of additively manufactured lattice structures, Materials and Design 188 (2020) 108443. https://doi.org/10.1016/j.matdes.2019.108443.
[43] A. Aremu, I. Maskery, C. Tuck et al., A Comparative Finite Element Study of Cubic Unit Cells for Selective Laser Melting, 25th Solid Freeform Symposium (2014) 1238-1249.
[44] X.P. Tan, Y.J. Tan, C.S.L. Chow et al, Metallic powder-bed based 3D printing of cellular scaffolds for orthopaedic implants: A state-of-the-art review on manufacturing, topological design, mechanical properties and biocompatibility, Materials Science and Engineering C 76 (2017) 1328–1343. http://dx.doi.org/10.1016/j.msec.2017.02.094.
[45] L. Boniotti, S. Foletti, S. Beretta et al, Analysis of strain and stress concentrations in micro-lattice structures manufactured by SLM, Rapid Prototyping Journal 26/2 (2020) 370–380, DOI 10.1108/RPJ-10-2018-0270
[46] S. Liu, Y. C. Shin, Additive manufacturing of Ti6Al4V alloy: A review, Materials and Design 164 (2019) 107552. https://doi.org/10.1016/j.matdes.2018.107552.
[47] C. Y. Yap, C. K. Chua, Z. L. Dong et al, Review of selective laser melting: Materials and applications, Applied Physics Reviews 2 (2015). doi: 10.1063/1.4935926.
[48] M. Yakout, M.A. Elbestawi, S.C. Veldhuis, A study of the relationship between thermal expansion and residual stresses in selective laser melting of Ti-6Al-4V, Journal of Manufacturing Processes 52 (2020) 181–192.
[49] B. Wysocki, P. Maj, A. Krawczy´nska et al., Microstructure and mechanical properties investigation of CP titanium processed by selective laser melting (SLM), Journal of Materials Processing Technology 241 (2017) 13–23.
[50] M. Lowther, S. Louth, A. Davey et al, Clinical, industrial, and research perspectives on powder bed fusion additively manufactured metal implants, Additive Manufacturing 28 (2019) 565-584.
[51] R. Liu, Z. Wang, T. Sparks et al, Aerospace applications of laser additive manufacturing, Laser Additive Manufacturing (2017). http://dx.doi.org/10.1016/B978-0-08-100433-3.00013-0.
[52] SLM Solutions, Bugatti develops and builds functional components for high-performance vehicles with the SLM® additive manufacturing technology from SLM Solutions. https://www.slm-solutions.com/it/profilo-aziendale/press-room/press-releases/bugatti-develops-and-builds-functional-components-for-high-performance-vehicles-with-the-slm-additiv/ , 2019.
[53] X. Ni, D. Kong, Y. Wen et al, Anisotropy in mechanical properties and corrosion resistance of 316L stainless steel fabricated by selective laser melting, International Journal of Minerals, Metallurgy and Materials (2019). https://doi.org/10.1007/s12613-019-1740-x.

[54] F. Rosa, S. Manzoni, R. Casati, Damping behavior of 316L lattice structures produced by Selective Laser Melting, Materials and Design 160 (2018) 1010–1018. https://doi.org/10.1016/j.matdes.2018.10.035.
[55] M. Yakout, M.A. Elbestawi, S.C. Veldhuis, Density and mechanical properties in selective laser melting of Invar 36 and stainless steel 316L, Journal of Materials Processing Tech. 266 (2019) 397–420.
[56] V. Ripamonti, Caratterizzazione microstrutturale e frattografica di componenti in acciaio 316L prodotti tramite Selective Laser Melting, Bachelor Thesis, Alma Mater Studiorum - Università di Bologna, a.a. 2015-2016.
[57] W.S.W. Harun, M.S.I.N. Kamariah, N. Muhamad et al, A review of powder additive manufacturing processes for metallic biomaterials, Powder Technology 327 (2018) 128–151. https://doi.org/10.1016/j.powtec.2017.12.058.
[58] D. Wang, Y. Wang, J Wang et al, Design and Fabrication of a Precision Template for Spine Surgery Using Selective Laser Melting (SLM), Materials (2016) 9, 608. doi:10.3390/ma9070608.
[59] G. Allegri, A. Colpani, P.S. Ginestra et al, An experimental study on micro-milling of a medical grade Co-Cr-Mo alloy produced by selective laser melting, Materials 12 (2019).
[60] M. V. Mergulhão, C. E. Podestá, M. D. Martins das Neves, Mechanical Properties and Microstructural Characterization of Cobalt-Chromium (CoCr) Obtained by Casting and Selective Laser Melting (SLM), Materials Science Forum 899. doi:10.4028/www.scientific.net/MSF.899.534.
[61] L. Ren, K. Memarzadeh, S. Zhang et al, A novel coping metal material CoCrCu alloy fabricated by selective laser melting with antimicrobial and antibiofilm properties, Materials Science and Engineering C 67 (2016) 461–467. http://dx.doi.org/10.1016/j.msec.2016.05.069.
[62] H. R. Kim, S. Jang, Y. K. Kim et al, Microstructures and Mechanical Properties of Co-Cr Dental Alloys Fabricated by Three CAD/CAM-Based Processing Techniques, Materials (2016) 9, 596. doi:10.3390/ma9070596.
[63] M. Averyanova, P. Bertrand, B. Verquin, Manufacture of Co-Cr dental crowns and bridges by selective laser Melting technology, Virtual and Physical Prototyping (2011) 6:3, 179-185. DOI: 10.1080/17452759.2011.619083.
[64] M.R. León, I.M. Klemm, J. García-Arranz et al, 3D Metal Printing – Additive Manufacturing Technologies for Frameworks of Implant- Borne Fixed Dental Prosthesis, European Journal of Prosthodontics and Restorative Dentistry (2017). doi: 10.1922/EJPRD_RevillaLeon05.
[65] N. T. Aboulkhair, N. M. Everitt, I. Maskery et al, Selective laser melting of aluminum alloys, MRS BULLETIN 42 (2017). doi:10.1557/mrs.2017.63.
[66] J. Zhang, B. Song, Q. Wei et al, A Review of Selective Laser Melting of Aluminum Alloys: Processing, Microstructure, Property and Developing Trends, Journal of Materials Science and amp; Technology (2018). https://doi.org/10.1016/j.jmst.2018.09.004.
[67] O. Gharbi, S.K. Kairy, P.R. De Lima et al., Microstructure and corrosion evolution of additively manufactured aluminium alloy AA7075 as a function of ageing, npj Materials Degradation (2019) 3:40. https://doi.org/10.1038/s41529-019-0101-6.
[68] T. Yu, H. Hyer, Y. Sohn et al, Structure-property relationship in high strength and lightweight AlSi10Mg microlattices fabricated by selective laser melting, Materials and Design 182 (2019) 108062. https://doi.org/10.1016/j.matdes.2019.108062.
[69] Z.H. Xiong, S.L. Liu, S.F. Li et al, Role of melt pool boundary condition in determining the mechanical properties of selective laser melting AlSi10Mg alloy, Materials Science & Engineering A 740–741 (2019) 148–156. https://doi.org/10.1016/j.msea.2018.10.083.
[70] SLM Solutions, Bugatti produces motor bracket in series. https://www.slm-solutions.com/en/industries/automotive/bugatti-produces-motor-bracket-in-series/.

[71] J.Y. Ho, K.K. Wong, K.C. Leong et al, Convective heat transfer performance of airfoil heat sinks fabricated by selective laser melting, International Journal of Thermal Sciences 114 (2017) 213-228. http://dx.doi.org/10.1016/j.ijthermalsci.2016.12.016.
[72] C.Y. Yap, H.K. Tan, Z. Du et al, Selective laser melting of nickel powder, Rapid Prototyping Journal 23/4 (2017) 750–75. DOI 10.1108/RPJ-01-2016-0006.
[73] R. Muñoz-Moreno, V.D. Divya, S.L. Driver et al., Effect of heat treatment on the microstructure, texture and elastic nisotropy of the nickel-based superalloy CM247LC processed by selective laser melting, MaterialsScience&EngineeringA674(2016)529–539. http://dx.doi.org/10.1016/j.msea.2016.06.075.
[74] S. Soller, A. Barata, S Beyer et al., Selective laser melting (SLM) of Inconel 718 and Stainless Steel injectors for liquid rocket engines, SPC2016_312478.
[75] F. Caiazzo, V. Alfieri, G. Corrado et al., Laser powder-bed fusion of Inconel 718 to manufacture turbine blades, Int J Adv Manuf Technol (2017) 93:4023–4031. DOI 10.1007/s00170-017-0839-3
[76] A. Grosmann, J. Gosmann, C. Mittelstedt, Lightweight lattice structures in selective laser melting: Design, fabrication and mechanical properties, Materials Science & Engineering A 766 (2019) 138356. https://doi.org/10.1016/j.msea.2019.138356.
[77] D. K. Do, P. Li, The effect of laser energy input on the microstructure, physical and mechanical properties of Ti-6Al-4V alloys by selective laser melting, Virtual and Physical Prototyping (2016) 11:1, 41-47, DOI: 10.1080/17452759.2016.1142215.
[78] X. Zhao, S. Li, M. Zhang et al, Comparison of themicrostructures andmechanical properties of Ti–6Al–4V fabricated by selective laser melting and electron beam melting, Materials and Design 95 (2016) 21–31. http://dx.doi.org/10.1016/j.matdes.2015.12.135.
[79] W.M. Tucho, V.H. Lysne, Hå. Austbø et al, Investigation of effects of process parameters on microstructure and hardness of SLM manufactured SS316L, Journal of Alloys and Compounds (2018), doi: 10.1016/j.jallcom.2018.01.098.
[80] M. Dallago, S. Raghavendra, V. Luchin et al, Geometric assessment of lattice materials built via Selective Laser Melting, Materials Today: Proceedings 7 (2019) 353–361
[81] P. Köhnen, C. Haase, J. Bültmann et al, Mechanical properties and deformation behavior of additively manufactured lattice structures of stainless steel, Materials and Design 145 (2018) 205–217. https://doi.org/10.1016/j.matdes.2018.02.062.
[82] S. Y. Choy, C. Sun, K. F. Leong et al, Compressive properties of functionally graded lattice structures manufactured by selective laser melting, Materials & Design 131 (2017) 112–120. http://dx.doi.org/10.1016/j.matdes.2017.06.006.
[83] S. Y. Choy, C. Sun, K. F. Leong et al, Compressive properties of Ti-6Al-4V lattice structures fabricated by selective laser melting: Design, orientation and density, Additive Manufacturing 16 (2017) 213–224. http://dx.doi.org/10.1016/j.addma.2017.06.012.
[84] M. Leary, M. Mazur, J. Elambasseril et al, Selective laser melting (SLM) of AlSi12Mg lattice structures, Materials and Design 98 (2016) 344–357. http://dx.doi.org/10.1016/j.matdes.2016.02.127.
[85] M. Leary, M. Mazur, H. Williams et al, Inconel 625 lattice structures manufactured by selective laser melting (SLM): Mechanical properties, deformation and failure modes, Materials and Design 157 (2018) 179–199. https://doi.org/10.1016/j.matdes.2018.06.010.
[86] E. Liverani, A.H.A. Lutey, A. Fortunato et al, Characterization of lattice structures for additive manufacturing of lightweight mechanical components, MSEC2017-2835. DOI: 10.1115/MSEC2017-2835.
[87] P. Caravaggi, E. Liverani, A. Leardini et al, CoCr porous scaffolds manufactured via selective laser melting in orthopedics: Topographical, mechanical, and biological characterization, J Biomed Mater Res Part B (2019). DOI: 10.1002/jbm.b.34328.

[88] Z. Xiao, Y. Yang, R. Xiao et al, Evaluation of topology-optimized lattice structures manufactured via selective laser melting, Materials and Design 143 (2018) 27–37. https://doi.org/10.1016/j.matdes.2018.01.023.

[89] A. Ataee, Y. Li, M. Brandt et al, Ultrahigh-strength titanium gyroid scaffolds manufactured by selective laser melting (SLM) for bone implant applications, Acta Materialia 158 (2018) 354e368. https://doi.org/10.1016/j.actamat.2018.08.005.

[90] A. Cutolo, B. Engelen, W. Desmet et al, Mechanical properties of diamond lattice Ti–6Al–4V structures produced by laser powder bed fusion: On the effect of the load direction, journal of the mechanical behavior of biomedical materials 104 (2020) 103656. https://doi.org/10.1016/j.jmbbm.2020.103656.

[91] S. L. Campanelli, N. Contuzzi, A. D. Ludovico et al, Manufacturing and Characterization of Ti6Al4V Lattice Components Manufactured by Selective Laser Melting, Materials 2014, 7, 4803-4822. doi: 10.3390/ma7064803.

[92] Y. Amani, S. Dancette , P. Delroisse et al, Compression behavior of lattice structures produced by selective laser melting: X-ray tomography based experimental and finite element approaches, Acta Materialia 159 (2018) 395e407, https://doi.org/10.1016/j.actamat.2018.08.030.

[93] V. Mager, N. Balc, D. Leordean et al, Research on Producing Complex Metal Parts with Lattice Structure, by Selective Laser Melting, Applied Mechanics and Materials Vol. 371 (2013) 280-284. doi:10.4028/www.scientific.net/AMM.371.280.

[94] Y. Ibrahim, Z. Li, C.M. Davies et al, Acoustic resonance testing of additive manufactured lattice structures, Additive Manufacturing 24 (2018) 566–576. https://doi.org/10.1016/j.addma.2018.10.034.

[95] S. L. Sing, F. E. Wiria, W.Y. Yeong, Selective laser melting of lattice structures: A statistical approach to manufacturability and mechanical behavior, Robotics and Computer–Integrated Manufacturing 49 (2018) 170–180. http://dx.doi.org/10.1016/j.rcim.2017.06.006.

[96] T. Zhong, K. He, H. Li et al, Mechanical properties of lightweight 316L stainless steel lattice structures fabricated by selective laser melting, Materials and Design 181 (2019) 108076. https://doi.org/10.1016/j.matdes.2019.108076.

[97] C. N. Kelly, J. Francovich, S. Julmi et al, Fatigue behavior of As-built selective laser melted titanium scaffolds with sheet-based gyroid microarchitecture for bone tissue engineering, Acta Biomaterialia 94 (2019) 610–626. https://doi.org/10.1016/j.actbio.2019.05.046.

[98] I. Maskery, N.T.Aboulkhair, A.O. Aremu et al, A mechanical property evaluation of graded density Al-Si10-Mg lattice structures manufactured by selective laser melting, Materials Science&EngineeringA670(2016)264–274. http://dx.doi.org/10.1016/j.msea.2016.06.013.

[99] M. Wu, J. Chen, B. Lin et al, Improved fatigue endurance ratio of additive manufactured Ti-6Al-4V lattice by hot isostatic pressing, Materials and Design 134 (2017) 163–170. http://dx.doi.org/10.1016/j.matdes.2017.08.048.

[100] A. Cutolo, B. Neirinck, K. Lietaert et al, Influence of layer thickness and post-process treatments on the fatigue properties of CoCr scaffolds produced by laser powder bed fusion, Additive Manufacturing 23 (2018) 498–504. https://doi.org/10.1016/j.addma.2018.07.008.

[101] F. Brenne, T. Niendorf, H.J. Maier, Additively manufactured cellular structures: Impact of microstructure and local strains on the monotonic and cyclic behavior under uniaxial and bending load, Journal of Materials Processing Technology (2013), http://dx.doi.org/10.1016/j.jmatprotec.2013.03.013.

[102] B. Van Hooreweder, K. Lietaert, B. Neirinck et al, CoCr F75 scaffolds produced by additive manufacturing: Influence of chemical etching on powder removal and mechanical performance, Journal of the mechanical behavior of biomedical materials 68 (2017) 216–223. http://dx.doi.org/10.1016/j.jmbbm.2017.02.005.

[103] B. Van Hooreweder, Y. Apers, K. Lietaert et al, Improving the fatigue performance of porous metallic biomaterials produced by Selective Laser Melting, Acta Biomaterialia 47 (2017) 193–202. http://dx.doi.org/10.1016/j.actbio.2016.10.005.

[104] F. Liu , D. Z. Zhang, P. Zhang et al, Mechanical Properties of Optimized Diamond Lattice Structure for Bone Scaffolds Fabricated via Selective Laser Melting, Materials 2018, 11, 374. doi: 10.3390/ma11030374.

[105] S. Limmahakhun, A. Oloyede, K. Sitthiseripratip et al, Stiffness and strength tailoring of cobalt chromium graded cellular structures for stress-shielding reduction, Materials and Design 114 (2017) 633–641. http://dx.doi.org/10.1016/j.matdes.2016.11.090.

[106] F.S.L. Bobbert, K. Lietaert, A.A. Eftekhari et al, Additively manufactured metallic porous biomaterials based on minimal surfaces: A unique combination of topological, mechanical, and mass transport properties, Acta Biomaterialia 53 (2017) 572–584. http://dx.doi.org/10.1016/j.actbio.2017.02.024.

[107] L. Mullen, R. C. Stamp, P. Fox et al, Selective Laser Melting: A Unit Cell Approach for the Manufacture of Porous, Titanium, Bone In-Growth Constructs, Suitable for Orthopedic Applications. II. Randomized Structures, Journal of Biomedical Materials Research Part B: Applied Biomaterials (2009). DOI: 10.1002/jbm.b.31504.

[108] S. Raghavendra, A. Molinari, V. Fontanari et al, Tensile and compression properties of variously arranged porous Ti-6Al-4V additively manufactured structures via SLM, Procedia Strucutral Intrgtity 13 (2018) 149-154. 10.1016/j.prostr.2018.12.025.

[109] X. Lijun, S. Weidong, Additively-manufactured functionally graded Ti-6Al-4V lattice structures with high strength under static and dynamic loading: Experiments, International Journal of Impact Engineering 111 (2018) 255–272. http://dx.doi.org/10.1016/j.ijimpeng.2017.09.018.

[110] M. Zhao, D. Z. Zhang ,F. Liu et al, Mechanical and energy absorption characteristics of additively manufactured functionally graded sheet lattice structures with minimal surfaces, International Journal of Mechanical Sciences 167 (2020) 105262. https://doi.org/10.1016/j.ijmecsci.2019.105262.

[111] D.S.J. Al-Saedi, S.H. Masood, M. Faizan-Ur-Rab et al, Mechanical properties and energy absorption capability of functionally graded F2BCC lattice fabricated by SLM, Materials and Design 144 (2018) 32–44. https://doi.org/10.1016/j.matdes.2018.01.059.

[112] J. Sienkiewicz, P. Płatek, F. Jiang et al, Investigations on the Mechanical Response of Gradient Lattice Structures Manufactured via SLM, Metals 10 (2020) 213. doi:10.3390/met10020213.

[113] T. Maconachie, M. Leary, B. Lozanovski et al, SLM lattice structures: Properties, performance, applications and challenges, Materials and Design 183 (2019) 108137. https://doi.org/10.1016/j.matdes.2019.108137.

[114] J. Kessler, N. Bâlc, A. Gebhardt et al, Basic research on lattice structures focused on the reliance of the cross sectional area and additional coatings, MATEC Web of Conferences 94 (2017). DOI: 10.1051/matecconf/20179403008.

[115] J. Hajnyš, M. Pagáč, T. Zlámal et al, Stiffness of 316L stainless steel support structures proposed for the SLM process, MATEC Web of Conferences 244 (2018). https://doi.org/10.1051/matecconf/201824401008.

[116] I. Maskery, A. Aremu, M. Simonelli et al, The BCC unit cell for latticed SLM parts; mechanical properties as a function of cell size, 25th Solid Free Form Symposium (2014) 688-701.

[117] L. Löber, D. Klemm, U. Kühn et al, Rapid manufacturing of cellular structures of steel or titaniumalumide, Materials Science Forum Vol. 690 (2011) 103-106. doi:10.4028/www.scientific.net/MSF.690.103

[118] C. N. Kelly, N. T. Evans, C. W. Irvin et al, The effect of surface topography and porosity on the tensile fatigue of 3D printed Ti-6Al-4V fabricated by selective laser melting, Materials Science & Engineering C 98 (2019) 726–736. https://doi.org/10.1016/j.msec.2019.01.024.

[119] A. Barbas, A.-S. Bonnet, P. Lipinski et al, Development and mechanical characterization of porous titanium bone substitutes, Journal of the Mechanical Behavior of Biomedical Materials 9 (2012) 34–44. doi:10.1016/j.jmbbm.2012.01.008.

[120] S. Raghavendra, A. Molinari, V. Fontanari et al, Effect of strut cross section and strut defect on tensile properties of cubic cellular structure, Mat Design Process Comm. (2019). DOI: 10.1002/mdp2.118.

[121] J. Niu, H. L. Choo, W. Sun et al, Numerical study on load-bearing capabilities of beam-like lattice structures with three different unit cells, Int J Mech Mater Des (2018) 14:443–460. https://doi.org/10.1007/s10999-017-9384-3(01

[122] D. Kang, S. Park, Y. Son et al, Multi-lattice inner structures for high-strength and light-weight inmetal selective laser melting process, Materials and Design 175 (2019) 107786. https://doi.org/10.1016/j.matdes.2019.107786.

[123] Y. Shen, W. Cantwell, Y. Li, Skin-core adhesion in high performance sandwich structures, J Zhejiang Univ-Sci A (Appl Phys & Eng) (201)4 15(1):61-67. doi:10.1631/jzus.A1300283.

[124] Y. Shen, S. McKown, S. Tsopanos et al, The Mechanical Properties of Sandwich Structures Based on Metal Lattice Architectures, Journal of Sandwich structures and materials 12 (2010). DOI: 10.1177/1099636209104536.

[125] B. Van Hooreweder, J. Kruth, Advanced fatigue analysis of metal lattice structures produced by Selective Laser Melting, CIRP Annals - Manufacturing Technology 66 (2017) 221–224. http://dx.doi.org/10.1016/j.cirp.2017.04.130.

[126] N. Contuzzi, S.L. Campanelli, C. Casavola et al, Manufacturing and Characterization of 18Ni Marage 300 Lattice Components by Selective Laser Melting, Materials 2013, 6, 3451-3468. doi:10.3390/ma6083451.

[127] G. De Pasquale, F. Luceri, M. Riccio, Experimental Characterization of SLM and EBM Cubic Lattice Structures for Lightweight Applications, Experimental Mechanics (2019). https://doi.org/10.1007/s11340-019-00481-8.

[128] Q. Feng, Q. Tang, Y. Liu et al, Quasi-static analysis of mechanical properties of Ti6Al4V lattice structures manufactured using selective laser melting, Int J Adv Manuf Technol (2017). DOI 10.1007/s00170-017-0932-7.

Section 2.2

[1] M Lowther, S. Louth, A. Davey, et al., “Clinical, industrial, and research perspectives on powder bed fusion additively manufactured metal implants”, Additive Manufacturing 28 (2019): 565-584.

[2] C. Yan, L. Hao, A. Hussein, et al., “Advanced lightweight 316L stainless steel cellular lattice structures fabricated via selective laser melting”, Materials and Design 55 (2014): 533-541.

[3] P.S. Ginestra, E. Ceretti, A. Fiorentino, “Potential of modeling and simulations of bioengineered devices: Endo-prostheses, prostheses and orthoses”, Proceedings of the Institution of Mechanical Engineers, Part H: Journal of Engineering in Medicine 230(7) (2016): 607-638.

[4] D. Gastaldi, G. Parisi, R. Lucchini, et al., “A Predictive Model for the Elastic Properties of a Collagen-Hydroxyapatite Porous Scaffold for Multi-Layer Osteochondral Substitutes”, International Journal of Applied Mechanics 7(4) (2015): 1550063.

[5] P.S. Ginestra, A. Fiorentino, E. Ceretti, “Micro-structuring of titanium collectors by laser ablation technique: a novel approach to produce micro-patterned scaffolds for tissue engineering applications”, Procedia CIRP 65 (2017): 19-24.

[6] P.S. Ginestra, S. Pandini, A. Fiorentino, et al., "Micro-structured scaffold for guided cellular orientation: Poly(ε-caprolactone) electrospinning on laser ablated titanium collector", CIRP Journal of Manufacturing Science and Technology 19 (2017): 147-157.
[7] M. Leary, M. Mazur, H. Williams, et al., "Inconel 625 lattice structures manufactured by selective laser melting (SLM): Mechanical properties, deformation and failure modes", Materials and design 157 (2018): 179-199.
[8] F. Marbury, "Characterization of SLM Printed 316L Stainless Steel and Investigation of Micro Lattice Geometry. PhD dissertation (2017).
[9] J.Y. Rho, L. Kuhn-Spearing, P. Zioupos, "Mechanical properties and the hierarchical structure of bone", Medical Engineering and Physics 20 (1998): 92-102.
[10] M Mahmoudi, A. Elwany, A. Yadollahi, et al., "Mechanical properties and microstructural characterization of selective laser melted 17-4 PH stainless steel", Rapid Prototyping Journal 23 (2017): 280-294.
[11] N. Jin, F. Wang, Y. Wang, et al., "Failure and energy ab-sorption characteristics of four lattice structures under dynamic loading", Materials and design 169 (2019): 107655.
[12] I. Maskery, L. Sturm, A.O. Aremu, et al., "Insights into the mechanical properties of several triply periodic minimal surface lattice structures made by polymer additive manufacturing", Polymer 152 (2018): 62-71.
[13] Z. Zhang, T. Peng, S. Xu, "The influence of scanning pattern on the part properties in powder bed fusion processes: an experimental study", Procedia CIRP 61 (2017): 606-611.
[14] E. Ceretti, P.S. Ginestra, P.I. Neto, A. Fiorentino and J.V.L. Da Silva, "Multi-layered scaffolds production via Fused Deposition Modeling (FDM) using an open source 3D printer: process parameters optimization for dimensional accuracy and design reproducibility", Proedia. CIRP 65 (2017): pp. 13-18.
[15] F. Liu, D.Z. Zhang, P. Zhang, M. Zhao, J. Salman, "Mechanical Properties of Optimized Diamond Lattice Structure for Bone Scaffolds Fabricated via Selective Laser Melting", Materials 11 (2018): 374. doi:10.3390/ma11030374.

Chapter 3

Section 3.1

[1] Kleinberg TT, Tzekov RT, Stein L, Ravi N, Kaushal S. Vitreous Substitutes: A Comprehensive Review. Surv Ophthalmol 2011;56:300–23.
[2] Milston R, Madigan MC, Sebag J. Vitreous floaters: Etiology, diagnostics, and management. Surv Ophthalmol 2016;61:211–27.
[3] Donati S, Caprani SM, Airaghi G, Vinciguerra R, Bartalena L, Testa F, et al. Vitreous substitutes: The present and the future. Biomed Res Int 2014;2014.
[4] Ankamah E, Sebag J, Ng E, Nolan JM. Vitreous antioxidants, degeneration, and vitreo-retinopathy: Exploring the links. Antioxidants 2020;9.
[5] Sommer F, Pollinger K, Brandl F, Weiser B, Teßmar J, Blunk T, et al. Hyalocyte proliferation and ECM accumulation modulated by bFGF and TGF-β1. Graefe's Arch Clin Exp Ophthalmol 2008;246:1275–84.
[6] Alovisi C, Panico C, Sanctis U De, Eandi CM. Vitreous Substitutes: Old and New Materials in Vitreoretinal Surgery. J Ophthalmol 2017;2017.
[7] Boneva SK, Wolf J, Rosmus D-D, Schlecht A, Prinz G, Laich Y, et al. Transcriptional Profiling Uncovers Human Hyalocytes as a Unique Innate Immune Cell Population. Front Immunol 2020;11:567274.

[8] Ali E, Ferraro RM, Lanzi G, Masneri S, Piovani G, Mazzoldi EL, et al. Generation of induced pluripotent stem cell (iPSC) lines from a Joubert syndrome patient with compound heterozygous mutations in C5orf42 gene. Stem Cell Res 2020;49:102007.
[9] Ferraro RM, Masneri S, Lanzi G, Barisani C, Piovani G, Savio G, et al. Establishment of three iPSC lines from fibroblasts of a patient with Aicardi Goutieres syndrome mutated in RNaseH2B. Stem Cell Res 2019;41:101620.
[10] Kashiwagi Y, Nishitsuka K, Takamura H, Yamamoto T, Yamashita H. Cloning and characterization of human vitreous tissue-derived cells. Acta Ophthalmol 2011;89:538–43.
[11] Nuzzi R, Bergandi L, Zabetta LC, D'Errico L, Riscaldino F, Menegon S, et al. In vitro generation of primary cultures of human hyalocytes. Mol Vis 2020;26:818–29.
[12] Nishitsuka K, Kashiwagi Y, Tojo N, Kanno C, Takahashi Y, Yamamoto T, et al. Hyaluronan production regulation from porcine hyalocyte cell line by cytokines. Exp Eye Res 2007;85:539–45.
[13] Sommer F, Kobuch K, Brandl F, Wild B, Framme C, Weiser B, et al. Ascorbic acid modulates proliferation and extracellular matrix accumulation of hyalocytes. Tissue Eng 2007;13:1281–9.
[14] Ferraro RM, Ginestra PS, Lanzi G, Giliani S, Ceretti E. Production of Micro-patterned Substrates to Direct Human iPSCs-derived Neural Stem Cells Orientation and Interaction. Procedia CIRP 2017;65:225–30.
[15] Sta. Agueda JRH, Chen Q, Maalihan RD, Ren J, da Silva ÍGM, Dugos NP, et al. 3D printing of biomedically relevant polymer materials and biocompatibility. MRS Commun 2021;11:197–212.
[16] Schmidleithner C, Kalaskar DM. Stereolithography. In: Cvetković D, editor. 3D Print., Rijeka: IntechOpen; 2018.
[17] Riva L, Mazzoldi EL, Ginestra PS, Ceretti E, Giliani SC. Eye model for floaters' studies: production of 3D printed scaffolds. Prog Addit Manuf 2022.

Section 3.2

[1] X. Lumi, M. Hawlina, D Glavač et al., "Ageing of the vitreous: From acute onset floaters and flashes to retinal detachment", Ageing Research Reviews 21 (2015) 71–77. http://dx.doi.org/10.1016/j.arr.2015.03.006
[2] R. Milston, M.C. Madigan, J. Sebag, "Vitreous floaters: Etiology, diagnostics, and management", survey of ophthalmology 6 1 (2 0 1 6) 2 1 1-2 2 7. http://dx.doi.org/10.1016/j.survophthal.2015.11.008
[3] G.K. Broadhead, T. Hong, A.A. Chang, "To Treat or Not to Treat: Management Options for Symptomatic Vitreous Floaters", Asia Pac J Ophthalmology 9 (2020) 96–103. 10.1097/APO.0000000000000276.
[4] M. Kalavar, S. Hubschman, J. Hudson et al., "Evaluation of Available Online Information Regarding Treatment for Vitreous Floaters", Seminars in Ophthalmology 36:1-2 (2021) 58-63, https://doi.org/10.1080/08820538.2021.1887898.
[5] S. Cipolletta, A. Beccarello, A. Galan, "A Psychological Perspective of Eye Floaters", Qualitative Health Research 22 (11) (2012) 1547–1558. DOI: 10.1177/1049732312456604.
[6] J. Kokavec, Z. Wu, J.C. Sherwin et al., "Nd:YAG laser vitreolysis versus pars plana vitrectomy for vitreous floaters", Cochrane Database of Systematic Reviews Issue 6 (2017). DOI: 10.1002/14651858.CD011676.pub2
[7] E.H. Ryan, "Current treatment strategies for symptomatic vitreous opacities", Current Opinion in Ophthalmology 32(13) 2021 198-202. Doi: 10.1097/ICU.0000000000000752.
[8] O.S. Fenton, M. Paolini, J. Andresen et al., "Outlooks on Three-Dimensional Printing for Ocular Biomaterials Research", JOURNAL OF OCULAR PHARMACOLOGY AND THERAPEUTICS 36 (2020).
[9] Y.L. Yap, Y.S.E. Tan, H.K.J. Tan at al., "3D printed bio-models for medical applications, Rapid Prototyping Journal 23/2 (2017) 227–235. DOI 10.1108/RPJ-08-2015-0102.

[10] J. SEDLAK, O. VOCILKA, M. SLANY et al., "DESIGN AND PRODUCTION OF EYE PROSTHESIS USING 3D PRINTING", MM SCIENCE JOURNAL (2020). DOI: 10.17973/MMSJ.2020_03_2019127.
[11] P. Xie, Z. Hu, X. Zhang at al., "Application of 3-Dimensional Printing Technology to Construct an Eye Model for Fundus Viewing Study", PLoS ONE 9(11) (2014). Doi: 10.1371/journal.pone.0109373.
[12] C.M. Phan, M. Shukla, H. Walther et al., "Development of an In Vitro Blink Model for Ophthalmic Drug Deliver", Pharmaceutics 13 (2021). https://doi.org/10.3390/pharmaceutics13030300.
[13] D.A. Lobo, P.S. Ginestra, "Cell Bioprinting: The 3D-Bioplotter™ Case", Materials 12(23) (2019) 4005. https://doi.org/10.3390/ma12234005
[14] M.E. Kupfer, W.H. Lin, V. Ravikumar et al., "In Situ Expansion, Differentiation, and Electromechanical Coupling of Human Cardiac Muscle in a 3D Bioprinted, Chambered Organoid", Circulation Research 127 (2020) 207–224. DOI: 10.1161/CIRCRESAHA.119.316155.
[15] A.C. Sommer, E.Z. Blumenthal, "Implementations of 3D printing in ophthalmology", Graefes Arch Clin Exp Ophthalmol 257 (2019) 1815–1822. https://doi.org/10.1007/s00417-019-04312-3.
[16] R.M. Ferraro, P. S. Ginestra, G. Lanzi et al., "Production of micro-patterned substrates to direct human iPSCs-derived neural stem cells orientation and interaction", Procedia CIRP 65 (2017) 225 – 230. Doi: 10.1016/j.procir.2017.04.044.
[17] P.S. Ginestra, S. Pandini, E. Ceretti, "Hybrid multi-layered scaffolds produced via grain extrusion and electrospinning for 3D cell culture tests", Rapid Prototyping Journal 26/3 (2020) 593–602. DOI 10.1108/RPJ-03-2019-0079.
[18] J.R.H. Sta. Agueda, Q. Chen, R.D. Maalihan et al., "3D printing of biomedically relevant polymer materials and biocompatibility", MRS Communications (2021). https://doi.org/10.1557/s43579-021-00038-8
[19] C. Schmidleithner, D.M. Kalaskar, "Stereolithography", in: D. Cvetković (Eds.), 3D Printig (2018). DOI: 10.5772/intechopen.78147.
[20] S. Kreß, R. Schaller-Ammann, J. Feiel et al., "3D Printing of Cell Culture Devices: Assessment and Prevention of the Cytotoxicity of Photopolymers for Stereolithography", Materials 13 (2020). doi:10.3390/ma13133011.

Chapter 4

Section 4.1

[1] J. Kokavec, S.H. Min, M.H. Tan, et al., "Biochemical analysis of the living human vitreous", Clinical and Experimental Ophthalmology 44 (2016): 597–609 doi: 10.1111/ceo.12732.
[2] N.K. Tram, K.E. Swindle-Reilly, "Rheological Properties and Age-Related Changes of the Human Vitreous Humor", Front. Bioeng. Biotechnol. 6 (2018):199. doi: 10.3389/fbioe.2018.00199.
[3] M. Angi, H. Kalirai, S.E. Coupland, et al., "Proteomic Analyses of the Vitreous Humour", Hindawi Publishing Corporation, Mediators of Inflammation, Volume 2012, Article ID 148039, doi:10.1155/2012/148039.
[4] A. Osmanovic, "TREATING VITREOUS FLOATERS WITH ND:YAG LASER VITREOLYSIS: DETERMINED BY VISION RELATED QUALITY OF LIFE QUESTIONNAIRE ", Master's thesis, of Split, School of Medicine (2019).
[5] S. Donati, S.M. Caprani, G. Airaghi, et al., "Vitreous Substitutes: The Present and the Future", Hindawi Publishing Corporation, BioMed Research International, Volume 2014, Article ID 351804, http://dx.doi.org/10.1155/2014/351804.
[6] J. Sebag, "Vitreous and Vision Degrading Myodesopsia", Progress in Retinal and Eye Research 79 (2020), 100847. https://doi.org/10.1016/j.preteyeres.2020.100847.

[7] Q. Lin, J.Y.C. Lim, K Xue, et al., “Polymeric hydrogels as a vitreous replacement strategy in the eye”, Biomaterials 268 (2021), 120547. https://doi.org/10.1016/j.biomaterials.2020.120547.
[8] M. Levin, N. Cohen, “The effects of aging on the mechanical properties of the vitreous”, Journal of Biomechanics 119 (2021), 110310. https://doi.org/10.1016/j.jbiomech.2021.110310.
[9] M. Kalavar, S. Hubschman, J. Hudson, et al., “Evaluation of Available Online Information Regarding Treatment for Vitreous Floaters”, Seminars in Ophthalmology (2021), 36:1-2, 58-63, DOI: 10.1080/08820538.2021.1887898.
[10] G.K. Broadhead, T. Hong, A.A. Chang, “To Treat or Not to Treat: Management Options for Symptomatic Vitreous Floaters”, Asia Pac J Ophthalmol (Phila) (2020);9:96–103. DOI: 10.1097/APO.0000000000000276.
[11] T. Sakamoto, T.Ishibashi, “Hyalocytes: Essential Cells of the Vitreous Cavity in Vitreoretinal Pathophysiology?”, Retina. 2011 Feb; 31(2):222-8. doi: 10.1097/IAE.0b013e3181facfa9.
[12] K.A. van Overdam, E.M. Bush, R.M. Verdijk, et al., “The role of vitreous cortex remnants in proliferative vitreoretinopathy formation demonstrated by histopathology: A case report”, American Journal of Ophthalmology Case Reports 24 (2021), 101219. https://doi.org/10.1016/j.ajoc.2021.101219.
[13] W. Halfter, J. Sebag, E.T. Cunningham Jr., “II.E. Vitreoretinal Interface and Inner Limiting Membrane”, (2014). DOI:10.1007/978-1-4939-1086-1_11.
[14] J. Sebag, “Vitreous: the resplendent enigma”, Br J Ophthalmol 93 (2009), pp. 969-991. doi:10.1136/bjo.2009.157313.
[15] L. Riva, E.L. Mazzoldi, P.S. Ginestra, et al., “Eye model for floaters’ studies: production of 3D printed scaffolds”, Progress in Additive Manufacturing (2022). https://doi.org/10.1007/s40964-022-00288-5.
[16] Ž.P. Kaˇcarevi´, P.M. Rider, S. Alkildani, et al., “An Introduction to 3D Bioprinting: Possibilities, Challenges and Future Aspects”, Materials (2018) 11, 2199. doi:10.3390/ma11112199.
[17] O.S. Fenton, M. Marion, J.L. Andersen, et al., “Outlooks on Three-Dimensional Printing for Ocular Biomaterials Research”, JOURNAL OF OCULAR PHARMACOLOGY AND THERAPEUTICS (2020) 36, Number 1. DOI: 10.1089/jop.2018.0142.
[18] A. Schulz, K. Januschowski, P. Szurman, “Novel vitreous substitutes: the next frontier in vitreoretinal surgery”, Curr Opin Ophthalmol (2021) 32:288–293. DOI:10.1097/ICU.0000000000000745.
[19] B.S. Kim, S. Das, J. Jang, et al., “Decellularized Extracellular Matrix-based Bioinks for Engineering Tissue- and Organ-specific Microenvironments”, Chem. Rev. (2020) 120, 10608−1066. https://dx.doi.org/10.1021/acs.chemrev.9b00808.
[20] G.C.J. Lindberg, A. Longoni, K.S. Lim, et al., “Intact vitreous humor as a potential extracellular matrix hydrogel for cartilage tissue engineering applications”, Acta Biomaterialia 85 (2019), pp. 117–130. https://doi.org/10.1016/j.actbio.2018.12.022.

Chapter 5

Section 5.1

[1] Fassi, I. and Legnani, G. (2013) ‘Robotics: State of the art and future trends’. Nova Science Publishers, New York.
[2] Virk, G. S., Moon, S., Gelin, R. (2008) ‘ISO standards for service robots’, Advances In Mobile Robotics, 2008 pp. 133-138. https://doi.org/10.1142/9789812835772_0016.
[3] Speich, J. E., Rosen, J. (2004) ‘Medical robotics’, Encyclopedia of biomaterials and biomedical engineering, 983, 993.
[4] Maciejasz, P., Eschweiler, J., Gerlach-Hahn, K., Jansen-Troy, A., and Leonhardt, S. (2014) ‘A survey on robotic devices for upper limb rehabilitation’, Journal of neuroengineering and rehabilitation, Vol.11(1), pp. 1-29. https://doi.org/10.1186/1743-0003-11-3.

[5] Liu, W., Yin, B., Yan, B. (2016) 'A survey on the exoskeleton rehabilitation robot for the lower limbs', 2nd International Conference on Control, Automation and Robotics (ICCAR), 2016, pp. 90-94. IEEE.
[6] Salcudean, S.E., Bell, G., Bachmann, S., Zhu, W.H., Abolmaesumi, P., and Lawrence, P. D. (1999,) 'Robot-assisted diagnostic ultrasound–design and feasibility experiments', International Conference on Medical Image Computing and Computer-Assisted Intervention, pp. 1062-1071. Springer, Berlin, Heidelberg.
[7] Von Haxthausen, F., Böttger, S., Wulff, D., Hagenah, J., García-Vázquez, V., and Ipsen, S. (2021) 'Medical robotics for ultrasound imaging: current systems and future trends', Current Robotics Reports, 2021 Vol.2, pp. 1-17. doi: 10.1007/s43154-020-00037-y.
[8] Hans, S., Delas, B., Gorphe, P., Ménard, M., and Brasnu, D. 2012 'Transoral robotic surgery in head and neck cancer', European annals of otorhinolaryngology, head and neck diseases, 2012 Vol.129(1), pp. 32-37. DOI: 10.1016/j.anorl.2011.06.003.
[9] Wu, Y., Wang, F., Fan, S., and Chow, J.K.F. (2019) 'Robotics in dental implantology', Oral and Maxillofacial Surgery Clinics, 2019 Vol.31(3), pp. 513-518. DOI: 10.1016/j.coms.2019.03.013.
[10] Ananth, H., Kundapur, V., Mohammed, H.S., Anand, M., Amarnath, G.S., and Mankar, S. (2015) 'A review on biomaterials in dental implantology', International journal of biomedical science, 2015 Vol. 11(3), pp. 113-120.
[11] Grischke, J., Johannsmeier, L., Eich, L., and Haddadin, S. (2019) 'Dentronics: Review, first concepts and pilot study of a new application domain for collaborative robots in dental assistance', International Conference on Robotics and Automation (ICRA), 2019 pp. 6525-6532. DOI:10.1109/ICRA.2019.8794139. Montreal, Canada.
[12] Emami, E., de Souza, R.F., Kabawat, M., and Feine, J.S. (2013) 'The impact of edentulism on oral and general health', International journal of dentistry, 2013. doi: 10.1155/2013/498305.
[13] Resnik, R. (2020) 'Misch's contemporary implant dentistry e-book', Elsevier Health Sciences.
[14] Yeshwante, B., Baig, N., Tambake, S.S., Tambake, R., Patil, V., and Rathod, R. (2017) 'Mastering dental implant placement: A review, J. Appl. Dent. Med. Sci, 2017 vol.3, pp.220-227.
[15] Novaes Jr, A.B., Souza, S.L.S.D., Barros, R.R.M.D., Pereira, K.K.Y., Iezzi, G., and Piattelli, A. (2010) 'Influence of implant surfaces on osseointegration', Brazilian dental journal, 2010 Vol.21, pp. 471-481. https://doi.org/10.1590/S0103-64402010000600001.
[16] Mankin, H. J. (1992) 'Nontraumatic necrosis of bone (osteonecrosis)', New England Journal of Medicine, 1992 Vol.326(22), pp.1473-1479. DOI: 10.1056/NEJM199205283262206.
[17] Azari, A., Nikzad, S. (2008) 'Computer-assisted implantology: historical background and potential outcomes—a review', The International Journal of Medical Robotics and Computer Assisted Surgery, 2008 Vol.4(2), pp.95-104. DOI: 10.1002/rcs.188.
[18] Manzini, B.M., Machado, L.M.R., Noritomi, P.Y. and DA Silva, J.V.L. (2021) 'Advances in Bone tissue engineering: A fundamental review', J Biosci, 2021 Vol 46(17). https://doi.org/10.1007/s12038-020-00122-6.
[19] Kinoshita H., Nagahata M., Takano N., Takemoto S., Matsunaga S., Abe S., Yoshinari M. and Kawada E. (2016) 'Development of a drilling simulator for dental implant surgery', Journal of dental education, 2016 Vol.80(1), pp.83-90.
[20] Bin Kamisan MAA, Yokota K., Ueno T., Kinoshita H., Homma S., Yajima Y., Abe S. and Takano N. (2016) 'Drilling force and speed for mandibular trabecular bone in oral implant surgery', Biomaterials and Biomechanics in Bioengineering, 2016 Vol.3(1), pp.15-26. DOI:10.12989/BME.2016.3.1.015.
[21] Bin Kamisan, M.A.A, Yokota, K., Ueno, T., Kinoshita, H., Homma, S., Yajima, Y., Abe, S. and Takano N. (2016) 'Quantitative study of force sensing while drilling trabecular bone in oral implant surgery', Journal of Biomechanical Science and Engineering, 2016 Vol.11(3). https://doi.org/10.1299/jbse.15-00550.
[22] Chand, R., Sharma, V.S., Trehan, R. (2021) 'Investigating mechanical properties of 3D printed parts manufactured in different orientations on multijet printer' International Journal of Mechatronics and Manufacturing Systems, Vol. 14, No. 2, pp 164.179. DOI: 10.1504/IJMMS.2021.119157.
[23] Etemad-Shahidi, Y., Qallandar, O.B., Evenden, J., Alifui-Segbaya, F. and Ahmed, K.E. (2020) 'Accuracy of 3-Dimensionally Printed Full-Arch Dental Models: A Systematic Review', J. Clin. Med., 2020 Vol.9, 3357. doi:10.3390/jcm9103357.

[24] Kushwaha, A., Anand Kumar, S., Velu, R. (2021) 'Selective laser melting of titanium alloys: effect of processing parameters on microstructure and mechanical properties', International Journal of Mechatronics and Manufacturing Systems, 2021 Vol.14 No.2, pp.128 – 142. DOI: 10.1504/IJMMS.2021.119156.
[25] Komjaty, F., Wisznovszky, E.S., Culda L.I. (2021) 'Study on the influence of technological parameters on 3D printing with sla technology', MATEC Web of Conferences, 2021. https://doi.org/10.1051/matecconf/202134301003.
[26] Chand, R., Sharma, V.S., Rajeev, T. (2021) 'Investigating mechanical properties of 3D printed parts manufactured in different orientations on Multijet printer', Research Square, 2021. https://doi.org/10.21203/rs.3.rs-247844/v1.
[27] Vălean, C., Marșavina, L., Mărghitaș, M., Linul, E., Razavi, J. and Berto, F. (2020) 'Effect of manufacturing parameters on tensile properties of FDM printed specimens', Procedia Structural Integrity, 2020 Vol. 26, pp. 313–320. http://creativecommons.org/licenses/by-nc-nd/4.0/.
[28] Lüchtenborg, J., Burkhardt, F., Nold, J., Rothlauf, S., Wesemann, C., Pieralli, S., Wemken, G., Witkowski, S. and Spies, B.C. (2021) 'Implementation of Fused Filament Fabrication in Dentistry', Appl. Sci., 2021 Vol.11, 6444. https://doi.org/10.3390/app11146444
[29] Alam, F., Shukla, V.R., Varadarajan, K.M. and Kumar, S. (2020) 'Microarchitected 3D printed polylactic acid (PLA) nanocomposite scaffolds for biomedical applications', journal of the mechanical behavior of biomedical materials, 2020 Vol.103, 103576. https://doi.org/10.1016/j.jmbbm.2019.103576
[30] Meglioli, M., Naveau, A., Macaluso, G.M. and Catros, G. (2020) '3D printed bone models in oral and craniomaxillofacial surgery: a systematic review', 3D Printing in Medicine, 2020 Vol.6:30. https://doi.org/10.1186/s41205-020-00082-5.
[31] Favier, V., Zemiti, N., Caravaca Mora, O., Subsol, G., Captier, G., Lebrun, R., Crampette, L., Mondain, M. and Gilles, B. (2017) 'Geometric and mechanical evaluationof 3D-printing materials for skull base anatomical education and endoscopic surgery simulation - Afirst step to create reliable customized simulators', PLoS ONE, 2017 Vol.12(12). https://doi.org/10.1371/journal.pone.0189486
[32] Hochman, J.B., Kraut, J., Kazmerik, K. and Unger, B.J. (2014) 'Generation of a 3D Printed Temporal Bone Model with Internal Fidelity and Validation of the Mechanical Construct', Otolaryngology – Head and Neck Surgery, 2014 Vol.150(3), pp. 448–454. DOI: 10.1177/0194599813518008.
[33] Díaz-Álvarez, A., Díaz-Álvarez, J., Feito, N. and Santiuste, C. (2021) 'Drilling of biocomposite materials: Modelling and experimental validation', Simulation Modelling Practice and Theory, 2021 Vol. 106, 102203. https://doi.org/10.1016/j.simpat.2020.102203.
[34] Bajpai, P.K., Debnath, K. and Singh, I. (2017) 'Hole making in natural fiber-reinforced polylactic acid laminates: An experimental investigation', Journal of Thermoplastic Composite Materials, 2017 Vol.30(1), pp. 30-46. DOI: 10.1177/0892705715575094.
[35] Kumar, R., Kumar, M., Chohan, J.S. (2021) 'The role of additive manufacturing for biomedical applications: A critical review', Journal of Manufacturing Processes, 2021 Vol. 64, pp. 828-850. https://doi.org/10.1016/j.jmapro.2021.02.022.
[36] Colpani A., Fiorentino A., Ceretti E. (2018) '3D printing for health & wealth: Fabrication of custom-made medical devices through additive manufacturing', AIP Conference Proceedings 1960, 2018. ISBN 9780735416635. DOI 10.1063/1.5034998.
[37] Fiorentino A., Piazza C., Ceretti E. (2016) 'Anti-migration Enhanced Tracheal Stent Design, Rapid Manufacturing and Experimental Tests', Rapid Prototyping Journal, 2016, Vol.22(1), pp.178-188. ISSN 1355-2546. DOI 10.1108/RPJ-06-2014-0072.
[38] Fryman, J., Matthias, B. (2012) 'Safety of industrial robots: From conventional to collaborative applications', ROBOTIK 2012; 7th German Conference on Robotics, 2012 pp. 1-5. Munich, Germany.
[39] Rao, Y.V.D., Parimi, A.M., Rahul, D.S.P., Patel, D., and Mythreya, Y.N. (2017) 'Robotics in dental implantation', Materials Today: Proceedings, 2017 Vol.4(8), pp. 9327-9332. https://doi.org/10.1016/j.matpr.2017.07.292.

Chapter 6

Section 6.1

[1] J. Singh Chohan et al., Pre and post processing techniques to improve surface characteristics of FDM parts: a state of art review and future applications, Rapid Prototyping Journal, 23/3 (2017) 495–513.
[2] F. M. Mwema etal., Fused Deposition Modeling, Manufacturing and Surface Engineering.
[3] S. Vyavahare et al., Fused deposition modelling: a review, Rapid Prototyping Journal, 26/1 (2020) 176–201.
[4] N. Jayanth et al., Effect of chemical treatment on tensile strength and surface roughness of 3D-printed ABS using the FDM process, VIRTUAL AND PHYSICAL PROTOTYPING VOL. 13, NO. 3, (2018) 155–163.
[5] R. Anitha et al., Critical parameters influencing the quality of prototypes in fused deposition modelling, Journal of Materials Processing Technology, Vol. 118 Nos 1/3, (2001) 385-388.
[6] C.J.L. Pérez, Analysis of the surface roughness and dimensional accuracy capability of fused deposition modeling processes, International Journal of Production Research, Vol. 40 No. 12, (2010) 2865-2881.
[7] F. Lavecchia et al., Computer Numerical Controlled Grinding and Physical Vapor Deposition for Fused Deposition Modelled Workpieces, Advances in Materials Science and Engineering, (2018).
[8] L.M. Galantucci., Improvement of fused deposition modelled surfaces through milling and physical vapor deposition", (2014).
[9] R. Singh et al., Experimental investigations for surface roughness and dimensional accuracy of FDM components with barrel finishing", Proceedings of the National Academy of Sciences, India Section A: Physical Sciences, Vol. 87 No. 3, (2017) 455-463.
[10] T.H. Bhatia Singh et al., Performance analysis of vapour finishing apparatus for surface enhancement of FDM parts, Materials Today: Proceedings 26 (2020) 3497–3502.
[11] A. Garg et al., Chemical vapor treatment of ABS parts built by FDM: Analysis of surface finish and mechanical strength, Int J Adv Manuf Technol (2017) 89:2175–2191.
[12] S.N.H. Mazlan et al., Surface Finish and Mechanical Properties of FDM Part After Blow Cold Vapor Treatment, Journal of Advanced Research in Fluid Mechanics and Thermal Sciences 48, Issue 2 (2018) 148-155.
[13] A. Colpani et al., Characterization of chemical surface finishing with cold acetone vapours on ABS parts fabricated by FDM, Production Engineering 13(3), (2019) 437-447.
[14] C. Kuo et al., Polishing mechanism for ABS parts fabricated by additive manufacturing, Int J Adv Manuf Technol (2017) 91:1473–1479.

Section 6.2

[1] Monzón MD, Ortega Z, Martínez A, Ortega F (2015) Standardization in additive manufacturing: activities carried out by international organizations and projects. Int J Adv Manuf Technol 76(5-8):1111-1121.
[2] Chandramohan D, Marimuthu K (2011) Rapid prototyping/rapid tooling - A over view and its applications in orthopaedics. International Journal of Advanced Engineering Technology 2(4):435-448.
[3] Allegri G, Colpani A, Ginestra PS, Attanasio A (2019) An experimental study on micro-milling of a medical grade Co-Cr-Mo alloy produced by Selective Laser Melting. Materials 12(13):2208. https://doi.org/10.3390/ma12132208
[4] Gibson I, Rosen DW, Stucker B (2010) Additive manufacturing technologies. Springer-Verlag New York, New York, NY.
[5] Colpani A, Fiorentino A, Ceretti E (2018) 3D printing for health & wealth: Fabrication of custom-made medical devices through additive manufacturing. AIP Conference Proceedings 1960, 140006. https://doi.org/10.1063/1.5034998
[6] Vijayaraghavan V, Garg A, Jasmine SLL, Panda B, Mahapatra SS (2015) Process characterisation of 3D-printed FDM components using improved evolutionary computational approach. Int J Adv Manuf Technol 78(5-8):781-793.
[7] Sood AK, Equbal A, Toppo V, Ohdar RK, Mahapatra SS (2012) An investigation on sliding wear of FDM built parts. CIRP J Manuf Sci Technol 5: 48–54. DOI: 10.1016/j.cirpj.2011.08.003.

[8] Audiana V.U, Setiawan B,. Sumari A.D.W., Wibowo S. (2021) Control position of the double nozzles on the Y (+) and Y (-) axis of 3D symmetric bilateral printing using G-Code. IOP Conf. Ser.: Mater. Sci. Eng. 1073 012072
[9] Spoerk M, Gonzalez-Gutierrez J, Sapkota J, Schuschnigg S, Holzer C (2018) Effect of the printing bed temperature on the adhesion of parts produced by fused filament fabrication. Plastics, Rubber and Composites, 47:1, 17-24, DOI: 10.1080/14658011.2017.1399531.
[10] Gurrala PK, Regalla SP (2014) Part strength evolution with bonding between filaments in fused deposition modelling. Virtual Phys Prototyp 9(3):141-149. DOI: 10.1080/17452759.2014.913400
[11] Fiorentino A, Marenda GP, Ceretti E, Piazza C, Hendrichs N (2014) Challenges in design and production of customized tracheal stents. High Value Manufacturing: Advanced Research in Virtual and Rapid Prototyping - Proceedings of the 6th International Conference on Advanced Research in Virtual and Physical Prototyping, 597-602. DOI: 10.1201/b15961-109
[12] Ivanova O, Williams C, Campbell T (2013) Additive manufacturing (AM) and nanotechnology: Promises and challenges. Rapid Prototyping Journal 19(5).
[13] Ahn D, Kweon JH, Kwon S, Song J, Seokhee L (2009) Representation of surface roughness in fused deposition modelling. J Mater Process Tech 209:5593-5600. DOI: 10.1016/j.jmatprotec.2009.05.016
[14] Kalyan K, Singh J, Phull GS, Soni S, Singh H, Kaur G (2018) Integration of FDM and vapour smoothing process: Analyzing properties of fabricated ABS replicas. Materials Today: Proceedings 5:27902-27911
[15] Singh J, Singh R, Singh H (2017) Experimental investigations for dimensional accuracy and surface finish of polyurethane prototypes fabricated by indirect rapid tooling: a case study. Progress in Additive Manufacturing 2(1-2):85-97.
[16] Sood AK, Ohdar RK, Mahapatra SS (2009) Improving dimensional accuracy of Fused Deposition Modelling processed part using grey Taguchi method. Materials and Design 30:4243-4252. DOI: 10.1016/j.matdes.2009.04.030.
[17] Zamani J, Hemati MH, Morsaluie R (2014) An experimental comparison on dimensional accuracy of wax patterns of gas turbine blades produced by rapid tooling. Arabian Journal for Science and Engineering 39:7289-7297.
[18] Fiorentino A, Marenda GP, Marzi R, Ceretti E, Kemmoku DT, Da Silva JVL (2012) Rapid prototyping techniques for individualized medical prosthesis manufacturing. Innovative Developments in Virtual and Physical Prototyping - Proceedings of the 5th International Conference on Advanced Research in Virtual and Physical Prototyping, 589-594. DOI: 10.1201/b11341-94
[19] Huang X, Ye C, Wu S, Guo K, Mo J (2009) Sloping wall structure support generation for fused deposition modelling. Int J Adv Manuf Technol 42(11):1074-1081. DOI: 10.1007/s00170-008-1675-2
[20] Tamburrino F.,Barone S.,Paoli A., Razionale A:V. (2021) Post-processing treatments to enhance additively manufactured polymeric parts: a review, Virtual and Physical Prototyping, 16:2, 221-254, DOI: 10.1080/17452759.2021.1917039
[21] Castro-Casado D. (2021) Chemical treatments to enhance surface quality of FFF manufactured parts: a systematic review, Progress in Additive Manufacturing 6:307–319. https://doi.org/10.1007/s40964-020-00163-1
[22] Sardinha M., Vicente C.M.S., Frutuoso N., Leite M., Ribeiro R., Reis L. (2021) Mat Design Process Comm. 3:e151. https://doi.org/10.1002/mdp2.151
[23] Chohan JS, Singh R, Boparai KS (2016) Mathematical modelling of surface roughness for vapour processing of ABS parts fabricated with fused deposition modelling. Journal of Manufacturing Processes 24:161-169.
[24] Lavecchia F, Percoco G, Pei E.J, Galantucci L.M (2018) Computer Numerical Controlled Grinding and Physical Vapor Deposition for Fused Deposition Modelled Workpieces. Advances in Materials Science and Engineering 2018. doi:10.1155/2018/9037490.William RE, Melton VL (1998) Abrasive flow finishing of Stereolithography prototypes. Rapid Prototyping Journal 4:56-67. DOI: 10.1108/13552549810207279
[25] Singh R, Trivedi A, (2017) Experimental Investigations for Surface Roughness and Dimensional Accuracy of FDM Components with Barrel Finishing. Proc. Natl. Acad. Sci., India, Sect. A Phys. Sci. 87, 455–463. https://doi.org/10.1007/s40010-017-0367-4

[26] Lalehpour A, Barari A (2016) Post processing for Fused Deposition Modeling Parts with Acetone Vapour Bath. IFAC-PapersOnLine 49(31):42-48. DOI: 10.1016/j.ifacol.2016.12.159
[27] Kuo C, Mao R (2016) Development of a precision surface polishingsystem for parts fabricated by fused deposition modeling. Mater Manuf Process 31:1–6. https:// doi. org/ 10. 1080/ 10426 914.2015. 10905 94
[28] Kuo C, Chen C, Chang S (2017) Polishing mechanism for ABS parts fabricated by additive manufacturing. Int J Adv Manuf Technol 91(5–8):1473–1479
[29] Jayanth N, Senthil P, Prakash C (2018) Effect of chemical treatment on tensile strength and surface roughness of 3D-printed ABS using the FDM process. Virtual Phys Prototyp 13(3):155–163
[30] Garg A, Bhattacharya A, Batish A (2017) Chemical vapor treatment of ABS parts built by FDM: analysis of surface finish and mechanical strength. Int J Adv Manuf Technol 89:2175–2191. https:// doi. org/ 10. 1007/ s00170- 016- 9257-1
[31] Colpani A, Fiorentino A, Ceretti E (2019) Characterization of chemical surface finishing with cold acetone vapours on ABS parts fabricated by FDM. Prod Eng Res Devel 13(3):437–447. https:// doi. org/ 10. 1007/ s11740- 019- 00894-3
[32] Gao H, Kaweesa DV, Moore J, Meisel NA (2017) Investigating the impact of acetone vapor smoothing on the strength and elongation of printed ABS parts. JOM 69(3):580–585. https://doi. org/ 10.1007/ s11837- 016- 2214-5
[33] Kesvarakul R, Limpadapun K (2019) The study and development of factor affecting the smoothness in 3D printed part surface treatment via acetone vapor. Key Eng Mater 821:174–180. https://doi.org/ 10. 4028/ www. scien tific. net/ KEM. 821. 174
[34] Lalehpour A, Janeteas C, Barari A (2018) Surface roughness of FDM parts after post-processing with acetone vapor bath smoothing process. Int J Adv Manuf Technol 95:1505–1520. https:// doi. org/ 10. 1007/ s00170- 017- 1165-5
[35] Riva L, Fiorentino A, Ceretti E (2022) Characterization of the chemical finishing process with a cold acetone bath of ABS parts fabricated by FFF. Selected topics in manufacturing. Lecture notes in mechanical engineering. Springer, Cham. https:// doi. org/ 10.1007/ 978-3- 030- 82627-7_5
[36] International Organization for Standardization. (1996). Geometrical Product Specifications (GPS) — Surface texture: Profile method — Rules and procedures for the assessment of surface texture (ISO Standard No. 4288:1996). http:// store. uni. com/ catalogo/ en- iso- 4288- 1997/? josso_ back_ to= http:// store. uni. com/josso- secur ity- check. php& josso_ cmd= login_ optio nal& josso_partn erapp_ host= store. uni. com
[37] Montgomery D (2001) Design and analysis of experiments. Wiley 38. Vyavahare S, Kumar S, Panghal D (2020) Experimental study of surface roughness, dimensional accuracy and time of fabrication of parts produced by fused deposition modelling. Rapid Prototyp J 26(9):1535–1554. https:// doi. org/ 10. 1108/ RPJ- 12- 2019- 0315
[38] Vyavahare S, Kumar S, Panghal D (2020) Experimental study of surface roughness, dimensional accuracy and time of fabrication of parts produced by fused deposition modelling. Rapid Prototyp J 26(9):1535–1554. https:// doi. org/ 10. 1108/ RPJ- 12- 2019- 0315

Section 6.3

[1] Gastaldi D, Parisi G, Lucchini R, Contro R, Bignozzi S, Ginestra PS, Filardo G, Kon E, Vena P. A predictive model for the elastic properties of a collagen-hydroxyapatite porous scaffold for multi-layer osteochondral substitutes. 2015; 7(4): 1550063.
[2] Ginestra P, Ceretti E, Fiorentino A. Potential of modeling and simulations of bioengineered devices: enfoprostheses, prostheses and orthoses. Proceedings of the Institution of Mechanical Engineers Part H Journal of Engineering in Medicine 2016; 230 (7).
[3] Allegri G, Colpani A, Ginestra PS, Attanasio A. An experimental study on micro-milling of a medical grade Co-Cr-Mo alloy produced by selective laser melting. Materials 2019; 12 (13). Article number 2208.
[4] Ginestra P, Pandini S, Fiorentino A, Benzoni P, Dell'Era P, Ceretti E. Microstructured scaffold for cellular guided orientation : PCL electrospinning on laser ablated titanium collector. CIRP Journal of Manufacturing Science and Technology. 2017; 19: 147-157.

[5] Ginestra P, Fiorentino A, Ceretti E. Micro-structuring of titanium collectors by laser ablation technique: a novel approach to produce micro-patterned scaffolds for tissue engineering applications. Procedia Cirp 2017; 65: 19-24.
[6] Brouqui, P., Rousseau, M. C., Stein, A., Drancourt, M., & Raoult, D. Treatment of Pseudomonas aeruginosa-infected orthopedic prostheses with ceftazidime-ciprofloxacin antibiotic combination. Antimicrobial agents and chemotherapy. 1995; 39(11), 2423-2425.
[7] Moran, E., Masters, S., Berendt, A. R., McLardy-Smith, P., Byren, I., & Atkins, B. L. Guiding empirical antibiotic therapy in orthopaedics: the microbiology of prosthetic joint infection managed by debridement, irrigation and prosthesis retention. Journal of Infection. 2007; 55(1), 1-7.
[8] Hsieh, P. H., Lee, M. S., Hsu, K. Y., Chang, Y. H., Shih, H. N., & Ueng, S. W. Gram-negative prosthetic joint infections: risk factors and outcome of treatment. Clinical Infectious Diseases. 2009; 49(7), 1036-1043.
[9] Uækay, I., & Bernard, L. Gram-negative versus gram-positive prosthetic joint infections. Clinical infectious diseases. 2010; 50(5), 795-795.
[10] Janson, O., Gururaj, S., Pujari-Palmer, S., Ott, M. K., Strømme, M., Engqvist, H., & Welch, K. Titanium surface modification to enhance antibacterial and bioactive properties while retaining biocompatibility. Materials Science and Engineering: C. 2019; 96, 272-279.
[11] Cox SC, Jamshidi P, Eisenstein NM, Webber MA, Burton H, Moakes RJ, Grover LM. Surface finish has a critical influence on biofilm formation and mammalian cell attachment to additively manufactured prosthetics. ACS Biomaterials Science & Engineering 2017; 3(8): 1616-1626.
[12] Ginestra, P., Ceretti, E., Lobo, D., Lowther, M., Cruchley, S., Kuehne, S., Villapun, V., Cox, S., Grover, L., Shepherd, D., Attallah, M., Addison, O., Webber, M. Post processing of 3D printed metal scaffolds: A preliminary study of antimicrobial efficiency. Procedia Manufacturing 2020; 47, pp. 1106-1112.